HR EXCELLENCE IN RESEARCH

Jerzy Haber
INSTITUTE OF CATALYSIS AND SURFACE CHEMISTRY
POLISH ACADEMY OF SCIENCES

Mariusz Borkowski

Influence of liquid physicochemical properties on single bubble motion and stability of foam films and foams

PhD Thesis

Supervisor: dr hab. Jan Zawała

KRAKÓW 2023

Acknowledgments

For the Supervisor, without whom this thesis would not have been possible.

J. Z.

For the Best Friend, for every day motivation.

K. B.

For the One, who has always been behind me but now is absent.

A. K.

Summary 1
Streszczenie 7
List of symbols and abbreviations 15
Theoretical background 21
1. Introduction 23
2. Bubble motion in liquids 25
  2.1. Drag coefficient 25
  2.2. Temperature effect 29
3. Gas/liquid interfaces 31
  3.1. Fundamental adsorption models 31
  3.2. Helfand–Frisch–Lebowitz model 32
4. Thin liquid films 37
  4.1. Dynamic adsorption layer 37
  4.2. Symmetry of coverage 39
5. Foams 41
  5.1. Foam stability 41
  5.2. Synergistic systems 42
Experimental part 45
1. Influence of temperature on rising bubble dynamics in water and *n*-pentanol solutions - (**article D1**) 47
2. Experimental and theoretical study of adsorption of synthesized amino acid core-derived surfactants at air/water interface - (**article D2)** 51
3. Effect of initial adsorption coverage and dynamic adsorption layer formation at bubble surface in stability of single foam films - (**article D3)** 53
4. Coalescence of surface bubbles: The crucial role of motion-induced dynamic adsorption layer - (**article D4)** 55
5. Amino-acids surfactants and n-octanol mixtures – sustainable, efficient, and dynamically-triggered foaming systems - (**article D5)** 57
Concluding remarks 59
References 65
Academic achievements during PhD 73
Scientific articles attached 81
Co-authors declarations 83

Summary

The movement of a bubble in a solution of a surface-active substance, its collisions with the liquid/gas surface, and the accompanying adsorption process are elementary phenomena underlying the creation of dispersed systems that are very important from a practical point of view, i.e. foams. Bubble movement analyzed in **article D1**, stability of thin liquid film (TLF) discussed in **article D3** and **article D4**, as well as real foams discussed in **article D5**, depend on many physicochemical factors, including the presence and architecture of the dynamic adsorption layer (DAL) induced by a bubble movement. Analyzes of the local velocity profile (LVP) of an air bubble rising in a surfactant solution indicate two critical areas informing about the hydrodynamic boundary conditions at the liquid/gas interface: (i) the first, when the maximum velocity is reached, with more symmetrical adsorption layer and (ii) the second one, when the velocity reaches a limiting value and the distribution of surfactants becomes significantly asymmetric. In the second case, uneven distribution of adsorption coverage leads to the formation of a surface tension gradient, causing the so-called Marangoni effect, which is a surface flow in the direction opposite to the drag force of the continuous phase. This immobilizes the interface, inhibits the internal gas circulation inside the bubble, and increases the drag of the liquid medium, which manifests itself in a gradual reduction and then establishment of a constant (terminal) velocity of the rising air bubble, which is much lower than its velocity in a pure liquid. In recent years, many theoretical models have appeared, trying to explain and predict the kinetics of DAL formation in aqueous solutions of surfactants with different surface activities in a mathematical way. However, the basic limitation of the applicability of the existing models is the fact that they only describe stationary conditions, i.e. they allow for calculations of the bubble velocity for a fully formed DAL when the bubble velocity is constant (steady-state conditions). Currently, there is no general theory describing the kinetics of DAL formation in solutions of surfactants with different surface activity for a wide range of Reynolds numbers (Re). The bubble velocity depends primarily on the properties of the interphase boundary (which is modified by the adsorption of surfactants). In pure liquids, however, the basic parameter influencing the bubble velocity is the physicochemical properties of the continuous phase. In many industrial processes in which bubbles are a crucial element of the system (i.e. froth flotation, bioprocessing, food beverage manufacturing, oil recovery, foam generation and fractionation, treatment of wastewater, as well as in natural in oceans where aerosols are produced by rising bubbles, influencing the global climate), these properties are modified by changing the temperature of the liquid, which primarily affects its viscosity, density, and surface tension. Due to the controversy existing in the literature on the influence of temperature on the velocity of air bubbles in water, it was decided to conduct systematic research, which allowed for the formulation of many valuable conclusions (**article D1**). To verify the largely contradictory observations existing in the literature, LVP analyses were carried out using two independent techniques in thermostated conditions. An experimental approach was supported by the CFD (Computational Fluid Dynamics) numerical calculations. The first experimental approach was a well-known (classic) method based on recording (using a high-speed camera) and analyzing a sequence of photos of a rising bubble. The second, alternative method, described for the first time in the literature in this application, was the method of determining LVP using ultrasounds. Research supported by the CFD calculations showed that changes in liquid temperature in the range of $5-45°\ C$ do not change the hydrodynamic boundary conditions of a rising bubble in clean water, and its surface is completely mobile. Based on experimental relations and CFD calculations of the bubble shape for the tested temperature range, it was shown that the equilibrium diameter of the bubble changes as a function of temperature to a negligible extent. However, significant changes in bubble deformation were demonstrated, which could be predicted with very good accuracy based on existing semi-empirical models. Based on the dependences of the Webber and Reynolds numbers as a function of deformation and Moore's equations, the drag coefficient was determined, showing (according to the predictions assuming the total mobility of the liquid/gas interface for water) that the temperature, and more precisely associated changes in physicochemical parameters (density, viscosity, surface tension), practically do not change the value of this coefficient. Determined dependence of the Weber and Reynolds numbers as a function of temperature allowed for the derivation of empirical equations relating to the basic parameters describing the movement of an air bubble in water, which may have practical applications because these dependencies are satisfied in a wide range of Reynolds numbers. In the case of experiments with *n*-pentanol solutions, it was shown that the temperature causes the terminal velocity to be established more quickly. This rising velocity is lower for the higher temperature, which means that the increase in temperature causes (i) an increase in the adsorption coverage of the bubble surface (the coverage increases faster over time) and (ii) the DAL on the surface of the rising bubble is established faster and the liquid/gas surface becomes immobilized earlier. Both of these observations are consistent with the laws of diffusion. For the tested systems, it was also shown that the minimum bulk concentration of surfactant causing complete immobilization of the bubble surface (described based on the CMV parameter - Concentration at Minimum Velocity) is constant and does not depend on temperature.

An important phenomenon influencing the physicochemical properties of the gas/liquid interface and the stability of TLF (as described in **article D3** and **article D4)**, and finally the stability of real foams (as shown in **article D5)**, apart from the DAL formation (**article D1**), is the adsorption process itself. Because **article D5** describes the tests performed on real foams stabilized with new amino acid surfactants, an important issue was the description of the adsorption properties of these surfactants, which would allow for the determination of basic parameters related to their conformation and configuration in the adsorption layer. The research described in **article D2** shows an experimental and theoretical description of the adsorption properties of newly synthesized, "green" and biodegradable surfactants (AAS - Amino-Acid Surfactant), containing a hydrophilic part based on an amino acid molecule modified with an aliphatic C_{12} carbon chain. The study of the surface properties of AASs was based on measurements of equilibrium surface tensions using two independent measurement techniques, i.e. the Wilhelmy method and the bubble shape analysis method. The theoretical description of the adsorption properties was carried out based on the HFL (Helfand-Frisch-Lebowitz) isotherm, using additionally the results of parallel calculations by means of molecular dynamics and DFT (Density Functional Theory) methods. In addition to the description of the adsorption parameters of the tested amino acid surfactants, it was shown that the AASs have the ability to form hydrogen bonds (HB), which are of key importance in the case of characteristic ability of the AASs to reduce the surface tension and stabilize real foams (**article D5**).

The research described in **article D1** confirmed the significant impact of dynamic conditions and the presence and concentration of surface-active substances on the hydrodynamic boundary conditions on a moving liquid/gas surface. According to the literature on the subject, surface properties are a parameter that determines the stability of thin films (TLF), therefore, in the next stage, the influence of the presence of DAL on the drainage rate of single foam films formed in dynamic conditions was examined. The TLF stability tests for the considered hydrodynamic conditions were carried out in an automatic measurement system adapted to record the lifetime of a single bubble on the free surface of solutions. The experimental work was supplemented with theoretical calculations using the RDI (Radoev-Dimitrov-Ivanov) model describing the drainage kinetics of the foam film, which took into account the different architecture of the adsorption coverage at the liquid/gas interfaces. Calculations and experiments showed that the stability of the foam film varies, depending on whether the film is formed by a bubble colliding with the free surface of the surfactant solution at maximum or terminal velocity. For the first time, it was decided to look at the observed phenomenon quantitatively by determining directly the time evolution of the TLF thickness (**article D4**). Research using the interferometric method (Dynamic Fluid-Film Interferometry - DFI) showed a significant differences in the kinetics of films drainage depending on the DAL architecture, proving therefore strong impact of the DAL on the TLF stability.

In the last part of this dissertation (**article D5**), using the results of the experiments described in **article D1-D4**, the foaming properties of systems stabilized by the previously described AASs (**article D2**) were examined in mixtures with *n*-octanol - C_8OH (a model non-ionic surfactant that was used in the studies described in **articles D3 and D4**). The aim of these studies was to search for potential synergistic effects. The adsorption properties of the mixtures were checked by measuring the surface tension using the bubble shape analysis method. The foamability and foam stability of pure AASs solutions and their mixtures with *n*-octanol were tested using the DFA method (Dynamic Foam Analysis). Aggregation analysis was performed using the dynamic light scattering (DLS) method. The experimental results were supported by molecular dynamics (MD) calculations. It was shown that in the case of all tested AASs solutions, the addition of the C_8OH caused a synergistic effect, which, although small in the case of changes in equilibrium surface tension, was spectacular in the case of the solutions foamability. A thorough analysis of the tested systems showed that aggregates ,which did not form in pure solutions of both the AAS and C_8OH, were formed in mixed solutions. Time stability of aggregates depended on the AASs concentration . It has been proven that the synergistic effect observed in the foam formation process is a consequence of the development of micelles (aggregates). Under equilibrium conditions, they act as a buffer, stabilizing the surface tension and allowing its minor changes, only, while under dynamic conditions, when the interface area is rapidly developed, these aggregates may disintegrate supplementing the solution with molecules that stabilize the emerging foam films.

Streszczenie

Ruch pęcherzyka w roztworze substancji powierzchniowo-aktywnej, jego zderzenia z powierzchnią ciecz/gaz oraz towarzyszący temu proces adsorpcji, jest elementarnym zjawiskiem leżącym u podstaw tworzenia bardzo ważnych z punktu widzenia praktycznego układów zdyspergowanych, tj. pian. Ruch pęcherzyka analizowany z **artykule D1** oraz stabilność cienkich filmów pianowych (ang. TLF – Thin Liquid Film) omawianych w **artykule D3** i **D4**, jak również pian rzeczywistych (w **artykule D5)**, zależy od wielu czynników fizykochemicznych, w tym od obecności i architektury indukowanej ruchem pęcherzyka dynamicznej warstwy adsorpcyjnej (ang. DAL – Dynamic Adsorption Layer). Analizy profili prędkości (ang. LVP – Local Velocity Profile) pęcherzyka powietrza unoszącego się w roztworze surfaktantów wskazują dwa krytyczne obszary, informujące o hydrodynamicznych warunkach brzegowych na granicy faz ciecz/gaz: (i) pierwszy, kiedy to ustala się maksymalna prędkość, a warstwa adsorpcyjna jest bardziej symetryczna oraz (ii) drugi, kiedy to prędkość przyjmuje wartość graniczną, a rozkład surfaktantów staje się wyraźnie niesymetryczny. Ten ostatni, nierównomierny rozkład pokrycia adsorpcyjnego, prowadzi do powstania gradientu napięcia powierzchniowego, powodującego tzw. zjawisko Marangoniego, będące przepływem powierzchniowym w kierunku przeciwnym do działania siły oporu fazy ciągłej. Powoduje to unieruchomienie powierzchni międzyfazowej, zahamowanie wewnętrznej cyrkulacji gazu w pęcherzyku oraz wzrost oporu ośrodka ciekłego, co objawia się stopniowym zmniejszaniem, a następnie ustaleniem stałej prędkości unoszącego się pęcherzyka powietrza, która jest znacznie mniejsza niż jego prędkość w czystej cieczy. W ostatnich latach pojawiło się wiele teoretycznych modeli próbujących wyjaśnić i przewidzieć kinetykę tworzenia się DAL w roztworach wodnych surfaktantów o różnej aktywności powierzchniowej w sposób matematyczny. Podstawowym ograniczeniem stosowalności istniejących modeli jest fakt, iż opisują one tylko warunki stacjonarne, tj. pozwalają na obliczenie prędkości pęcherzyka dla w pełni utworzonej DAL, kiedy to prędkość pęcherzyka przyjmuje wartość stałą. Aktualnie nie istnieje ogólna teoria opisująca kinetykę tworzenia się DAL w roztworach związków powierzchniowo czynnych o różnej aktywności powierzchniowej oraz dla szerokiego zakresu liczb Reynoldsa. Prędkość pęcherzyka zależy przede wszystkim od właściwości granicy międzyfazowej (która modyfikowana jest poprzez adsorpcję substancji powierzchniowo czynnych). W czystych cieczach jednakże podstawowym parametrem wpływającym na prędkość są właściwości fizykochemiczne fazy ciągłej. W wielu procesach przemysłowych, w których pęcherzyki stanowią kluczowy element układu (tj.

flotacja, bioprzetwarzanie i produkcja napojów spożywczych, odzysk ropy naftowej, frakcjonowanie piany, oczyszczanie ścieków, a także w naturalnych oceanach, gdzie aerozole powstają w wyniku wznoszących się pęcherzyków, wpływając na globalny klimat), właściwości te modyfikowane są poprzez zmianę temperatury cieczy, która wpływa przede wszystkim na jej lepkość, gęstość oraz napięcie powierzchniowe. Z uwagi na istniejące w literaturze przedmiotu kontrowersje dotyczące wpływu temperatury na prędkości pęcherzyków powietrza w wodzie, zdecydowano się na przeprowadzenie systematycznych badań, które pozwoliły na sformułowanie wielu cennych wniosków (**artykuł D1**). W celu weryfikacji istniejących w literaturze, w dużej mierze wykluczających się obserwacji, przeprowadzono analizy LVP z wykorzystaniem dwóch niezależnych technik w warunkach termostatowanych, wspartych obliczeniami numerycznymi CFD (ang. Computational Fluid Dynamics). Pierwszą z nich była dobrze znana (klasyczna) metoda, oparta na analizie zarejestrowanych przy pomocy szybkiej kamery sekwencji zdjęć unoszącego się pęcherzyka. Drugą, alternatywną, pierwszy raz opisaną w literaturze w tym zastosowaniu, była metoda wyznaczana LVP z zastosowaniem ultradźwięków. Badania wsparte obliczeniami CFD wykazały, iż zmiany temperatury cieczy w zakresie $5-45°\,C$ nie powodują zmiany hydrodynamicznych warunków brzegowych unoszącego się pęcherzyka w czystej wodzie, a jego powierzchnia jest całkowicie ruchliwa. W oparciu o zależności eksperymentalne oraz obliczenia CFD kształtu pęcherzyka dla badanego zakresu temperatur wykazano, że średnica równowagowa pęcherzyka w funkcji temperatury zmienia się w stopniu zaniedbywalnym. Wykazano natomiast poważne zmiany w deformacji pęcherzyka, które z bardzo dobrą dokładnością można było przewidzieć na podstawie istniejących modeli półempirycznych. W oparciu o zależności liczb Webber'a oraz Reynolds'a w funkcji deformacji oraz równań Moore'a wyznaczono współczynnik oporu, wykazując (zgodnie z przewidywanymi wynikającymi z całkowitej ruchliwości granicy faz ciecz/gaz dla wody), że zmiany temperatury, a ściślej wynikające z nich modyfikacje parametrów fizykochemicznych cieczy (gęstość, lepkość, napięcie powierzchniowe), nie zmieniają praktycznie wartości tego współczynnika. Określenie zależności liczb Weber'a i Reynolds'a w funkcji temperatury pozwoliło na wyprowadzenie empirycznych równań wiążących ze sobą podstawowe parametry opisujące ruch pęcherzyka powietrza w wodzie, co może mieć praktyczne zastosowanie, ponieważ zależności te są spełnione w szerokim zakresie liczb Reynolds'a. W przypadku eksperymentów z roztworami *n*-pentanolu wykazano, że temperatura powoduje szybsze ustalenie się prędkości granicznej. Prędkość ta jest tym mniejsza, im wyższa jest temperatura, co oznacza, że wzrost temperatury powoduje (i) wzrost pokrycia adsorpcyjnego powierzchni pęcherzyka (pokrycie szybciej narasta w czasie) oraz, że (ii) DAL na powierzchni unoszącego się pęcherzyka jest szybciej ustalana i wcześniej dochodzi do unieruchomienia powierzchni ciecz/gaz. Obie te obserwacje są zgodne z prawami dyfuzji. Dla testowanych układów wykazano również, że minimalne stężenie objętościowe surfaktantu, powodujące całkowite unieruchomienie powierzchni pęcherzyka (opisane w oparciu o parametr CMV - ang. Concentration at Minimum Velocity) jest stałe i nie zależy od temperatury.

Ważnym zjawiskiem wpływającym na właściwości fizykochemiczne granicy faz gaz/ciecz i stabilność TLF, o którym mowa w **artykule D3** i **artykule D4**, oraz finalnie na stabilność rzeczywistych pian badaną w **artykule D5,** poza efektami hydrodynamicznymi generującymi powstawanie DAL (**artykule D1**), jest sam proces adsorpcji. Ponieważ w **artykule D5** opisano badania jakim poddawano piany rzeczywiste stabilizowane nowymi surfaktantami aminokwasowymi, ważnym zagadnieniem był opis właściwości adsorpcyjnych tychże surfaktantów, który pozwoliłby na określenie podstawowych parametrów związanych z ich konformacją oraz konfiguracją w warstwie adsorpcyjnej. Badania opisane w **artykule D2** dotyczą eksperymentalnego i teoretycznego opisu właściwości adsorpcyjnych nowo syntetyzowanych, „zielonych" i biodegradowalnych substancji powierzchniowo czynnych (AAS – Amino-Acid Surfactant), zawierających hydrofilową część opartą o cząsteczkę aminokwasu modyfikowaną alifatycznym łańcuchem węglowym C_{12}. Badanie właściwości powierzchniowych AASs opierało się na pomiarach równowagowych napięć powierzchniowych z wykorzystaniem dwóch niezależnych technik, tj. metody Wilhelmy'ego i metody analizy kształtu pęcherzyka. Teoretyczny opis właściwości adsorpcyjnych przeprowadzono w oparciu o izotermę HFL (ang. Helfand-Frisch-Lebowitz), wykorzystując do tego celu dodatkowo wyniki równolegle przeprowadzonych obliczeń metodami dynamiki molekularnej oraz DFT. Oprócz opisu parametrów adsorpcyjnych badanych surfaktantów aminokwasowych wykazano, że AASs mają zdolność tworzenia wiązań wodorowych (HB) co ma kluczowe znaczenie w przypadku ich charakterystycznego wpływu na zdolność obniżenia napięcia powierzchniowego i stabilizacji pian rzeczywistych (**artykule D5**).

Badania opisane w **artykule D1** potwierdziły istotny wpływ warunków dynamicznych oraz obecności i stężenia substancji powierzchniowo-aktywnych na hydrodynamiczne warunki brzegowe na poruszającej się powierzchni ciecz/gaz. Zgodnie z literaturą przedmiotu właściwości powierzchniowe są parametrem decydującym o stabilności cienkich filmów (TLF), dlatego w kolejnym etapie przebadano wpływ obecności DAL na szybkość wyciekania filmów pianowych utworzonych w warunkach dynamicznych. Badania stabilności TLF dla rozpatrywanych warunków hydrodynamicznych przeprowadzono w automatycznym systemie pomiarowym przystosowanym do optycznej rejestracji czasu życia pojedynczego pęcherzyka na swobodnej powierzchni roztworów (TLF). Prace eksperymentalne uzupełniono obliczeniami teoretycznymi z wykorzystaniem modelu RDI (Radoev-Dimitrov-Ivanov) opisującego kinetykę wyciekania filmu pianowego, który brał pod uwagę różną architekturę pokrycia adsorpcyjnego na granicach faz ciecz/gaz. Obliczenia oraz eksperymenty pozwoliły wykazać, że stabilność filmu pianowego jest różna, w zależności od tego, czy film ten tworzy pęcherzyk poruszający się w roztworze surfaktantu z maksymalną lub graniczną prędkością. Po raz pierwszy zaobserwowanemu zjawisku postanowiono przyjrzeć się w sposób ilościowy, wyznaczając kinetyki wyciekania TLF w sposób eksperymentalny (**artykuł D4**). Badania z wykorzystaniem metody interferometrycznej (ang. Dynamic Fluid-Film Interferometry - DFI) wykazały istotny wpływ DAL na dynamikę wyciekania filmów pianowych. Wykazane w sposób ilościowy (na podstawie zmierzonych wartości zmieniającej się w czasie grubości filmów) różnice w kinetyce wyciekania filmów świadczyły o istotnym wpływie DAL na modyfikację hydrodynamicznych warunków na powierzchni pęcherzyka.

W ostatniej części tej rozprawy (**artykule D5**), wykorzystując wyniki eksperymentów opisanych w **artykule D1-D4**, zbadano właściwości pieniące układów stabilizowanych opisanymi wcześniej AASs (**artykuł D2**) w mieszaninach z *n*-oktanolem (modelowym, niejonowym surfaktantem, który wykorzystywano w badaniach opisanych w **artykule D3** i **artykule D4**), poszukując potencjalnych efektów synergistycznych. Własności adsorpcyjne mieszanin sprawdzano poprzez pomiar napięcia powierzchniowego metodą analizy kształtu pęcherzyka. Spienialność czystych roztworów AASs oraz ich mieszanin z oktanolem, jak również stabilność piany testowano metodą DFA (ang. Dynamic Foam Analysis). Analizę agregacji przeprowadzono metodą dynamicznego rozpraszania światła (DLS - Dynamic Light Scattering). Wyniki eksperymentów poparto symulacjami metodą dynamiki molekularnej (MDS). Wykazano, że w przypadku wszystkich badanych roztworów AASs, dodatek C_8OH powodował efekt synergistyczny, który choć niewielki w przypadku zmian równowagowego napięcia powierzchniowego, był spektakularny w przypadku spienialności roztworów. Dokładna analiza badanych układów pozwoliła wykazać, że w mieszanych roztworach dochodzi do powstawanie agregatów masowych, które nie tworzą się w czystych roztworach zarówno AAS jak i C_8OH, a których stabilność czasowa jest zależna od stężenia AASs. Udowodniono, że przyczyną obserwowanego w procesie powstawania pian efektu synergistycznego jest rozwój miceli (agregatów). W warunkach równowagowych działają one na zasadzie buforu, stabilizując napięcie powierzchniowe i pozwalając tylko na niewielkie jego zmiany, natomiast w warunkach dynamicznych, kiedy dochodzi do szybkiego rozwinięcia powierzchni adsorpcyjnej, agregaty te mogą ulegać rozpadowi, dostarczając w ten sposób do roztworu cząsteczek stabilizujących powstające filmy pianowe.

List of symbols and abbreviations

Symbols:

A_{eff} – effective radii

A – area of surface

Ar – Archimedes number

a – spherical molecules of a diameter

b – adsorption constant

c – concentration

C_d – drag coefficient

d_b– bubble equivalent diameter

F_b– buoyancy force

F_d– drag force

G – Gibbs free energy

$G_{(\chi)}$ – geometric coefficients

$G(\lambda, \rho)$ – contact correlation function of molecules touching a λ-cule

$G(l, p)$ – contact radial distribution function, for pure systems of particles characterized by a diameter a

$G(1, \rho, \rho_\lambda)$ – contact radial distribution function between two typical molecules in a system

g – gravitational constant

$H_{(\chi)}$ – geometric coefficients

H_s – parameter describing molecular interactions between neighboring adsorbed surfactants

k – Boltzmann constant

L – distance between capillary and free solution surface

p – pressure

R – gas constant

R_b – bubble equivalent radius ($d_{eq}/2$)

Re – Reynolds number

S – entropy

T– temperature

u_t – bubble terminal velocity

$u(r)$ – molecule-molecule potential function

$u(r/\lambda)$ – molecule-solute interaction potential

V_b – bubble volume

W – work

We – Weber number

y_2 – close-packing varies

Greek symbols:

Γ – surface concentration

Γ_∞– limiting surface concentration

λ-cule

μ – chemical potential

ρ – density

ρ_l – liquid phase density

ρ – particle number density

ρ_λ– λ-cule density

$\rho G(\lambda, \rho)$ –density of rigid sphere molecules of diameter a in contact with a single "solute" sphere

σ – surface tension

χ – bubble deformation ratio

ω – single parameter related to the area per molecule in the close-packed surface layer

Abbreviations:

AAS – aminoacid surfactant

BoD – bubble-on-demand

C_{12}-Ala – *N*-lauroyl-L-alanine

C_{12}-Val – *N*-lauroyl-L-valine

C_{12}-Leu – *N*-lauroyl-L-leucyne

C_{12}-Pro – *N*-lauroyl-L-proline

C_{12}-Phe – *N*-lauroyl-L-phenylalanine

CMC – critical micelle concentration

CFD – computational fluid dynamics

CSC – critical synergistic concentrations

CCD – charge-coupled device camera

CTAB – *N*-hexadecyltrimethylammonium bromide

C_8OH– *n-octanol*

DTAB – *N*-dodecyltrimethylammonium bromide

DFT– density functional theory

DAL – dynamic adsorption layer

DFI – dynamic film interferometry

DNS – direct numerical simulations

DFA – dynamic foam analysis

DLS – dynamic light scattering

HB – hydrogen bonding

HFL – Helfand–Frisch–Lebowitz adsorption model

L-Ala – L-alanine

L-Val – L-valine

L-Leu – L-leucine

L-Pro – L-proline,

L-Phe – L-phenylalanine

LVP- local velocity profile

MDS – molecular dynamics simulations

NMR – nuclear magnetic resonance

RDI – Radoev-Dimitrov-Ivanov model

RSC – rear stagnant cap

SDS –sodium dodecyl sulfate

STDE – surface quasi-two dimensional electrolyte

TLF – thin liquid film

Triton X-100 – 2-[4-(2,4,4-trimethylpentan-2-yl)phenoxy]ethanol

Tween 20 – polyoxyethylene (20) sorbitan monolaurate

Tween 60 – polyoxyethylene (60) sorbitan monolaurate

Tween 80 – polyoxyethylene (80) sorbitan monolaurate

Theoretical background

1. Introduction

As shown in **Fig. 1** foam is a dispersed system consisting of a huge number of small air bubbles separated by a thin liquid film (TLF) in a continuous liquid phase. Moreover, TLF being a thin layer of the solution contains two adsorption layers (interfaces) stabilized with surface-active compounds or mixtures of them. In the second case, stabilizing synergistic or antagonistic effects can be considered. Foamability and foam stability are two crucial factors that can be used to define each foam-dispersed system created by TLFs. These two parameters mainly refer to how much foam a given system produces at a given airflow and how stable the obtained foam is over time. However, these two factors are closely related to the characteristics of the foam and the distribution of the size and shape of the bubbles creating TLF and finally the real foam. A convenient tool representing TLF-creating foam is a system in which a rising air bubble creates a TLF with a free surface of solution. The described situation is used as a laboratory model to predict the stability of foam films creating real foams and, ultimately, the foams themselves. Since the process of foam formation is a dynamic phenomenon, its contributions should be considered in the same categories. This means that the foam film can be formed under various conditions covering the surface of the bubble. Two cases of asymmetry in the distribution of surface coverage are considered: the first one is when the coverage is symmetrical, and the second one is when it is not symmetrical. The existence of both cases effectively differentiates factors such as disjoining pressure or Laplace pressure which have a strong influence on the stability of foam films created in these conditions. Complementary to the presented description of dynamic adsorption layer formation factors affecting TLF and its stability is the hydrodynamic description of the rinsing bubble. However, apart from the symmetry of the adsorption covering, another factor that has a huge impact on the stability of TLF as well as real foams is surfactants'

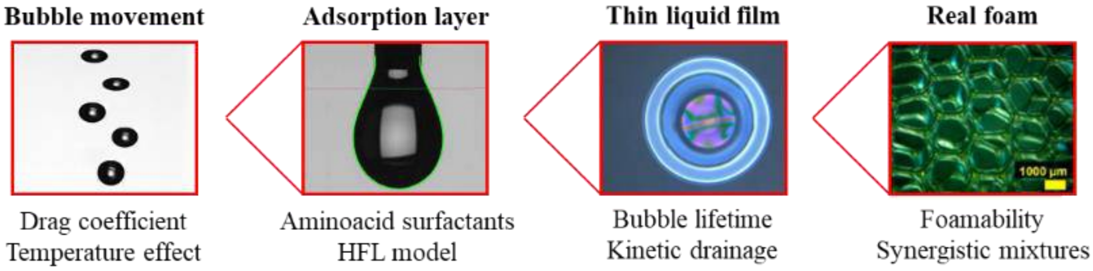

Figure 1. *From the hydrodynamic description of the air bubble rising, across the adsorption layer stabilized by aminoacid surfactants, described by the Helfand–Frisch–Lebowitz model, and estimation of stability of thin liquid films (DFI image) to stability of real foam stabilized by synergistic systems besis of aminoacid surfactants.*

adsorption at the interfaces. The theoretical description of the adsorption equilibrium using an appropriate adsorption model leads to obtaining fitting parameters characteristic for a given compound.

2. Bubble motion in liquids

Scientists have been fascinated by the phenomenon of a single bubble rising in water for many years. The gas bubbles motion in a liquid has huge practical importance and often determines the efficiency and overall profitability of industrial processes in chemical and petrochemical (oil recovery[1]), mineral processing industries (foam flotation[2, 3]) industrial processes (bioprocessing[4], food beverage manufacturing[5], foam fractionation, treatment of wastewater) as well as in natural (e.g. in oceans where aerosols are produced by rising bubbles, influencing the global climate[6–8]). For all of the aforementioned processes, the air bubble's drag coefficient while rising through the liquid medium is a parameter of crucial importance for a rising bubble dynamics.

2.1. Drag coefficient

The forces of gravity and drag are experienced by every body moving through a viscous material. In the case of a bubble, two scenarios are usually considered - movement in pure liquids and in surfactant (mostly aqueous) solutions. Regardless of the physicochemical parameters of the liquid, the theoretical description of the bubble movement and the calculation of its velocity require knowledge of the drag coefficient. For many years, scientists have tried to predict the C_d value by developing many models[9] (such for example Levich, Moore, and Clift models), both for pure liquids and surfactant solutions, to calculate the terminal velocity (u_T) of moving bubbles.

When the bubble rises with a terminal velocity u_T, under steady-state conditions, the force of buoyancy F_b is equal to the force of drag F_d of a continuous medium:

$$F_b = V_b \Delta\rho g \qquad \text{Eq. 1}$$

$$F_d = 0.5 A C_d \rho_l u_t^2 \qquad \text{Eq. 2}$$

where V_b is a bubble volume, $\Delta\rho$ is a difference between gas and liquid phases (for gas bubbles $\Delta\rho \approx \rho_l$), g is the gravitational constant, A is a bubble projected area and ρ_l is the density of a liquid phase. A comparison of these equations, assuming a bubble spherical shape, leads to the general equation for the u_T of a bubble rising in pure liquids and surfactant solutions:

$$u_T = \sqrt{\frac{4d_b\Delta\rho g}{3C_d\rho_l}} \qquad \text{Eq. 3}$$

Trivial mathematical transformations of Eq. 3, lead to the equation for the drag coefficient:

$$C_d = \frac{8R_b g}{3u_t^2} \qquad \text{Eq. 4}$$

where R_b is a bubble radius. This is a general formula that can be applied to any system when the bubble is moving at a terminal velocity. The bubble velocity can be calculated directly only for so-called creeping flow conditions, i.e. for very low Reynolds numbers ($Re << 1$), therefore for applications very limited from the practical point of view. For most of the interesting cases, the drag coefficient can be approximated using mathematical models, either purely theoretical or semi-empirical.

In general, according to the Moore theory the drag coefficient C_d for mobile liquid/gas interface (pure liquid) can be expressed as:

$$C_d = \frac{48}{Re} G_{(\chi)} \left[1 + \frac{H_{(\chi)}}{Re^{0.5}}\right] \qquad \text{Eq. 5}$$

The coefficients $G_{(\chi)}$ and $H_{(\chi)}$ are geometric coefficients, depending on the deformation of the bubble ($\chi = d_h/d_v$, where d_h and d_v are horizontal and vertical diameters, respectively), which can be approximated with good accuracy by the polynomial equations[10, 11]:

$$G_{(\chi)} = 0.4466\chi^2 + 0.4256\chi + 0.1287 \qquad \text{Eq. 6}$$

$$H_{(\chi)} = 0.0195\chi^4 - 0.2134\chi^3 + 1.7026\chi^2 - 2.1461\chi - 15732 \qquad \text{Eq. 7}$$

For the case of a bubble rising in pure liquids, where a liquid/gas interface is completely mobile (fluid), the early model was described by Levich[12]. It is satisfied for $Re > 50$ and the bubble diameter $d_b > 0.5\,mm$. Above this value, the ascending bubbles undergo strong deformation during the motion, leading to the adoption of a spheroidal shape, for which an increase in drag coefficients is observed. For those hydrodynamic conditions of medium flow, the Moore model is better fulfilled which assumes energy dissipation in the near-surface layer. Another description of the drag coefficient of a rising bubble was shown by Clift[13] in the form of a semi-empirical equation, which is fulfilled for $Re < 150$. A similar semi-empirical analysis was given by Masliyah et al.[14] for bubble motion in pure water, which is satisfied when $Re > 130$. A different approach to description of the drag coefficient was presented by Karamaneva[15, 16], who proposed an expression for the velocity of the bubble related to its geometry. In addition, the drag coefficient has been expressed more thoroughly - its value depended not on the Reynolds number but on the Archimedes number (Ar). Another description was proposed by Rodrigue et al.[17, 18] by applying characteristic flow (Fl) and velocity (Ve), whose values were introduced by Hassan[19]. Comparison of the models discussed above, with experimental data obtained for a wide range of bubble diameters by Pawliszak et al.[20] and Zawała & Niecikowska[21] is shown in **Fig. 1a**. The presented dependences show that no above-mentioned model allows for an accurate description of the bubble velocity within the broad diameter ranges. Also, Moore's model, which is assumed to show good agreement over a wide range of Re ($100 < Re < 10000$), does not allow for an accurate description of the bubble velocity for $d_b > 1.2\ mm$, which was previously noted by Clift et al.[13] and Duineveld et al.[22]. Such differences may result from different degrees of water purity, because bubble velocity is a very sensitive parameter to minimal impurities. A new approach to use the Moore model to calculate the velocity of deformed bubbles with a wide range of diameters: $0.6 - 2\ mm$, was shown by Manica[11], who applied empirical equation derived by Legendre et al.[9] to capture the bubble deformation. This model is shown in **Fig. 2a** as a pink line.

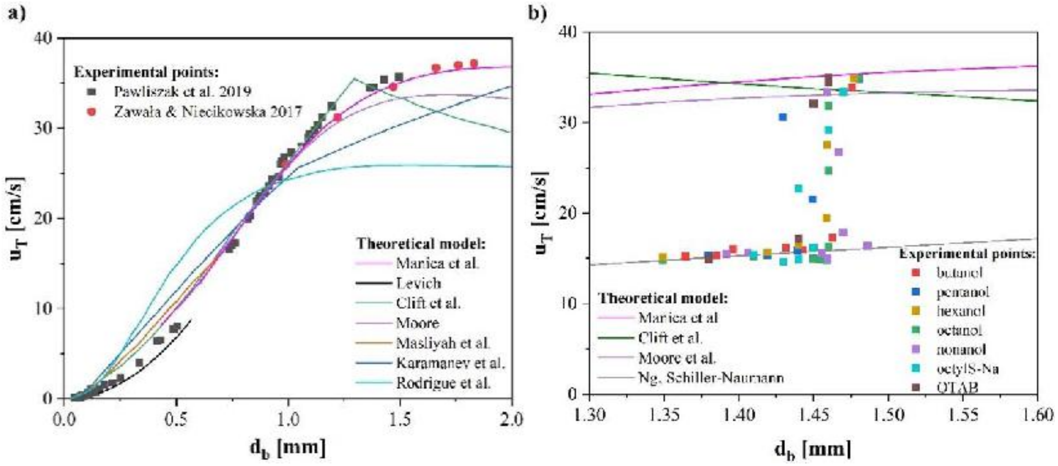

Figure 2. a) *Comparison of experimental values of bubble terminal velocity in pure liquids (points) with results calculated from various theoretical models (lines) for various bubble diameters.* ***b)*** *Comparison of experimental terminal bubble velocities in solutions of non-ionic and ionic surface-active substances (points) and theoretical predictions of selected models (lines), as a function of bubble diameter.*

In the case of bubble motion in a surfactant solution, the problem with the value of C_d is similar – it can be predicted only for very small Reynolds numbers. The main theoretical and experimental studies of ascending bubble motion in surfactant solutions are focused on the bubble motion with a completely immobilized surface. In this case, the bubble behaves as a solid sphere of similar density. Such bubble behavior is a consequence of motion-induced immobilization of the liquid/gas interface, caused by so-called dynamic adsorption layer (DAL) formation (more details on the DAL formation and structure are presented in **theoretical section 4.1**). The DAL means uneven distribution of surfactant molecules at a rising bubble surface, which causes surface tension gradients, and Marangoni stresses leading to a significant increase of the hydrodynamic drag of a continuous medium. It has been shown that in the case of laminar flow, the drag coefficient of a bubble with a completely immobilized interface can be described by the Stokes equation[13]. For much larger Reynolds numbers ($Re < 800$), it is possible to apply a model proposed by Schiller and Naumann[13]. On the other hand, Clift's analysis of the data for bubble motion in pure liquids and surfactant solutions allowed to derive a semi-empirical equation for the bubble terminal velocity[13]. Ng et al.[23, 24], according to the equation describing Oseen's law, proposed the value of the drag coefficient for $0.2 < Re < 20000$. Comparison of terminal bubble velocity calculated according to selected models with velocities determined experimentally are shown in **Fig. 2b**. Theoretical relations for the Clift, Moor, and Manica model for the bubble velocity in pure water are also shown, as well as the predictions of the Ng and Schiller-Naumann models, which assume complete immobilization of the liquid/gas surface.

As seen in **Fig. 2b**, the terminal velocity of a single bubble varies within the limits predicted by models developed for a completely mobile and completely immobilized liquid/gas interface. Intermediate velocities indicate only partial retardation of the fluidity of a bubble surface and depend strictly on the surfactant concentration and coverage of the dynamic adsorption layer. Existing models allow for determining the bubble terminal velocity, only (i.e. under steady-state conditions, when the DAL is fully formed at the bubble surface, there is a balance between F_b and F_d, and C_d is practically constant). Unfortunately, there is no general theory describing the kinetics of DAL formation, therefore, up to now, it is not possible to predict initial bubble velocity variations (before terminal velocity establishment) for a wide range of Re (despite several latest attempts[25]).

2.2. Temperature effect

The influence of liquid temperature on bubble motion parameters has not been fully systematized so far, although this effect has significance for engineering and industrial applications. In the literature many different, sometimes even contradictory data are shown, and the current knowledge on this effect is incomplete. As an example the data on bubble terminal velocities as a function of temperature for pure water presented by Leifer et al.[26], are shown in **Fig. 3a**. Experiments for different liquid temperatures ranging from 0 to 40° C showed a decrease in the rising terminal velocity, the magnitude of which was influenced by the bubble diameter.

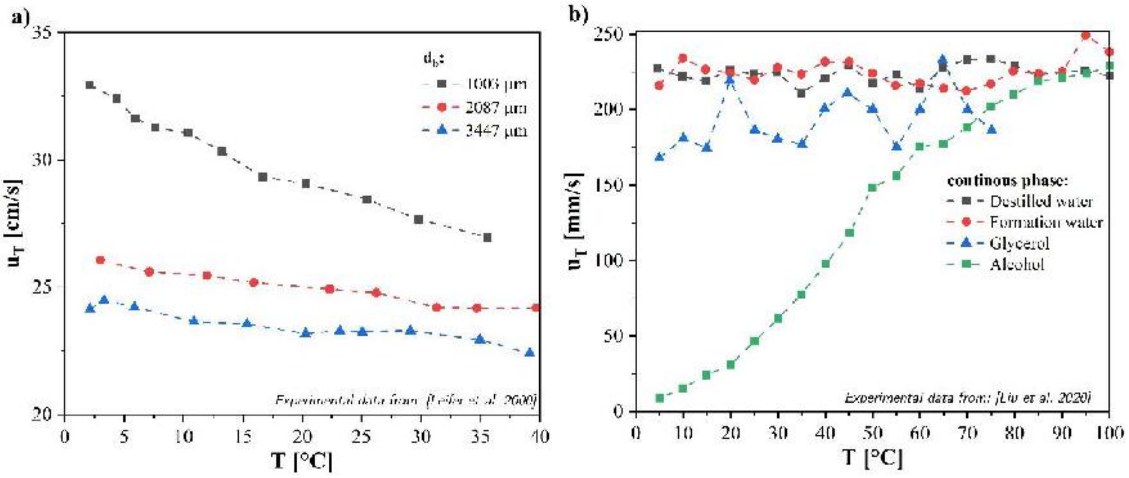

Figure 3. a) *Noted rise terminal bubble velocity as a function of temperature for 1003, 2087, and 3447 μm mean radius bubbles.* ***b)*** *Bubble terminal velocity vs. temperature in different stagnant liquids.*

Similar studies but with opposite conclusions were conducted by Issaoui and Ben Mansour[27] for the motion of bubbles between 30 and 60° C. These experiments indicated a slight increase in bubble velocity with increasing temperature. Zhang et al.[28] showed the profiles of bubble velocity in tap water and Triton X-100 surfactant solutions in the temperature range of $6 - 40°\ C$. The conducted research has shown that the maximum and final velocity of the bubbles also increases with the increase in temperature (**Fig. 4a-c**). Moreover, they proved that the terminal velocity of the bubble was reached faster when the temperature was higher.

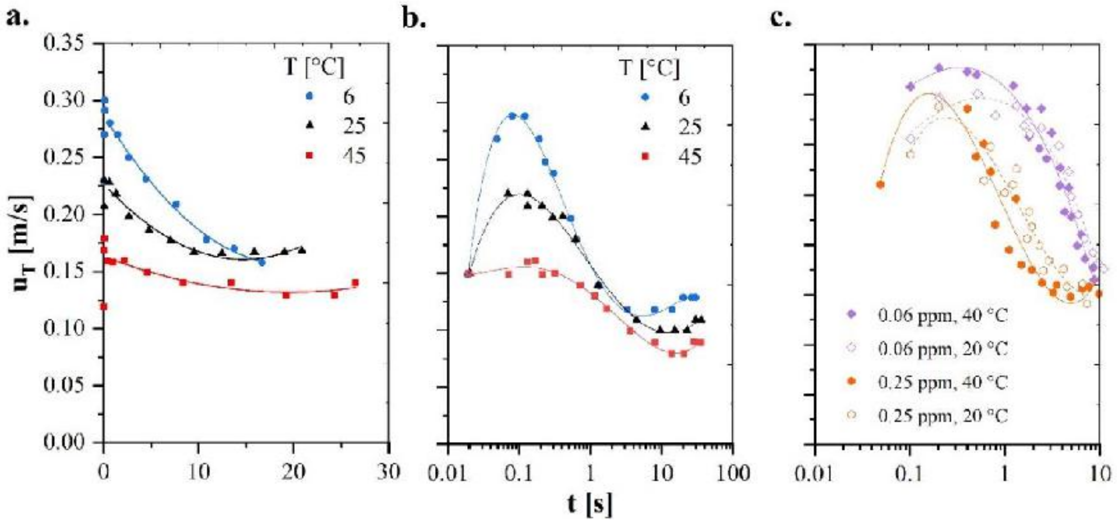

Figure 4. a) *The velocity profiles for an ascending bubble with* $d_b = 0.8\,mm$ *in tap water in various three temperatures.* ***b)*** *The velocity profiles for an ascending bubble with* $d_b = 0.8\,mm$ *in* $12.5\,x\,10^{-5}\,M$ *aqueous solutions of Triton X-100 in various three temperatures.* ***c)*** *The velocity profiles of ascending bubbles with* $d_b = 1.5\,mm$ *for solution in the variation of temperature and concentration of Dowfroth 250.*

In contrast, practically no temperature influence on the terminal velocity in distilled water for $0 - 100°\,C$ for a bubble of $3.3 - 6.1\,mm$ has been shown by Liu et al.[29] (**Fig. 4b**).

Okawa et al.[30] studied the temperature effect on a single bubble rise in distilled water, but this work was focused mostly on a comparison between the influence of the temperature on bubble path oscillations and the method of bubble formation. Only two temperature values, low ($15°\,C$) and high ($90°\,C$) were studied, and in the majority of cases, the terminal velocities differed significantly from the theoretical predictions, assuming slip boundary conditions at the liquid/gas interface.

The presented literature is controversial and shows contradictory results. This was the main reason to study the influence of temperature on the drag coefficient of a single rising bubble in pure water as well as in a surfactant solution, to verify the dependence of the C_d value on the liquid temperature. The results of these studies are discussed later in the experimental part of this thesis (**1 chapter of the experimental section, based on article D1**).

3. Gas/liquid interfaces

The rising of an air bubble in surfactant solutions, properties of the dynamic adsorption layer, stability of thin liquid films as well as real foams are influenced by adsorption processes. Therefore, this chapter takes into consideration the adsorption of surfactants at the interface with particular attention to the description of the adsorption properties of a new class of biodegradable, green, highly surface-active amino acid surfactants AASs. Description of the adsorption properties of surfactants is carried out by the use of mathematical models that allow obtaining adsorption parameters such as adsorption constant b, surface concentration Γ, and area per one adsorbed molecule ω, for which the properties of the tested compounds can be compared.

3.1. Fundamental adsorption models

The thermodynamic Gibbs model assumes a mathematically divided surface with arbitrarily chosen interfacial regions. The properties of this virtual space-dividing surface are zero thickness and volume[31]. The main assumption of this model is to change its parameters discretely; in both phases, the concentration of component i is constant. Considering the surface equilibrium conditions in the bulk, surface tension (σ) can be expressed by the following equation:

$$\sigma = \left(\frac{\partial \mathrm{G}}{\partial \mathrm{A}}\right)_{T,p,i} \qquad \text{Eq. 8}$$

where G is Gibbs free energy and A is an area, thus, the Gibbs adsorption isotherm can be formulated as:

$$\Gamma = -\frac{1}{RT}\frac{d\sigma}{dlnc} \qquad \text{Eq. 9}$$

where c is its bulk concentration, R is the gas constant and T is temperature. Nevertheless, the afore-provided description covers only the basis behind the well-known Gibbs model, thus, one should note that a wide variety of models aiming to describe interface adsorption processes exist, and the Gibbs model is just one of them. Other more complex models based on the Gibbs model are models such as a model for describing proteins[32–34] taking into account the conformation of the protein, surface quasi-two dimensional electrolyte (STDE) model proposed by Warszyński et al.[35, 36, 37], where the importance of the charge is considered. One of the important models is the Frumkin model, which is an extension of the Langmuir model and assumes interactions of hydrocarbon chains.

The Frumkin adsorption model can be derived based on assumptions of the Langmuir model, however, it additionally presumes additional interactions between molecules in the adsorption layer[38, 39]. The isotherm's formula can be expressed as[40]:

$$bc = \frac{\Gamma\omega}{1 - \Gamma\omega} e^{-2H_s\Gamma\omega} \qquad \text{Eq. 10}$$

where H_s is the parameter describing molecular interactions between neighboring adsorbed surfactants. It should be noted that for $H_s = 0$, the term $e^{-2H_s\Gamma\omega}$ is equal to 1, which means that the Frumkin isotherm is simplified to the Langmuir isotherm. Solving Frumkin's isotherm (Eq. 10) numerically leads to obtaining a non-trivial dependence of $\Gamma_{(c)}$, as compared with the Langmuir approach. The advantage of this model is that it describes the adsorption of many types of surfactants more accurately.

This model was used in the first attempt to describe the adsorption properties of amino acid surfactants. Satisfactory fitting parameters were achieved for equilibrium surface tension, but not for dynamic conditions. Bearing in mind these preliminary results for the Frumkin model, another model was used, i.e. Helfand–Frisch–Lebowitz model, for which satisfactory fitting parameters were obtained (see discussion in **2 chapter of the experimental section, based on article D2**). Therefore, the next chapter contains a detailed description of the model used in the experimental part.

3.2. Helfand–Frisch–Lebowitz model

The HFL (Helfand–Frisch–Lebowitz) isotherm is based on the assumption that molecules are two-dimensional, hard disk-like particles[41]. The HFL approach relies on defining first a radial distribution function $G(\lambda, \rho)$, such that $\rho G(\lambda, \rho)$ is the density of the rigid, spherical molecules of a diameter a, which are in touch with a single "solute" sphere of a diameter b, where: $\lambda a = {}^{1}\!/_{2}\,(a + b)$ with ρ being the particle number density (N/A). The importance of λ can be seen when considering a typical molecule-molecule potential function - $u(r)$, employing λ allows to evaluation of the molecule-solute interaction potential, which is given by $u(r/\lambda)$. As a result, even for more complex potentials, the solute is effectively a scaled-down version of the regular molecules. Such a scaled particle has been termed an λ-cule. The value of λ can vary from 0 to infinity. When $\lambda = O$, the λ-cule is able to completely penetrate all molecules and become a free particle. On the other hand, when it increases to $\lambda = {}^{1}/_{2}$, it is considered critical, because it is the first point at which the λ-cule may interact with more than one molecule at the same time. When $\lambda = 1$, it implies that $b = a$, making the λ-cule particle the same as the other molecules. Thus $G(1, \rho)$ should be considered as a contact radial distribution function, for pure systems of particles characterized by a diameter a. Finally, when the value λ approaches to ∞ , the λ-cule may be seen as a planar rigid wall.

The pressure p, and chemical potential μ, of a two-dimensional fluid of rigid spheres, are given by:

$$\frac{p}{\rho kT} = 1 + \frac{1}{2}\pi\rho a^2 G(1, \rho) \qquad \text{Eq. 11}$$

$$\frac{\mu}{kT} = ln\rho\Lambda^2 + 2\pi\rho a^2 \int_0^1 \lambda \mathrm{G}(\lambda, \rho)\mathrm{d}\lambda \qquad \text{Eq. 12}$$

The work W, arising from expanding the λ-cule, can be evaluated by computing the correlation function of the contacting molecules, as in the equation:

$$G(\lambda, \rho) = (2\pi\rho a^2 \lambda kT)^{-1} \frac{\partial W(\lambda)}{\partial \lambda} \qquad \text{Eq. 13}$$

For $\lambda < {}^{1}/_{2}$:

$$G(\lambda, \rho) = \frac{1}{(1 - \pi\rho a^2 \lambda^2)} \qquad \text{Eq. 14}$$

Moreover, introducing the thermodynamic relation $p = \int_0^\rho \rho'(\partial \mu/\partial \rho')_T \, d\rho'$, allows to express the G parameter to be expressed in terms of p and μ, as written below:

$$\frac{1}{2}\pi\rho^2 G(1, \rho) = \rho^2 \int_0^1 2\pi\lambda G(\lambda, \rho) d\lambda - \int_0^\rho \rho' d\rho' \int_0^1 2\pi\lambda G(\lambda, \rho') d\lambda \qquad \text{Eq. 15}$$

Eq. 15 can be simplified by introducing Eq. 14, and differentiating with respect to p:

$$\rho^2\frac{\partial \mathrm{G}(1,\rho)}{\partial \rho}+2\rho G(1,\rho)$$

$$=\frac{1}{2}\left(\frac{\rho}{1-(\frac{\pi\rho}{4})}\right)+4\rho\int_{1/2}^{1}\lambda G(\lambda,\rho)d\lambda+4\rho^2\int_{1/2}^{1}\lambda\frac{\partial \mathrm{G}(\lambda,\rho)}{\partial \rho}d\lambda \qquad \text{Eq. 16}$$

Finally, an infinite condition has been found by equating Eq. 11 to $p/kT=\rho G(\infty)$, which holds in two dimensions as well:

$$G(\infty)=1+\frac{1}{2}\pi\rho a^2 G(1) \qquad \text{Eq. 17}$$

If the form of G in λ is known, these conditions can be used to determine the equation of state. The G function is related to a function Q by the equation:

$$Q(\lambda,\rho)=-\rho a^2\int_0^{\lambda}2\pi\lambda' G(\lambda',\rho)d\lambda'-\rho^2a^2$$

$$\int_0^{\lambda}2\pi\lambda'\frac{\partial \mathrm{G}(\lambda',\rho)}{\partial \rho}d\lambda'+\pi\rho a^2\lambda^2 G(\lambda,\rho) \qquad \text{Eq. 18}$$

and Q is formulated by:

$$Q(\lambda,\rho)=-\frac{1}{2}\pi\rho^2a^2\frac{\partial \mathrm{G}\big(1,\rho,\rho_\lambda\big)_{\rho_\lambda}}{\partial \rho_\lambda}=0 \qquad \text{Eq. 19}$$

where: $G(1,\rho,\rho_\lambda)$ is the contact radial distribution function between two typical molecules in a system, with a molecular density of ρ, and for λ-cule density equal to ρ_λ. When differentiating the functions G and Q with respect to λ, certain derivatives may exhibit discontinuities, which implies that these functions can be closely approximated only by analytical solutions. The form which interpolates a $\lambda=\infty$ and $\lambda={}^{1}/_{2}$ reducing behavior of Q is:

$$Q(\lambda,\rho)=\omega(\rho)\left(\lambda-\frac{1}{2}\right)^2 \qquad \text{Eq. 20}$$

Eq. 18 shows that such a Q is consistent with a G of the form:

$$G = \phi(\rho\lambda^2) + A(\rho) + \frac{B(\rho)}{\lambda} \qquad \text{Eq. 21}$$

The function $\phi(\rho\lambda^2)$ vanishes, because when considering the limit $\rho\lambda^2 = \text{const.}$ leads to the G function in form:

$$G = A(\rho) + \frac{B(\rho)}{\lambda} \qquad \text{Eq. 22}$$

The fundamental thermodynamic equation for work, i.e. $dW = pdV + \sigma dS$, when describing the expanding of a λ-cule, is expressed as:

$$dW = 2\pi pa^2\lambda d\lambda + 2\pi\sigma ad\lambda \qquad \text{Eq. 23}$$

where the σ is independent of λ, by Eq. 13, is entered into the form (Eq. 22) for λ.

Using the continuity of G to match (Eq. 21) to (Eq. 14) at $\lambda = 1/2$ and the infinity condition (Eq. 17), the parametric functions of p, $A(\rho)$, and $B(\rho)$ may be found. As a substitute for the infinity requirement, the integral equation (Eq. 15) can be employed. The equation of state obtained in this manner is:

$$\frac{p}{\rho kT} = \frac{1}{(1 - y_2)^2} \qquad \text{Eq. 24}$$

where $y_2 = \pi\rho a^2/4$ for close packing varies from 0 to 0.907.

The complete function $G(\lambda, \rho)$ is determined by:

$$G(\lambda, \rho) = [(1 - y_2)^2]^{-1} + 1/2\{(1 - y_2)^{-1} - [(1 - y_2)^2]^{-1}\}\lambda^{-1} \qquad \text{Eq. 25}$$

Following Eq. 13, 22, and 23, relates to the surface tension by the following formula:

$$\frac{\sigma}{\rho akT} = \frac{1}{2}[(1 - y_2)^{-1} - (1 - y_2)^{-2}] \qquad \text{Eq. 26}$$

4. Thin liquid films

Motion of a single bubble can be considered as an elementary act of a foam formation, which is formed when the number of bubbles arriving at the solution surface exceeds the number of rupturing ones. The stability of foams (similar to other dispersed systems), strictly depends on the stability of the separating thin liquid (foam) films (TLFs). Bubbles' coalescence and timescale of foam collapse can be correlated to the kinetics of drainage of TLFs, which rupture when so-called critical thickness (associated with intermolecular interactions) is reached. In the literature, there are many different approaches for the assessment of a single TLF stability. In this thesis, the approach allowing consideration of dynamic conditions of the TLFs formation was used. The stability of foam was assessed by measurements of single bubble stability at a solution surface. In this type of experiment, it is possible to consider the influence of the "bubble history" before the TLF formation, mainly a state of the dynamic adsorption layer on the stability of the TLF formed under dynamic conditions. The effect related to the state of DAL and the stability of the foam film formed under such conditions was investigated by two independent approaches: (i) quantitative (single bubble lifetime technique – see discussion **in chapter 3 of the experimental section, based on article D3**) and (ii) qualitative (interferometric methods – **chapter 4 of the experimental section, based on article D4**).

4.1. Dynamic adsorption layer

In contrast to a bubble at rest, a gas bubble rising in a solution of a surface-active substance (SAS) has a distinct, specific distribution of adsorption layer[42] (DAL - Dynamic Adsorption Layer). The continuous medium's viscous drag, which pulls adsorbed surfactant molecules toward the rear of the bubble, causes the DAL to form. As a result, the top pole of the bubble has a depletion zone, and in the limiting scenario, can be entirely devoid of surfactant molecules[42]. According to Levich's analysis, a rising bubble surface's leading pole continuously expands as its rear portion is compressed[43]. Adsorbing molecules fill the newly formed part of the bubble surface, while the adsorbed surface-active molecules must desorb in the compressed rear part. As a result, the bubble surface covering exhibits a concentration gradient that leads to the Marangoni effect which immobilizes the surface, with the $\Gamma(\theta)$ increasing in the direction perpendicular to the bubble motion. The amount of adsorbed surfactants increases from the leading pole

$(\theta = 0)$ to the rear pole $(\theta = \pi)$ (see **Fig. 5b**). In a limiting scenario, the leading part of the bubble is almost completely free of surfactant molecules and mobile, while the rear part, where so-called "rear stagnant cap" (RSC) is formed, is covered by a compressed adsorption layer and remain immobile. The cap angle ψ (**Fig. 5b**) can be used to identify the RSC when there is a strong transition between these two portions. As a result, the adsorption layer on the surface of a rising bubble differs from that of a bubble at rest. Dynamic adsorption layer is the name given to such an adsorption layer that depicts a concentration gradient along the surface. A quantitative dynamic theory should therefore take into consideration the common solution of the diffusion equation, but it also has to include how surface motion affects the adsorption-desorption processes. The impact of the adsorption layer on the motion of the surface must also be incorporated into the hydrodynamic equations. However, a quantitative DAL theory is necessary for this purpose.

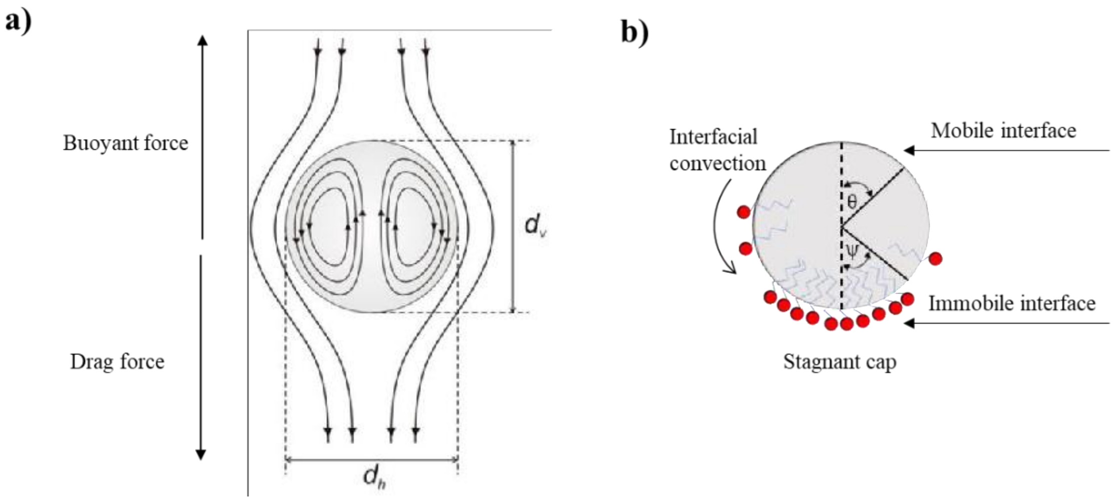

***Figure 5. a)** Diagrammatic visualization of the gas circulations inside a bubble moving in liquid. **b)** The SAS molecule's distribution in homogeneous at the surface of a rising bubble in surfactant solutions.*

The fact that present theories have only addressed the structure of the DAL under steady-state conditions (bubble terminal velocity) is a severe disadvantage. The formation of the DAL is a dynamic process having its own kinetics, which depends on surface-activity and concentration of surfactants. These kinetics of the DAL formation can be tracked by the monitoring of the bubble motions and determination of the bubble LVP. For a proper description of the stage of DAL formation (before steady-state conditions) for a quantitative interpretation of experimental data, a determination of the non-steady DAL theory is needed.

4.2. Symmetry of coverage

Depending on the stage of the DAL formation, influencing the architecture of the adsorption layer, bubbles, during mutual collisions, can form symmetrical or non-symmetrical liquid films. The stability (lifetime) of a non-symmetrical foam film is always different from that of a symmetrical one with initial equilibrium and non-equilibrium surfactant coverage on both interfaces. This is because the magnitude of the surface tension gradients induced, and thus the surface rheological properties of the foam films, are determined not only by the average degree of adsorption coverage but also by surfactant distribution during the foam film formation. Due to the flow of the solution out of the thinning film in the case of the symmetrical film, surface concentration gradients are induced, and both surfaces can be partially or completely immobilized. The upper interface of the non-symmetrical film has the equilibrium surfactant surface concentration, whereas the lower interface formed by the top part of the rising bubble is assumed to be initially surfactant depleted. It means that, while the fluidity of upper surface of the film can be retarded, the lower surface is completely mobile.

The main experimental studies on the stability of foam films formed in dynamic conditions as pioneers were conducted by Jachmiska, Warszyński & Małysa[44,45]. The direction of these studies was based on the determination of the stability of foam films formed in conditions when a symmetrical and non-symmetric foam film is formed with a non-equilibrium surface coverage[44]. The average lifetime of the bubbles was found to be shorter when the free surface of the n-butanol solution was placed farther ($L = 39.5\ cm$) from the point of a bubble formation than when the surface was placed closer ($L = 4\ cm$). The same research team conducted similar experiments for n-octanol solutions. **Fig. 6** shows how the concentration of **a)** n-butanol and **b)** n-octanol solution affects the average duration of bubbles at the solution surface located "far" and "close". Results shown as squares are related to locations "close", while results for locations "far" are shown as hollow squares. The bubble durations (lifetimes) are longer for location "close" ($L = 4\ cm$) across the whole range of the examined for n-butanol and n-octanol concentrations.

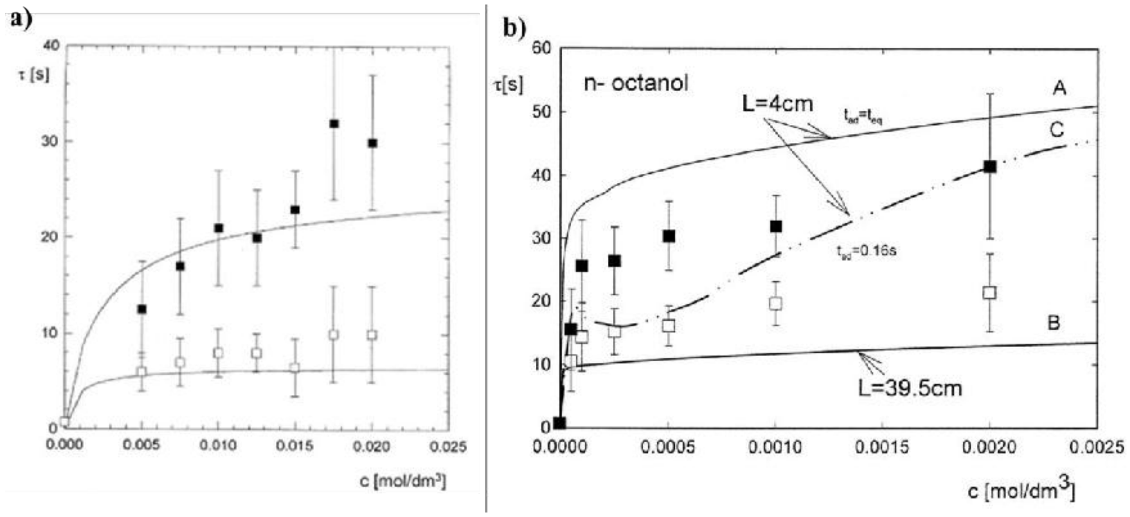

Figure 6 a) *The average bubble lifetime for n-butanol solutions concentration for a distance of* 4 *cm (close square) and* 39.5 *cm (open square) from capillary to the free solution surface (Reproduce from Jachimska et al.*[44]*).* ***b)*** *The average bubble lifetime for n-octanol solutions concentration for a distance of* 4 *cm (close square) and* 39.5 *cm (open square), (taken from Jachimska et al.*[45]*).*

Due to the fact that there are no direct methods to show if a dynamic adsorption layer exists at a rising bubble surface, the experiments described above were used to prove it indirectly. Jachmiska, Warszyśki & Małysa tried to check whether DAL is formed and affects the stability of a single foam film and the kinetics of its coalescence. In this sense, the lifetime of a bubble at a solution surface was used as a sensitive probe of the film’s interfacial properties.

In the experimental part **(chapter 3 of the experimental section, based on article D3)**, the extension of the method developed by Jachmiska, Warszyśki & Małysa (with a bubble trap allowing control over bubble adsorption coverage) was presented. In addition, for the first time, variations in foam film drainage kinetics caused by the DAL existence were determined quantitatively using a specially designed set-up employing the dynamic interferometry method **(chapter 4 of the experimental section, based on article D4).**

5. Foams

The ability of a foam to hold its shape and fend off collapse over time is referred to as foam stability. For many industrial uses, including the processing of food and drink, cosmetics, and oil and gas extraction, it is crucial to comprehend foam stability. The most common foams employed in formulations are aqueous foams, which are gas dispersion in aqueous solutions. However, due to their thermodynamic instability, these systems defoam by evaporation, coarsening (also known as Ostwald ripening), liquid drainage, and coalescence, among other defoaming mechanisms. Foam stabilization has traditionally involved the use of polymers, surfactants, or combinations of these materials. Therefore, these types of systems are constantly being developed, not only to achieve high industrial parameters but also to be in harmony with the environment.

5.1. Foam stability

Foam is defined as a two-phase system in which gas is dispersed in a liquid. A liquid film's face between two bubbles is a lamella, and junctions with three or more bubbles are plateau boundaries. A vertex is created where four Plateau borders intersect.

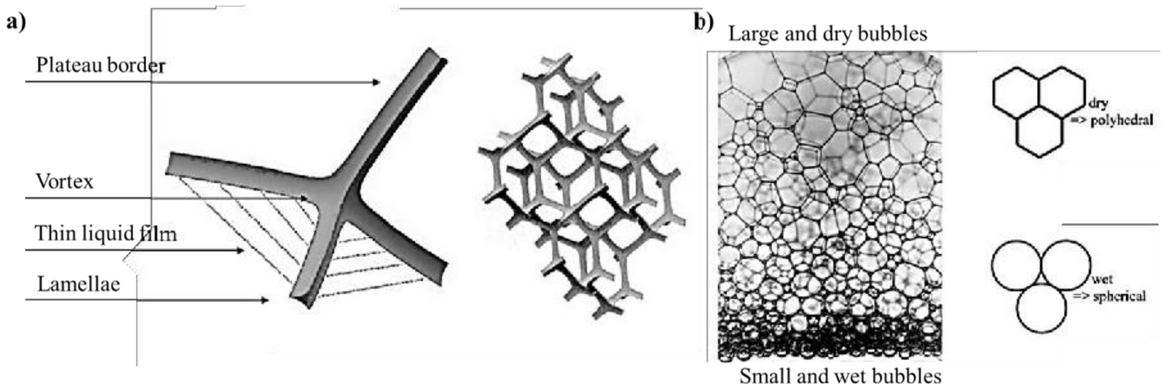

Figure 7. a) *The elementary structure of real foam dispersed system.* ***b)*** *The bubble shape distribution under the foaming process.*

The amount of liquid or gas in the foam determines how the bubbles are shaped. A shift in bubble shape indicates the progression from a wet foam to a dry foam, as seen in **Fig. 7b**. Along the edges of the Plateau, the foam grows more polyhedral as the liquid drains out and the bubbles combine.

Foam stability is determined by the relation between surface tension σ and excess pressure Δp and it is the law of Laplace and Young for a single bubble: $\Delta p = 4\sigma/r$ where r is bubble radius. The bubble's surface area is driven to be as small as possible by surface tension, but the excess pressure balances this effect, and the bubble size reaches equilibrium. Factors affecting the surface energy and mechanism of foam stability are the film elasticity effect (Gibbs and Marangoni effects), viscous surface layer formation, reduced gas diffusion through the lamellae, and electric double-layer repulsion[46].

5.2. Synergistic systems

The interactions between mixed adsorption layer molecules at a multicomponent interface can lead to obtaining better macroscopic system features than would be anticipated from the properties of each single component[47,48]. Synergism refers to the strengthening of the effects under consideration. It is well-known in the literature that binary surfactant mixtures improve surface properties (surface tension, foamability, or floatability) than pure surfactant solutions at lower concentrations. A binary surfactant mixture's physicochemical characteristics can be efficiently modified by properly designed additives. The formation of strong hydrogen bonds between the hydrophilic additives and water molecules, created with the addition of additive molecules, cause the three-dimensional matrix of water (solvent) molecules to break.[49] Additionally, additives have been investigated as morphological modifiers and lead to efficient charge filtering and cause a shift in micelle morphology from spherical to wormlike[50]. Such changes in adsorption efficiency, foamability, or flotability or any physicochemical parameter in the surfactant mixture, unexpectable relative to the individual component contribution, are called synergistic effects . The main types of synergistic systems based on surfactants are nonionic-anionic surfactants (this type of synergistic mixtures - amino acid surfactants & *n*-octanol is considered in the experimental part), nonionic-cationic and anionic-cationic. The properties of these types of systems are discussed below.

Nonionic-anionic surfactant mixtures have found usage in a variety of processes, including increased oil recovery[50], adjusting interfacial curvature[51], phenanthrene adsorption utilizing activated carbon[52], and more[53]. The anionic surfactant has a negative charge on its head, in contrast to the nonionic surfactant's absence of charge. A considerable amount of research has been done on the micellization behavior of a binary mixture of sodium dodecyl sulfate (SDS) and nonionic surfactants in five different forms (Triton X-100, Tween 20, Tween 60, Tween 80, and Tween 85)[54]. Through their binary mixes, they have demonstrated a synergistic effect. Stronger interactions between ionic surfactants with hydrophobic sections and somewhat longer tails and the hydrophobic portions of SDS result in the creation of mixed micelles. The SDS-Tween 80 micellar system had the greatest synergistic effect, whereas the SDS-Tween 85 micellar system had the opposite effect. This is most likely because each of its three hydrophobic tails included a double bond, which kept the system sterically rigid.

Nonionic-Cationic surfactant mixtures contain an anionic surfactant that has a negative charge on its head, in contrast to a nonionic surfactant's absence of charge. Numerous studies have been conducted on the micellization behavior of a binary mixture of sodium dodecyl sulfate (SDS) and nonionic surfactants in five distinct forms (Triton X-100, Tween 20, Tween 60, Tween 80, and Tween 85)[54]. Through their binary mixes, they have demonstrated a synergistic effect. Stronger interactions between ionic surfactants with hydrophobic sections and somewhat longer tails and the hydrophobic portions of SDS result in the creation of mixed micelles.

Anionic – Cationic surfactant system is possibly one of the mixed micellar systems that have been investigated the most, and there are great evaluations of it accessible in the literature[55]. High-performance detergents have been created using the strong electrostatic interaction between the cationic and anionic head groups, which facilitates micellar aggregation[56]. Solubilization, phase separation, and surface modification can all be precisely controlled by carefully adjusting the content of the anion-rich or cation-rich component[57]. Since cationic and anionic surfactants have oppositely charged heads, when they are combined in an identical ratio (stochiometric ratio) at pre or post-micellar concentration, they mutually neutralize their charges. The precipitation redissolves when one of the components (cationic or anionic) is increased, causing micelles to form in the combined solution, demonstrating the effect of the micellization process[58–60]. The ratio of each component surfactant determines whether a binary mixture of this type of surfactant has a synergistic or antagonistic impact. Systems of cationic and anionic surfactants, or cationic surfactant solutions, are distinct from one another. Due to the synergistic effect, the CMC in a mixed surfactant system is lower than in a pure surfactant system [61–63].

Another considered system, based on macromolecular frothers and low molecular surfactants, are synergistic mixtures containing proteins[64], polyelectrolyte[65], polymer[66] as well as nanoparticles[66].

The origin of synergistic and antagonistic effects is mainly caused by electrostatic, non-covalent, and hydrogen interactions. The most important contributions to these effects are described below.

Electrostatic interaction is one of the most important driving forces behind the aggregation as well as the micellization process[67]. The micellar aggregation is facilitated by electrostatic repulsion between molecules of like-charged surfactant[67]. This has been accomplished throughout the years by the introduction of counterions with opposing charges[68,69] . Smaller counterions are more productive in electrostatic charge screening, resulting in lower CMCs and micellization enthalpies[69,70].

Noncovalent interactions such as cation-π and π- π can stabilized micellar aggregates in solution such as in drug delivery in biological systems[71]. CMCs are reduced at low concentration regimes as a result of the cation-cation interaction between cationic surfactants and the electron cloud of the electron-rich additive or co-surfactant. At increased concentration, the same can result in significant morphological changes of the micellar aggregates and can also reduce (ultralow) equilibrium surface tension of the mixed micellar system and affect other physicochemical properties like surface excess, interaction parameters, etc.

Hydrogen interactions between the cationic head groups of the surfactant monomers and the interfacial water molecules cause the micelle to be anchored, improving its stability[72,73], inside the bulk solvent, in the case of single chain[74] as well as double chain cationic surfactant micelles. In non-aqueous solvents, such as toluene, stable core-shell micelle formation was caused by hydrogen bonding between two polystyrene-based block copolymers[74]. The micelle's monomeric surfactants are bonded much stronger thanks to the presence of numerous hydrogen bonds[75,76].

Experimental part

1. Influence of temperature on rising bubble dynamics in water and *n*-pentanol solutions - (**article D1**)

The investigation of bubble motion in water and pentanol solutions and the impact of temperature are the topics of the first **article (D1)** of the experimental part of this dissertation. The useful technique in the description of the hydrodynamic properties of the liquid/gas interface is a measurement of the local velocity profiles (LVP) of the rising bubble. Experiments were carried out using two independent measurement techniques. The first one is well-known and widely described in the literature. In this method, a high-speed camera, which allows for the registration of the bubble movement sequences, is used. This method enables the simultaneous registration of a bubble deformation and velocity profiles. It is highly accurate, however requires a lot of time and complex image analysis. An alternative method, described and implemented for this application by the author of this dissertation for the first time in the literature, is much faster and can be used when information on a bubble deformation is not required. This method of LVP measurement utilizes an ultrasound approach. This approach is especially effective in opaque or turbid solutions, where camera observations are difficult or impossible. On the other hand, a precise value of the speed of sound in a liquid is required for proper calculation of a rising bubble velocity, which can depend on solution composition, temperature, and potential presence of dispersed solid particles. The application of this method is based on a special measuring probe and an ultrasonic controller where a sound wave is generated with an appropriate frequency matched to the size of the bubble, to be able to observe the signal in the form of a scattered wave on this object. The tests were carried out in a thermostatic system, which allowed for the monitoring of changes in the hydrodynamic properties of the liquid medium and its integration with the gas phase as a function of temperature. In addition to the experiments, computational fluid dynamics (CFD) calculations were also carried out using the Gerris[77] open-source solver which enables the numerical solution of governing equations, describing the conservation of momentum and mass of incompressible viscous liquid with a given viscosity and surface tension, and the bubble interface reconstruction and tracking with the volume-of-fluid approach. By applying specific physicochemical parameters moderated by temperature i.e. (density, viscosity, surface tension), it was possible to recreate the variations in the shape of the bubble with very good accuracy (compared to experimentally determined bubble shape).

During CFD calculations a constant bubble size was assumed. This assumption has been confirmed experimentally (also in **article D4**), where it has been shown that the bubble equivalent diameter changes to a very small extent as a function of temperature. Experiments performed using two independent experimental methods, supported by numerical calculations and an analysis of the results, showed that, for a clean system, the temperature did not change the hydrodynamic boundary conditions at the rising bubble surface. Under various temperatures of pure water, the hydrodynamic boundary conditions of the bubbles of a given size remained unchanged and was fully slip. Concerning the bubble's diameter, an increase in the temperature from 5 to $45° C$ caused only a slight size modification. In turn, the bubble deformation varied significantly: the deformation ratio increased with the water temperature and its value was accurately quantified using Legendre's equation. Further hydrodynamic considerations were based on parameters that are more useful in fluid mechanics and industry, i.e. Reynolds (Re) and Weber (We) dimensionless numbers. The dependence of the bubble shape as a function of Weber number can be approximated with a very good correlation with the empirical dependence described by Legrende. However, in the case of a bubble shape defined by Reynolds numbers as a function of Weber numbers, the situation was more complex. For measurements at a constant temperature, the Re vs. We relation could be approximated by a linear relationship, while for measurements at different temperatures, a non-linear dependence was revealed. According to We and Re number relation and deformation for different temperatures, the drag coefficient according to the Moore equation was calculated. Based on these calculations, very large differences were noticed in the case of the equation describing the drag coefficient of a bubble with a completely immobilized surface (characteristic to solid particle) and with a completely mobile surface (pure liquids, where there is no surfactant adsorbed at a rising bubble surface).

In addition to the previous analysis, the empirical relation between Weber and Reynolds numbers i.e. bubble terminal velocity as a temperature function $u_T(T)$, Reynold's number as Weber number function $Re(We)$, and Weber and Reynolds number as temperature function were presented (see Table 3 in **article D1**). These empirical relations have various scientific as well as industrial applications because are satisfied in a wide range of Reynolds numbers. From the ultrasonic measurements of a bubble velocity as a function of temperature, it was shown that the temperature increase caused the terminal velocity to be established faster. Moreover, temperature increases resulted in lower terminal velocity values. This means, that (i) the coverage of the bubble surface was greater (it was increasing faster over time), (ii) the dynamic structure of the adsorption layer was established faster, and (iii) the bubble surface became immobilized earlier, which is consistent with laws of diffusion. It was shown, moreover, that the concentration values at minimum bubble velocity (CMV), calculated from experiments of a bubble rising in n-pentanol solutions of different concentrations, were practically identical for all temperatures. It meant that, despite the difference in the absolute bubble velocity, the concentration, causing the complete immobilization of the rising bubble surface (above which no further velocity decrease could be noticed) was temperature-independent.

2. Experimental and theoretical study of adsorption of synthesized amino acid core-derived surfactants at air/water interface - (**article D2)**

The adsorption performance of surfactants and parameters allowing the description of this process are very important factors for understanding the effect of modification of the physicochemical properties of the gas/liquid interfaces and stability of thin liquid foam films (considered in **article D3** and **article D4**) and real foams (**article D5**). Since **article D5** deals with real foams stabilized by amino-acid surfactants (AASs), in this chapter, the basic adsorption properties of the AASs and theoretical description of this process will be discussed (**based on article D2 and the theoretical background presented in theoretical section 3.2**).

In the presented research, an experimental and theoretical description of the adsorption properties of synthesized, “green” and biodegradable surface-active substances, with the hydrophilic aminoacid part (L-alanine, L-valine, L-leucine, L-proline, and L-phenylalanine) modified by aliphatic carbon chain C_{12} was undertaken. The high chemical purity (> 98%) of AASs was confirmed by NMR spectra and melting point. The study of the surface properties of AASs was based on the measurements of the equilibrium surface tensions with the use of two independent measurement techniques, i.e. the Wilhelmy plate and the analysis of the bubble shape methods. Moreover, the pKa was determined based on the measurements of pH and conductivity. The experimentally determined values of dissociation constants were within the range from 4.61 for C_{12}-Pro to 5.41 for C_{12}-Phe, which proves that the tested compounds are weak acids. Therefore, based on dissociation constants, the dependence of the degree of dissociation as a function of pH was plotted. The fraction of the non-dissociated form of surfactants was always above 0.1. Having this in mind, in further studies, contribution from the dissociated part was considered, only.

The theoretical description of the adsorption properties was carried out with the use of HFL (Helfand-Frisch-Lebowitz) isotherm based on 2D hard disk-like particles. The verification and validation of the theoretical model were examined by a simulation with the use of literature surface tension isotherms data for tert-isopropyl phosphine oxide and n-alkyl dimethyl phosphine oxides with the hydrophobic chain length from 7 to 13 carbon atoms. The effective radii, A_{eff} and the limiting surface concentration, Γ_{∞} of the examined surfactants' hydrophilic headgroups were calculated using molecular dynamics simulations (MDS) to give physical meaning to the isotherm parameters concerning their molecular characteristics. Density functional theory (DFT) calculations using the CAM-B3LYP functional and the 6-31G + (d, p) basis set were used to calculate the optimized structures for each AAS. The optimized structures were then imported into the YASARA Structure Molecular Dynamics Software.

The acquired data showed that, as anticipated, the hydrophobicity of the amino acid side group enhances the surface activity of the surfactants. Additionally, the surface activity of AASs is substantially higher than that of a typical cationic surfactant with twelve carbon atoms in the alkyl chain, dodecyltrimethylammonium bromide (DTAB), and it follows the gradation of hydrophobicity of amino acids PRO < ALA < VAL < LEU < PHE. While the surface activities of C_{12}-VAL, C_{12}-ALA, and C_{12}-PRO were intermediate between those of dodecanol and dodecyl-trimethyl ammonium bromide (DTAB), those of C_{12}-PHE and C_{12}-LEU were similar to those of dodecanol. This is caused by an increase in the proportion of the molecule's neutral form that has a protonated carboxylic group as well as the hydrophobicity of the amino acid headgroup. At room temperature, the examined surfactants lack a CMC, and their surface activity is constrained by their solubility. The AASs have the ability to form HB (hydrogen bonds) and this feature will be crucial in the interpretation of the results presented in **article D5**. As a result, the AASs can create intermolecular hydrogen bonds between their molecules, causing high surface coverage. By executing the optimization geometry of the dimers, the energy of dimerization for all AASs has been calculated.

Although numerous papers have demonstrated the studied compounds' capacity to lower solution surface tension, there have been very few attempts to theoretically describe the adsorption process using a model that would allow for the extraction of useful physicochemical parameters. This research was aimed to fill this gap. The use of the new AASs in conventional surfactant applications is promising, and testing of other desired properties will follow. These tests include those for foamability, determining the kinetics of dynamic adsorption layer formation at the interface of rising bubbles, determining the stability of single liquid films, and studying the crystalline structure of the obtained AASs to comprehend the dimerization of AASs. Some of the research directions mentioned above have been implemented, while the foaming properties of these compounds are part of this dissertation and are included in **article D5.**

3. Effect of initial adsorption coverage and dynamic adsorption layer formation at bubble surface in stability of single foam films - (**article D3)**

As was shown in the theoretical and experimental (**article D1**) part concerning the movement of a bubble in a solution of a surfactant, the bubble velocity undergoes significant variations before terminal velocity establishment and depends on surfactant concentration. The local velocity profiles of the rising air bubble in solutions of surfactants are characterized by two critical regions. The first one is associated with maximum velocity and the second with terminal velocity. As was already discussed, this fact is a consequence of the DAL formation and can be used to assess the kinetics of this process. In this part of the dissertation, the influence of the state of the dynamic adsorption layer on the single TLF stability probed by the bubble lifetime approach is presented (based on the results published in the **article D3** and the theoretical background presented in **theoretical section 4.2**).

Tests of TLF stability were carried out in an automatic measuring system, where the lifetime of a single bubble on a free surface of solutions was measured using a CCD camera. The measuring system consisted of a glass column filled with the test solution, a single bubble generation set-up ("Bubble-on-demand" generator with precise adsorption time control), a glass trap used to control the adsorption time, and a bubble recording system with a camera connected to a PC with developed recording software. In the research, n-hexadecyltrimethylammonium bromide (CTAB), polyoxyethylenesorbitan monooleate (Tween80), and n-octanol were used as model surfactants.

The experiments were carried out without and with the use of a trap to control the adsorption time. In each case, the lifetime of the bubble on the free surface was tested for two distances, between capillary and free surface, i.e. (i) $L = 15\ cm$ (terminal bubble velocity), and (ii) distance for which the maximum velocity of the rising air bubble was observed for a given compound with a given concentration. Experimental work was supplemented by theoretical calculations using the RDI model (Radoev-Dimitrov-Ivanov). This model was used to determine the drainage kinetics of foam films and the critical thickness of foam film rapture.

As was already noted, the goal was to check how the DAL structure, in conjunction with the degree of initial bubble adsorption coverage, affected the stability of a single foam film created when a bubble collided with the free surface of the solution. The lifetime of foam films created by bubbles colliding with solutions surfaces with impact velocities equal to: (i) terminal velocity - u_t (indicating that the DAL structure is fully formed and the bubble surface is partially or completely immobilized during the rising period), and (ii) maximum velocity - u_{max}, where the DAL formation has just begun but the bubble surface is still mobile, has been investigated.

It was shown that the bubble lifetime was different, as evidenced by a comparison of the lifetime of a liquid film formed by a bubble traveling across a range of distances in a solution of surface-active substances. Since the DAL architecture had been fully constructed over a longer distance, the concentration of surfactant molecules at the top pole of the bubble forming the bottom interface of the liquid (foam) film was depleted. The hydrodynamic boundary conditions in such case was shifted towards more slip and drainage of the liquid film was quicker. At shorter distances, due to the fact that the DAL had not yet been established, the bubble adsorption coverage was uniform. As a result, the liquid film that was created was symmetrical and drained far more slowly. The theoretical calculations of liquid film drainage, based on the RDI model, provided additional evidence that this analysis and findings were accurate. The liquid film attained similar thickness in all of the examples under consideration, regardless of the bubble's travel distance, which is typical of an equilibrium liquid film.

These studies showed that the stability of liquid films formed by bubbles with various starting adsorption coverage degrees can be similar. This effect should be associated with a similar degree of liquid/gas (bubble) interface immobilization, according to the analysis of liquid film stability for a range of initial adsorption coverage values. Additionally, it was indirectly demonstrated that the final degree of bubble adsorption coverage can reach the equilibrium value in some circumstances (for a long enough distance covered by the bubble before the liquid film formation).

The presented research will be continued in article **article D4** where the observed effects will be shown quantitatively for the first time in the literature. Understanding the effects of the stability of foam films is also crucial in the analysis of real foams discussed in **article D5**.

4. Coalescence of surface bubbles: The crucial role of motion-induced dynamic adsorption layer - (**article D4)**

Hydrodynamic analyses of bubble rising in surfactant solutions conducted in **article D3** confirmed the existence of two critical regions associated with the bubble motion: (i) at terminal velocity, due to the DAL presence of the hydrodynamic boundary conditions at a top pole of the rising bubble surface were strongly shifted towards more slip, (ii) characteristic shape of the bubble velocity profiles, with maximum velocity existence, indicates starting point of the DAL formation – before this point bubble surface coverage can be assumed symmetrical. Previous, qualitative studies, based on bubble lifetime measurements (**article D3**) have shown how important the existence of a motion-induced dynamic adsorption layer at a rising bubble surface is for a single foam film drainage kinetics. The conducted tests showed that TLF formed under conditions when the surface is immobilized (bubble maximum velocity) is characterized by greater stability than that under slip conditions (bubble terminal velocity and full DAL development). This part of the experimental dissertation (**article D4**) provided the first quantitative proof of the importance of the state of the dynamic adsorption layer on the stability of thin liquid foam films. For the first time, quantitative measurements of the drainage kinetics of foam films formed under dynamic conditions have been shown.

The experiments were carried out using the system with a CCD camera. Subsequent bubble motion stages were systematically analyzed to take into account the bubble history before the TLF formation: (i) bubble motion (local velocity profile - LVP) (ii) bubble collisions with a free surface and (iii) the liquid film drainage. The stage No. (iii) was carried out using the dynamic film interferometry (DFI) method, allowing direct determination of the thickness of the thin liquid foam film formed between the free solution surface and the bubble as a function of time. Experimental studies were supported by theoretical calculations of adsorption kinetics according to the Frumkin model (discussed wider in the theoretical part) using the IsoFit software package developed by E. Aksenenko as well as Direct Numerical Simulations (DNS) allowing for modeling the surfactants distribution along the bubble surface.

In studies on bubble motion, it has been shown that, for the chosen surfactant concentration range, the bubble equivalent diameter depends to a small extent on surfactant concentration.

The bubble velocity upon the arrival on the surface for the short column differed greatly from the velocity under steady-state conditions established in the long column due to the occurrence of maxima at the LVPs. Therefore, attempts were made to analyze the bubble bouncing. It was discovered that these velocity discrepancies have a significant impact on the dynamics of colliding bubbles bouncing at the air/solution interface of the free surface.

Time evolutions of the thin liquid film thickness (drainage kinetic) were calculated using image analysis for low concentrations that were determined by the LVP method. Measurements were carried out for both column lengths (distances “close” and “far”) and the same concentrations under similar humidity conditions. Since all curves significantly overlap, the surfactant dosage has a minimal impact on the dynamics of thinning for $L = 1\ cm$ (distance “close”). On the other hand, when the concentration is altered, the $L = 40\ cm$ (distance “far”) instance exhibits behaviors that are fundamentally different, where the kinetics depend more strongly on the concentration. Moreover, when comparing the kinetics for the same concentrations for $L = 1$ cm and $L = 40\ cm$, greater differences in drainage dynamics are observed for lower concentrations. A significant influence of the evaporation effect on the drainage kinetics was also demonstrated for conditions $L = 40$. When comparing humidity-saturated conditions (RH > 85%) with non-saturated conditions, for $c = 1\ x\ 10^{-4}\ M$, for the short column, has been that late-time thinning is dominated by evaporation. While the film thickness in saturated conditions ($> 85\%$) still follows the power law, it decreases for $RH = 40\%$ due to quicker evaporation in the late thinning regime.

Several numerical simulations were run using the same computational approach to show the redistribution of surfactant molecules at a bouncing bubble surface. During the simulation, very good agreement with the experimental data was obtained.

The conducted research confirms the research hypothesis adopted in **article D3**, concerning the strong influence of the dynamic adsorption layer on the kinetics of foam film drainage, formed in dynamic conditions.

5. Amino-acids surfactants and n-octanol mixtures – sustainable, efficient, and dynamically-triggered foaming systems - (**article D5)**

As was mentioned above, the motion of a single bubble having a surfactant adsorption layer is a fundamental step of foam formation. After the characterization of elementary parameters related to this phenomenon, real foam systems were investigated. In this part of the research, the foaming properties of synergistic systems based on the previously described biodegradable amino acid surfactants described in **article D2**, mixed with *n*-octanol (C_8OH, tested as a non-ionic surfactant in **article D3** and **article D4**) were examined. The adsorption behavior of the mixtures was tracked by tensiometry (surface tension measurement with analysis of a bubble shape method). The foamability and foam stability were carried out by dynamic foam analysis (DFA). The aggregation analysis was based on dynamic light scattering (DLS). Experimental results were supported by molecular dynamics simulations (MDS).

In all surface tension measurements for mixtures C_{12}-ALA and C_{12}-LEU (for lower and higher concentrations of n-octanol), a synergistic reduction of surface tensions was demonstrated. The greatest effect was observed in the case of the less branched chain head of amino acid surfactant, i.e. C_{12}-ALA. In the case of C_{12}-PHE, antagonistic adsorption properties were noted. According to these data, critical synergistic concentrations (CSC) for surface tensions were determined.

Following that, experiments on foambility and foam stability were conducted. Pure solutions of amino acid surfactants at the studied concentrations showed very weak foamability. Moreover, the foamability of the tested n-octanol solutions was also examined. Finally, the synergistic foaming properties of the mixtures containing aminoacid surfactant with *n*-octanol were investigated. Strong synergistic foaming properties were demonstrated for all the tested systems. In addition, the critical synergistic concentration of foambility was also determined.

Molecular dynamics simulations have confirmed the observed synergistic effects in surface tension measurements and especially in foamability tests. In addition, the simulations indicated the possibility of the formation of aggregates that could be behind the observed foaming effects. This issue was the subject of the dynamic light scattering analysis. The number of hydrogen bonds between the AAS-AAS (also computed by DFT calculations in **article D2**) and AAS-C_8OH in the systems with a greater C_8OH

concentration was estimated to better understand the behavior of the AAS surfactants. Compared to systems without hydrogen bonds (such as CTAB/C_8OH), additional interactions might change the surfactant ordering in the monolayer. The AAS-C_8OH hydrogen bond formation affinity decrease could be ordered as follows: C_{12}-ALA > C_{12}-LEU > C_{12}-PHE. This represented the degree of AAS and C_8OH interaction and, consequently, the stability of such mixtures at the interface. Due to hydrogen bonding interactions, the C_{12}-ALA and C_8OH formed a relatively stable interfacial monolayer.

As shown above, according to the MD simulations, adding C_8OH can result in aggregates formation in the majority of the investigated mixed surfactant systems, and this effect should get stronger as the concentration of AASs rises. To verify this assumption, dynamic light scattering measurements were performed. For the C_{12}-ALA/C_8OH mixtures aggregates' presence in the bulk was revealed.

It can be concluded that for all of the AASs under study, adding C_8OH to the solution causes a synergistic effect that, while modest for changes in equilibrium surface tension, is spectacular for solution foaming performance. When combined with AASs, C_8OH causes the production of bulk aggregates, which are not present in pure AASs solutions and whose time stability is dependent on the concentration of AASs. The development of micelles (aggregates), which under equilibrium conditions results in slight fluctuations in surface tension, is thought to be the cause of the synergistic effect for all AASs under investigation. The aggregates are carried by convection (by continuous mixing) to the newly generated air/liquid interface under highly dynamic conditions of the foam formation.

Concluding remarks

The bubble movement analysis conducted in **section 2** of the theoretical background and experimental investigation of bubble motion in water and n-pentanol solution and the impact of temperature conducted in **article D1** and described in **section 1** of the experimental part allowed for the following conclusions:

- temperature $(5 - 45°\ C)$, in the case of water, does not change the hydrodynamic boundary conditions of the rising bubble. Independently on the temperature value the bubble surface remains fully slip,
- the drag coefficient was determined, showing in line with the expectations resulting from the total mobility of the liquid/gas interface for water, that the temperature and the physicochemical parameters resulting from its change (density, viscosity) do not change it to a significant extent,
- the dependencies of the Weber and Reynolds numbers as a function of temperature were presented,
- for n-pentanol solutions, it was shown that the temperature causes the terminal velocity to be established faster, but it is also lower, which means that the bubble surface coverage is greater (it increases faster over time) and that the DAL is established faster and the bubble surface is immobilized earlier, which is consistent with the laws of diffusion.

In addition to the hydrodynamic effects described above, the stability of thin liquid films and real foams is also influenced by adsorption. The research on surface properties of newly synthesized, biodegradable aminoacid surfactants AASs conducted in **article D2** and described in **section 2** of the experimental part together with the theoretical description using HLF isotherms, described in more detail in **section 3.2** lead to the following conclusions:

- procedures for the synthesis of amino acid surfactants have been developed,
- description of adsorption properties of aminoacid surfactants using physicochemical parameters resulting from the HFL isotherm used and characteristic for the surface adsorption properties of a given compound,
- using molecular dynamics simulations, the geometries of amino acid surfactants and the Van der Waals surface of their hydrophilic groups have been computed,
- possibility of formation of the AAS dimers driven by hydrogen bonds was revealed which is crucial for the interpretation of the results presented in **article D5**,

- energy, enthalpy, and free energy of dimerization by DFT computations have been estimated.

The research conducted in **article D1** regarding the hydrodynamic description of bubble rising in the liquid phase and previous studies of stability of thin liquid films formed under dynamic conditions pioneered by Jachimska, Warszyśki & Małysa analyzed in **section 4.2** of theoretical background were continued in **article D3** and described in **section 3** of the experimental part. The conducted experiments led to the following conclusions:

- the strong influence of the state of the dynamic adsorption layer on the foam film created under given conditions,
- the results of the studies conducted revealed that the TLF formed under conditions of surface immobilization (bubble maximum velocity) is more stable than that formed under slip conditions (bubble terminal velocity and full DAL development).

The conclusions made in the previous **article D3** were verified for the first time in the literature in a quantitative manner using the dynamic film interferometry (DFI) supported by DNS simulation. The unique experimental results regarding the kinetics of TLF drainage under the dynamic condition shown in **article D4** and described in **section 4** of the experimental part lead to conclusions:

- it was shown that the collision of a bubble with a free solution surface at different stages of the DAL formation has a significant impact on the dynamics of colliding bubbles bouncing at the air/solution interface,
- the surfactant dosage does not affect the dynamics of thinning for $L = 1\ cm$ (distance "close"), as all curves greatly overlap, on the other hand, the $L = 40\ cm$ (distance "far") instance demonstrates behaviors that are fundamentally different when the concentration is changed, where the kinetics depend more heavily on the concentration,
- additionally, significant differences in drainage dynamics are seen for lower concentrations when comparing the kinetics for the same concentrations for $L = 1\ cm$ and L=40 cm; higher concentrations cause these discrepancies to vanish.

Finally, the high surface active amino acid surfactants described in **article D2** and **section 2** of the experimental part, characterized by the ability to form surface hydrogen bonds, were used together with *n*-octanol the well-described nonionic surfactant (**article D2** and **article D3**) as synergistic foaming mixtures in **article D5**. According to the assessments of the mixture' surface activity, foamability and foam stability, and volumetric mass aggregation, it was found that:

- all of the examined AASs experience a synergistic effect when C_8OH is added to the AASs solution. This effect is modest for changes in equilibrium surface tension but spectacular when it comes to solution foaming performance,
- the amount of C_8OH in the mixture causes the production of bulk aggregates, which are not present in pure AASs solutions and whose temporal stability relies on the concentration of AASs,
- the development of micelles (aggregates), which under equilibrium conditions results in slight fluctuations in surface tension, is thought to be the cause of the synergistic effect for all AASs under investigation. The aggregates are carried by convection (by continuous mixing) to the freshly generated air/liquid interface because of the dynamic conditions of the foam formation.

The conducted research not only fills the gap in the available, sometimes contradictory literature regarding the hydrodynamic description of the bubble movement in liquids of different temperatures but also constitutes a continuation of the decade's work on the stability of foam films. The presented experiments are often filled for a wide range of Reynolds numbers, which allows for many industrial applications indicated in the literature review.

Moreover, new surface-active compounds (aminoacid surfactant – AASs) with high development potential were used as surfactants and described in the research, which are and will be the subject of continued work under several grants remaining in the interests of the author of this dissertation.

Additionally, during the conceptual work, several unique measurement apparatuses were developed:

- automatic, ultrasonic system for recording the local velocity profiles (LVP) of an ascending bubble liquid medium in thermostated conditions,
- automatic system for recording the lifetime of a single air bubble on the surface of a free solution,
- interferometric system for dynamic measurement of the thickness of liquid foam films.

References

1. Heeres, A. S., Heijnen, J. J., van der Wielen, L. A. M. & Cuellar, M. C. Gas bubble induced oil recovery from emulsions stabilised by yeast components. *Chem. Eng. Sci.* **145**, 31–44 (2016).
2. Kulkarni, A. A. & Joshi, J. B. Bubble formation and bubble rise velocity in gas-liquid systems: A review. *Ind. Eng. Chem. Res.* **44**, 5873–5931 (2005).
3. A.V. Nguyen, H. J. S. *Colloidal Science of Flotation*. (Marcel Dekker, Inc, 2004).
4. Bavarian, F.; Fan, L. S.; Chalmers, J. J. Microscopic Visualization of Insect Cell-Bubble Interactions. I: Rising Bubbles, Air-Medium Interface, and the Foam Layer. *Biotechnol. Prog.* **7**, 140–150 (1991).
5. Liger-Belair, G.; Marchal, R.; Robillard, B.; Dambrouck, T. . & Maujean, A.; Vignes-Adler, M.; Jeandet, P. On the Velocity of Expanding Spherical Gas Bubbles Rising in Line in Supersaturated Hydroalcoholic Solutions: Application to Bubble Trains in Carbonated Beverages. *Langmuir* **16**, 1889–1895 (2000).
6. Blanchard, D. C. The Electrification of the Atmosphere by Particles from Bubbles in the Sea. *Prog. Ocean.* **1**, 73–202 (1963).
7. Lewis, E. R.; Lewis, E. R.; Lewis, R.; Schwartz, S. E. Sea Salt Aerosol Production: Mechanisms, Methods, Measurements, and Models. *Am. Geophys. Union* **152**, (2004).
8. Andreas, E. L.; Edson, J. B.; Monahan, E. C.; Rouault, M. P. . & Smith, S. D. The Spray Contribution to Net Evaporation from the Sea: A Review of Recent Progress. *Boundary-Layer Meteorol* **72**, 3–52 (1995).
9. Kosior, D. & Zawala, J. Initial degree of detaching bubble adsorption coverage and the kinetics of dynamic adsorption layer formation. *Phys. Chem. Chem. Phys.* **20**, 2403–2412 (2018).
10. M. Rastello, J.L. Marie, M. L. No Title. *J. Fluid Mech* **683**, 434 (2011).
11. R. Manica, E. Klaseboer, D. Y. C. C. No Title. *Soft Matter* **12**, 3271 (2013).
12. V.G. Levich. *Physicochemical Hydrodymanics*. (Prentice-Hall, 1962).
13. R. Clift, J.R. Grace, M. E. W. *Bubbles, Drops, and Particles*. (Academic Press, 1978).
14. J. Masliyah, R. Jauhari, M. G. No Title. *Chem. Eng. Sci* **49**, 1905 (1994).
15. Karamanev, D. G. Rise of gas bubbles in quiescent liquids. *AIChE J.* **40**, 1418–1421 (1994).
16. Karamanev, D. G. Equations for calculation of the terminal velocity and drag coefficient of solid spheres and gas bubbles. *Chem. Eng. Commun.* **147**, 75–84 (1996).
17. Rodrigue, D. Drag coefficient-Reynolds number transition for gas bubbles rising steadily in viscous fluids. *Can. J. Chem. Eng.* **79**, 119–123 (2001).
18. Rodrigue, D. Generalized correlation for bubble motion. *AIChE J.* **47**, 39–44 (2001).
19. Abou-El-Hassan, M. E. A generalized bubble rise velocity correlation. *Chem. Eng.*

Commun. **22**, 243–250 (1983).

20. Pawliszak, P. *et al.* Mobile or Immobile? Rise Velocity of Air Bubbles in High-Purity Water. *J. Phys. Chem. C* (2019) doi:10.1021/acs.jpcc.9b03526.

21. Zawala, J. & Niecikowska, A. "Bubble-on-demand "generator with precise adsorption time control. *Rev. Sci. Instrum.* **88**, (2017).

22. Duineveld, P. C. No Title. *J. Fluid Mech* **292**, 325 (1995).

23. S. Ng, P. Warszynski, M. Zembala, K. M. No Title. *Physicochem. Probl. Miner. Process* **33**, 143 (1999).

24. S. Ng, P. Warszynski, M. Zembala, K. M. No Title. *Miner. Eng* **13**, 1515 (2000).

25. Dukhin, S. S., Lotfi, M., Kovalchuk, V. I., Bastani, D. & Miller, R. Dynamics of rear stagnant cap formation at the surface of rising bubbles in surfactant solutions at large Reynolds and Marangoni numbers and for slow sorption kinetics. *Colloids Surfaces A Physicochem. Eng. Asp.* **492**, 127–137 (2016).

26. Leifer, I., Patro, R. K. & Bowyer, P. A study on the temperature variation of rise velocity for large clean bubbles. *J. Atmos. Ocean. Technol.* **17**, 1392–1402 (2000).

27. Issaoui, R. & Mansour, L. Ben. Experimental study of temperature effects on bubble characteristics and gas holdup in electroflotation column. *Desalin. Water Treat.* **162**, 186–192 (2019).

28. Zhang, Y., Sam, A. & Finch, J. A. Temperature effect on single bubble velocity profile in water and surfactant solution. *Colloids Surfaces A Physicochem. Eng. Asp.* **223**, 45–54 (2003).

29. Liu, N. *et al.* Experimental Investigations of Single Bubble Rising in Static Newtonian Fluids as a Function of Temperature Using a Modified Drag Coefficient. *Nat. Resour. Res.* **29**, 2209–2226 (2020).

30. Okawa, T., Tanaka, T., Kataoka, I. & Mori, M. Temperature effect on single bubble rise characteristics in stagnant distilled water. *Int. J. Heat Mass Transf.* **46**, 903–913 (2003).

31. Aveyard R., D. A. H. *An Introduction to the principles of surface chemistry*. (Cambridge University Press, 1973).

32. Fainerman, V. B., Lucassen-Reynders, E. H. & Miller, R. Description of the adsorption behaviour of proteins at water/fluid interfaces in the framework of a two-dimensional solution model. *Adv. Colloid Interface Sci.* **106**, 237–259 (2003).

33. Fainerman, V. B. & Miller, R. Equilibrium and dynamic characteristics of protein adsorption layers at gas-liquid interfaces: Theoretical and experimental data. *Colloid J.* **67**, 393–404 (2005).

34. Fainerman, V. B., Aksenenko, E. V., Krägel, J. & Miller, R. Thermodynamics, interfacial pressure isotherms and dilational rheology of mixed protein-surfactant adsorption layers. *Adv. Colloid Interface Sci.* **233**, 200–222 (2016).

35. Para, G., Jarek, E., Warszyński, P. & Adamczyk, Z. Effect of electrolytes on surface tension of ionic surfactant solutions. *Colloids Surfaces A Physicochem. Eng. Asp.* **222**, 213–222 (2003).

36. Para, G., Jarek, E. & Warszynski, P. The surface tension of aqueous solutions of cetyltrimethylammonium cationic surfactants in presence of bromide and chloride counterions. *Colloids Surfaces A Physicochem. Eng. Asp.* **261**, 65–73 (2005).

37. Para, G., Jarek, E. & Warszynski, P. The Hofmeister series effect in adsorption of cationic surfactants-theoretical description and experimental results. *Adv. Colloid Interface Sci.* **122**, 39–55 (2006).

38. Aksenenko, E. V. 7. Software tools to interpret the thermodynamics and kinetics of surfactant adsorption. *Stud. Interface Sci.* **13**, 619–648 (2001).

39. Fainerman, V.B., and Miller, R. *Thermodynamics of Adsorption of Surfactants at the Fluid Interfaces. In Surfactants Chemistry, Interfacial Properties, Applications*. (Elsevier, 1998).

40. Chang, C. H. & Franses, E. I. Adsorption dynamics of surfactants at the air/water interface: a critical review of mathematical models, data, and mechanisms. *Colloids Surfaces A Physicochem. Eng. Asp.* **100**, 1–45 (1995).

41. Helfand, E., Frisch, H. L. & Lebowitz, J. L. Theory of the two- and one-dimensional rigid sphere fluids. *J. Chem. Phys.* **34**, 1037–1042 (1961).

42. Dukhin, S. S. *et al.* Dynamics of Rear Stagnant Cap formation at the surface of spherical bubbles rising in surfactant solutions at large Reynolds numbers under conditions of small Marangoni number and slow sorption kinetics. *Adv. Colloid Interface Sci.* **222**, 260–274 (2015).

43. Manuscripts and Abstracts for Spring 1965 Meeting. 2010 (1964).

44. Jachimska, B., Warszyñski, P. & Małysa, K. Effect of motion on lifetime of bubbles at n-butanol solution surface. *Colloids Surfaces A Physicochem. Eng. Asp.* **143**, 429–440 (1998).

45. Jachimska, B., Warszynski, P. & Malysa, K. Influence of adsorption kinetics and bubble motion on stability of the foam films formed at n-octanol, n-hexanol and n-butanol solution surface. *Colloids Surfaces A Physicochem. Eng. Asp.* **192**, 177–193 (2001).

46. A, J. W. *Foams: Physics, chemistry and structure*. (Springer, 1989).

47. Wiertel-Pochopien, A., Batys, P., Zawala, J. & Kowalczuk, P. B. Synergistic Effect of Binary Surfactant Mixtures in Two-Phase and Three-Phase Systems. *J. Phys. Chem. B* **125**, 3855–3866 (2021).

48. Zawala, J., Wiertel-Pochopien, A., Larsen, E. & Kowalczuk, P. B. Synergism between Cationic Alkyltrimethylammonium Bromides (CnTAB) and Nonionic n-Octanol in the Foamability of Their Mixed Solutions. *Ind. Eng. Chem. Res.* **59**, 1159–1167 (2020).

49. Liu, Q. *et al.* Effect of Additives on Surfactant Micelle Shape Transformation: Rheology and Molecular Dynamics Studies. *J. Phys. Chem. C* **123**, 2922–2932 (2019).

50. Lu, S. & Somasundaran, P. Tunable synergism/antagonism in a mixed nonionic/anionic surfactant layer at the solid/liquid interface. *Langmuir* **24**, 3874–3879 (2008).

51. Lu, S., Wu, J. & Somasundaran, P. Micellar evolution in mixed nonionic/anionic surfactant systems. *J. Colloid Interface Sci.* **367**, 272–279 (2012).

52. Hou, Z., Li, Z. & Wang, H. The interaction of sodium dodecyl sulfonate and petroleum sulfonate with nonionic surfactants (Triton X-100, Triton X-114). *Colloids Surfaces A Physicochem. Eng. Asp.* **166**, 243–249 (2000).

53. Agneta, M., Zhaomin, L., Chao, Z. & Gerald, G. Investigating synergism and antagonism of binary mixed surfactants for foam efficiency optimization in high salinity. *J. Pet. Sci. Eng.* **175**, 489–494 (2019).

54. Ćirin, D. M., Poša, M. M., Krstonošić, V. S. & Milanovič, M. L. Konduktometrijsko ispitivanje mešovitih micela na-dodecilsulfata i nejonskog surfaktanta (Triton X-100, Tween 20, Tween 60, Tween 80 ili Tween 85) u vodenim rastvorima. *Hem. Ind.* **66**, 21–28 (2012).

55. Phaodee, P. & Sabatini, D. A. Anionic and Cationic Surfactant Synergism: Minimizing Precipitation, Microemulsion Formation, and Enhanced Solubilization and Surface Modification. *J. Surfactants Deterg.* **24**, 551–562 (2021).

56. Akbas, H. & Sidim, T. The viscous properties of anionic/cationic and cationic/nonionic mixed surfactant systems. *Colloid J.* **67**, 525–530 (2005).

57. Sohrabi, B., Gharibi, H., Tajik, B., Javadian, S. & Hashemianzadeh, M. Molecular interactions of cationic and anionic surfactants in mixed monolayers and aggregates. *J. Phys. Chem. B* **112**, 14869–14876 (2008).

58. Bhattarai, A., Pathak, K. & Dev, B. Cationic and anionic surfactants interaction in water and methanol–water mixed solvent media. *J. Mol. Liq.* **229**, 153–160 (2017).

59. Abdul Rub, M., Azum, N. & Asiri, A. M. Binary Mixtures of Sodium Salt of Ibuprofen and Selected Bile Salts: Interface, Micellar, Thermodynamic, and Spectroscopic Study. *J. Chem. Eng. Data* **62**, 3216–3228 (2017).

60. Mal, A., Bag, S., Ghosh, S. & Moulik, S. P. Physicochemistry of CTAB-SDS interacted catanionic micelle-vesicle forming system: An extended exploration. *Colloids Surfaces A Physicochem. Eng. Asp.* **553**, 633–644 (2018).

61. Varade, D. *et al.* Effect of salt on the micelles of cetyl pyridinium chloride. *Colloids Surfaces A Physicochem. Eng. Asp.* **259**, 95–101 (2005).

62. Maiti, K., Bhattacharya, S. C., Moulik, S. P. & Panda, A. K. Physicochemical studies on ion-pair amphiphiles: Solution and interfacial behaviour of systems derived from sodium dodecylsulfate and n- alkyltrimethylammonium bromide homologues. *J. Chem. Sci.* **122**, 867–879 (2010).

63. Nie, H. Q. & Hou, W. G. Vesicle formation induced by layered double hydroxides in the catanionic surfactant solution composed of sodium dodecyl sulfate and dodecyltrimethylammonium bromide. *Colloid Polym. Sci.* **289**, 775–782 (2011).

64. MacKie, A. & Wilde, P. The role of interactions in defining the structure of mixed protein-surfactant interfaces. *Adv. Colloid Interface Sci.* **117**, 3–13 (2005).

65. Penfold, J., Thomas, R. K. & Taylor, D. J. F. Polyelectrolyte/surfactant mixtures at the air-solution interface. *Curr. Opin. Colloid Interface Sci.* **11**, 337–344 (2006).

66. Bureiko, A., Trybala, A., Kovalchuk, N. & Starov, V. Current applications of

foams formed from mixed surfactant-polymer solutions. *Adv. Colloid Interface Sci.* **222**, 670–677 (2015).

67. Long, P. *et al.* Influence of counterions on micellization of tetramethylammonium perfluorononanoic carboxylate in 1-butyl-3-methylimidazolium ionic liquid. *J. Phys. Chem. B* **116**, 7669–7675 (2012).

68. Freire, S., Bordello, J., Granadero, D., Al-Soufi, W. & Novo, M. Role of electrostatic and hydrophobic forces in the interaction of ionic dyes with charged micelles. *Photochem. Photobiol. Sci.* **9**, 687–696 (2010).

69. Ropers, M. H., Czichocki, G. & Brezesinski, G. Counterion effect on the thermodynamics of micellization of alkyl sulfates. *J. Phys. Chem. B* **107**, 5281–5288 (2003).

70. Gallivan, J. P. & Dougherty, D. A. Cation-π interactions in structural biology. *Proc. Natl. Acad. Sci. U. S. A.* **96**, 9459–9464 (1999).

71. Ke, X. *et al.* Role of non-covalent and covalent interactions in cargo loading capacity and stability of polymeric micelles. *J. Control. Release* **193**, 9–26 (2014).

72. Chakraborty, G., Bardhan, S. & Saha, S. K. Unfolding of Tryptophanoctyl Ester and Elastic Deformation of Host Micelles via RR’3N+···π Interaction: Conceivable Relevance to Wrapping Process of Receptor Mediated Endocytosis. *ChemPhysChem* **22**, 2535–2549 (2021).

73. Chakraborty, G. *et al.* Interaction of Tyrosine Analogues with Quaternary Ammonium Head Groups at the Micelle/Water Interface and Contrasting Effect of Molecular Folding on the Hydrophobic Outcome and End-Cap Geometry. *J. Phys. Chem. B* **122**, 2355–2367 (2018).

74. Chakraborty, G., Paulchowdhury, M., Bardhan, S. & Saha, S. K. Surface activity and modifying effects of 1-Naphthol, 2-Naphthol and 2,3-Dihydroxynaphthalene on self-assembled nanostructures of 1-Hexadecyl-3-methylimidazolium chloride. *Colloids Surfaces A Physicochem. Eng. Asp.* **516**, 262–273 (2017).

75. Ghasemi, A. & Bagheri, A. Effects of alkyl chain length on synergetic interaction and micelle formation between a homologous series of n-alkyltrimethylammonium bromides and amphiphilic drug propranolol hydrochloride. *J. Mol. Liq.* **298**, 111948 (2020).

76. Muherei, M. A. & Junin, R. Investigating Synergism in critical micelle concentration of anionic-nonionic surfactant mixtures before and after equilibration with shale. *J. Appl. Sci. Res.* **5**, 181–189 (2009).

77. Popinet, S. Gerris: A tree-based adaptive solver for the incompressible Euler equations in complex geometries. *J. Comput. Phys.* **190**, 572–600 (2003).

Academic achievements during PhD

Articles:

- **2023**

T. Mazur, Ł. Mazur, M. Borkowski, T. Kuciel, M. Szuwarzyński, Polymer-nanoparticle thin scaffolds with any-shape magnetic field gradients, Colloids and Surfaces A: Physicochemical and Engineering Aspect, 677 (2023) 132413.

M. Borkowski, P. Batys, O. M. Demchuk, P. Kowalczuk, J. Zawała, Synergistic effects in solutions of aminoacid surfactants mixed with n-octanol, Industrial & Engineering Chemistry Research, 62 (2023) 13498−13509.

J. Zawała, J. Miguet, P. Rastogi, O. Atasi, M. Borkowski, B. Scheid, G. G. Fuller, Coalescence of surface bubbles: The crucial role of motion-induced dynamic adsorption layer, Advances in Colloid and Interface Science, 317 (2023) 102916.

K. Kubiński, K. Górka, M. Janeczko, A. Martyna, M. Kwaśnik, M. Masłyk, E. Zięba, J. Kowalczuk, P. Kuśtrowski, M. Borkowski, A. Boguszewska-Czubara, A. Klimeczek, O. M. Demchuk. Silver Is Not Equal to Silver: Synthesis and Evaluation of Silver Nanoparticles with Low Biological Activity, and Their Incorporation into C12Alanine-Based Hydrogel. Molecules 28 (2023) 1194.

- **2022**

M. Szuwarzynski, Ł Mazur, M. Borkowski, K. Mackosz, K. Giżynski, T. Mazur, Enhanced Assembly of Ag Nanoparticles for Surface-Independent Fabrication of Conductive Patterns, ACS Applied Nano Materials ACS 5 (2022) 12711–12719.

M. Borkowski, Ł. Mazur, K. Maćkosz, T. Mazur, M. Szuwarzyński, Low roughness, elevated stiffness and thickness-modulated surface nanocomposites based on the controlled deposition of polystyrene nanoparticles, Journal of Materials Research and Technology Elsevier 19 (2022) 2799-2809.

B. Pucelik, A. Sulek, M. Borkowski, A. Barzowska, M. Kobielusz, J. M. Dabrowski, Synthesis and Characterization of Size- and Charge-Tunable Silver Nanoparticles for Selective Anticancer and Antibacterial Treatment, Applied Materials & Interfaces ACS 14 (2022) 14981–14996.

M. Borkowski, S. Orvalho, P. Warszyński, O.M. Demchuk, E. Jarek, J. Zawała, Experimental and theoretical study of adsorption of synthesized amino acid core derived surfactants at air/water interface, Phys. Chem. Chem. Phys. 24 (2022) 3854-3864.

• 2021

M. Borkowski, J. Zawała, Influence of temperature on rising bubble dynamics in water and n-pentanol solutions, Minerals 11 (2021) 1067.

•2020

M. Borkowski, D. Kosior, J. Zawała, Effect of initial adsorption coverage and dynamic adsorption layer formation at bubble surface in the stability of single foam films, Colloids Surf. A: 589 (2020) 124446.

•2019

K. Michal Pietrusiewicz, M. Borkowski, D. Strzelecka, K. Kielar, W. Kicinska, S. Karevych, R. Jasinski, O. M. Demchuk, A General Phenomenon of Spontaneous Amplification of Optical Purity under Achiral Chromatographic Conditions, Symmetry (2019) 11(5), 680.

Conferences:

- **2023**

Bubble and drop, 11-16.06.2023, Maria Curie-Skłodowska University in Lublin, Poland
type of attendance: presentation – "Synergistic foaming systems based on surface-modified magnetic nanoparticles and amino acid surfactants in destabilization of real foams in a magnetic field.", M. Borkowski, J. Zawała, G. Gochev, B. Braunschweig, D. Lupa

- **2022**

ACCORD - Interdisciplinary conference of drug sciences, 26-28.05.2022, Warsaw, type of attendance: poster – "Preparation and assessment of new drug carriers based on silver nanoparticles containing hydrogels"- O. M. Demchuk, M. Masłyk, K. Kubiński, K. Górka, M. Janeczko, A. Martyna, M. Kwaśnik, M. Borkowski, A. Boguszewska-Czubara, J. Kowalczuk

23rd International Symposium in surfactants in solutions, 11-16.09.2022, Lublin, Poland, type of attendance: poster – "Adsorption behavior of mixed solutions of chosen amino-acid surfactants and n-octanol at liquid/gas interface" - M. Borkowski, P. Batys, J. Zawała

36th European Colloids & Interface Society Conference, 04-09.09.2022, Crete, Greece, type of attendance: poster – "Experimental and theoretical study of adsorption of amino-acid surfactants at air/water interfaces" - M. Borkowski, S. Orvalho, P.Warszyński, O. Demchuk, E. Jarek, J. Zawała

Cancer and Oncology Research Endeavour Symposium, 2022, Erbil, Iraq
type of attendance: presentation – "Fine-tuning the activity of biocompatible nanoparticles in advanced tumor models: towards the buildup of magic (nano) bullets for cancer therapy" - B. Pucelik, A. Sułek, A. Barzowska, M. Borkowski, J.M. Dąbrowski

EUFOAM, 2022, Kraków, Poland
type of attendance: poster – "Synergistic effects in solutions of amino-acid surfactants mixed with n-octanol" – M. Borkowski, P. Batys, J. Zawała
type of attendance: poster – "Dynamic adsorption layer and foam film stability probed by dynamic fluid-film interferometry" - J. Zawała, J. Miguet, B. Scheid, M. Borkowski, P. Rastogi, G.G Fuller

• 2021

34th Marian Smoluchowski's Symposium on Statistical Physics, 27-29.09.2021, Kraków, Poland (conference held online)

type of attendance: poster – "Influence of a magnetic field on the drainage mechanism of thin liquid films and real foams stabilized by magneto-reactive surfactants" – M. Borkowski, B. Scheid, J. Zawała

Physicochemistry of Interfaces – instrumental methods, 2021, Lublin, Poland

type of attendance: presentation – „Influence of a magnetic field on the drainage mechanism of thin liquid films and real foams stabilized by magneto-reactive surfactants" – M. Borkowski, B. Scheid, J. Zawała

type of attendance: poster – "The influence of the dynamic adsorption layer on the drainage kinetics of foam films" – M. Borkowski, B. Scheid, J. Zawała

• 2019

LV Polish Annual Conference on Catalysis, 08-10.04.2019, Kraków, Poland

type of attendance: poster – "Mesoporous carbon replicas modified with ammonia as catalysts for the oxidative dehydrogenation of ethylbenzene to styrene" – I. Szewczyk, M. Borkowski, M. Drozdek, P. Kuśtrowski

Scientific internships:

01/02/2023 – 28/02/2023 **Center for Soft Nanoscience**
Institute of Physical Chemistry
University Münster
Corrensstr. 28/30, 48149 Münster, Germany

Research topic: Qualitative analysis by sum frequency generation spectroscopy of the structure of air/liquid interfaces stabilized with C_{12}-ARG and surface-modified magnetic nanoparticles.

01/09/2022 – 30/10/2022 **Department of Geoscience and Petroleum**
Norwegian University of Science and Technology
S. P. Andersens veg 15a, 7031 Trondheim, Norway

Research topic: Investigation of the foamability and floatability of two-component mixtures based on commercial frothers and flotation agents together with biodegradable amino acid surfactants.

07/11/2021 – 20/11/2021 **Transfers, Interfaces & Processes (TIPs)**
Université libre de Bruxelles
Avenue F.D. Roosevelt 50, 1050 Brussels, Belgium

Research topic: Theoretical description (comsol simulations) of the phenomenon of drainage of foam films in dynamic conditions.

10/2019 – 11/2021 **Academic Centre for Materials and Nanotechnology**
AGH University of Science and Technology
al. Mickiewicza 30, 30-059 Kraków, Poland

Research topic: Optoelectronic layouts for processing information on flexible substrates.

08/2019 – 10/2019 **Institute of Fundamental Chemical Processes**
Czech Academy of Sciences
Rozvojova 2/135, Prague 6, Czech Republic

Research topic: Investigation of the phenomenon of foam film coalescence in solutions of eco-friendly surfactants based on amino acid compounds.

Funding:

NCN Preludium 21 grant - 2022/45/N/ST8/02307: Synergistic foaming systems based on surface-modified magnetic nanoparticles and biodegradable amino acid surfactants in the controlled destabilization of real foams in a magnetic field. As project leader.

NCN Sonata BIS 10 grant - 2020/38/E/ST8/00173: Synergistic effects of mixed bit-surfactant solutions on the stability of liquid films under dynamic conditions - basic research on application potential in the flotation separation process. As project contractor.

NCN Opus 13 grant - 2017/25/B/ST8/01247: In search of effective and environmentally friendly foaming agents and emulsifiers - a quantitative description of the stability of thin liquid films in solutions of eco-friendly surfactants. As a project contractor.

NCN Sonata 14 grant - 2018/31/D/ST5/02813: Flexible optoelectronic and information processing devices. As a project contractor.

Polish National Agency for Academic Exchange – NAWA PROM – 13/PROM/2022: Qualitative analysis by sum frequency generation spectroscopy of the structure of air/liquid interfaces stabilized with C12-ARG and surface-modified magnetic nanoparticles.

Polish National Agency for Academic Exchange – NAWA PROM – 14/PROM/2022: Investigation of the foamability and floatability of two-component mixtures based on commercial frothers and flotation agents together with biodegradable amino acid surfactants.

ERASMUS + project - 2018-1-PL01-KA103-047692: The investigation of coalescence kinetics in solutions of surface-active substances (aminoacid surfactants).

Polish National Agency for Academic Exchange NAWA - Bilateral exchange Poland Belgium: Theoretical description (comsol simulations) of the phenomenon of drainage of foam films in dynamic conditions**.**

Scientific articles attached

Co-authors declarations

minerals MDPI

Article

Influence of Temperature on Rising Bubble Dynamics in Water and *n*-pentanol Solutions

Mariusz Borkowski and Jan Zawala *

Jerzy Haber Institute of Catalysis and Surface Chemistry, Polish Academy of Sciences, ul. Niezapominajek 8, 30-239 Krakow, Poland; mariusz.borkowski@ikifp.edu.pl
* Correspondence: jan.zawala@ikifp.edu.pl

Abstract: Data in the literature on the influence of water temperature on the terminal velocity of a single rising bubble are highly contradictory. Different variations in bubble velocity with temperature are reported even for potentially pure systems. This paper presents a systematic study on the influence of temperature between 5 °C and 45 °C on the motion of a single bubble of practically constant size (equivalent radius 0.74 ± 0.01 mm) rising in a clean water and *n*-pentanol solution of different concentrations. The bubble velocity was measured by a camera, an ultrasonic sensor reproduced in numerical simulations. Results obtained by image analysis (camera) were compared to the data measured by an ultrasonic sensor to reveal the similar scientific potential of the latter. It is shown that temperature has a significant effect on the velocity of the rising bubble. In pure liquid, this effect is caused only by modifying the physicochemical properties of the water phase, not by changing the hydrodynamic boundary conditions at the bubble surface. In the case of the solutions with surface-active substances, the temperature-change kinetics of the dynamic adsorption layer formation facilitate the immobilization of the liquid/gas interface.

Keywords: temperature; bubble; drag coefficient; terminal velocity; dynamic adsorption layer

check for updates

Citation: Borkowski, M.; Zawala, J. Influence of Temperature on Rising Bubble Dynamics in Water and *n*-pentanol Solutions. *Minerals* **2021**, *11*, 1067. https://doi.org/10.3390/min11101067

Academic Editor: María Ángeles Martín-Lara

Received: 18 August 2021
Accepted: 27 September 2021
Published: 29 September 2021

Publisher's Note: MDPI stays neutral with regard to jurisdictional claims in published maps and institutional affiliations.

Copyright: © 2021 by the authors. Licensee MDPI, Basel, Switzerland. This article is an open access article distributed under the terms and conditions of the Creative Commons Attribution (CC BY) license (https://creativecommons.org/licenses/by/4.0/).

1. Introduction

The hydrodynamics of a single bubble are a crucial matter for such engineering and environmental applications as froth flotation, foam fractionation, waste treatment, oil recovery, pulp and paper, distillation, the aeration of water reservoirs and pipe flow (cavitation) [1–4]. Moreover, bubble motion is important for the design of bubble columns and reactors, where the motion is strictly correlated to mass transfer rates [5]. Furthermore, the description of bubble motion in solutions of surface-active substances (SAS) is used to determine the evolution and development of the dynamic adsorption layer (DAL) [6], the properties of which are essential for predicting real foam stability [7].

The current state of the subject in the literature consists of a vast number of reports showing the impact of bubble size and shape [8,9], surface tension [10], density, viscosity in both phases [11–13] and the type of surfactant [14–17] on single-bubble motion characteristics. Surprisingly, reports on the influence of temperature on the velocity of rising bubbles, even in pure liquids, are quite scarce, despite the fact that this effect has significance for engineering and industrial applications. Moreover, they show considerable contradictory data and trends. Leifer [18] showed that for clean bubbles in water at different temperatures an increase from 0 to 40 °C caused a decrease in the rising velocity, the magnitude of which was influenced by the bubble diameter. Okawa et al. [19] considered the temperature effect on single bubble rise characteristic in distilled water, but this work was focused mostly on a comparison between the influence of the temperature on bubble path oscillations and the method of bubble formation. Only two temperature values, low (15 °C) and high (90 °C) were studied, and in the majority of cases the terminal velocities differed significantly from the theoretical predictions, assuming slip boundary conditions at the liquid/gas interface. Zhang et al. [20] determined the bubble rise velocity profiles in tap water and solutions of Triton X-100 surfactants in the temperature range 6–40 °C and found that, with an increasing temperature, the bubble maximum and terminal velocity also increased. Moreover, they showed that the bubble terminal velocity was reached faster when the temperature was higher. The bubble characteristics in a bubble column between 30 and 60 °C was studied by Issaoui and Ben Mansour [21]. They found that an increase in liquid temperature caused only a slight increase in the bubble rise velocity. Liu et al. [22] reported no temperature influence on the terminal velocity in distilled water for 0–100 °C for bubble of 3.3–6.1 mm.

As can be seen, the literature is full of conflicting information. The most probable reason is a surface purity issue and the rising bubble's great sensitivity to presence of even traces of surface-active contaminants, which was recently analyzed in a high-quality study by Pawliszak et al. [23]. It seems that, except for the work by Zhang et al. [20], who were perfectly aware of the properties of the system they studied, the experiments were conducted in undefined systems (i.e., contaminated liquids), where velocity was randomly influenced by uncontrolled concentrations of surface-active impurities. In this paper, special care was taken to reduce the number of parameters influencing bubble hydrodynamics (i.e., a constant bubble radius was used). In addition, we were sure that, according to the conclusions given in Pawliszak et al. [23], we were working in a bubble size range where the liquid/gas interface was fully mobile in distilled water. In addition, to check the temperature influence on the kinetics of the dynamic adsorption layer formation at the rising bubble surface, the experiments were also carried out in several chosen concentrations of *n*-pentanol. The research was conducted using two techniques (visual observations and ultrasonic sensor readings) to increase the certainty of the results and to check the reliability and usefulness of the ultrasonic sensor for determining bubble velocity profiles. The ultrasonic technique, based on the well-known Doppler effect, is not new in fluid dynamics [24]; however, the literature is limited to reports on the determination of bubble velocities in columns [25,26] or tubes (Taylor bubbles) [27,28]. To the best of our knowledge, the use of ultrasound has never been reported for the monitoring of a single bubble rise velocity to determine the kinetics of the formation of the dynamic adsorption layer at the liquid/gas interface.

2. Materials and Methods

2.1. Materials

Commercially available *n*-pentanol (>99%), a non-ionic surfactant, was purchased from Merck. All solutions in experiments were prepared in ultrapure water (Direct-Q3 UV Water Purification System by Millipore, Burlington, MA, USA, conductivity <0.7 µS/cm). The values of surface tension, density and dynamic viscosity at studied temperatures were taken from the engineering tables [29]. Details on the temperature-dependent physical properties of the water were taken from [29] and are given in Table 1.

Table 1. Physical properties of water under various temperatures, studied in the paper.

No.	Temperature (°C)	Density (kg/m^3)	Viscosity ((Pa·s $\times 10^{-3}$)	Surface Tension (mN/m)
1	5	999.9	1.52	74.9
2	15	999.1	1.14	73.5
3 [1]	20	998.2	1.00	72.8
4	25	997.0	0.89	72.0
5	35	994.1	0.72	70.4
6	45	990.2	0.60	68.8

[1] experimental data on bubble velocity and deformation from [30].

2.2. Methods

Variations in the local velocities of a single bubble rising in an aqueous phase of different physicochemical properties (tuned by a temperature modification), according to the values given in Table 1) were determined using digital camera observations coupled with image analysis and ultrasonic sensor data. The set-ups used for both experimental approaches are schematically illustrated in Figure 1, and, in both cases, the main parts were identical: a square glass column (40 mm × 40 mm × 400 mm) with a thick-walled glass capillary (inner diameter d_c = 0.0753 mm) sealed at the bottom and an automatic bubble generator (Bubble-on-Demand [28]) to form a single bubble with control over its detachment frequency (adjusted to 60 s). Moreover, in both experimental approaches, the column with the tested liquid was placed and sealed inside the larger, outer square glass column (60 mm × 60 mm × 400 mm) to maintain the liquid's temperature in the inner column at the desired level. Before each experimental series, the temperature was adjusted using a circulating water bath (Thermo Scientific SC100-A10, Waltham, MA, USA), and this process was controlled by an electronic thermometer immersed in the inner column liquid.

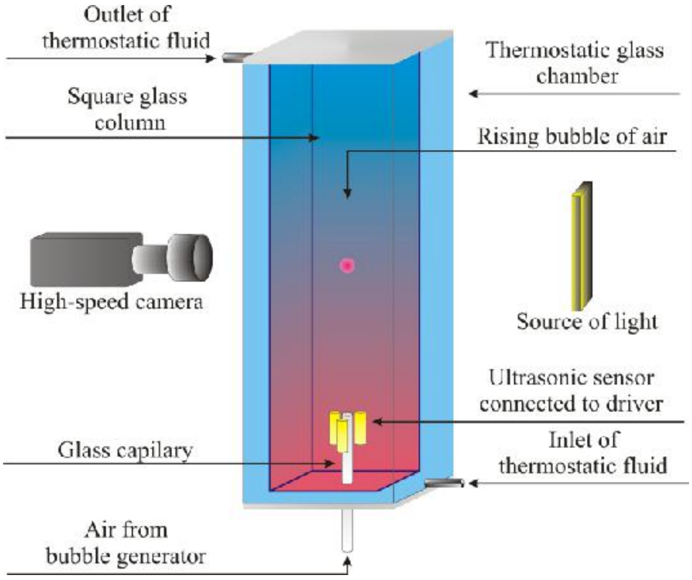
Outlet of thermostatic fluid
Thermostatic glass chamber
Square glass column
Rising bubble of air
High-speed camera
Source of light
Ultrasonic sensor connected to driver
Glass capilary
Inlet of thermostatic fluid
Air from bubble generator

Figure 1. Schematic illustration of the experimental set-up used to determine bubble rising velocity in the aqueous phase of various temperatures using camera and an ultrasonic sensor.

It has to be added here that, for experiments in pure water, only the period of rectilinear bubble motion was analyzed. It was observed during the experiments that, after a given distance, the bubble path deviated from a straight line. Moreover, the distance at which this deviation was noticed was generally shorter for higher water temperature. This distance, however, was much larger than needed for the bubble to reach terminal velocity, but an analysis of a temperature-dependent bubble path was beyond the of scope of this paper. For *n*-pentanol, establishment of terminal velocity strictly depended on the kinetics of the dynamic adsorption layer (DAL) formation. For this particular reason, longer distances covered by the bubble were analyzed, and for a particular pentanol solution concentration, the terminal velocity was calculated from the period where the bubble's oscillatory motion was observed.

2.2.1. Velocity Determination by Camera and Image Analysis

Details on the experimental protocol and image analysis algorithms used for bubble velocities determination by visual observations can be found elsewhere [10,30,31]. Briefly, in this method, the local bubble velocity could be calculated from analyzing the bubble photos recorded by a CCD camera at equal time intervals. In our case, bubble motion was recorded by the SpeedCam MacroVis (Ettlingen, Germany) at 100 fps. The frame-by-frame analysis of the collected movies was automatized by an in-house-written Python script (using OpenCV 3.4.13 and PIL 7.2.0 modules). The values of a local rising bubble velocity were calculated as:

$$u = \frac{\Delta L}{\Delta t} \tag{1}$$

where $\Delta L = (x_{i+1} - x_{i-1})^2 + (y_{i+1} - y_{i-1})^2$, while $(x_{i+1} - x_{i-1})$ and $(y_{i+1} - y_{i-1})$ are the vertical and horizontal coordinates of a subsequent position of the rising bubble geometrical center within a time interval that matched the camera frequency. For experiments in pure water, the significance of the vertical coordinates' constituents was negligible. Furthermore, with pictures of the rising bubble, the so-called equivalent bubble diameter (d_{eq}) and ratio of the bubble deformation (χ) were calculated as:

$$d_{eq} = \sqrt[3]{d_v {d_h}^2} \tag{2}$$

$$\chi = \frac{d_h}{d_v} \tag{3}$$

where d_v and d_h are the bubble's vertical and horizontal diameters, respectively. These parameters were used further to analyze the hydrodynamics of the rising bubble under different temperature conditions.

2.2.2. Velocity Determination by Ultrasound

In this approach the ultrasonic sensor mounted on the bottom of the liquid column, transmitted and received at 5 MHz. The bubble rising velocity was determined analyzing the variations in the temporal evolution of a position of the registered signal formed as a result of ultrasonic waves reflected from the rising bubble surface. An example of the signal as a function of distance of the bubble from the capillary is presented in Figure 2. The parameters of the sensor and the time dependent signal position were controlled and recorded by the driver (OPBOX 2.0 mini ultrasonic box), and the software was elaborated by PBP OPTEL (Wrocław, Poland) [32]. The bubble position of the maximum signal value was acquired in constant time intervals of 87.8 ms. The values of the local bubble velocities were calculated by differentiating the temporal evolution of the signal position. For each of the selected temperatures (see Table 1), the velocity as a function of time was measured independently for 10 subsequent single bubbles. It is worth highlighting that, for an accurate determination of the signal temporal evolution, the information about the speed of sound in the liquid phase was necessary. Its values, presented in Table 2, were temperature d-pendent and taken directly from the engineering tables [29].

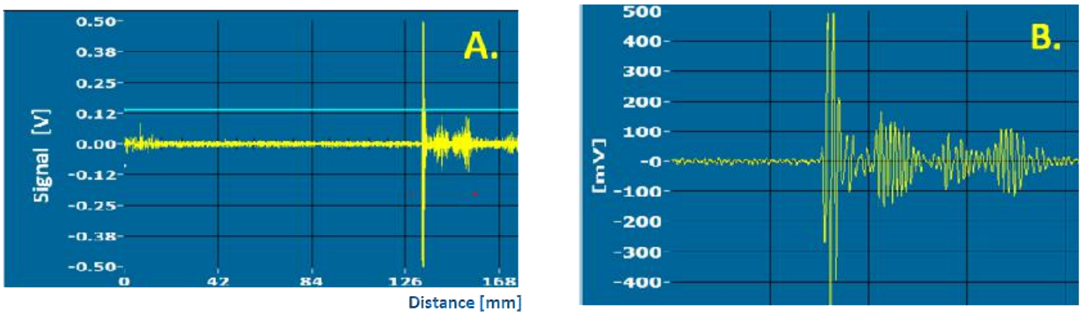

Figure 2. (**A**) Example of the signal registered during bubble rise in the liquid (aqueous phase) as a function of distance; (**B**) magnified signal (magnification area marked by the red line).

Table 2. Speed of sound used to determine the rising bubble using an ultrasonic sensor (taken from Eng. Toolbox [29]).

No.	Temperature (°C)	Sound Velocity in Pure Water (m/s)
1	5	1427
2	15	1465
3	25	1495
4	35	1518
5	45	1534

2.2.3. Numerical Calculations

Modelling of rectilinear bubble motion in liquid of properties of water under different temperature conditions (according to Table 1) was performed using spatial discretization and numerical scheme implemented in a Gerris Flow Solver (release on 6 December 2013), which is described in detail elsewhere [33–35].

The numerical algorithms of Gerris were used to solve the governing equations describing the conservation of momentum and mass of an incompressible liquid in the form:

$$\rho\left(\frac{\partial \boldsymbol{u}}{\partial t}+\boldsymbol{u}\cdot\nabla\boldsymbol{u}\right)=-\nabla p+\nabla\cdot(2\mu\boldsymbol{Q})+\sigma\kappa\delta_s\boldsymbol{n} \tag{4}$$

$$\nabla\cdot\boldsymbol{u}=0 \tag{5}$$

$$\boldsymbol{Q}=\frac{1}{2}\left(\nabla\boldsymbol{u}+(\nabla\boldsymbol{u})^T\right) \tag{6}$$

where $\boldsymbol{Q}$ is a strain rate tensor; $\boldsymbol{u}$ is the fluid velocity vector; ρ is the fluid density and μ is its viscosity; p is pressure; t is time; σ is surface tension; δ_s is a Dirac distribution function (expressing the fact that the surface tension term was concentrated at the interface); κ and $\boldsymbol{n}$ are the curvature and normal unit vector to the interface, respectively [33]. The liquid column of height H = 150 mm and radius L, containing a gas bubble of radius R_b = 0.745 mm, was described by an axisymmetrical cylindrical coordinate system. The chosen value of L was directly related to the numerical (adaptive) grid size, as discussed by Popinet [33] and Zawala [36], and was adjusted for results convergence. It was found that, to obtain the converged data, the L had to be at least 10 mm, which corresponded to the minimum size of the numerical grid cell equal to 4.9 µm. This was consistent with the results of similar calculations presented by Zawala [36]. Initially, at t = 0, the center of the motionless spherical bubble was set 3 mm above the bottom of the liquid column at the symmetry axis (x = 0). After acceleration, constant speed (terminal velocity) of the bubble was established after t = 0.10 s. The bubble motion parameters were calculated for the time period t = 0.14–0.16 s. The liquid density, viscosity and surface tension were taken from Table 1 to mimic the bubble rise in the aqueous phase of different temperatures.

A comparison between experimentally obtained photos of the rising bubble under steady-state conditions and the corresponding numerically reproduced bubble outlines is presented in Figure 3. A very good qualitative agreement between these sets of data was found. The quantitative analysis of the data is presented further in the paper.

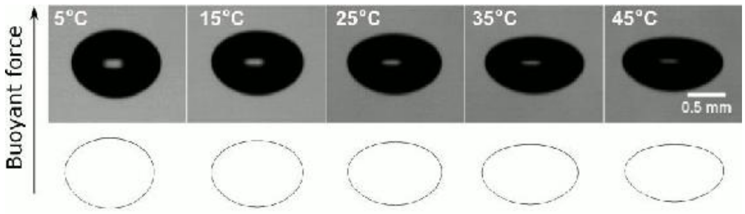

Figure 3. Qualitative comparison of the bubble shapes observed experimentally and determined by means of numerical calculations.

3. Results

3.1. Bubble Rising in Pure Water

Values of the bubble radius ($R_b = d_{eq}/2$), calculated from the camera registered rising bubble photos are presented in Figure 4 (d_c = 0.0753 mm). In addition, the values reported by Zawala and Niecikowska [30] acquired for bubbles formed at capillaries of various d_c but a constant temperature T = 21 ± 1 °C were given for comparison. The solid line represents the theoretical size of the bubble detaching from the capillary, which can be calculated by balancing the buoyant (detaching) force:

$$F_b = V_b \Delta\rho g \tag{7}$$

and capillary (attachment) force:

$$F_c = \pi d_c \sigma cos\theta \tag{8}$$

where V_b is the bubble volume; Δρ is the density difference between the liquid (ρ_l) and gas (ρ_g) phases; σ is the surface tension; θ is the contact angle (equal to 0 for a clean glass capillary surface); g is the gravitational constant. At the moment of bubble detachment, F_b equaled F_c, and this relation could be rearranged to give an equation known as Tate's law [20,37]:

$$R_b = \left(\frac{3}{4}\frac{d_c\sigma}{\Delta\rho g}\right)^{1/3} \tag{9}$$

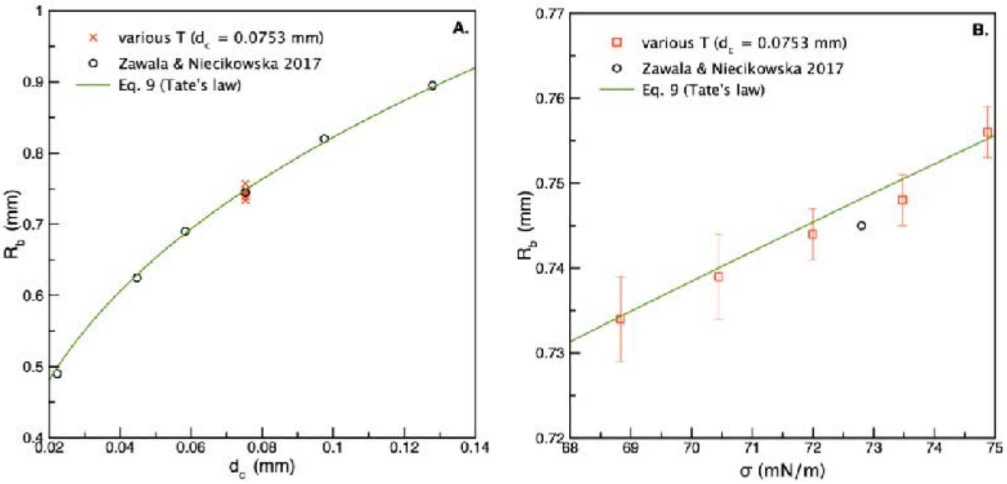

Figure 4. Radius of the bubble rising in water (measured by image analysis) as a function of (**A**) capillary orifice diameter and (**B**) water surface tension variations caused by the temperature changes.

As seen in Figure 4A, a very good agreement between the experimental data and theoretical predictions of Equation (9) for water at T = 21 ± 1 °C was obtained [30]. The R_b values measured in water of different T were also consistent with the predictions; nevertheless, slight deviations from the theoretical line could be observed, caused by variations in the water physicochemical parameters, especially surface tension values. Figure 4B presents a comparison of the R_b as a function of water surface tension (Table 1), and a quite good match between experimental and theoretical values was found. This proved that the bubble was generated (by the elaborated BoD generator [30]) under conditions that allowed the establishment of an equilibrium between F_b and F_c, so the bubble R_b could also be considered at equilibrium. It was seen that a decrease in the σ value caused by the water temperature increased from 5 °C to 45 °C, resulting in only a slight variation in the R_b (from 0.757 ± 0.005 to 0.734 ± 0.005).

A comparison of the terminal bubble velocities (u_t) is presented in Figure 5. The terminal velocity was shown as a function of the temperature. For T = 20 °C, the value from Zawala and Niecikowska's [30] paper was used. The dashed lines in Figure 5 are second-order polynomials fitted separately to each of the datasets. The solid line is the average polynomial fit. It was evident that the bubble velocity measured by the ultrasonic sensor (u_s) was higher than for the image analysis (u_c). However, the fitted dashed lines indicated that the relative difference between the camera and ultrasonic datasets was similar, so it was caused by a systematic rather than a random factor. It can be presumed that this difference was probably caused by assumptions made on the sound wave speed in the water phase and the different temperature values for which were taken directly from the engineering tables (see Table 2). The difference could have been caused, for example, by wave interference with the column walls. As seen in the inset in Figure 5, the difference between data obtained by both techniques, quantified by the u_s/u_c ratio, was of order of 2–5%. The average second-order polynomial fit, which accurately described the trend of terminal velocity variations (in cm/s) with temperature (expressed in °C) within the range (solid line in Figure 5) was given as:

$$u_t(T) = -0.003 \cdot T^2 + 0.3195 \cdot T + 29.827 \tag{10}$$

For CFD data, an agreement with the experimental results decreased with an increasing temperature. This effect was a consequence of an increasing bubble deformation (see Figure 3), i.e., the increase in the bubble d_h caused an increase in the drag force resulting from column wall proximity, which could be associated with the so-called wall effect). As seen, both for the ultrasonic and camera methods, the standard deviation values for average terminal velocity were quite small, indicating a good reproducibility. It should be highlighted, however, that, for the camera method, the terminal velocity was calculated from only one experimental run. The ultrasonic sensor, because of its simplicity and swiftness of measurement, allowed for multiple measurements of a bubble velocity profile, which increased the statistical soundness of the terminal velocity values.

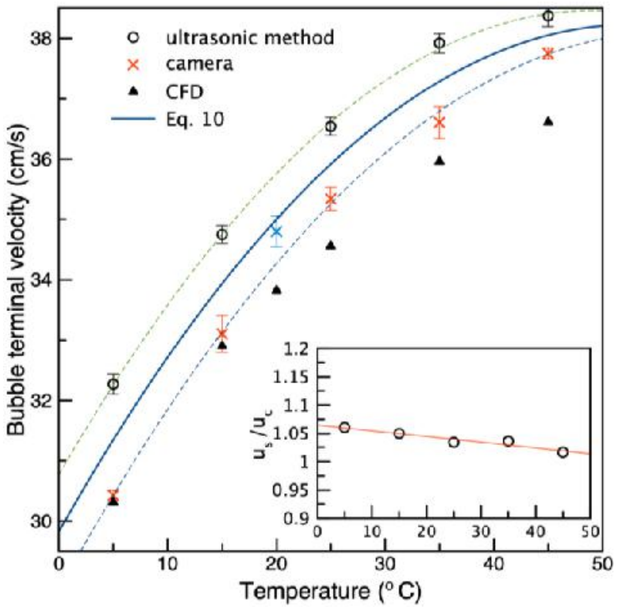

Figure 5. Terminal velocity of the rising bubble formed at orifice of d_c = 0.0753 mm in water of temperature ranging from 5 °C to 45 °C (see Table 1 for details), determined using ultrasonic and camera techniques.

Usually, to characterize the bubble dynamics in liquids, various dimensionless numbers are used to allow correlation and comparison between variations in the bubble motion parameters and shape pulsations under different physicochemical conditions. This helps to determine the useful general expressions and dependencies, which could be extended for other systems with comparable bubble shape changes and flow regimes. In our case, for a description of bubble dynamics, the deformation ratio χ (determined on the basis of image analysis) and the rising velocities measured by the two different techniques under different physical conditions (see Table 1), were described using Reynolds (*Re*) and Weber's (*We*) numbers, which allowed a direct comparison with the relations in the models in the literature. In addition, this comparison was used to assess the reliability of the ultrasonic method for determining the bubble dynamics in the aqueous phase. The *Re* and *We* were calculated as:

$$Re = \frac{d_{eq}\rho_l u_t}{\mu} \tag{11}$$

$$We = \frac{d_{eq}\rho_l {u_t}^2}{\sigma} \tag{12}$$

Figure 6A presents experimentally determined χ values as a function of the Weber number calculated for experimental data by Zawala and Niecikowska [30] and for the data obtained in our studies under various temperatures. Moreover, the data from the numerical calculations were given for comparison. In addition, the empirical relation by Legendre et al. [38] in the form:

$$\chi = \frac{1}{1 - \frac{9}{64}We} \tag{13}$$

was plotted in Figure 6A as a solid line. Quite a good agreement between the data and the relation given by Equation (9) was found. Again, the most significant difference was registered for the ultrasonic method. This was a consequence of the above-mentioned difference in the u_t values. Nevertheless, it can be assumed that, in the R_b range, the variations in the bubble χ vs. We were reasonably described by the Legendre relation [38].

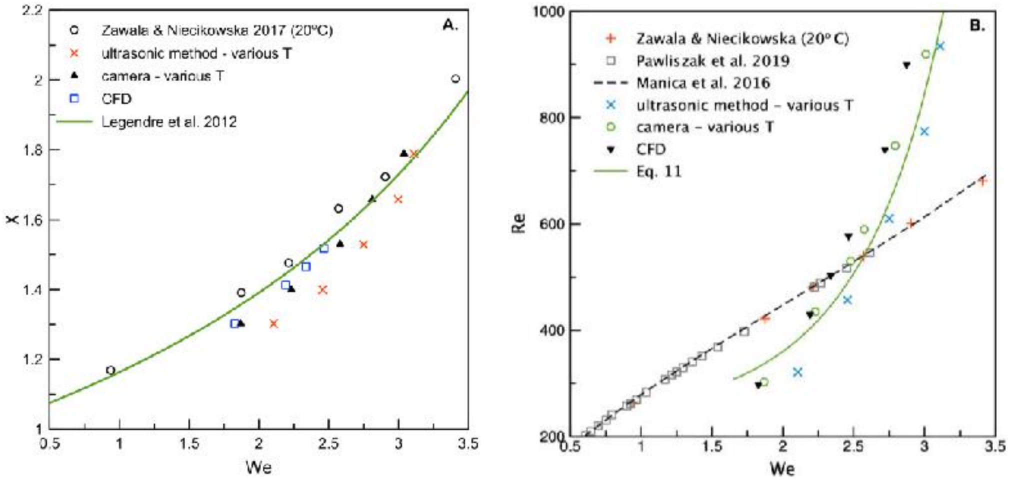

Figure 6. Dependence between (**A**) rising bubble deformation ratio and Weber number, and (**B**) Reynolds number and Weber number determined on the basis of various techniques.

The dependence of *Re* on *We* is given in Figure 6B. Here, it was possible to compare the data with the literature results by Pawliszak et al. [23] (experiments at room temperature) and the theoretical predictions reported by Manica et al. [13,39], which allowed the calculation of terminal velocities for rising bubbles of different shapes, assuming a slip hydrodynamic boundary condition at the liquid/gas interface (i.e., when there was no adsorption layer at the bubble surface). As was seen, the agreement of the different sets of literature data, i.e., the bubble velocities determined at the room temperature (21 ± 1 °C), was almost perfect. This was, however, not the case for the u_t determined for various T, where a completely different trend was revealed. Intuitively, it could have been expected that this new trend would have been caused not by a modification of the bubble hydrodynamic boundary conditions, but by the liquid physicochemical parameters only. To show the correctness of this claim, the results presented in Figure 6B were analyzed according to the model by Moore, allowing a direct calculation of the bubble drag coefficient (C_D). For this purpose, a common relation between *We* and *Re* (necessary for further calculations) was quantified. For experiments at room temperature (literature data) the relation between *Re* and *We* was almost linear and was approximated (in the considered R_b range) by:

$$Re = 185.90We + 66.88 \tag{14}$$

while for various temperature conditions by the Equation (see solid green line in Figure 6B):

$$Re(T) = 251.29 \cdot e^{0.0449 \cdot We(T)^3} \tag{15}$$

To calculate the theoretical drag coefficient associated with the rise of the deformed bubbles in water (clean liquid/gas interface) at various temperatures, the relation elaborated by Moore [38], which is confined to a thin viscous sublayer according to his theory of viscous flow around the bubble, was used:

$$C_{D(M)} = \frac{48}{Re} G(\chi) \cdot \left[1 - \frac{2.21 \cdot H(\chi)}{Re^{1/2}}\right] \tag{16}$$

where $G(\chi)$ and $H(\chi)$ are geometrical factors calculated by Moore [40], which were accurately approximated by the equations given by Loth [41] and Rastello et al. [42]:

$$G(\chi) = 0.1287 + 0.4256 \cdot \chi + 0.4466 \cdot \chi^2 \tag{17}$$

$$H(\chi) = 0.8886 + 0.5693 \cdot \chi - 0.4563 \cdot \chi^2 \tag{18}$$

To calculate the values as a function of *Re*, the empirical relations between χ and *We* (Equation (13)) as well as *Re* and *We* (Equations (14) and (15)) were used. The drag coefficient of the experimentally observed bubbles was calculated from the general expression for the drag force (F_d) acting on the object moving in a liquid phase:

$$F_d = 0.5AC_D\rho_l {u_t}^2 \tag{19}$$

where A is the object projected area (for the spherical bubble equal to $\pi {R_b}^2$). Under steady-state conditions, when the rising velocity was constant (terminal), the $F_d = F_b$. After rearrangement, assuming that for the rising bubble the $\Delta\rho \simeq \rho_l$, the C_D was calculated using experimentally determined R_b and u_t values, as

$$C_D = \frac{8R_b g}{3{u_t}^2} \tag{20}$$

Figure 7 presents the determined C_D as a function of Re, calculated using Equations (11)–(20). In addition, the values of the drag coefficient of a particle with no-slip hydrodynamic boundary conditions [43] in the form:

$$C_{D(C)} = \frac{24}{Re} \cdot \left(1 + 0.15Re^{0.687}\right) + \frac{0.42}{1 + 42500Re^{-1/16}} \tag{21}$$

were also plotted. As could be expected, the Moore model very accurately described the literature data, obtained at room temperature in pure water. It was seen, moreover, that, after considering the temperature effect by means of Equations (14) and (15), the experimental data (determined both by ultrasonic and camera techniques) were also very well described. It showed evidence that, under various temperatures of pure water, the hydrodynamic boundary conditions of bubbles of various sizes remained unchanged and could be assumed as fully slip.

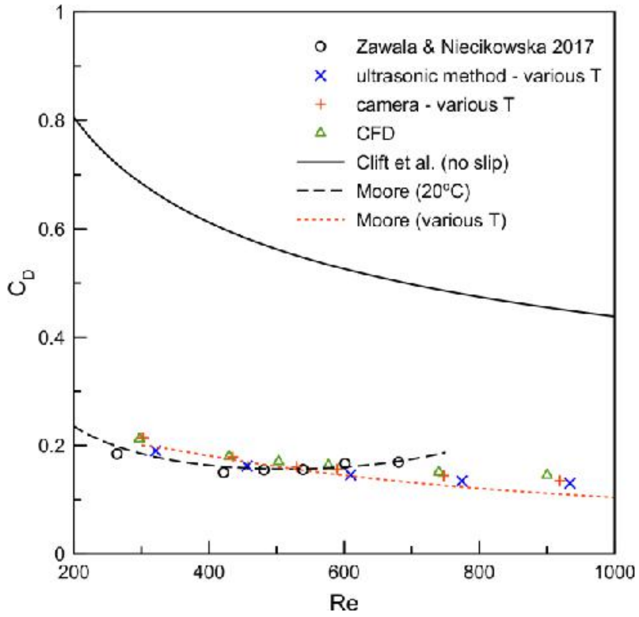

Figure 7. Drag coefficient of the bubble rising in water of various temperatures. Points—experimental values calculated according to Equation (20); lines—theoretical predictions of Clift et al. (immobile liquid/gas interface) and Moore (mobile liquid/gas interface).

Moreover, the above analysis showed that the ultrasonic method of bubble velocity determination was reliable but not as accurate as visual observations because it depended on an arbitrarily chosen speed of the sound value, which had to be used during the velocity analysis. Moreover, it did not allow for the determination of the bubble deformation ratio. Nevertheless, the ultrasonic method was significantly faster and gave a much better level of statistical confidence in a remarkably reduced time. In our opinion, it can be successfully used as a reliable tool for single bubble velocity measurements, especially in opaque or turbid solutions where camera observations were difficult or impossible.

In addition, experiments on the bubble motion in water of different temperatures allowed for the determination of the useful relations between the dimensionless numbers and the T values. These relations, which are presented in Figure 8, could be expressed as:

$$We(T) = -3.18 \cdot 10^{-4} \cdot T^2 + 0.043 \cdot T + 1.775 \tag{22}$$

$$Re(T) = 15.45 \cdot T + 222.49 \tag{23}$$

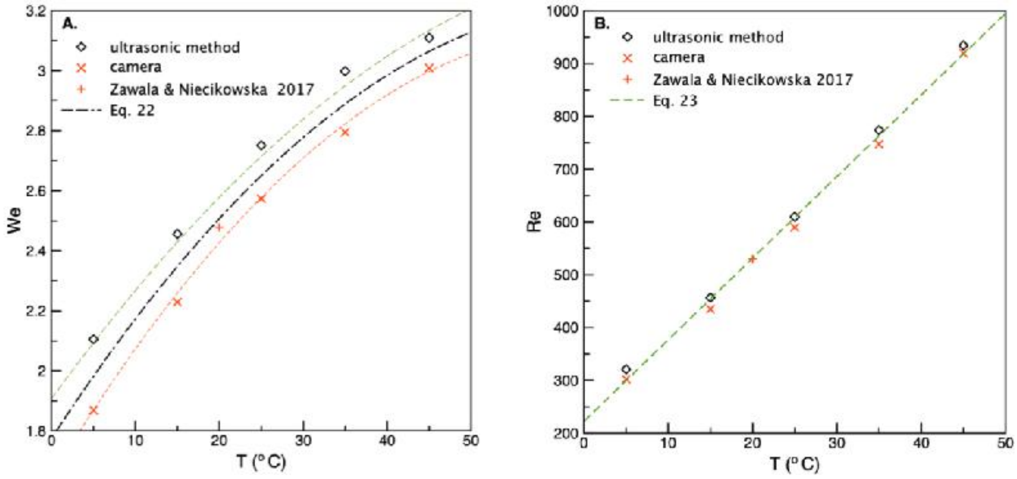

Figure 8. Temperature dependence of (**A**) Weber number and (**B**) Reynolds number associated with a bubble rising in water.

All the empirically determined relations between the various parameters during the period of rectilinear bubble rising under a steady-state condition in water of different temperatures are shown in Table 3. We believe that these relations could also be used for different bubble shapes and sizes under rectilinear motion.

Table 3. Empirical relations between various parameters useful for the description of bubble dynamics in water of different temperature (for 200 < Re < 1000).

No.	Dependence	Empirical Relation (Valid for Bubble in Water Tat emperature = 5–45 °C)
1	Terminal velocity vs. Temperature	$u_t(T) = -0.003 \cdot T^2 + 0.3195 \cdot T + 29.827$ (Equation (10))
2	Reynolds vs. Weber number	$Re(T) = 251.29 \cdot e^{0.0449 \cdot We(T)^3}$ (Equation (15))
3	Weber number vs. Temperature	$We(T) = -3.18 \cdot 10^{-4} \cdot T^2 + 0.043 \cdot T + 1.775$ (Equation (22))
4	Reynolds number vs. Temperature	$Re(T) = 15.45 \cdot T + 222.49$ (Equation (23))

3.2. *Bubble Velocity Variations in n-pentanol Solutions of Various Concentrations and Temperature*

3.2.1. Analysis of the Local Velocity Profiles in Different Temperatures

Profiles of the local bubble velocity (i.e., velocity variations as a function of the distance covered by the bubble in various concentrations of *n*-pentanol solutions) are presented in Figure 9. The data redrawn from Zawala et al. [44] were compared with corresponding profiles taken by the ultrasonic sensor. The literature data were obtained using the classical camera technique and manual frame-by-frame image analysis [44].

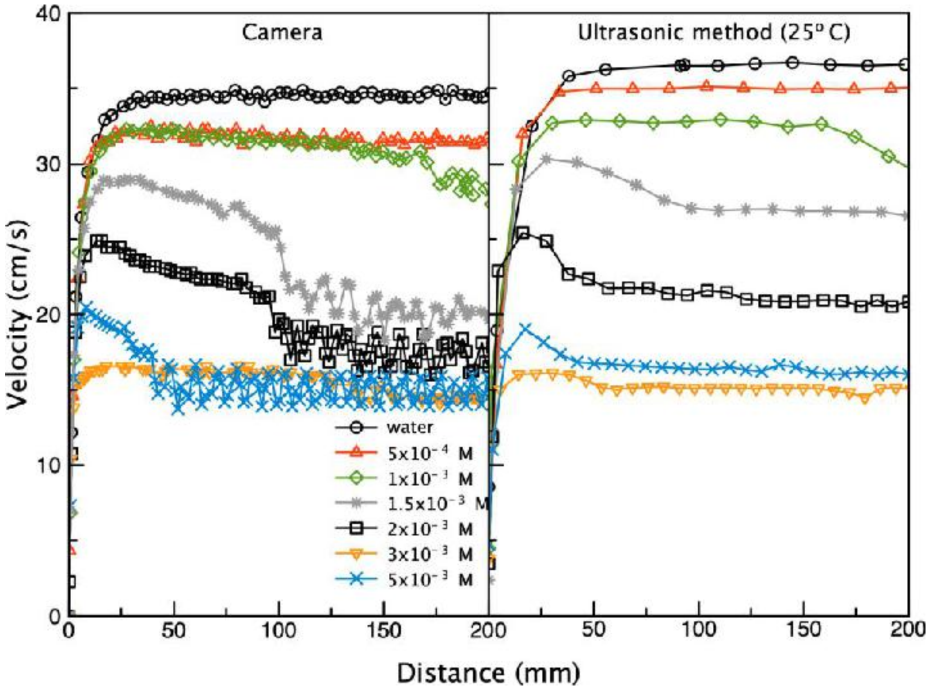

Figure 9. Comparison of the bubble local velocity profiles obtained on the basis of camera and image analysis approach (data redrawn from [44]) and using ultrasonic technique.

Despite the slightly different temperatures of the solutions (our measurements were performed in 25 °C, while the literature results were reported at 21 °C), quite a good agreement between the two sets of data was seen. All characteristic bubble velocity changes, including the maximum deceleration and the moment of the terminal velocity establishment, were accurately captured. It is well established that these characteristic velocity variations can serve as fingerprints for the dynamic behavior of the adsorption/desorption processes at the solution/air interface [31]; in other words, they can be used to track the development and stages of the formation of the so-called dynamic adsorption layer (DAL). For example, the maximum bubble velocity was an indication that the DAL did not yet form but just started [45]. The terminal velocity establishment meant that the DAL was fully formed; that is, there was an uneven distribution of surfactant molecules, with a depletion zone at the bubble top pole [6,44,45]. As seen in Figure 9, the ultrasonic method can be used as a complementary tool for these purposes. As already mentioned, a main advantage was its speed—there was no need for a time-consuming image analysis step. On the other hand, ultrasonic measurements did not provide any information about bubble size and deformation or the evolution of bubble shape with time or distance. As was shown by Krzan et al. [45], this is an additional important parameter that can be used to analyze the DAL formation at moving liquid/gas interfaces.

To elucidate the influence of the temperature on kinetics of the DAL formation, each bubble velocity profile, taken in the *n*-pentanol solution of considered temperature (Table 1) was normalized according to the maximum velocity value (u_{max}). The u_{max} values for chosen *n*-pentanol concentration are presented in Table 4. As seen, the bubble maximum velocity increased with the temperature—this result was consistent with the reports by Zhang et al. [20], who observed a similar trend in Triton X-100 solution of concentration 1.25×10^{-4} mol/m^3. Figure 10 presents a comparison of normalized velocity for three chosen *n*-pentanol concentrations. The concentration 1×10^{-4} and 5×10^{-3} M corresponded to the concentrations where the DAL was established just after the bubble acceleration period, while the concentration 1.5×10^{-3} M was intermediate, where the DAL formation was associated with a maximum velocity existence.

Table 4. Temperature dependence of the bubble maximum velocity in *n*-pentanol solution of concentration 1.5×10^{-3} M.

c (mol/dm^3)	Temperature (°C)	u_{max} (cm/s)
1.5×10^{-3}	5	24.6
	15	29.9
	25	30.3
	35	33.0
	45	34.6

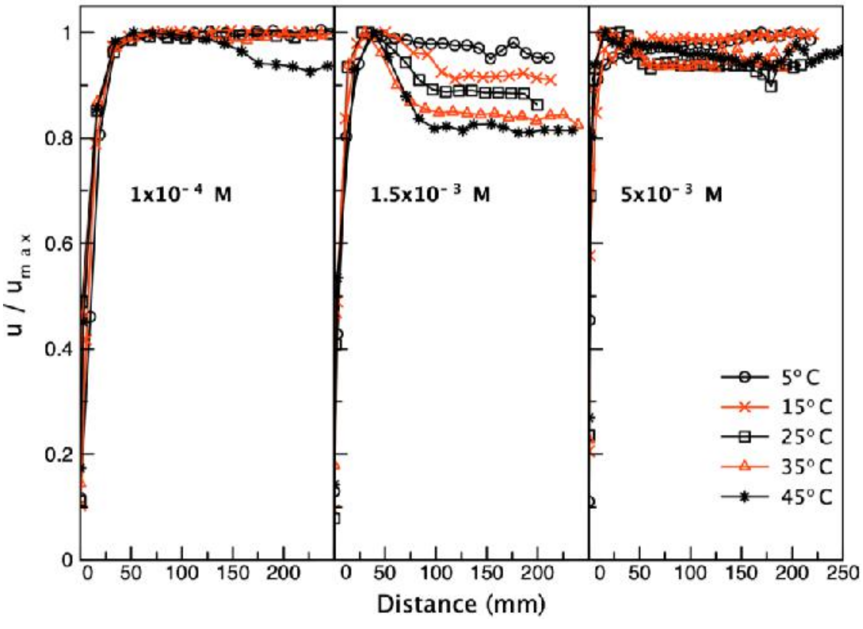

Figure 10. Comparison of profiles of the bubble velocity for three chosen concentrations of *n*-pentanol solutions of different temperatures.

As seen for 1×10^{-4} M and 1.5×10^{-3} M, the effect of increasing the solution temperature was similar to that of increasing the solution concentration (compare with the data in Figure 9). It was especially pronounced for 1.5×10^{-3} M, where the terminal velocity decreased as the temperature increased and, in addition, the moment of its establishment shifted slightly towards shorter distances (i.e., the DAL was established a little bit faster). The explanation of this effect was rather obvious: a higher temperature meant a higher bubble velocity and a simultaneous increase in the rate of convective diffusion transport of the *n*-pentanol molecules to the rising bubble surface. Similar trends were shown in the solution of Triton X-100 by Zhang et al. [20]

3.2.2. Analysis of Terminal Velocity (at a Distance of 200 mm)

The effect of temperature on the terminal velocities was further analyzed according to the empirical equation developed by Kowalczuk et al. [17]:

$$u_t = u_{min} + (u_w - u_{min}) \cdot e^{-3\left(\frac{c}{CMV}\right)^2} \tag{24}$$

where u_w is the bubble velocity in water (maximum possible); u_{min} is the minimum velocity of the bubble (with fully immobilized interface); c is the surface-active substance bulk concentration; CMV is the so-called concentration at minimum velocity. As was discussed elsewhere [14–16], the CMV can be used as a very useful tool for characterizing the kinetics of surfactant adsorption at the rising bubble interface (the kinetics of bubble surface immobilization), solution foaming properties and a comparison of these factors for different types of surface-active substances.

Figure 11A presents the u_t values for bubble velocity at 200 mm. In the great majority of experiments, this distance was enough to establish terminal velocity in all *n*-pentanol concentrations, except for $1{\times}10^{-3}$ M (see Figure 9). For this specific case, especially for lower temperatures, the calculated u_t values were slightly higher than those corresponding to the fully developed DAL. The points presented in Figure 11 were experimental data, while the lines were predictions of Equation (24), which described the u_t vs. c dependence very accurately for all temperature ranges. As expected, the CMV values, calculated as a fitting parameter of Equation (24) and presented in Table 5, were practically identical for all temperature values. That meant that, despite the difference in absolute bubble velocity values, the concentration that caused the complete immobilization of the rising bubble surface (above which no further velocity decrease was noticed) was temperature-independent.

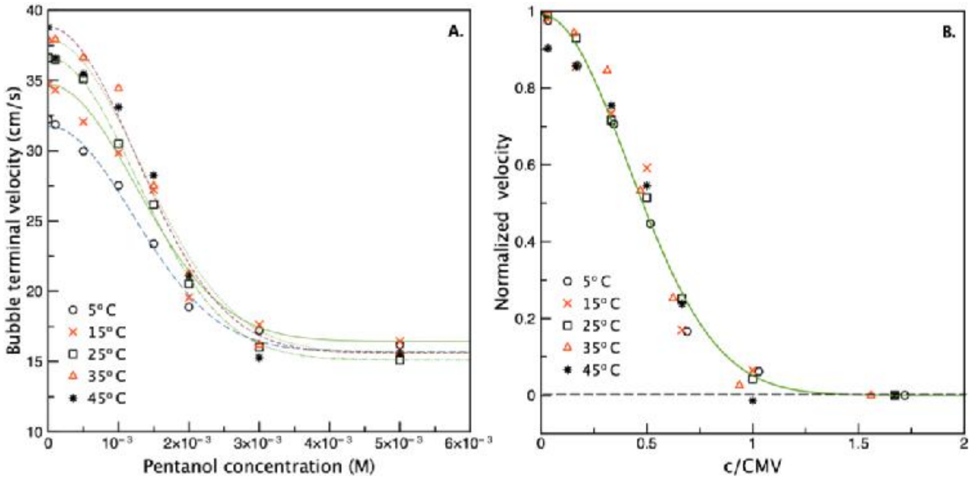

Figure 11. Influence of temperature on (**A**) bubble terminal velocity as a function of *n*-pentanol concentration and (**B**) normalized velocity ($(u_t - u_{min})/(u_{max} - u_{min})$) as a function of c/CMV (data acquired using the ultrasonic method).

Table 5. Values of the concentration at minimum velocity (CMV) for *n*-pentanol solutions of different temperatures.

No.	**Temperature (°C)**	**CMV (mol/dm^3)**
1	5	2.9×10^{-3}
2	15	3.0×10^{-3}
3	20	3.0×10^{-3}
4	25	3.2×10^{-3}
5	35	3.0×10^{-3}

By plotting the normalized bubble velocity $(u_t - u_{min})/(u_w - u_{min})$ vs. c/CMV values, all experimental data taken for different temperatures were seen to converge in one universal curve, which indicated that the *n*-pentanol influenced the bubble rising velocity in a similar manner. It was the final evidence that the temperature, in this case, influenced only the kinetics of adsorption of the *n*-pentanol at the liquid/gas interface.

4. Conclusions

Experiments performed using two independent experimental methods, supported by numerical calculations and an analysis of the results, showed that, for a clean system, the temperature did not change the hydrodynamic boundary conditions at the rising bubble surface. Under various temperatures of pure water, the hydrodynamic boundary conditions of the bubbles of a given size remained unchanged and could be assumed to be fully slip. An increase in the rising velocity was caused only by modifying the physicochemical parameters of the water (density, viscosity and surface tension). Concerning the bubble's diameter, an increase in the temperature from 5 to 45 °C caused only a slight size modification. In turn, the bubble deformation varied significantly: the deformation ratio increased with the water temperature and its value was accurately quantified using Legendre's equation.

It was shown, moreover, that the concentration values at minimum bubble velocity (CMV), calculated from experiments of a bubble rising in *n*-pentanol solutions of different concentrations, were practically identical for all temperatures. It meant that, despite the difference in the absolute bubble velocity, the concentration, causing the complete immobilization of the rising bubble surface (above which no further velocity decrease could be noticed) was temperature-independent. The temperature only influenced the timescale of the bubble surface immobilization. This observation confirmed the results presented by Zhang et al. [20], which associated this effect with an increase in diffusion kinetics of the surfactant molecules.

The results and analysis showed that the ultrasonic method of determining the rising velocity of a single bubble was reliable, yet not as accurate as a visual observation because the ultrasonic sensor depended on an arbitrarily chosen speed of sound in a liquid phase, which had to be used during calculations. Moreover, it did not allow for the determination of the bubble deformation ratio, which (according to the literature) is an important parameter for helping to quantify the dynamic adsorption layer formation stages. On the other hand, the ultrasonic method was significantly faster and gave a much better level of statistical confidence in a remarkably reduced time. In our opinion, it can be successfully used as a reliable tool for single bubble velocity measurements, especially in opaque or turbid solutions, where camera observations are difficult or impossible.

Author Contributions: Conceptualization, M.B. and J.Z.; methodology, M.B. and J.Z.; software, J.Z.; validation, M.B. and J.Z.; formal analysis, M.B. and J.Z.; investigation, M.B.; resources, J.Z.; data curation, J.Z.; writing—original draft preparation, M.B. and J.Z.; writing—review and editing, M.B. and J.Z.; visualization, M.B. and J.Z.; supervision, J.Z.; project administration, J.Z.; funding acquisition, J.Z. All authors have read and agreed to the published version of the manuscript.

Funding: This research was partially funded by the National Science Centre, grant number 2017/25/B/ST8/01247, and partially supported in a frame of the ICSC PAS statutory task.

Acknowledgments: Partial financial support from (NCN grant no) is acknowledged with gratitude.

Conflicts of Interest: The authors declare no conflict of interest. The funders had no role in the design of the study; in the collection, analyses, or interpretation of data; in the writing of the manuscript; or in the decision to publish the results.

Nomenclature

d_c	diameter of the capillary orifice
d_{eq}	bubble equivalent diameter
d_h	horizontal (major) bubble axis
d_v	vertical (minor) bubble axis
R_b	bubble equivalent radius ($d_{eq}/2$)
ρ_l	liquid phase density
ρ_g	gas phase density
g	gravitational constant
σ	surface tension
F_b	buoyant (attachment) force
F_c	capillary (detachment) force
F_d	drag force
θ	contact angle between air and water phases
V_b	bubble volume
u_t	bubble terminal velocity
u_s	bubble terminal velocity by ultrasonic method
u_c	bubble terminal velocity by image analysis
We	Weber number
Re	Reynolds number
C_D	drag coefficient
A	bubble's projected area
χ	bubble deformation ratio

References

1. Kulkarni, A.A.; Joshi, J.B. Bubble formation and bubble rise velocity in gas-liquid systems: A review. *Ind. Eng. Chem. Res.* **2005**, *44*, 5873–5931. [CrossRef]
2. Kannan, A.; Hristov, P.; Li, J.; Zawala, J.; Gao, P.; Fuller, G.G. Surfactant-laden bubble dynamics under porous polymer films. *J. Colloid Interface Sci.* **2020**, *575*, 298–305. [CrossRef]
3. Sarafraz, M.M.; Shadloo, M.S.; Tian, Z.; Tlili, I.; Alkanhal, T.A.; Safaei, M.Z.; Goodarzi, M.; Arjomandi, M. Convective Bubbly Flow of Water in an Annular Pipe: Role of Total Dissolved Solids on Heat Transfer Characteristics and Bubble Formation. *Water* **2019**, *11*, 1566. [CrossRef]
4. Ellahi, R.; Zeeshan, A.; Hussain, F.; Safaei, M.R. Simulation of cavitation of spherically shaped hydrogen bubbles through a tube nozzle with stenosis. *Int. J. Numer. Methods Heat Fluid Flow* **2020**, *30*, 2535–2549. [CrossRef]
5. Nguyen, A.V.; Evans, G.M. Attachment interaction between air bubbles and particles in froth flotation. *Exp. Therm. Fluid Sci.* **2004**, *28*, 381–385. [CrossRef]
6. Dukhin, S.S.; Kovalchuk, V.I.; Gochev, G.G.; Lotfi, M.; Krzan, M.; Malysa, K.; Miller, R. Dynamics of Rear Stagnant Cap formation at the surface of spherical bubbles rising in surfactant solutions at large Reynolds numbers under conditions of small Marangoni number and slow sorption kinetics. *Adv. Colloid Interface Sci.* **2015**, *222*, 260–274. [CrossRef]
7. Borkowski, M.; Kosior, D.; Zawala, J. Effect of initial adsorption coverage and dynamic adsorption layer formation at bubble surface in stability of single foam films. *Colloids Surf. A Physicochem. Eng. Asp.* **2020**, *589*, 124446. [CrossRef]
8. Zawala, J.; Malysa, K. Influence of the Impact Velocity and Size of the Film Formed on Bubble Coalescence Time at Water Surface. *Langmuir* **2011**, *27*, 2250–2257. [CrossRef]
9. Krasowska, M.; Malysa, K. Kinetics of bubble collision and attachment to hydrophobic solids: I. Effect of surface roughness. *Int. J. Miner. Process.* **2007**, *81*, 205–216. [CrossRef]
10. Kosior, D.; Zawala, J. Initial degree of detaching bubble adsorption coverage and the kinetics of dynamic adsorption layer formation. *Phys. Chem. Chem. Phys.* **2018**, *20*, 2403–2412. [CrossRef]
11. Suñol, F.; González-Cinca, R. Rise, bouncing and coalescence of bubbles impacting at a free surface. *Colloids Surf. A Physicochem. Eng. Asp.* **2010**, *365*, 36–42. [CrossRef]

12. Sanada, T.; Watanabe, M.; Fukano, T. Effects of viscosity on coalescence of a bubble upon impact with a free surface. *Chem. Eng. Sci.* **2005**, *60*, 5372–5384. [CrossRef]
13. Manica, R.; Klaseboer, E.; Chan, D.Y.C. The hydrodynamics of bubble rise and impact with solid surfaces. *Adv. Colloid Interface Sci.* **2016**, *235*, 214–232. [CrossRef]
14. Tan, Y.H.; Rafiei, A.A.; Elmahdy, A.; Finch, J.A. Bubble size, gas holdup and bubble velocity profile of some alcohols and commercial frothers. *Int. J. Miner. Process.* **2013**, *119*, 1–5. [CrossRef]
15. Tan, Y.H.; Finch, J.A. Frother structure-property relationship: Effect of hydroxyl position in alcohols on bubble rise velocity. *Miner. Eng.* **2016**, *92*, 1–8. [CrossRef]
16. Tan, Y.H.; Finch, J.A. Frother structure-property relationship: Effect of alkyl chain length in alcohols and polyglycol ethers on bubble rise velocity. *Miner. Eng.* **2016**, *95*, 14–20. [CrossRef]
17. Kowalczuk, P.B.; Zawala, J.; Drzymala, J. Concentration at the minimum bubble velocity (CMV) for various types of flotation frothers. *Minerals* **2017**, *7*, 118. [CrossRef]
18. Leifer, I.; Patro, R.K.; Bowyer, P. A study on the temperature variation of rise velocity for large clean bubbles. *J. Atmos. Ocean. Technol.* **2000**, *17*, 1392–1402. [CrossRef]
19. Okawa, T.; Tanaka, T.; Kataoka, I.; Mori, M. Temperature effect on single bubble rise characteristics in stagnant distilled water. *Int. J. Heat Mass Transf.* **2003**, *46*, 903–913. [CrossRef]
20. Zhang, Y.; Sam, A.; Finch, J.A. Temperature effect on single bubble velocity profile in water and surfactant solution. *Colloids Surf. A Physicochem. Eng. Asp.* **2003**, *223*, 45–54. [CrossRef]
21. Issaoui, R.; Ben Mansour, L. Experimental study of temperature effects on bubble characteristics and gas holdup in electroflotation column. *Desalin. Water Treat.* **2019**, *162*, 186–192. [CrossRef]
22. Liu, N.; Yang, Y.; Wang, J.; Ju, B.; Brantson, E.T.; Tian, Y.; Dong, Y.; Mahlalela, M. Experimental Investigations of Single Bubble Rising in Static Newtonian Fluids as a Function of Temperature Using a Modified Drag Coefficient. *Nat. Resour. Res.* **2020**, *29*, 2209–2226. [CrossRef]
23. Pawliszak, P.; Ulaganathan, V.; Bradshaw-Hajek, B.; Manica, R.; Beattie, D.A.; Krasowska, M. Mobile or Immobile? Rise Velocity of Air Bubbles in High-Purity Water. *J. Phys. Chem. C.* **2019**, 15131–15138. [CrossRef]
24. Wongsaroj, W.; Hamdani, A.; Thong-un, N.; Takahashi, H.; Kikura, H. Ultrasonic Measurement of Velocity Profile on Bubbly Flow Using a Single Resonant Frequency. *Multidiscip. Digit. Publ. Inst. Proc.* **2018**, *2*, 549. [CrossRef]
25. Batsaikhan, M.; Hamdani, A.; Kikura, H. Velocity measurement on two-phase air bubble column flow using array ultrasonic velocity profiler. *Int. J. Comput. Methods Exp. Meas.* **2018**, *6*, 86–97. [CrossRef]
26. Li, J.; Zhang, H.; Li, D.; Chen, H. On the Performance of Wireless-Energy-Transfer-Enabled Massive MIMO Systems with Superimposed Pilot-Aided Channel Estimation. *IEEE Access* **2015**, *3*, 2014–2027. [CrossRef]
27. Nakamura, H. Trace: Tennessee Research and Creative Exchange Application of Ultrasound for Bubble Measurement in Water and Mercury. Master's Thesis, University of Tennessee, Knoxville, TN, USA, 2010.
28. Azevedo, M.B.; De Faccini, J.L.H.; Su, J. Ultrasonic Measurements of Bubble Shape and Liquid Film Thickness of a Taylor Bubble Rising in a Stagnant Water Column. In Proceedings of the 2013 International Nuclear Atlantic Conference—INAC, Recife, Brazil, 24–29 November 2013.
29. Engineering ToolBox, Velocity of Sound in Water. 2004. Available online: https://www.engineeringtoolbox.com/sound-speed-water-d_598.html (accessed on 26 August 2021).
30. Zawala, J.; Niecikowska, A. Bubble-on-demand generator with precise adsorption time control. *Rev. Sci. Instrum.* **2017**, *88*, 095106. [CrossRef]
31. Ulaganathan, V.; Gochev, G.; Gehin-Delval, C.; Leser, M.E.; Gunes, D.Z.; Miller, R. Effect of pH and electrolyte concentration on rising air bubbles in β-lactoglobulin solutions. *Colloids Surf. A Physicochem. Eng. Asp.* **2016**, *505*, 165–170. [CrossRef]
32. Optel Sp. z o.o. Available online: https://www.optel.eu/ (accessed on 25 August 2021).
33. Popinet, S. An accurate adaptive solver for surface-tension-driven interfacial flows. *J. Comput. Phys.* **2009**, *228*, 5838–5866. [CrossRef]
34. Fuster, D.; Agbaglah, G.; Josserand, C.; Popinet, S.; Zaleski, S. Numerical simulation of droplets, bubbles and waves: State of the art. *Fluid Dyn. Res.* **2009**, *41*, 065001. [CrossRef]
35. Popinet, S. Gerris: A tree-based adaptive solver for the incompressible Euler equations in complex geometries. *J. Comput. Phys.* **2003**, *190*, 572–600. [CrossRef]
36. Zawala, J. Energy balance in viscous liquid containing a bubble: Rise due to buoyancy. *Can. J. Chem. Eng.* **2016**, *94*, 586–595. [CrossRef]
37. Tate, T. On the magnitude of a drop of liquid formed under different circumstances. *Lond. Edinb. Dublin Philos. Mag. J. Sci.* **1864**, *27*, 176–180. [CrossRef]
38. Legendre, D.; Zenit, R.; Velez-Cordero, J.R. On the deformation of gas bubbles in liquids. *Phys. Fluids* **2012**, *24*, 043303. [CrossRef]
39. Manica, R.; Klaseboer, E.; Chan, D.Y.C. The impact and bounce of air bubbles at a flat fluid interface. *Soft Matter* **2016**, *12*, 3271–3282. [CrossRef]
40. Moore, D.W. The velocity of rise of distorted gas bubbles in a liquid of small viscosity. *J. Fluid Mech.* **1965**, *23*, 749–766. [CrossRef]
41. Loth, E. Drag of non-spherical solid particles of regular and irregular shape. *Powder Technol.* **2008**, *182*, 342–353. [CrossRef]

42. Rastello, M.; Marié, J.L.; Lance, M. Drag and lift forces on clean spherical and ellipsoidal bubbles in a solid-body rotating flow. *J. Fluid Mech.* **2011**, *682*, 434–459. [CrossRef]
43. Skelland, A.H.P.; Clift, R.; Grace, J.R.; Weber, M.E. *Bubble, Drops, and Particles*; Academic Press, Inc.: Cambridge, UK, 1978; pp. 1–380.
44. Zawala, J.; Swiech, K.; Malysa, K. A simple physicochemical method for detection of organic contaminations in water. *Colloids Surf. A. Physicochem. Eng. Asp.* **2007**, *302*, 293–300. [CrossRef]
45. Krzan, M.; Zawala, J.; Malysa, K. Development of steady state adsorption distribution over interface of a bubble rising in solutions of n-alkanols (C5, C8) and n-alkyltrimethylammonium bromides (C8, C12, C16). *Colloids Surf. A Physicochem. Eng. Asp.* **2007**, *298*, 42–51. [CrossRef]

PCCP

PAPER

View Article Online
View Journal | View Issue

Check for updates

Cite this: *Phys. Chem. Chem. Phys.*, 2022, **24**, 3854

Open Access Article. Published on 20 January 2022. Downloaded on 8/17/2023 8:25:15 PM.
This article is licensed under a Creative Commons Attribution 3.0 Unported Licence.

Experimental and theoretical study of adsorption of synthesized amino acid core derived surfactants at an air/water interface

M. Borkowski,[a] S. Orvalho,[b] P. Warszyński,[a] Oleg M. Demchuk,[cd] E. Jarek[a] and J. Zawala *[ae]

The adsorption characteristics of amino acid surfactants, synthesized as substances with different volumes and hydrophilic head properties, have been previously described experimentally, without robust theoretical explanation. A theoretical model enabling the characterization of the adsorption behavior and physicochemical properties of this type of biodegradable surfactants, based on molecular structure, would be beneficial for assessment of their usefulness in colloids and interface science in comparison with typical surface-active substances. In this paper, the adsorption behaviour of synthesized amino acid surfactants at the liquid/gas interface was analyzed experimentally (by surface tension measurements using two independent techniques) and theoretically by means of an elaborate model, considering the volume of the surfactant hydrophilic "head" and its ionization degree. It was shown that the adsorption behavior of the synthesized compounds can be successfully described by the proposed model, including the Helfand–Frisch–Lebowitz isotherm based on the equation of state of 2D hard disk-like particles, with molecular properties of surfactant particles obtained using molecular dynamics simulations (MDS). Model parameters allow for direct comparison of physicochemical properties of synthesized amino acid surfactants with other ionic and non-ionic surface-active substances. Furthermore, it was revealed that intermolecular hydrogen bonds allow the formation of surfactant dimers with high surface activity.

Received 20th November 2021,
Accepted 11th January 2022

DOI: 10.1039/d1cp05322a

rsc.li/pccp

Introduction

Due to the characteristic molecular structure responsible for their surface-active properties, surfactants are widespread in a vast number of important industrial and technological applications and everyday human life. They are widely used as detergents, foaming enhancers, emulsifiers, wettability modifiers, and coating agents in many different fields such as detergency, fibers, food, polymers, pharmaceuticals, the pulp-paper industry, as corrosion inhibitors as well as in mineral processing and oil recovery applications.[1–3] In most applications, synthetic surfactants are used, and their production, which exceeds millions of tons per year, is cheap and well optimized. On the other hand, usage of such large quantities of surface-active substances in industry and households is one of the greatest sources of environmental pollution (60 wt% of total surfactants produced enters the aquatic environment[3,4]). Due to environmental concerns, the potential replacement of synthetic surfactants by environment-friendly alternatives is extensively investigated.[3,5,6]

To replace conventional surfactants, new "green" compounds must retain functional properties while simultaneously reducing their environmental impact. One of the groups of compounds having the potential to become superior to conventional surfactants are amino acid surfactants (AASs). These are simple compounds with tunable features and great potential as sustainable, low toxicity and biodegradable substances. AASs properties depend on their synthesis path. Suitable, properly chosen synthesis pathways allow for AASs' extensive structural diversity affecting their physicochemical properties,[2] determining the sites of alkyl chain substitution (*N*-substituted, *C*-substituted, or both *N*- and *C*-substituted compounds) and the number of attached chains (linear chain, Gemini, and bolaamphiphile forms). The type of proteinogenic amino acids chosen for the synthesis determines the final product polarity, adsorption features, surface activity and acid–base behavior.[2,7–9]

The search for environment-friendly surfactants requires their thorough characterization, including the determination

---

[a] *Jerzy Haber Institute of Catalysis and Surface Chemistry Polish Academy of Sciences, ul. Niezapominajek 8, 30-239 Krakow, Poland. E-mail: jan.zawala@ikifp.edu.pl*
[b] *Institute of Chemical Process Fundamentals, Czech Academy of Sciences, Rozvojova 135/1, 165 02 Prague 6, Suchdol, Czech Republic*
[c] *Faculty of Science and Health, The John Paul II Catholic University of Lublin, 1h-Konstantynów St., 20-708 Lublin, Poland*
[d] *SBŁ-Pharmaceutical Research Institute, 8-Rydygiera St., 01-793 Warsaw, Poland*
[e] *Department of Chemical Engineering, Stanford University, 443 Via Ortega, Shriram Center, Stanford, CA 94305, USA*

Open Access Article. Published on 20 January 2022. Downloaded on 8/17/2023 8:25:15 PM. This article is licensed under a Creative Commons Attribution 3.0 Unported Licence.

of molecular structure and surface activity. This paper presents the analysis of the adsorption behavior of five AASs based on alanine, valine, leucine, proline, and phenylalanine, with an amide bond connecting the polar head-group (originating from natural amino acids) and a hydrophobic tail (originating from lauric acid, a natural fatty acid). The adsorption of the synthesized compounds at the liquid/gas interface is analyzed experimentally and a theoretical model is proposed for AASs adsorption behavior and surface activity. The model integrates the results of molecular dynamics of surfactant molecules at the interface with the conventional description of the adsorption in terms of the surface tension isotherm. The proposed model uses the HFL (Helfand–Frisch–Lebowitz) isotherm based on the equation of state of 2D hard disk-like particles, with the effective headgroup size obtained using molecular dynamics simulations (MDS). Applying DFT (density functional theory) computations, we also demonstrate that intermolecular hydrogen bonds between amide groups of surfactants can contribute to the formation of dimers that affects the surface activity of the investigated surfactants.

Materials and methods

Chemicals

All the amino acid surfactants (AASs) studied in this paper were synthesized by condensation of proper amino acid (L-alanine, L-valine, L-leucine, L-proline, and L-phenylalanine) with dodecanoyl (lauroyl) chloride (Fig. 1), obtained from the reaction of lauric acid with thionyl chloride. The synthesis details are described in Appendix A. The chemicals used in the synthesis of lauroyl chloride and of the final products were purchased from Avantor Performance Materials Poland S. A. and Merck KGaA. The solutions of synthesized surfactants used in the study were prepared with ultrapure water (Direct-Q3 UV Water Purification System by Millipore, conductivity <0.7 μS cm^{-1} and surface tension equals 72.4 mN m^{-1} at 22 °C).

The structural formulas of five surfactants with different hydrophilic heads (amino acid), namely: *N*-lauroyl-L-alanine (C12-ALA), *N*-lauroyl-L-valine (C12-VAL), *N*-lauroyl-L-leucine (C12-LEU), *N*-lauroyl-L-proline (C12-PRO), and *N*-lauroyl-L-phenylalanine (C12-PHE), are shown in Appendix B, together with the results of the purity analysis of the synthesized compounds. The purity of the AASs was verified by NMR spectra, and by the melting point (Mp.) determination. ^{1}H NMR (500 MHz) and ^{13}C NMR (125 MHz) spectra were recorded on a Bruker AVANCE 500 MHz spectrometer using $CDCl_3$ (deuterated chloroform) as a solvent. All the physical and spectral data of the synthesized AASs was consistent with those found in literature[10,11] and are listed in Appendix B.

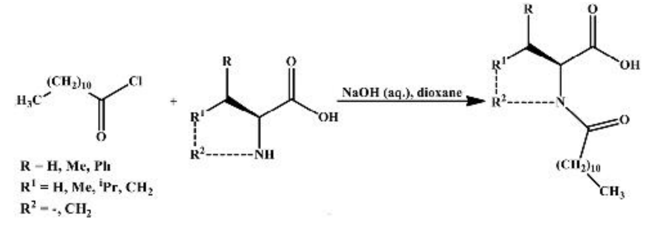

Fig. 1 Synthesis of the amino acid surfactants (AASs).

Methods

All measurements of interfacial and bulk physicochemical properties of the AASs were carried out at controlled temperature (21 ± 1 °C). Standard cleaning procedures were followed before each measurement, including careful cleaning of the sample vessel with a cleaning agent (Mucasol – a commercially available laboratory cleaning liquid) and thorough rinsing with ultrapure water. In a typical experimental run, the surfactant solution of a given concentration was tested according to the following sequence: (i) determination of equilibrium value of surface tension, (ii) determination of solution pH, and (iii) its conductivity.

Equilibrium surface tension measurements

Equilibrium values of surface tension were measured using two independent methods: (i) Wilhelmy plate method in a Krüss Tensiometer, Type K11 and (ii) bubble shape method in PAT-1 tensiometer (SINTERFACE Technologies, Berlin, Germany). In the Wilhelmy plate technique, a standard platinum plate (wetted perimeter 40.198 mm) and 60 mL solution were used for each measurement. The surface tension of the solution was measured for 1000 s, recorded at 2-second intervals. Equilibrium surface tension for a given solution concentration was calculated as the average from the values being constant in time. In the bubble shape method, the surface tension values were determined by analyzing the shape of a submerged bubble attached to a U-shaped needle. The Young–Laplace equation, relating the curvature of a liquid meniscus and its surface tension, was fitted to describe the bubble shape. The surface tension in this case was measured for 2 h, and the equilibrium surface tension values were calculated accordingly.

Solution pH and conductivity determination

The conductivity and pH of the tested solutions were measured using a WTW conductometer, Type LF 330i, with probe TetraCon 325, covering a conductivity range: 0.1 μS cm^{-1} –2 S cm^{-1}, and a WTW pH meter, Type 340i, with probe SenTix 41. Before each series of measurements, the measuring electrodes were thoroughly rinsed with ultrapure water (reference values: pH $\sim$5.8 and conductivity $\sim$0.7 μS cm^{-1}).

Determination of the acid dissociation constant

The values of the acid dissociation constant K_A were determined by the weak acid titration method, using NaOH solution as a strong base.[12] Detailed experimental and data evaluation procedures are described in Appendix C. The titration procedure was monitored independently by pH and conductivity measurements using an Elmetron CPS-505 pH/conductivity meter equipped with the electrode Elmetron EPS-1 for measuring pH and an Elmetron EC-60 for measuring conductivity.

Open Access Article. Published on 20 January 2022. Downloaded on 8/17/2023 8:25:15 PM.
This article is licensed under a Creative Commons Attribution 3.0 Unported Licence.

Theoretical description of the adsorption process – adsorption isotherm

The HFL (Helfand–Frisch–Lebowitz) isotherm based on the equation of state of 2D hard disk-like particles[13] was used to describe the synthesized AASs adsorption at the water/air interface. That exact equation for the 2D equation of state can also be derived based on the scaled particles theory[14] and extended to mixtures of hard disks with various diameters.[15] Accounting for the intermolecular interactions in the adsorbed layer in the Frumkin-like manner[16] and applying the Gibbs adsorption equation for the adsorption equilibrium,[17] the equation for the adsorption isotherm was obtained in the form:

$$\frac{c_n}{\alpha_n}(1-\theta_n)\exp\left[\frac{2\theta_n^2-3\theta_n}{(1-\theta_n)^2}\right]=\theta_n\exp(-2H_s\theta_n/RT) \quad (1)$$

where: c_n is the concentration of surfactant, α_n is the surface activity of the surfactant, a measure of the standard free energy of adsorption, $\theta_n = \Gamma_n/\Gamma_{n\infty}$ is the relative surfactant surface concentration, where Γ_n is surface concentration, while $\Gamma_{n\infty}$ is the limiting surfactant surface concentration of the closely packed monolayer and H_s is the surface interaction parameter, accounting mainly for the attractive lateral intermolecular interaction between adsorbed surfactant molecules (*e.g.* London dispersion, dipole–dipole, hydrogen bonding). In the scaled particles theory, the limiting surface concentration is directly dependent on the size of the hard disk:

$$\Gamma_{n\infty}=\frac{1}{N_A\pi A_{\text{eff}}^2} \quad (2)$$

where: N_A is the Avogadro constant and A_{eff} is the hard disk radius. By the numerical solution of eqn (1), the dependence between relative surface concentration of surfactant and its concentration in the bulk was found and the surface tension isotherm was described by the integration of the Gibbs equation for a diluted solution of non-ionic surfactant:

$$d\gamma=-RT\frac{\Gamma_n}{c_n}dc_n \quad (3)$$

The calculated isotherm can be fitted to the experimental data with three fitting parameters (A_{eff}, α_n, H_s) to obtain the parameters of the model for a given AASs with different amino acid head group. The quality of the fit was evaluated based on the χ^2 value defined as:

$$\chi^2=\sum_{i=1}^{n_e}\frac{(\gamma_e-\gamma_f)^2}{n_e} \quad (4)$$

where: γ_e and γ_f are the experimental and fitted values of surface tension, and n_e is the number of experimental points for a given isotherm.

To assign physical meaning to the isotherm parameters with respect to the molecular properties of the studied surfactants, molecular dynamics simulations (MDS) were used to determine the effective size of the surfactants' hydrophilic part, A_{eff}, that can be used in the eqn (1) and (2). The following procedure was applied:

- The optimized structures of all AASs were obtained by quantum mechanics computations, using density functional theory (DFT) with CAM–B3LYP functional and 6-31G + (d, p) basis set. Solvation effects (water) were accounted for applying the SMD (solvation model) variation of the Polarizable Continuum Model,[18] while the partial atomic charges were calculated according to the Merz–Singh–Kollman method.[19] All DFT calculations were carried out using the Gaussian 09 program.[20]
- The optimized structure, obtained in the previous step, was imported to the YASARA Structure Molecular Dynamics Software,[21] placed in the simulation box with the size of 6 × 6 × 3.5 nm and filled with water molecules (TIP3P, density 1 g dm^{-3}). The simulation was run for 20 ns using AMBER 14 force field[22] to equilibrate the system.
- Next, the simulation box was extended in the z coordinate to 12 nm to obtain a water slab with two interfaces. When the simulations were running, the transfer of a surfactant molecule to one of the interfaces was observed.

The simulations were continued for 35 ns, and at least ten snapshots were randomly taken. Representative snapshots for all the AASs are illustrated in Fig. 2. The conformation of the surfactant at the interface was analyzed at every snapshot and the hydrophilic headgroup of the surfactant that preferentially contacted with water sub-phase was determined (marked by the grayish contour in Fig. 2).

Fig. 3. shows the optimized structures of surfactants with marked hydrophilic parts of molecules. The effective radii of the hydrophilic part of surfactants were determined using the formula:

$$A_{\text{eff}}=\frac{3V}{S} \quad (5)$$

where V is the van der Waals volume of the hydrophilic head group shown in Fig. 3. and S is the respective van der Waals surface. Their values and the radii of gyrations of surfactant headgroups were calculated using algorithms implemented in the YASARA Structure software.[21] The A_{eff} were then used in eqn (1) for the fitting to the experimentally obtained adsorption isotherms. Therefore, the number of adjustable parameters in eqn (1) was

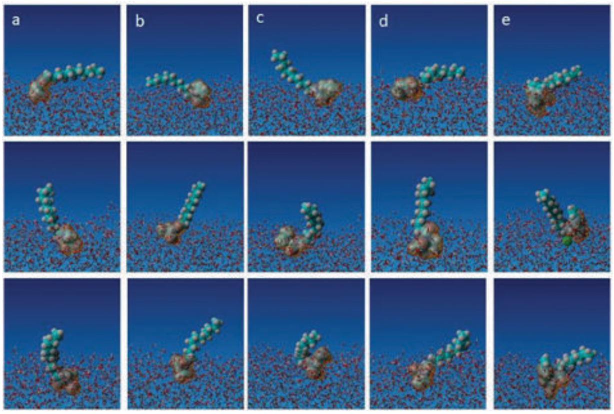

Fig. 2 Example of results obtained by molecular dynamic simulations: selected snapshots of amino acid surfactant molecule at air/water interface respectively for (a) C12-ALA (b) C12-VAL, (c) C12-LEU, (d) C12-PRO, (e) C12-PHE.

Open Access Article. Published on 20 January 2022. Downloaded on 8/17/2023 8:25:15 PM.
This article is licensed under a Creative Commons Attribution 3.0 Unported Licence.

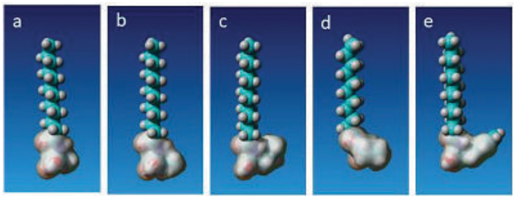

Fig. 3 Optimized geometries of amino acid surfactants for (a) C12-ALA (b) C12-VAL, (c) C12-LEU, (d) C12-PRO, (e) C12-PHE. The van der Waals surface of the hydrophilic headgroup is marked by the grayish contour.

reduced to two, α_n and H_s, as the third one, A_{eff}, could be determined independently.

Energy of dimerization

The minimized structures of AASs dimers were obtained by quantum mechanics computations, using density functional theory (DFT) with wB97XD functional, which includes corrections for the London dispersion and long-range interactions, using 6-31G + (d,p) basis set. Solvation effects (water), as above, were accounted for applying the SMD variation of the Polarizable Continuum Model. The calculations started by placing two molecules with minimized geometries with parallel oriented hydrophobic chains and random orientation of the headgroup. Then the optimizing procedure was run until convergence was achieved and the energy and free energy of the dimer were obtained. The optimizing procedure was repeated three times for different initial orientations of headgroups and the conformation with the lowest energy was selected. The energy, enthalpy, and free energy of dimerization were calculated according to: $\Delta E_{dimerization} = E_{dimer} + 2E_{surfactant}$. All calculations were carried out using the Gaussian 09 program.[20]

Results and discussion

To verify and validate our theoretical description of surfactant adsorption at the air/water interface, we selected literature data on surface tension isotherms of model non-ionic surfactants, namely *tert*-isopropyl phosphine oxide[23] and *n*-alkyl dimethyl phosphine oxides[24] with the hydrophobic chain length from 7 to 13 carbon atoms. The surface tension isotherms for those model surfactants are illustrated in Fig. 4, together with fits of the theoretical model based on their molecular size. The best-fit parameters are resumed in Table 1. *Tert*-isopropyl phosphine oxide is a disk-like molecule; therefore, it seems to be a perfect model surfactant to verify the HFL model for the hard disk based on its molecular size. Due to its branched structure, its surface activity is low, with no lateral interactions between adsorbed molecules ($H_s = 0$).[23] After determining the effective size from the molecular data ($A_{eff} = 0.248$ nm), we could perfectly describe the experimental surface tension isotherms with only one adjustable parameter. For the homologous series of *n*-alkyl dimethyl phosphine oxides, we successfully fit the model with a single size of the headgroup (marked in Fig. 4B) and two adjustable parameters, α_n and H_s. The logarithm of the first one exhibits a linear dependence on the number of carbon atoms in the hydrophobic chain, in agreement with the Traube rule. The second one, H_s, shows the odd–even effect in the hydrocarbon chain length as described in.[24]

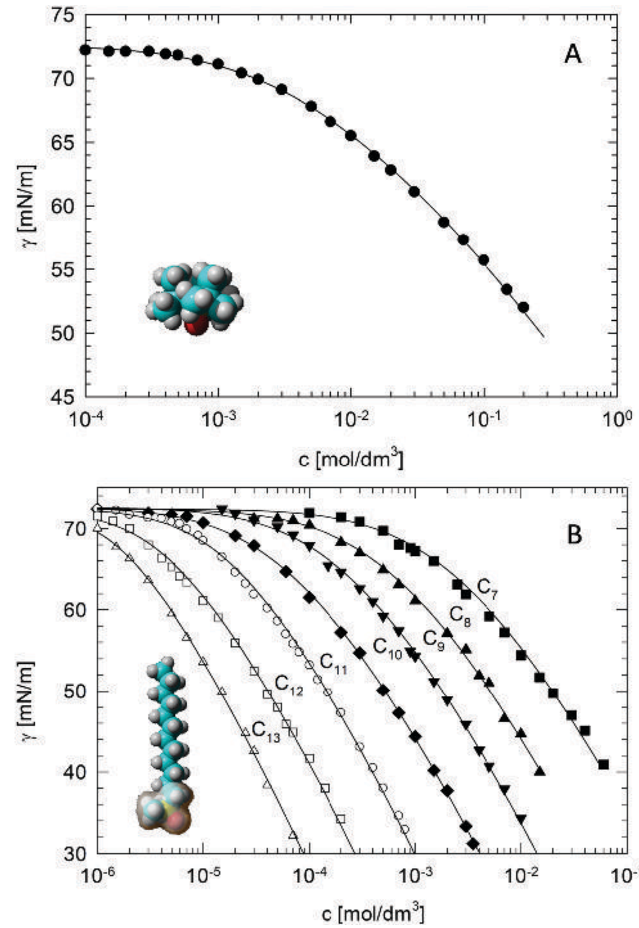

Fig. 4 Surface tension isotherms and molecular structures of: A – *tert*-isopropyl phosphine oxide and B – *n*-alkyl dimethyl phosphine oxides. Lines represent fits of the theoretical model.

Table 1 The effective diameter and the best-fit parameters of the theoretical model, based on the molecular dimensions, to the experimental isotherms of model surfactants. Adjustable parameters in bold

Surfactant	A_{eff} [nm]	α_n [mol dm^{-3}]	H_s [kJ mol^{-1}]	χ^2 [(mN m^{-1})^2]
Tert-isopropyl phosphine oxide	0.334	5.5×10^{-3}	0.0	0.02
N-alkyl dimethyl phosphine oxide				
C_7	0.248	2.90×10^{-3}	0.0	0.50
C_8		8.00×10^{-4}	0.3	0.26
C_9		3.00×10^{-4}	0.9	0.21
C_{10}		9.00×10^{-5}	1.2	0.07
C_{11}		4.50×10^{-5}	4.5	0.23
C_{12}		1.35×10^{-5}	4.9	0.24
C_{13}		7.70×10^{-6}	7.4	0.26

After the initial validation, the model was used to describe the adsorption performance of the synthesized AASs. In contrast to amino acids, AASs do not assume a zwitterionic form at moderate pH. They behave as weak acids with pK_a determined

Open Access Article. Published on 20 January 2022. Downloaded on 8/17/2023 8:25:15 PM. This article is licensed under a Creative Commons Attribution 3.0 Unported Licence.

Table 2 Experimentally determined pK_a values of the studied amino acid surfactants

No.	surfactant	pK_a
1	C12-ALA	4.63
2	C12-VAL	5.13
3	C12-LEU	5.41
4	C12-PHE	5.40
5	C12-PRO	4.61

by the protonation of a carboxylic group. The experimentally determined pK_a values of all studied AASs surfactants are presented in Table 2. Based on these pK_a values and on the measured pH of the surfactants' solutions, the dependence of the degree of dissociation (α) on their concentration was determined using the mass action law:

$$\alpha(c) = \frac{K_A}{K_A + 10^{-\mathrm{pH}(c)}} \tag{6}$$

where K_A is the dissociation constant of the carboxylic group of the surfactants and c is the total concentration of surfactant in the solution. The results are illustrated in Fig. 5, where the dependence of the fraction of non-dissociated surfactant $(1 - \alpha(c))$ on total surfactant concentration is given (solid line) together with the experimentally determined dependence of pH.

As illustrated in Fig. 5, the fraction of the non-dissociated form of surfactant is always above 0.1. In our previous studies,[25,26] we demonstrated that non-ionic surfactants with the same hydrocarbon chain are much more surface active than the respective ionic ones, and the difference in concentration of the onset of surface activity was near two orders of magnitude. This feature in particular was revealed when analyzing the pH dependence of the surface activity of alkanoic acids.[27] Therefore, in the analysis of surface tension isotherms of the studied AASs, we neglected the effect of ionic (dissociated) surfactant form and considered non-ionic form only, with the concentration given by:

$$c_n = c[1 - \alpha(c)] \tag{7}$$

where c is the total surfactant concentration. The equation of the adsorption isotherm (eqn (1)) used to describe the AASs system could be rewritten as:

$$\frac{c[1-\alpha(c)]}{a_n}(1-\theta_n)\exp\left[\frac{(2\theta_n^2 - 3\theta_n)}{(1-\theta_n)^2}\right] = \theta_n \exp\left(-\frac{2H_s\theta_n}{RT}\right) \tag{8}$$

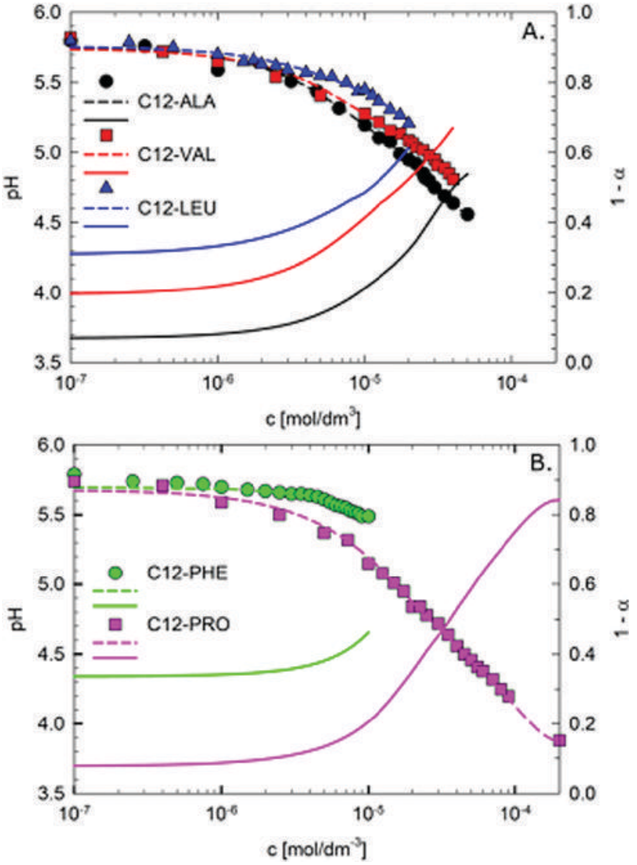

Fig. 5 Experimentally determined dependence of the pH of the solution on the concentration of amino acid surfactants (symbols, dashed line) for: (A) C12-ALA, C12-VAL, C12-LEU; (B) C12-PRO, C12-PHE. The respective dependence of the fraction of non-dissociated surfactant calculated using eqn (6). is shown as solid lines.

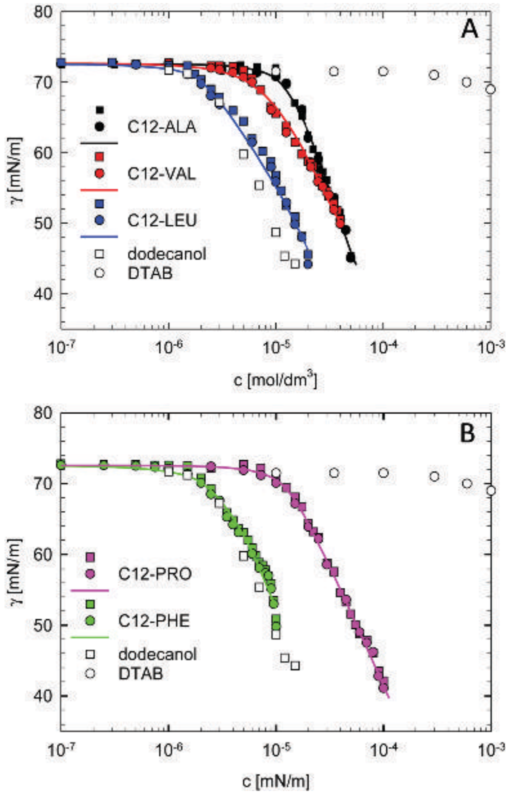

Fig. 6 Experimental surface tension isotherms of the amino acid surfactants (determined by Wilhelmy plate method – squares, bubble shape analysis – circles) for (A) C12-ALA, C12-VAL, N-C12-LEU; (B) C12-PRO, C12-PHE. Solid lines – best fits of the theoretical model to experimental points obtained using bubble shape analysis method. The experimental isotherms for dodecanol and DTAB are given for comparison.

Open Access Article. Published on 20 January 2022. Downloaded on 8/17/2023 8:25:15 PM. This article is licensed under a Creative Commons Attribution 3.0 Unported Licence.

Table 3 Calculated and best-fit parameters of the theoretical model fitted to the experimental adsorption isotherms (fitted parameters in bold)

Parameter	C12-ALA	C12-VAL	C12-LEU	C12-PHE	C12-PRO
A_{eff} [nm]	0.257	0.276	0.284	0.280	0.272
Rg_{hg}[nm]	0.204	0.233	0.256	0.241	0.231
$\Gamma_{n\infty}\cdot 10^{-10}$ [mol cm^{-2}]	8.002	6.938	6.553	6.741	7.144
$\alpha_n \cdot 10^{-5}$ [mol dm^{-3}]	4.2 ± 0.2	2.0 ± 0.2	0.86 ± 0.05	0.77 ± 0.05	2.0 ± 0.2
H_s [kJ mol^{-1}]	14.3 ± 0.4	11.3 ± 0.3	13.2 ± 0.4	13.4 ± 0.4	10.0 ± 0.4
χ^2 [(mN m^{-1})^2]	0.38	0.15	1.23	1.37	0.61

The experimental surface tension isotherms for the investigated AASs are illustrated in Fig. 6, together with the best fits of the theoretical model. Results obtained using two experimental methods, Wilhelmy plate (squares) and bubble shape analysis (circles), are presented. Almost perfect agreement between the two sets of data (indicating lack of diffusion limitation effects that may occur in surface tension measurements at low surfactant concentrations[28]) was revealed.

The effective radii of the hydrophilic headgroups of the surfactants, A_{eff}, and the limiting surface concentration, $\Gamma_{n\infty}$, were calculated based on the MDS procedure and - eqn (2) and (5), respectively, using van der Waals volumes of the hydrophilic headgroups (*cf.* Fig. 3). All the calculated and fitted isotherm parameters are presented in Table 3. The effective radii of the headgroups were *ca.* 0.4 Å bigger than their respective radii of gyration (Rg_{hg}). The fits to experimental surface tension isotherm were obtained with two adjustable parameters only, α_n and H_S.

The obtained results revealed that, as could be expected, the surfactants' surface activity increases (α_n parameter decreases) with the hydrophobicity of the amino acid side group: *N*-Lauroyl (L)-phenylalanine having benzene ring is more surface active than *N*-Lauroyl (L)-proline with more hydrophilic pyrrolidine loop. Moreover, the surface activity of AASs follows the gradation of hydrophobicity of amino acids PRO < ALA < VAL < LEU < PHE[29] and it is much higher than the one of a typical cationic surfactant with twelve carbon atoms in the alkyl chain -- dodecyltrimethylammonium bromide (DTAB), which has the onset of surface activity at the concentration 10^{-3} mol dm^{-3} (the studied AASs have surface activity onset at concentrations below 10^{-4} mol dm^{-3}) and the critical micelle concentration (CMC) above 10^{-2} mol dm^{-3}. The surface activities of C12-PHE and C12-LEU were similar to dodecanol (*cf.* Fig. 6), while those of C12-VAL, C12-ALA and C12-PRO were in-between the one of dodecanol and dodecyl-trimethyl ammonium bromide (DTAB). That is due to increasing both hydrophobicity of the amino acid headgroup and the fraction of the neutral form of the molecule with a protonated carboxylic group.

The calculated dependencies of surface concentration *versus* surfactant concentration in volume for the studied AASs are illustrated in Fig. 7. The investigated surfactants do not have a CMC at room temperature and their surface activity is limited by solubility. At the surfactant concentration corresponding to the respective solubility limit, the surface concentrations range from 4.6×10^{-10} mol cm^{-2} for C12-ALA to 3.7×10^{-10} mol cm^{-2} for C12-PHE and are much smaller than the ones determined by the effective molecular dimensions of surfactant headgroups (*cf.* Table 3).

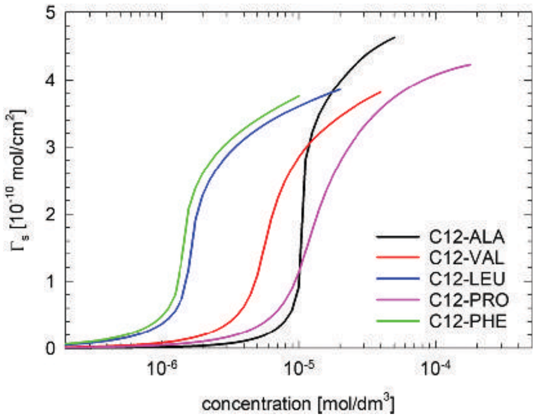

Fig. 7 The calculated dependence of surface concentration *vs.* bulk concentration resulting from the fitting of the model to the experimental surface tension isotherms.

The proposed theoretical model describes the experimental results very well with the χ^2 less than 1, except for C12-LEU and C12-PHE. The AASs are capable of making hydrogen bonds (HB).

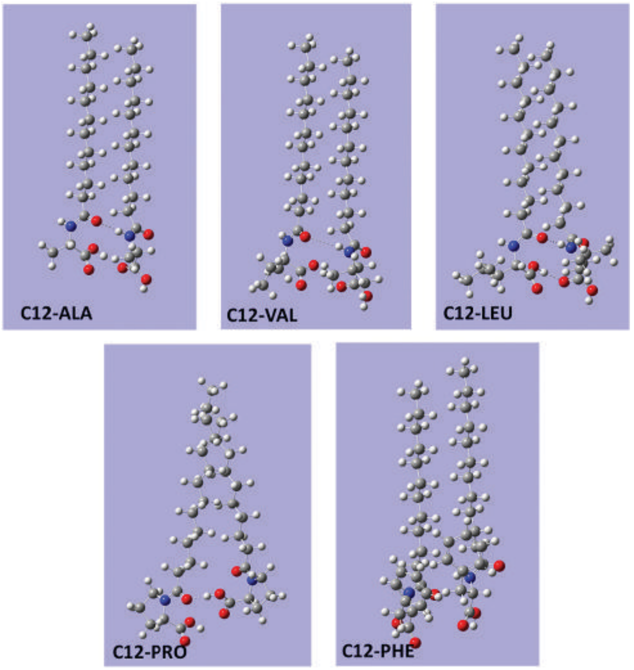

Fig. 8 The optimized structures of AAS dimers resulting from the DFT calculations.

Open Access Article. Published on 20 January 2022. Downloaded on 8/17/2023 8:25:15 PM.
This article is licensed under a Creative Commons Attribution 3.0 Unported Licence.

Table 4 The energy, enthalpy and free energy of dimerization resulting from DFT computations

Surfactant	Energy of dimerization [kcal mol^{-1}]	Enthalpy of dimerization [kcal mol^{-1}]	Free energy of dimerization [kcal mol^{-1}]
C12-ALA	23.07	23.66	3.71
C12-VAL	21.07	21.67	0.79
C12-LEU	24.72	25.31	5.53
C12-PHE	27.11	27.70	5.43
C12-PRO	18.30	18.89	1.29

The C12-ALA, C12-VAL, C12-LEU, C12-PHE have 3 HB acceptors (oxygen in carboxylic and amide group) and 2 donors (hydrogens of carboxylic and amide group), while C12-PRO has 3 HB acceptors (oxygen in carboxylic and amide groups) but only 2 donors in carboxylic group. Due to competition with water molecules, the carboxylic groups preferably participate in hydrogen bonds with hydration water. On the other hand, the amide group is adjacent to the hydrophobic tail and more exposed to the gas phase (*cf.* Fig. 2). Thus, at high surface coverage, it can form intermolecular hydrogen bonds. We attempted to evaluate the energy of dimerization for all AASs by performing the optimization geometry of the dimers. The resulting structures of the dimers are illustrated in Fig. 8, and the values of the energy, enthalpy and free energy of dimerization are given in Table 4. The determined free energy of dimerization was the highest for C12-LEU and C12-PHE and the lowest for C12-VAL and C12-PRO that agrees with the shape of surface tension isotherms. Strong intermolecular interactions can be evidenced by a high values of interaction parameter, H_s (*cf.* Table 3) for C12-ALA, C12-LEU and C12-PHE. Those values are much higher than for phosphinoxides despite similar size of the bulky headgroups (*cf.* Table 1). The latter are mainly determined by the dispersion interaction between hydrocarbon chains at the interface. For C12-PRO, the hydrogen bond can form between amide oxygen and the hydrogen of the carboxylic group that is entropically unfavorable.

As can be observed in Fig. 6, for C12-LEU and C12-PHE the end part of the isotherms, close to the solubility limit, is characterized by a steep slope. That can be a manifestation of the formation of highly surface-active dimers stabilized by hydrogen bond and for phenylalanine-based surfactant, additionally by a π–π stacking.[30]

Conclusions

Table 5 Comparison of the efficiency of adsorption of the new AASs with ionic surfactants with lipophilic lauroyl tail

	New AASs	DTAB[26]	SDS[26]
pC_{20}	4.55–5.1	2.00	2.50

Amino acid surfactants are biodegradable compounds with promising adsorption properties competitive to typical surface-active substances.[2,5,32] Although their ability to reduce solution surface tension is presented in many papers,[5,9,32–34] there is an acute lack of reported attempts for the robust theoretical description of the adsorption process by means of a model, allowing extraction of useful physicochemical parameters of the studied compounds. Our studies aim to fill this gap. Five amino acid based surfactants (AASs), derived from L-alanine, L-valine, L-leucine, L-proline, and L-phenylalanine, were successfully synthesized. The synthesized AASs present an amide bond connecting the polar head-group to a lipophilic lauroyl tail. The solutions of AASs at natural pH (*i.e.*, without any pH adjustments) contain both deprotonated, anionic and protonated non-ionic forms. Since, according to previous studies,[27] the non-ionic forms are much more surface active, their presence dominates the interfacial behavior. Therefore, the AASs adsorption isotherms could be successfully characterized by a theoretical model, based on the Helfand–Frisch–Lebowitz isotherm derived from the equation of state of 2D hard disk-like particles. The effective sizes of the hydrophilic headgroups of the AASs were obtained by molecular dynamics simulation and the adsorption isotherms were fitted by adjusting only two parameters, the surface activity of the surfactant and the surface interaction parameter. The new AASs show higher efficiency of adsorption (lower pC20[35]) than typical ionic surfactants (Table 5) but lower than rhamnolipids.[36] Their surface activity is comparable with non-ionic Triton or Tween,[37,38] and relative surface activity correlates with increasing hydrophobicity of the amino acid (Table 6). The use of the new AASs in typical surfactant applications is promising and the testing of other desired properties will follow: foamability tests, determination of the kinetics of dynamic adsorption layer formation at the interface of rising bubbles, stability of single liquid film, as well as studies of the crystalline structure of the obtained AASs to understand the AASs dimerization.

List of symbols and abbreviations.

c_n	The concentration of surfactant's form adsorbed at liquid/gas interface
c	The total concentration of surfactant
α_n	Surface activity of the surfactant being the measure of the standard free energy of adsorption
Γ_n	Surface concentration
$\Gamma_{n\infty}$	Limiting surfactant surface concentration of the closely packed monolayer
θ_n	Relative surfactant surface concentration
H_s	Surface interaction parameter approximating the attractive lateral interaction among the adsorbed surfactant hydrophobic tails
A_{eff}	Effective radii of the hydrophilic head of surfactants
V	van der Waals volume of hydrophilic head group of surfactants

Table 6 Relative hydrophobicity of the investigated amino acids and the efficiency of adsorption and surface activity of their respective AASs

Amino acid	Phe[a]	Leu	Val	Ala	Pro[b]
Hydrophobicity[31]	2.00	1.68	1.11	0.15	−0.25
pC_{20}	5.10	4.95	4.65	4.60	4.55
$\alpha_s \times 10^{-5}$ [mol dm^{-3}]	0.77	0.86	2.0	3.9	1.5

[a] most hydrophobic. [b] least hydrophobic.

Open Access Article. Published on 20 January 2022. Downloaded on 8/17/2023 8:25:15 PM.
This article is licensed under a Creative Commons Attribution 3.0 Unported Licence.

S	van der Waals surface of hydrophilic head group of surfactants
γ	Surface tension of solution
α	Dissociation degree
K_A	Dissociation constant of carboxylic group of the surfactant
χ	Measure of the difference between the model prediction and the experimental data
N_A	Avogadro constant
pC_{20}	Negative log of the bulk phase concentration necessary to reduce the surface tension by 20 mN m^{-1}
Rg_{hg}	Radius of gyration
R	Gas constant
T	Temperature
AASs	Amino acid surfactants
DFT	Density functional theory
MDS	Molecular dynamics simulations
SDM	Solvation model density
DMF	Dimethylformamide
TMS	Tetramethylsilane
C12-ALA	*N*-lauroyl-L-alanine
C12-VAL	*N*-lauroyl-L-valine
C12-LEU	*N*-lauroyl-L-leucine
C12-PRO	*N*-lauroyl-L-proline
C12-PHE	*N*-lauroyl-L-phenylalanine

Conflicts of interest

There are no conflicts to declare.

Appendix A (Synthesis of Lauroyl chloride and Amino acid surfactants)

Lauroyl chloride

300 mL of toluene, 0.5 mL of DMF (dimethylformamide) and 43 g of lauric acid (0.22 mol) were placed into the 500 mL round bottom flask equipped with a magnetic stirrer and a reflux condenser with a pipe for gas trapping of HCl (hydrochloric acid) and SO_2 (sulphur dioxide) produced in the reaction. 31 mL of $SOCl_2$ (0.44 mol) was added to the mixture, which was gently stirred. The mixture stirring was continued for 10 h, in mild reflux conditions, heated in the oil bath. The liberated gases were absorbed with sodium hydroxide solution. After completing the reaction, the reflux condenser was replaced with an adapter for simple distillation, and the majority of the solvent (about 250 mL) was distilled at ambient pressure. The remaining solvent was distilled under the vacuum at a temperature below 100 °C. The obtained lauroyl chloride was used in the AASs syntheses without additional purification.

N-Lauroyl-L-alanine (typical procedure)

A 250 mL round bottom flask equipped with a magnetic stirrer, dropping funnel, placed in an ice bath, was charged with L-alanine (4 g, 0.045 mol) and 30 mL of dioxane. A solution of NaOH (sodium hydroxide, 3.9 g, 0.098 mol) in 30 mL of water was slowly added to the stirred slurry, while the temperature was maintained at +5 °C. The solution of lauroyl chloride (10 g, 0.046 mol) in 30 mL of dioxane was slowly added to the stirred solution of freshly obtained sodium alaninate, maintaining the reaction temperature below +5 °C. The stirring at that temperature was prolonged for one more hour, and for the next 16 hours at ambient temperature, then 20 mL 12% HCl was added. The organic phase was diluted and separated with 50 mL of ^{t}BuOMe (methyl *tert*-butyl ether), washed with 30 mL of 2M HCl, and 30 mL of water, then dried with anhydrous $MgSO_4$ (magnesium sulfate). The drying agent was removed by filtration, solvents evaporated off under reduced pressure of rotary evaporator, and the product was purified by crystallisation from the mixture heptane/^{t}BuOMe to yield 8.5 g (71%) of product.

N-Lauroyl-L-leucine was prepared according to the typical procedure. The product was purified by crystallisation from the mixture hexane/toluene/DCM to yield 64% of the product.

N-Lauroyl-L-proline was prepared according to the typical procedure. The product was purified by crystallisation from the mixture hexane/toluene to yield 86% of the product.

N-Lauroyl-L-valine was prepared according to the typical procedure. The product was purified by crystallisation from the mixture hexane/toluene to yield 79% of the product.

N-Lauroyl-L-phenylalanine was prepared according to the typical procedure. The product was purified by crystallisation from the mixture hexane/toluene/DCM to yield 82% of the product.

Appendix B (Purity analysis and chemical structure of the synthesized amino acid surfactants)

Melting points (Mp.) were determined in open capillaries and are given as uncorrected values. The chemical shifts are reported in ppm, and calibrated to residual solvent peaks at 7.27 ppm and 77.00 ppm for ^1H and ^{13}C, respectively, or 0.00 ppm for TMS (tetramethylsilane) used as internal reference compounds (Fig. 9–13).

N-Lauroyl-L-alanine (C12-ALA)

Mp. = 85.0–86.0 °C.

^1H NMR (500 MHz, $CDCl_3$): δ = 10.03 (bs, 1H), 6.28 (bd, J = 6.9 Hz, 1H), 4.59 (q, J = 7.1 Hz, 1H), 2.25 (t, J = 7.6 Hz, 2H), 1.63 (bq, J = 6.6 Hz, 2H), 1.46 (d, J = 6.9 Hz, 3H), 1.35–1.22 (m, 17H), 0.88 (t, J = 6.6 Hz, 3H). ^{13}C NMR (DEPT, 125 MHz, $CDCl_3$): δ = 48.26, 36.45, 31.91, 29.60, 29.47, 29.33, 29.30, 29.18, 25.58, 22.69, 18.11, 14.11.

N-Lauroyl-L-valine (C12-VAL)

Mp. = 97.0–99.2 °C.

^1H NMR (500 MHz, $CDCl_3$): δ = 9.23 (bs, 1H), 6.12 (d, J = 8.5 Hz, 1H), 4.60 (dd, J = 8.5 Hz, 1H), 2.29–2.22 (m, 3H), 1.64 (q, J = 7.1 Hz, 2H), 1.35–1.25 (m, 16H), 0.99 (d, J = 6.9 Hz, 3H), 0.96 (d, J = 6.6 Hz, 3H), 0.88 (t, J = 6.9 Hz, 3H). 13C NMR (125 MHz,

Open Access Article. Published on 20 January 2022. Downloaded on 8/17/2023 8:25:15 PM. This article is licensed under a Creative Commons Attribution 3.0 Unported Licence.

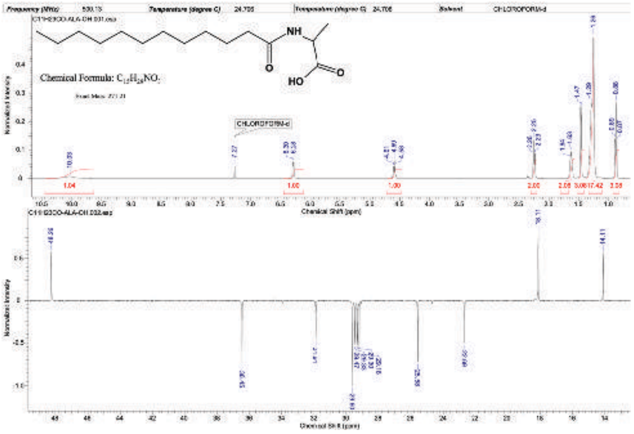

Fig. 9 The NMR spectrum of *N*-Lauroyl-L-alanine (C12-ALA).

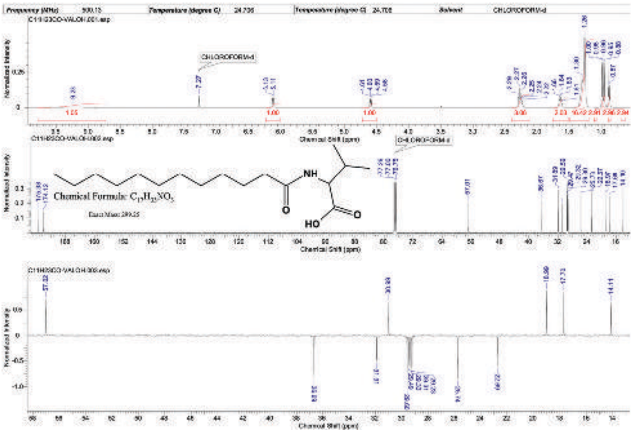

Fig. 10 The NMR spectrum of *N*-Lauroyl-L-valine (C12-VAL).

CDCl3): δ = 175.38, 174.12, 57.01, 36.67, 31.89, 30.98, 29.59, 29.47, 29.32, 29.30, 29.21, 25.73, 22.67, 18.97, 17.69, 14.10.

N-Lauroyl-L-leucine (C12-LEU)

Mp. = 105.3–105.5 °C.

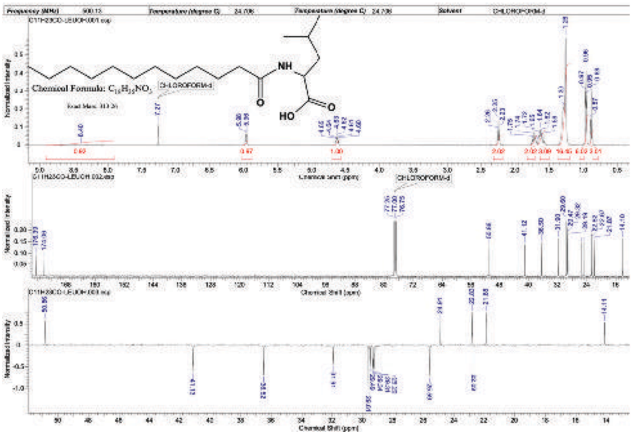

Fig. 11 The NMR spectrum of *N*-Lauroyl-L-leucine (C12-LEU).

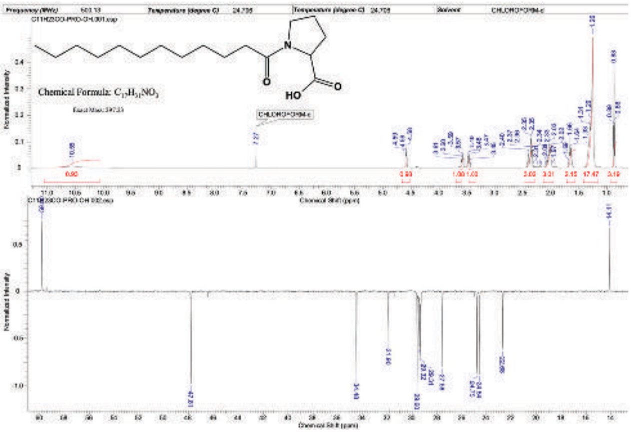

Fig. 12 The NMR spectrum of *N*-Lauroyl-L-proline (C12-PRO).

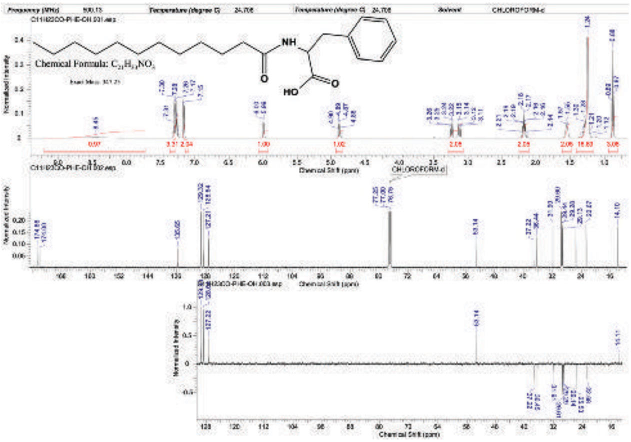

Fig. 13 The NMR spectrum of *N*-Lauroyl-L-phenylalanine (C12-PHE).

^{1}H NMR (500 MHz, CDCl$_3$): δ = 8.40 (bs, 1H), 5.97 (bd, *J* = 8.2 Hz, 1H), 4.62 (td, *J* = 8.5 Hz, 1H), 2.26 (t, *J* = 7.6 Hz, 2H), 1.76–1.68 (m, 2H), 1.76–1.68 (m, 2H), 1.67–1.57 (m, 3H), 1.35–1.25 (m, 16H), 0.96 (t, *J* = 5.0, 6H), 0.89 (t, *J* = 6.9, 3H). ^{13}C NMR (125 MHz, CDCl$_3$): δ = 176.39, 174.06, 50.86, 41.12, 36.50, 31.90, 29.60, 29.47, 29.30, 29.19, 25.58, 24.90, 22.82, 22.67, 21.87, 14.10.

N-Lauroyl-L-proline (C12-PRO)

Mp. = 55.1–56.3 °C.

^{1}H NMR (500 MHz, CDCl$_3$): δ = 10.55 (bs, 1H), 4.59 = 4.58 (m, 1H), 3.61–3.57 (m, 1H), 3.50 = 3.45 (m, 1H), 2.41 = 2.33 (m, 3H), 2.10–1.97 (m, 3H), 1.66 (q, *J* = 7.3, 2H), 1.40–1.20 (m, 16H), 0.88 (t, *J* = 6.9, 3H). ^{13}C NMR (125 MHz, CDCl$_3$): δ = 59.80, 47.81, 34.48, 31.90, 29.60, 29.47, 29.38, 29.32, 29.31, 27.58, 24.75, 24.54, 22.68, 14.11.

N-Lauroyl-L-phenylalanine (C12-PHE)

Mp. = 97.4–98.6 °C.

^{1}H NMR (500 MHz, CDCl$_3$): δ = 8.45 (bs, 1H), 7.31–7.24 (m, 3H), 7.17–7.15 (m, 2H), 5.99 (dd, *J* = 13.4, 5.5 Hz, 1H), 3.24

Open Access Article. Published on 20 January 2022. Downloaded on 8/17/2023 8:25:15 PM.
This article is licensed under a Creative Commons Attribution 3.0 Unported Licence.

(dd, J = 14.0, 5.5 Hz, 1H), 3.24 (dd, J = 14.0, 5.5 Hz, 1H), 2.18 (m, 2H), 1.60–1.50 (m, 2H), 1.35–1.20 (m, 16), 0.88 (t, J = 6.7 Hz, 3H). ^{13}C NMR (125 MHz, $CDCl_3$): δ = 174.66, 174.00, 135.65, 129.32, 128.64, 127.21, 53.14, 37.22, 36.44, 31.90, 29.32, 29.28, 29.13, 25.52, 22.67, 14.10.

Appendix C (Determination of the acid dissociation constant, K_A)

The values of the acid dissociation constant K_A were determined by the weak acid titration method, using NaOH solution as a strong base.[12] The titration procedure was monitored independently by pH and conductivity determination (see Fig. 14).

The titration process consisted of the gradual addition of NaOH solution from a burette to an Erlenmeyer containing 50 mL of the AAS solution, which was stirred continuously. The initial concentrations of the AASs and base solutions were identical. The experiment was aimed for the determination of the so-called equivalence point (see Fig. 14), at which the concentrations of the dissociated ([A−]) and non-dissociated ([HA]) form of the AAS are identical. To increase the accuracy of the pK_a determination, the equivalence point was approximated using 1st and 2nd derivative of the pH values (Fig. 14A). For conductivity results, the inflection point could be accurately determined from the raw data. The pK_a was determined as half of the equivalence point value, at which, according to the equation the [A−] = [HA], thus pK_a = pH.

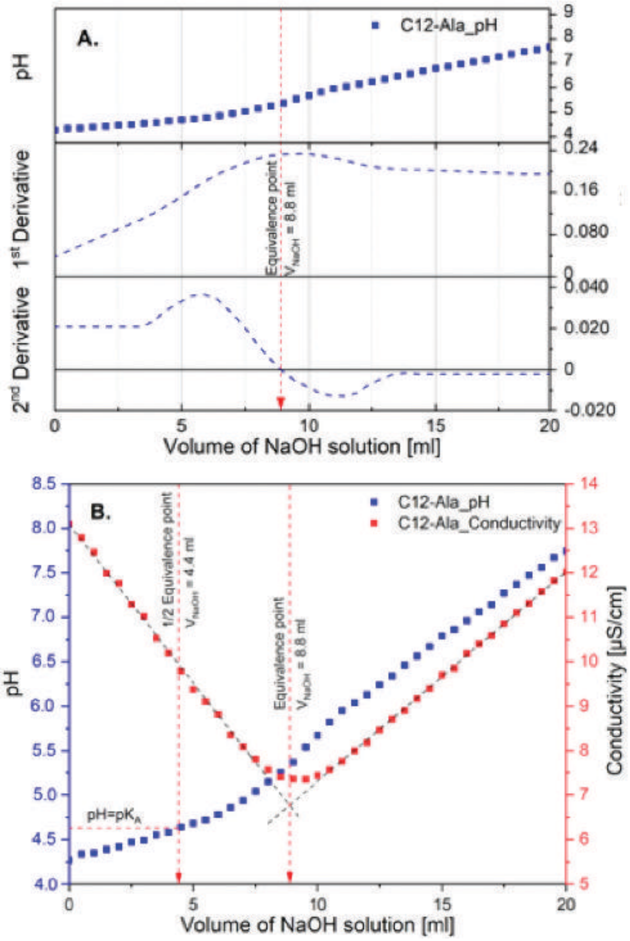

Fig. 14 Graphical determination of pK_a from pH and conductivity data: (A) determination of the equivalence (inflection) point using pH derivatives and (B) determination of the as a half of the inflection point approximated by the pH and conductivity measurements (data for C12-ALA).

Acknowledgements

Partial financial support from the Polish National Science Centre grant number 2019/33/B/NZ7/01608 & 2020/38/E/ST8/00173 is acknowledged with gratitude. The European Union Erasmus+ programme (project number: 2018-1-PL01-KA103-047692) is acknowledged for providing scholarship (financial support) for the research/mobility/traineeship. PW and JZ acknowledges partial financial support of the project by the statutory research fund of ICSC PAS. We also wish to thank John Belanger for proofreading this manuscript.

References

1 J. J. Morelli and G. Szajer, *J. Surfact. Deterg.*, 2000, **3**(4), 539–552.
2 D. B. Tripathy, A. Mishra, J. Clark and T. Farmer, *C. R. Chim.*, 2018, **21**, 112–130.
3 P. Johnson, V. J. Pinfield, V. Starov and A. Trybala, *Adv. Colloid Interface Sci.*, 2021, **288**, 102340.
4 A. Pradhan and A. Bhattacharyya, *J. Clean. Prod.*, 2017, **150**, 127–134.
5 R. Borders and K. Holmberg, *Adv. Colloid Interface Sci.*, 2015, **222**, 79–91.
6 C. N. Mulligan, S. K. Sharma and A. Mudhoo, *Biosurfactants: research trends and applications*. CRC Press, 2019, pp. 352.
7 L. Pérez, M. R. Infante, R. Pons, C. Moran, P. Vinardell, M. Mitjans and A. Pinazo, *Colloids Surf. B*, 2004, **35**(3), 235–242.
8 L. Pérez, A. Pinazo, M. T. García, M. del Carmen Moran and M. R. Infante, *New J. Chem.*, 2004, **28**(11), 1326–1334.
9 N. Wang, K. Yao, Y. Wang, J. Ti, J. Tan, C. Liu, G. Zhang, C. Wang and B. Xu, *J. Surfactants Deterg.*, 2020, **23**, 239–250.
10 A. Pal, Y. K. Ghosh and S. Bhattacharya, *Thetrahedron*, 2007, **63**, 7334–7348.
11 A. Makholf, F. Hubalek and F. A. Foger, WO2014060447A1, 2014.
12 M. Leonard, *Vogel's, Textbook of quantitative chemical analysis. Endeavour*, 5th edn, 1990, 14, 100.
13 E. Helfand, H. L. Frisch and J. L. Lebowitz, *J. Chem. Phys.*, 1961, **34**, 1037.
14 T. Boublik, *Mol. Phys.*, 1975, **29**, 421–428.
15 J. J. Talbot, X. Jin and N.-H. Wang, *Langmuir*, 1994, **10**, 1663–1666.
16 A. Frumkin, *Z. Phys. Chem.*, 1925, **116**, 466.

Open Access Article. Published on 20 January 2022. Downloaded on 8/17/2023 8:25:15 PM.
This article is licensed under a Creative Commons Attribution 3.0 Unported Licence.

17 I. B. Ivanov, K. P. Ananthapadmanabhan and A. Lips, *Adv. Colloid Interface Sci.*, 2006, **123-126**, 189–212.

18 A. V. Marenich, C. J. Cramer and D. G. Truhlar, *J. Phys. Chem. B*, 2009, **113**, 6378–6396.

19 B. H. Besler, K. M. Merz and P. A. Kollman, *J. Comput. Chem.*, 1990, **11**(4), 431–439.

20 M. J. Frisch, *Gaussian 09, Revision A.2*, Gaussian, Inc., Wallingford. CT, 2009.

21 E. Krieger and G. Vriend, *J. Comput. Chem.*, 2015, **36**, 996–1007.

22 D. A. Case, V. Babin, J. T. Berryman, R. M. Betz, Q. Cai, D. S. Cerutti, T. E. Cheatham, T. A. Darden, R. E. Duke and H. Gohlke, *et al.*, *AMBER 14*, University of California, San Francisco, CA, USA, 2014.

23 W. Barzyk, K. Lunkenheimer, P. Warszynski, A. Pomianowski and U. Rosenthal, *Prog. Colloid Polym. Sci.*, 2000, **116**, 107–112.

24 K. Lunkenheimer, K. Haage and R. Hirte, *Langmuir*, 1999, **15**, 1052–1058.

25 G. Para, E. Jarek, P. Warszyński and Z. Adamczyk, *Colloids Surf., A*, 2003, **222**(1-3), 213–222.

26 E. Jarek, P. Wydro, P. Warszyński and M. Paluch, *J. Colloids Interface Sci.*, 2006, **293**, 194–202.

27 E. Jarek, T. Jasiński, W. Barzyk and P. Warszyński, *Colloids Surf., A*, 2010, **354**(1-3), 188–196.

28 V. B. Fainerman, V. I. Kovalchuk, E. V. Aksenenko and R. Miller, *Langmuir*, 2016, **32**, 500–5509.

29 J. L. Cornette, K. B. Cease, H. Margalit, J. L. Spouge, J. A. Berzofsky and C. DeLisi, *J. Mol. Biol.*, 1987, **195**, 659–685.

30 A. Mohanty and J. Dey, *Langmuir*, 2007, **23**, 1033–1040.

31 G. Zhao and E. London, *Protein Sci.*, 2006, **15**(8), 1987–2001.

32 W. Qiao and Y. Qiao, *J. Surfactants Deterg.*, 2013, **16**, 821–828.

33 C. Moran, P. Clapes, F. Comelles, T. Garcıa, L. Perez, P. Vinardell, M. Mitjans and M. R. Infante, *Langmuir*, 2001, **17**, 5071–5075.

34 S. Miyagishi, T. Asakawa and M. Nishida, *J. Colloid Interface Sci.*, 1989, **131**, 68–73.

35 M. J. Rosen and J. T. Kunjappu, ed., *Surfactants and interfacial phenomena*, Wiley, Hoboken, NJ, 4th edn, 2012.

36 A. Zdziennicka and B. Janczuk, *J. Mol. Liq.*, 2017, **243**, 236–244.

37 K. Szymczyk, A. Zdziennicka and B. Janczuk, *J. Sol. Chem.*, 2018, **47**, 1824–1840.

38 V. B. Fainerman, S. V. Lylyk, E. V. Aksenenko, M. V. Makievski, J. T. Petkov, J. Yorke and R. Miller, *Colloids Surf., A*, 2009, **334**(1-3), 1–7.

Colloids and Surfaces A 589 (2020) 124446

Contents lists available at ScienceDirect

Colloids and Surfaces A

journal homepage: www.elsevier.com/locate/colsurfa

Effect of initial adsorption coverage and dynamic adsorption layer formation at bubble surface in stability of single foam films

M. Borkowski[a], D. Kosior[b], J. Zawala[a,*]

[a] Jerzy Haber Institute of Catalysis and Surface Chemistry Polish Academy of Sciences Polish Academy of Sciences, Ul. Niezapominajek 8, 30-239, Krakow, Poland
[b] Department of Inorganic and Analytical Chemistry, University of Geneva, 30 Quai Ernest Ansermet, 1205, Geneva, Switzerland

GRAPHICAL ABSTRACT

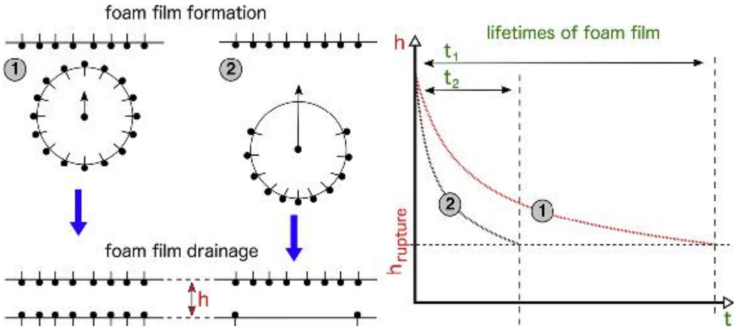

ARTICLE INFO

Keywords:
Bubble
Liquid film
Drainage
Adsorption coverage
Thickness
Lifetime

ABSTRACT

The paper presents the experimental studies on influence of degree of initial adsorption coverage and structure of the dynamic adsorption layer over a rising bubble on stability of single foam films formed at surfaces of solutions of surface-active-substances namely n-octanol, n-hexadecyltrimethylammonium bromide (CTAB) and polyoxyethylenesorbitan monooleate (Tween80). Stability of single foam films formed by the colliding bubble under different experimental conditions were determined on the basis of systematic measurements of a single bubble lifetime in self-elaborated set-up. The experiments were supplemented by theoretical calculations of values of rupture thicknesses of the foam films, determined according to the Radove-Dimitrov-Ivanov model of drainage, which allows to consider formation of symmetrical and unsymmetrical foam films, depending on estimated structure of the dynamic adsorption layer. It was found that film lifetime depends strongly on the structure (stage of development) of motion-induced dynamic adsorption layer over the rising bubble surface. Moreover, it was shown that the bubble with completely different degree of initial adsorption coverage can form foam film of similar stability. This effect was attributed to the fact that eventual degree of the bubble adsorption coverage can reach comparable (and in some cases even equilibrium) value before film formation with identical structure of the DAL and degree of liquid/gas interface immobilization.

1. Introduction

Liquid foam is thermodynamically unstable two-phase system composed of gas dispersed into a liquid phase. It is very important type of dispersed system, commonly utilized in either everyday life (cleaning, washing, shaving, cosmetics etc.) or many important

---

* Corresponding author.
E-mail address: nczawala@cyf-kr.edu.pl (J. Zawala).

https://doi.org/10.1016/j.colsurfa.2020.124446
Received 4 December 2019; Received in revised form 7 January 2020; Accepted 8 January 2020
Available online 09 January 2020
0927-7757/ © 2020 Elsevier B.V. All rights reserved.

technological, social and industrial applications (fire-fighting, froth flotation, oil recovery, foam fractionation, treatment of wastewater etc.). Foam, as every dispersed system, is formed and initially exists under dynamic conditions, as a consequence of energy input needed for dispersion of immiscible phases. Therefore, the initial stage of foam formation takes place in quite a non-equilibrium environment with lots of disturbances and perturbations related to violent collisions between gas bubbles. Bubbles collisions lead to the liquid film formation, i.e. layer of liquid (aqueous phase) separating the interacting liquid/gas interfaces. Mechanism of rupture of a single foam film formed by the bubble colliding with the free liquid surface (liquid/gas interface) has been studied both experimentally and theoretically by many authors [15–25]. According to the literature the stability of liquid films at the initial stage of their formation cannot be described using equilibrium quantities. Before reaching quasi-static conditions, the average thicknesses of such films are much larger than the range of specific forces of interactions in thin liquid layers (DLVO theory and disjoining pressure [1–3]). Such forces attain a meaningful value only at the liquid film thicknesses of the order of 100 nm (related to the so-called critical thickness of rupture), therefore they can be a decisive factor only, if the conditions of a system have a chance to be shifted (with time) towards quasi-equilibrium state. Under dynamic conditions such factors as non-equilibrium and non-uniform adsorption coverage, magnitude of liquid film thickness non-homogeneities [26] as well as interfaces area changes, leading to inducement of the surface elasticity forces, are dominant [1,27] and they determine if the liquid films can survive initial external disturbances and drain to thicknesses where forces of specific interactions start to operate [28].

Liquid film is a fundamental "brick" of the foam system, composed of millions of liquid layers separating interacting bubbles. It is well known that single foam film can be used as a probe of properties of the foam system as a whole. By studying properties of a single film, it is possible to determine factors responsible for its stability, which can be extrapolated (with some limitations) to much more complex system. Therefore, the liquid film properties have been extensively studied by many authors [3–9]. Overwhelming majority of such studies have been carried out under static conditions, with the use of specially designed equipment, where a great care has been undertaken to avoid external disturbances [3–9]. Undoubtful advantages of this methodology is ability to study very thin liquid layers, what makes it a very powerful tool for determination of magnitude of the interactions between separated phases at a molecular level (different components of disjoining pressure). Nevertheless, as described above, the real system is always formed under dynamic conditions, so the history related to magnitude of disturbances and degree of deviation from equilibrium can influence its further behaviour. This factor is very important and can be considered only, when experiments are carried out in the dynamic system. One of such extremely important factors is formation of dynamic adsorption layer (DAL [10–13]) over the surface of the rising gas bubble, prior to its collision with other liquid/gas interface [14–16], which can affect significantly the kinetics of drainage of the liquid (foam) film.

The rising velocity of a gas bubble in an aqueous phase is governed by the difference in densities of the liquid and gas phases, liquid viscosity, bubble size and shape, changes in the hydrostatic pressure, as well as state of adsorption layer. Generally, higher the adsorption coverage, lower the bubble speed. However, adsorption layer on a surface of a gas bubble rising in solution of surface-active substance (SAS) is different from that on a bubble in rest [10]. State of the DAL at rising bubble surface depends on a distance covered by the bubble in the liquid phase. The DAL is formed as a result of viscous drag of continuous medium, which pushes adsorbed SAS molecules towards bubble rear part. As a consequence, there is a depletion zone at the bubble's top pole, and in the limiting case the top part of the bubble can be completely free of the SAS molecules [10]. This gradient of coverage induces Marangoni effects, opposing shear flow and leads to immobilization of the bubble surface, which degree depends on the SAS concentration. The DAL formation is not instant phenomenon and usually some time is needed for complete development of its final architecture. The time-scale of the DAL formation is concentration-dependent. Recently it was shown that kinetics of the DAL formation depends strongly on degree of initial adsorption coverage at the detaching bubble surface [13] and can be quite different for constant bulk concentration but various (independently controlled) initial degrees of adsorption coverage. Development of the DAL can be successfully tracked by monitoring of rise velocity of a gas bubble is the SAS solutions [13,29]. Generally, three to four different bubble motion stages can be distinguished, depending on the SAS concentration [13,29–31]: (i) acceleration, (ii) maximum velocity, (iii) deceleration and (iv) terminal velocity. The maximum velocity means that the DAL is not established, yet, but the process of its formation is about to start. Equilibrium between opposed surface tension gradient forces and shear forces is being established during the deceleration stage. Terminal velocity establishment means that this equilibrium is reached and the DAL architecture is formed completely [13,29–31].

The paper presents experimental investigations on stability of a single foam film, formed by the bubble colliding with free surface of solutions of various surface-active substances. To estimate the influence of various factors such as solution concentration, state of the DAL at the colliding bubble surface and degree of initial adsorption coverage over the detaching bubble, improved methodology adapted from Jachimska et al. [14,15,20] was applied. It was shown that state of the DAL is crucial for kinetics of drainage of the liquid films formed. Moreover, it was proved that if the structure of the DAL induced before the liquid film formation is similar, the film stability is practically identical and independent on the initial bubble adsorption coverage (in solution of identical bulk concentration).

2. Materials and methods

2.1. Reagents

The experiments were carried out in solutions of commercial reagents (surface-active substances – SAS of different adsorption kinetics) of the highest available purity, purchased from Sigma Aldrich, namely: *n*-octanol, n-hexadecyltrimethylammonium bromide (CTAB) and polyoxyethylenesorbitan monooleate (Tween80). The value of critical micelle concentration (CMC) of CTAB and Tween80 was 2×10^{-4} M and 1×10^{-3} M, respectively. Ultra-pure water (Millipore, conductivity < $0.05\ \mathrm{S \cdot cm^{-1}}$ and surface tension $72.4\ \mathrm{mN\,m^{-1}}$) was used for solutions preparation. Before each experimental series, all involved glass parts of the laboratory equipment were washed with the diluted solution of Mucasol® - Schülke (commercially available laboratory cleaning liquid) purchased from Sigma Aldrich and then rinsed several times with large amount of the Milli-Q water. The glass capillary used for a single bubble formation was cleaned with diluted chromic mixture and rinsed repeatedly with ultra-pure water.

2.2. Experimental set-up

The lifetime of a single foam film formed by a bubble colliding with a free surface of SAS solutions of various concentrations was measured automatically in the apparatus developed in our laboratory, which is schematically presented in Fig. 1. The apparatus consisted of: (i) cylindrical glass column (40 mm in diameter) with the thick-walled capillary (inner diameter 0.075 mm) sealed at the bottom, (ii) single bubble generator (BoD – Bubble-on-Demand [32]), (iii) bubble trap connected to stepper motor for control over a degree of initial adsorption coverage (θ_i) at the liquid/gas interface (detaching bubble surface) [33], (iv) camera for the bubble lifetime determination, (v) polytetrafluoroethylene (Teflon) ring (inner diameter 38 mm, height 40 mm), mounted at the top of the column for formation of a liquid convex meniscus - it was focusing the bubble in the column center

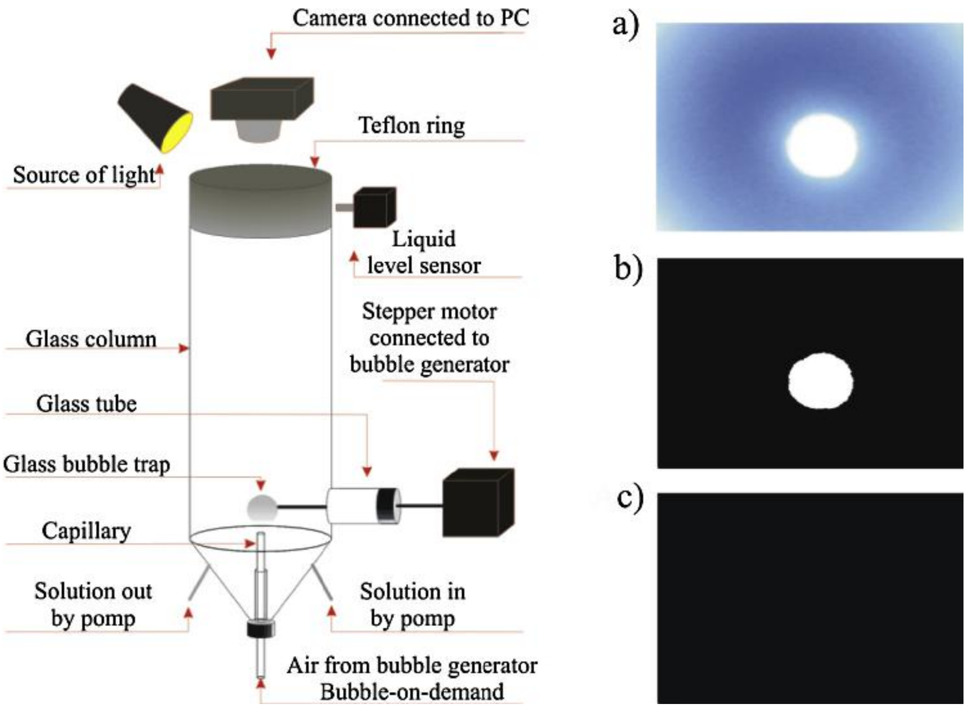

Fig. 1. Scheme of the experimental set-up and pictures presenting a) live camera top view, b) camera top view with threshold (bubble present at the solution surface), c) camera top view with threshold (no bubble at the solution surface).

during the period of drainage of the formed liquid film and (vi) a light source. A single bubble (equivalent diameter equal to 1.48 mm) was generated at the capillary with use of the BoD. The bubble diameter was precisely controlled and its changes were negligible due to very small variations in surface tension of the studied solutions [13]. The frequency of a single bubble formation (Δt_b) was controlled by the BoD settings. Generally, in the majority of experimental runs, the Δt_b was equal to 60 s. For experiments with the bubble trap the Δt_b was adjusted to experimental conditions and was longer, accordingly.

Precise control over the initial adsorption coverage at a detaching bubble surface (θ_i) was possible using the bubble trap. It was a glass dome attached to a glass stick connected to the stepper motor. The trap was controlled by the BoD software. After detachment, the bubble could be captured inside the dome for precisely adjusted time, also controlled by the BoD settings. This was an additional time (t_{trap}) available for adsorption of the SAS molecules at the liquid/gas interface. After the desired time, the trap could be rotated, releasing the bubble saturated with the SAS molecules to a desired degree. As a result, the total time available for adsorption was as follows [13]:

$$t_{ads} = t_{growth} + t_{trap} \tag{1}$$

where t_{growth} is a time of bubble area expansion before detachment from the capillary orifice (time of the bubble growth). The values of θ_i and equilibrium surface coverages were calculated theoretically, according to the approach presented in details elsewhere [13]. To prevent the bubble from attaching to the glass trap surface in CTAB cationic surfactant solutions (due to electrostatic interactions), the negatively charged liquid/glass interface was covered with a poly(diallyldimethylammonium chloride) (PDADMAC) layer [34].

The lifetime of a single bubble was measured using a camera mounted above the free solution surface, located at the top of the glass column (where Teflon ring was mounted). The bubble lifetime was calculated from the camera top view images as a time span between a moment of the bubble appearance at the liquid/gas interface (i.e. collision with solution surface and single foam film formation – see Fig. 1B) and the moment of bubble rupture, registered by the camera (see Fig. 1C), which was controlled using the Python script with OpenCV and PIL modules. To avoid light reflections perturbing the video image and bubble lifetime measurements, the outer side of the trap as well as the cylindrical column was painted black. Special care was taken to thoroughly clean the painted glass elements and to check whether the paint would not affect the water quality. In order to study the influence of structure of the dynamic adsorption layer (DAL) formed over the rising bubble surface on stability of the single foam films, two lengths of columns - 50 and 150 mm was used, allowing measurements of the bubble lifetime after various distances covered by the bubble in the SAS solutions.

The glass column was automatically filled with the tested SAS solutions before each experimental run and emptied after its finish using pumps controlled by a liquid level sensor. Drainage of the foam film is the stochastic phenomenon, therefore to obtain reasonable statistics, the lifetime of 200 single bubbles was measured for each studied SAS concentrations. Based on the lifetime distribution histograms, the most occurring (expected) value was determined using Gauss function fitting.

2.3. Calculations of kinetics of liquid film drainage and critical thickness of rupture

To estimate the kinetics of drainage of a single foam film formed by the bubble colliding with the free surface of the studied SAS solutions, the model of thinning developed by Radoev et al. [35–37] was used. This model, referenced further as RDI (Radoev-Dimitrov-Ivanov) model [16], takes into account the fluidity of the liquid/gas interface (hydrodynamic boundary conditions), which depends on the SAS surface concentration (Γ) and state of the dynamic adsorption layer at the bubble at the moment of liquid film formation. According to the RDI model, the liquid film thinning velocity (V) can be expressed as [35–37]:

$$V = -\frac{dh}{dt} = \frac{2h^3 \Delta P}{3\mu R_f^2}(1 + \alpha) \tag{2}$$

where h is a liquid film thickness, t is time, ΔP is a total pressure causing the drainage, μ is a fluid viscosity and R_f is the radius of the formed liquid film, which for a bubble of radius R_b in liquid of density ρ_l

and surface tension σ, under the gravitational acceleration g, can be calculated as:

$$R_f = \left(\frac{4gR_b^4\rho_l}{3\sigma}\right)^{1/2} \tag{3}$$

The first term of Eq. (2) is the Reynolds equation, describing thinning velocity of a liquid layer between two no-slip, parallel surfaces. Parameter α is introduced to consider different hydrodynamic boundary conditions at the bubble surface creating the film, which is interrelated strictly to the structure of adsorption layer. When equilibrium surface concentration (Γ_{eq}) is assumed both at the free solution surface (Γ_s) and bubble surface (Γ_b), i.e. when $\Gamma_s = \Gamma_b = \Gamma_{eq}$, the liquid film formed is symmetrical and the parameter α is given by [35,36]:

$$\alpha = b + \frac{h_s}{h} \tag{4}$$

Coefficients b and h_s from Eq. (4) can be calculated as:

$$b = \frac{3\mu D}{\Gamma_{eq}(\partial\sigma_{eq}/\partial c)} \tag{5}$$

$$h_s = \frac{6\mu D_s}{\Gamma_{eq}(\partial\sigma_{eq}/\partial\Gamma_{eq})} \tag{6}$$

where D is SAS bulk diffusion coefficient and D_s is surface diffusion coefficient. In our calculations, original symmetrical case given in [35–37] was modified and it was possible to consider the situation, where $\Gamma_s = \Gamma_{eq}$ and $\Gamma_b = \Gamma_i$, where Γ_i is initial surface concentration at the bubble after given value of the t_{ads}.

For unsymmetrical liquid film, i.e. for the case where $\Gamma_s = \Gamma_{eq}$ and $\Gamma_b = 0$, the α is given by [35,36]:

$$\alpha = 3 + 4b + \frac{h_s}{h} \tag{7}$$

In all calculations it was assumed that D for CTAB and n-octanol is equal to 4×10^{-6} cm^2/s, while for Tween80 equal to 1.8×10^{-6} cm^2/s [13]. The D_s was assumed as 4×10^{-5} cm^2/s for CTAB and n-octanol, and 1.8×10^{-5} cm^2/s for Tween80 [13]. To calculate the values of Γ_i and Γ_{eq}, the parameters of Frumkin isotherms and the numerical approach given in [13,38] (Ward-Tordai equation), was used. The value of σ_{eq} where taken from [13].

3. Results and discussion

As was mentioned above, our aim was to determine the influence of the DAL structure, interrelated additionally with the degree of initial bubble adsorption coverage, on the stability of single foam film formed by the bubble colliding with the free solution surface. To this end, the distance (L) between the capillary orifice (or bubble trap) and the free surface was adjusted basing on the local bubble velocity profiles (i.e. variations in velocity of the rising bubble with covered distance) determined for the tested SAS by Kosior and Zawala [13], for different values of the t_{ads}. The profiles, redrawn from the ref. [13], for n-octanol, CTAB and Tween80 solutions of various concentrations and t_{ads} values are shown in Fig. 2. Note that the velocity profiles were determined on the basis of the bubble images taken by the side CCD camera [13]. Note also that for Tween80 the concentration was constant and only the t_{ads} were changed gradually.

In order to elucidate the importance of the DAL state and t_{ads} values on a single foam film stability, we decided to compare the lifetime of foam films formed by the bubble colliding with the solutions surface with impact velocity equal to: (i) terminal velocity - u_t (indicating that the DAL structure is fully formed and the bubble surface is partially or fully immobilized during rising period) and (ii) maximum velocity - u_{max}, where the DAL formation has just started but the full architecture of the DAL is not established, yet. The values of distance corresponding to the maximum bubble velocity in each SAS concentrations and for different t_{ads} values were taken directly from the Fig. 2 (see vertical dashed lines L_1-L_6) [13]. Increased t_{ads} values are illustrated at velocity profiles with lines of different thickness (thicker line means longer t_{ads}). As seen in Fig. 2, for n-octanol and CTAB the t_{ads} (and simultaneously θ_i) increase did not cause the shift of the maxima position in respect the distance. Only the value of maximum velocity was smaller for higher t_{ads} values. Moreover, distance at which u_t was established was affected in similar manner - for longer t_{ads} this distance was shorter, indicating that the full structure of the DAL was established faster. In the case of Tween80, t_{ads} increase caused diminishing of the value of maximum velocity as well as shift of the maxima positions towards shorter distances. The experimental conditions were summarized in the Table 1. Values of the L_1-L_6 indicating distance where the bubble reached its maximum velocity are presented there and called L_{max}. In addition, the t_{ads}, θ_i and θ_i / θ_{eq} values (where θ_{eq} is the equilibrium adsorption coverage), are shown in Table 1. In all experiments, the L_t was assumed to be equal to 150 mm.

3.1. *Influence of adsorption coverage on stability of foam films formed by a bubble with terminal velocity*

In the first series of experiments, lifetime of the single bubble colliding with the free surface of SAS solutions of different concentrations were determined for the L_t = 150 mm, i.e. for the distance enough for the rising bubble to reach its terminal velocity. Fig. 3 presents values of the bubble lifetime at CTAB solution surface as a function of number of arriving bubbles. In Fig. 3A data for different CTAB concentrations and constant t_{ads} value are presented, while in Fig. 3B results for constant concentration and various t_{ads} are shown. It is seen clearly in Fig. 3A that for $t_{ads} = t_{growth} = 1.6$ s (experiments where the bubble trap was not used) the lifetime was longer for higher concentration. This is, of course well-known and expected effect – generally, stability of liquid films increases with increased SAS solutions concentration [1,3]. Much more interesting effect can be observed in Fig. 3B. Here, there is practically no difference between lifetime values for different $t_{ads.}$ It is rather surprising, as values of θ_i presented in Table 1 vary significantly – as seen θ_i for $t_{ads} = 301.6$ s is twice as higher as for $t_{ads} = 1.6$ s.

Fig. 4 presents corresponding distribution histograms of the lifetime values presented in Fig. 3. The lines are Gauss function fitted to determine the expected values of the bubble lifetime. Determined average lifetime values are given for each fitted curve. The data presented in Fig. 4 confirmed above-described observation - only the solution concentration increase caused significant prolongation of the bubble lifetime from 1.2 to almost 8 s. The lifetimes for different t_{ads} values were practically identical.

The average lifetime values determined for all studied n-octanol and CTAB solutions of different concentrations as well as t_{ads} values are summarized in Fig. 5. In Fig. 5A the lifetime values as a function of n-octanol and CTAB solutions concentration are shown, while in Fig. 5B, corresponding data are given as a function of the t_{ads}. As was expected, similarly to the CTAB case, also for n-octanol the average bubble lifetime increases with the solution concentration increase, but this effect is less steep in the considered n-octanol concentration range (Fig. 5A). Moreover, it is seen (Fig. 5B) that for identical concentration, average bubble lifetime is practically constant. This effect can be observed not only for n-octanol and CTAB solutions but also for Tween80, for which only one concentration but seven different values of t_{ads} were examined.

On first sight, it is rather surprising that the bubble detaching from the capillary with completely different value of the adsorption coverage (θ_i) forms a foam film of practically identical stability. To explain this effect, several facts need to be analyzed. The constant, terminal velocity of the rising bubble indicates that, independently on the θ_i value, the DAL is fully formed at the bubble surface. It has to be kept in mind that the θ_i given in Table 1 were initial adsorption coverages, calculated for detaching bubble. After the distance L equal to L_t,

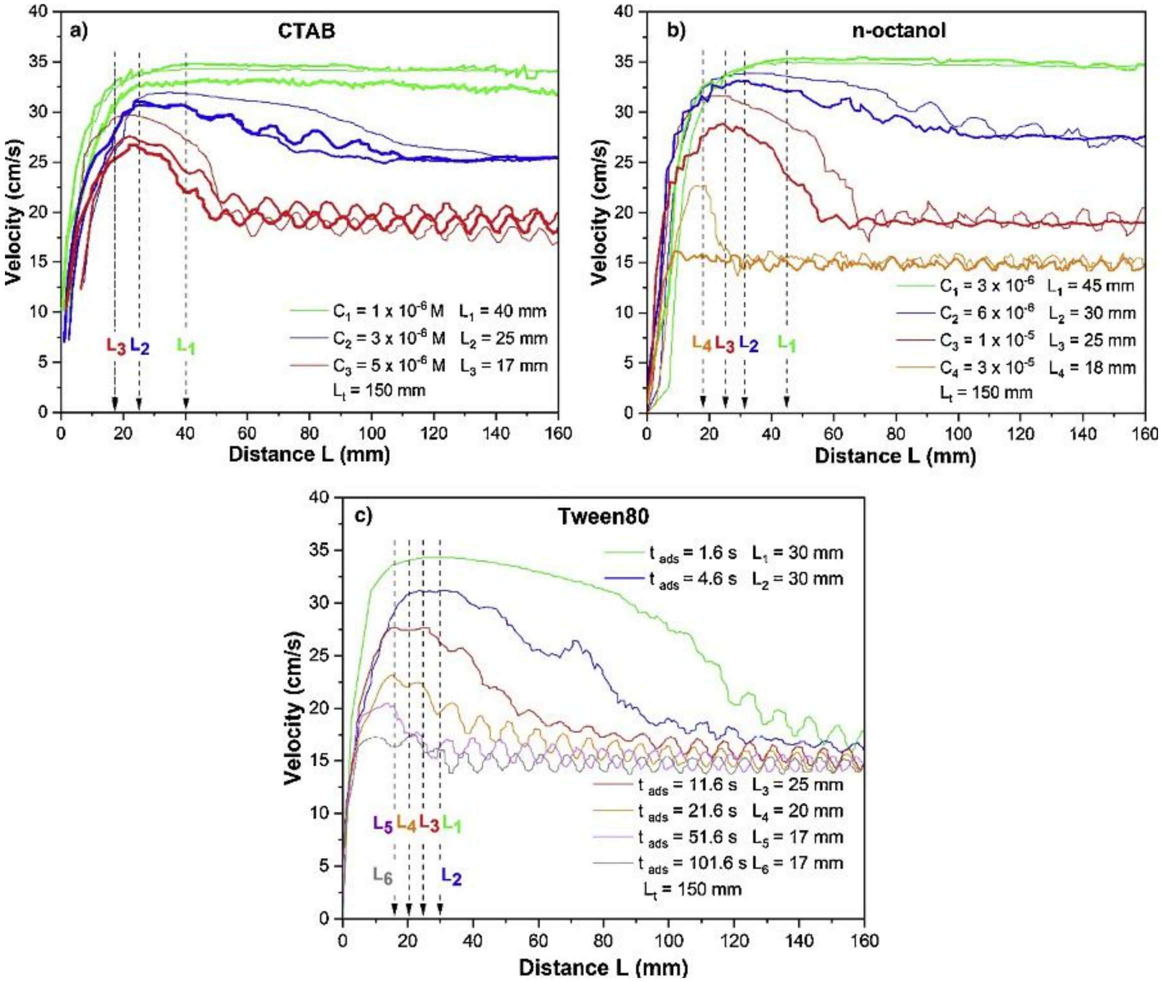

Fig. 2. Local bubble velocity variations as a function of distance covered by the bubble in (A) CTAB, (B) n-octanol and (C) Tween80 solutions of different concentrations, for various t_{ads} values. Vertical lines denoted as L_1-L_6 indicates the values of distance where the bubble reached its maximum velocity (L_{max} in Table 1).

Table 1

Distances between capillary and free surface, taken from Fig. 2, for different SAS concentration and t_{ads} values for which experiments were carried out.

SAS	C [M]	t_{ads} [s]	L_{max} [mm]	θ_i [%]	θ_i / θ_{eq}
CTAB	1×10^{-6}	1.6 / 21.6 / 301.6	40	0.34 / 0.61 / 0.76	0.41 / 0.75 /0.92
	3×10^{-6}		25	1.01 / 1.84 / 2.27	0.41 / 0.75 /0.92
	5×10^{-6}		17	1.68 / 3.06 / 3.77	0.41 / 0.75 / 0.92
octanol	3×10^{-6}	1.6 / 151.6	45	0.33 / 0.39	0.83 / 0.99
	6×10^{-6}		30	0.66 / 0.79	0.82 / 0.98
	1×10^{-5}		25	1.11 / 1.33	0.82 / 0.98
	3×10^{-5}		18	3.39 / 4.10	0.81 / 0.98
Tween	1×10^{-6}	1.6	30	0.76	0.01
		3.6	30	1.32	0.01
		10.6	25	2.01	0.02
		20.6	20	2.71	0.03
		50.6	17	4.12	0.04
		100.6	17	5.68	0.06

*L_t was taken as 150 mm for all studied S.

coverage of surface-active molecules at the bubble surface increases, as a result of adsorption during bubble rising period. In addition, the terminal velocity establishment for all θ_i values indicates similar state of the DAL formed at the bubble surface. In turn, similar state of the DAL means that bubble interface was immobilized in similar degree. Practically identical stability of the liquid film was additional proof of this effect. Moreover, analyzing the data from Table 1, it can be seen that in the case of experiment performed for n-octanol and CTAB solutions with the highest t_{ads} applied, bubble leaved the trap with the adsorption coverage almost equal to its equilibrium value. This means that during the bubble rising period, negligible amount of surface-active molecules was able to be adsorb at the bubble surface, because it was almost completely saturated and the θ_i /θ_{eq} was practically equal to 1 (equilibrium value). Identical stability of liquid films for different t_{ads} indicates that during the liquid film formation not only the liquid/gas (bubble) interface was immobilized in the comparable degree and the DAL state was comparable but also resultant adsorption coverage was similar, i.e. was very close to equilibrium. Thus, similar stability of liquid film for different θ_i values is most probably a consequence of the fact that eventual degree of the bubble adsorption coverage can reach the equilibrium value before film formation or at the initial stage of its drainage, with identical structure of the DAL and degree of liquid/gas interface immobilization.

Additional proof for correctness of this hypothesis is presented in Fig. 6, where values of calculated liquid film thickness (RDI model) at the moment of bubble rupture (after corresponding lifetime determined during experiments) are presented. Here, due to the fact that the DAL was fully formed at the bubble surface, unsymmetrical case given by Eqs. (2–6), and schematically presented in the picture inserted in the Fig. 6, was considered in calculations. As seen, in all cases the liquid film was stable enough to reach the thickness, whose order of magnitude can be associated with its equilibrium value (thicknesses

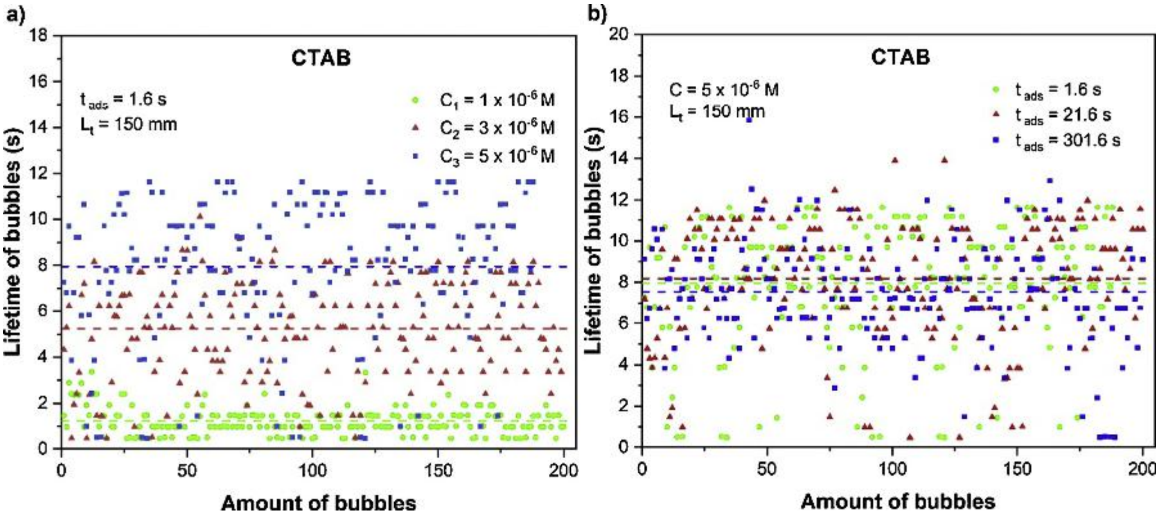

Fig. 3. Lifetime of the bubbles at CTAB solution surface for a) constant t_{ads} but different CTAB concentrations, b) constant CTAB concentrations but various t_{ads} values.

around 100 nm). Moreover, irrelevantly on the t_{ads} values, the rupture thicknesses for each studied SAS are practically identical. This is rather strong indication that the kinetics of liquid film drainage, determined by the state of adsorption layer at the film interfaces, was similar.

3.2. *Influence of adsorption coverage on stability of foam films formed by a bubble with maximum velocity*

Similar above-presented analysis was performed for the liquid films formed by the bubble which collided with maximum velocity with the surface of the SAS solutions. As already discussed, position of the maximum at the bubble velocity profile is concentration-dependent, therefore different values of distance between the bubble starting point and solution surface, corresponding to the L_{max}, were adjusted, depending on the SAS type and concentration (see Fig. 2 and Table 1).

Experimental results for all SAS studied are presented in Fig. 7, where interrelation between lifetime, solution concentrations and t_{ads} value is shown. As seen, again clear and expected effect of concentration is visible. Independently on the t_{ads} value, liquid film lifetime increases with increasing concentration of n-octanol (Fig. 7A) and CTAB (Fig. 7B). Nevertheless, unexpected decrease of the stability of liquid film can be noticed for constant concentration and prolonged t_{ads}. This effect is the most pronounced for the highest concentration of the studied SAS and can be observed for n-octanol, CTAB as well as Tween80 (Fig. 7C).

In order to approximate the source of this unexpected effect, the calculations of rupture thickness of the liquid film were again performed using the RDI drainage model. However, in this case, due to the fact that the DAL was not established yet at the bubble surface (maximum velocity), we applied the mode of the model which considers formation of symmetrical liquid film (see inserted scheme in Fig. 8) with uniform SAS coverage over the bubble surface equal to θ_i. To take into account influence of the additional adsorption time, different degree of uniformly distributed adsorption coverages, corresponding to t_{growth} or t_{trap}, respectively, were considered.

Fig. 8 presents the calculated rupture thicknesses after t_{ads} = 1.6 s, i.e. for the case where the bubble trap was not used, and for maximum t_{ads} applied for each studied SAS, resulting in different θ_i values. As seen in Fig. 8, the overall picture is similar to that presented in Fig. 6 – the draining liquid film the thicknesses, which are comparable with equilibrium values characteristic for the film formed and existing under quasi-static conditions. This situation can be observed for all SAS and solution concentrations, except 1×10^{-6} M CTAB where the calculated thickness was higher and equal to 174 nm. This was the only deviation,

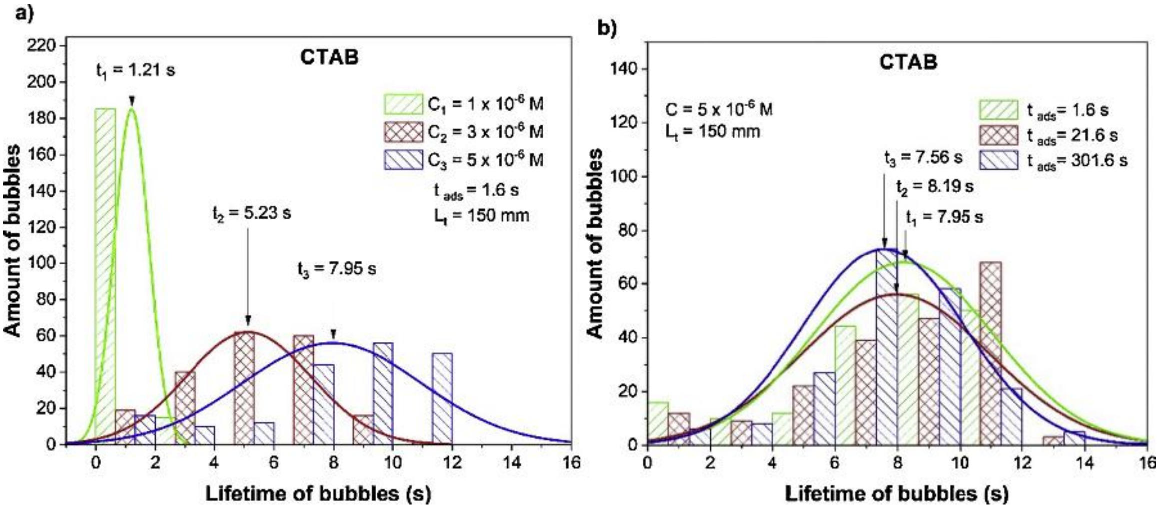

Fig. 4. Bubble lifetime distribution histograms, based on the results presented in Fig. 4, with fitted Gauss function, used for determination of the expected lifetime values.

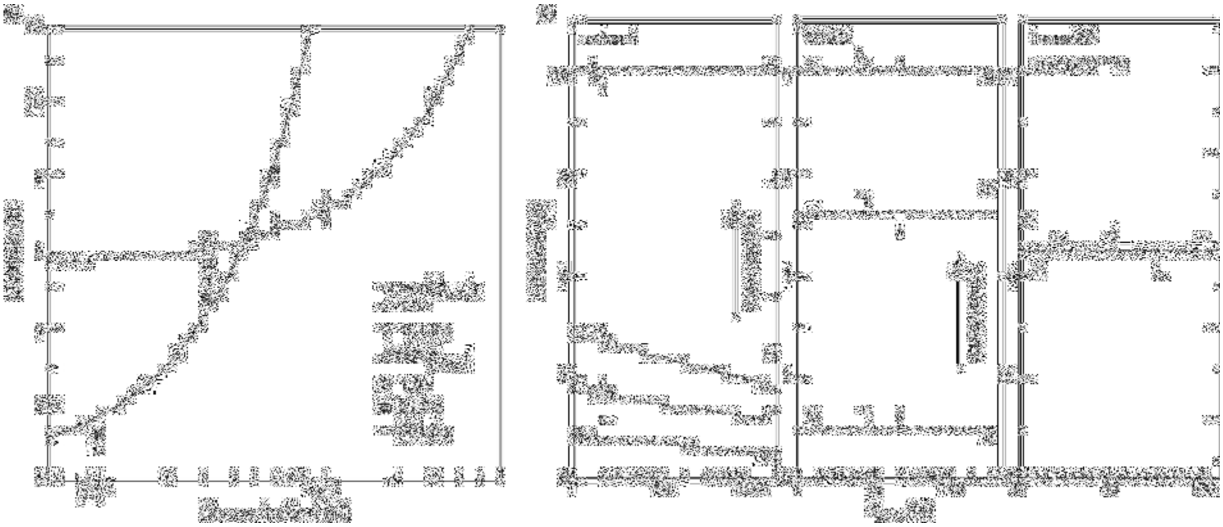

Fig. 5. Lifetime of a bubble at free surface of studied SAS solutions as a function of (A) solution concentration, (B) t_{ads} values (lines added to guide the eye, values of c_1 - c_4 for each SAS given in Table 1).

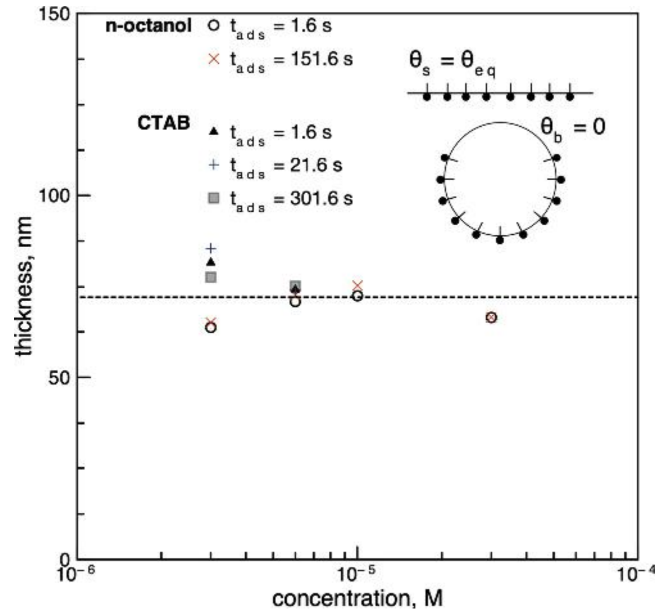

Fig. 6. Thickness of rupture of the single liquid film as a function of n-octanol and CTAB solutions concentrations. On the right plot, evolution of the thickness in time for the highest and lowest studied SAS solutions concentrations is presented.

but was observed for this concentration not only for $L = L_t$ but also $L = L_{max}$ (see below). However, except this only deviation, for constant concentration, clear decrease in the liquid film stability can be observed with t_{ads} increase, and this effect is the most pronounced for higher concentrations. These results indicate that higher is the bubble adsorption coverage, the higher is the thickness of rupturing. There is only one reasonable explanation of this effect – it was caused most probably by the bubble trap, which rotation disturbed the drainage as a result of convectional flow of the liquid induced near the free solution surface. Additional liquid flow acted as external disturbances, which perturbed the quasi-static conditions of the liquid film drainage. This conclusion is additionally supported by the fact that effect of decrease in the bubble lifetime is the highest for the smallest distances between the free solution surface and the moving trap surface (higher solution concentration), i.e. for the case where the disturbances are expected to be the strongest.

In the case of Tween80, similar calculations did not show corresponding trends. Independently on the L and t_{ads} values, the decrease of thickness in time followed the trend characteristic for unsymmetrical liquid film, where $\theta_s = \theta_{eq}$ and $\theta_b = 0$, despite the fact that experimental data indicated significant difference in kinetics of drainage between L_{max} and L_t cases. Most probably it was caused by the values of adsorption coverage of Tween80 molecules at the liquid/gas interface (see Table 1), which were too low to induce significant changes in rate of film drainage determined according to the RDI model.

3.3. *Stability of liquid film formed by the bubble with different structure of dynamic adsorption layer – a comparison*

Above presented analysis revealed that conditions of the liquid film drainage are different for L_t and L_{max}. In the case of L_t liquid film was formed and existed (was draining) in undisturbed environment, which was isolated from significant external disturbances. The bubble trap did not influence the drainage, because the distance between the trap and free solution surfaces was long enough. In the case of $L = L_{max}$, and experiments with the bubble trap ($t_{ads} > 1.6$ s), the trap rotation and induced liquid flow caused perturbation of the film drainage and was a reason of higher values of the film's rupture thicknesses. Therefore, in order to elucidate the influence of structure of the DAL induced at the colliding bubble surface on the liquid film stability, only the bubble lifetime values for $t_{ads} = 1.6$ s (no trap) was used, because only for this case the liquid film had a chance to reach its equilibrium values and the data for L_t and L_{max} can be compared.

Comparison between lifetime of the liquid film formed by the bubble at $L = L_t$ and $L = L_{max}$ for $t_{ads} = 1.6$ s are presented in Fig. 9. As seen, clear difference between the bubble lifetime values for these two distances can be observed both for n-octanol and CTAB. This is a consequence of different DAL structure. For L_t the DAL architecture was established fully, therefore the top pole of the bubble was practically completely devoid of any surface-active substances [10,11], as schematically presented in the picture inserted into Fig. 6. After liquid film formation, the bottom film interface was free of SAS molecules (the film was unsymmetrical), therefore hydrodynamic boundary conditions were strongly shifted towards more slip and the drainage was significantly faster, comparing to the L_{max} case. For L_{max}, the adsorption coverage was uniform, because, as a result of short distance covered by the rising bubble, the DAL was not established yet (see inserted picture in Fig. 8). As a consequence, liquid film formed was symmetrical and its drainage was significantly slower. In the case of Tween80 similar effect

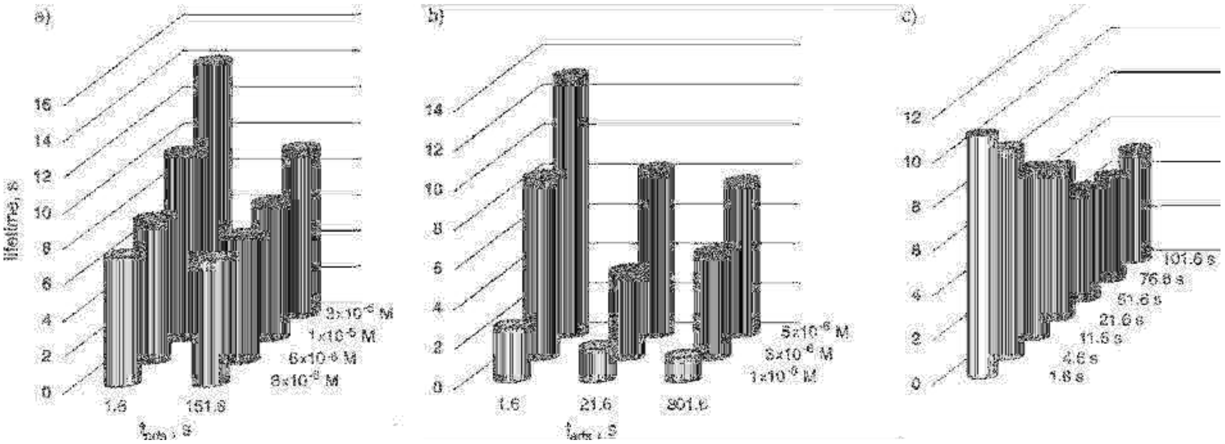

Fig. 7. Lifetime of a bubble at free surface of studied SAS solutions as a function of solution concentration and t_{ads} values for (A) n-octanol, (B) CTAB and (C) Tween80 (1×10^{-6} M).

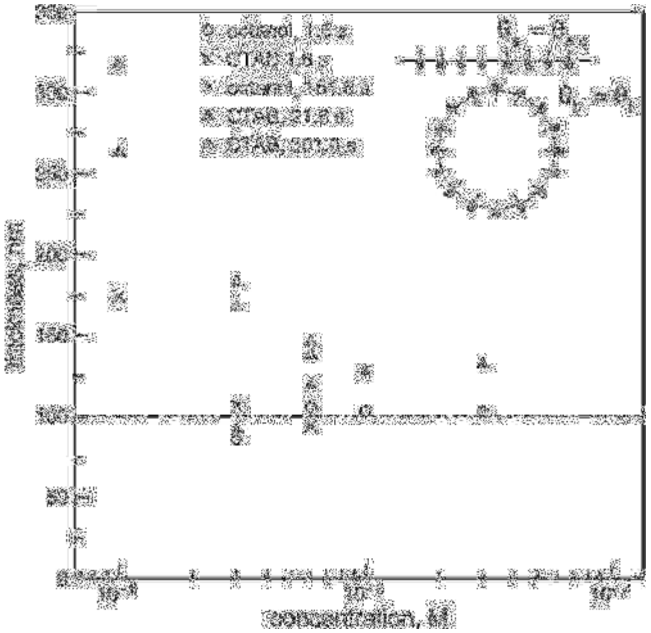

Fig. 8. Critical thickness of rupture of the liquid film formed by the colliding bubble in CTAB and n-octanol solutions after various $t_{ads.}$

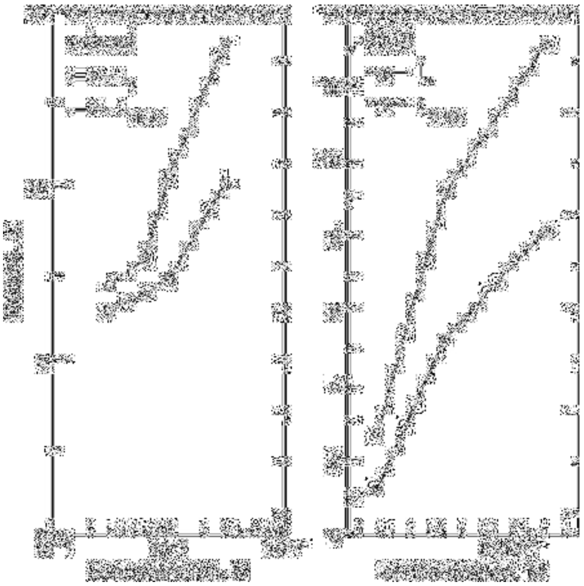

Fig. 9. Average bubble lifetimes determined for L_t and L_{max}, showing effect of the DAL formation in kinetics of the foam film drainage (t_{ads} = 1.6 s, experiments without bubble trap).

was observed – the bubble lifetime for $L = L_t$ was equal to 6 s, while for $L = L_{max}$ equal to 11 s.

Interestingly, lack of above analyzed effect for higher t_{ads} values (i.e. for the cases where the trap was applied) is an additional proof for correctness of the hypothesis of disturbances induced by the bubble trap. As presented in Fig. 10, the effect of the DAL existence, presented in Fig. 9, disappears for higher t_{ads} values. In the case of n-octanol and CTAB the effect of DAL is negligible for all t_{ads} studied. In the case of Tween80, the effect of DAL is visible only for smaller t_{ads} (higher L_{max} – see Table 1) and can be neglected for $t_{ads} > 50$ s.

4. Conclusions

Structure of the dynamic adsorption layer over the colliding bubble surface is crucial for kinetics of drainage of formed foam films. Comparison between lifetime of a liquid film formed by the bubble covering different distances in solution of surface-active substances revealed that the bubble lifetime is different. For longer distance the DAL architecture was established fully, therefore the top pole of the bubble was practically completely devoid of any surface-active substances so as the bottom interface of the formed liquid film. This caused shift of the hydrodynamic boundary conditions towards more slip and faster film drainage. For shorter distances covered by the bubble the adsorption coverage was uniform because the DAL was not established yet. As a consequence, the formed liquid film was symmetrical and its drainage was significantly slower. Additional proof of correctness of this analysis and conclusions was provide by the theoretical calculations of liquid film drainage. In all considered cases, independently on the distance covered by the bubble, the liquid film reached similar thickness, which was characteristic for equilibrium liquid film.

The performed experiments revealed that the stability of liquid film formed by the bubble with completely different degree of initial adsorption coverage can be similar. Analysis of liquid film stability for several different initial adsorption coverage values indicated that this effect should be related to similar degree of liquid/gas (bubble) interface immobilization. Moreover, it was proved indirectly that in certain cases (for long enough distance covered by the bubble prior the liquid film formation) eventual degree of the bubble adsorption coverage can reach the equilibrium value.

The experiments and calculations performed to determine the liquid

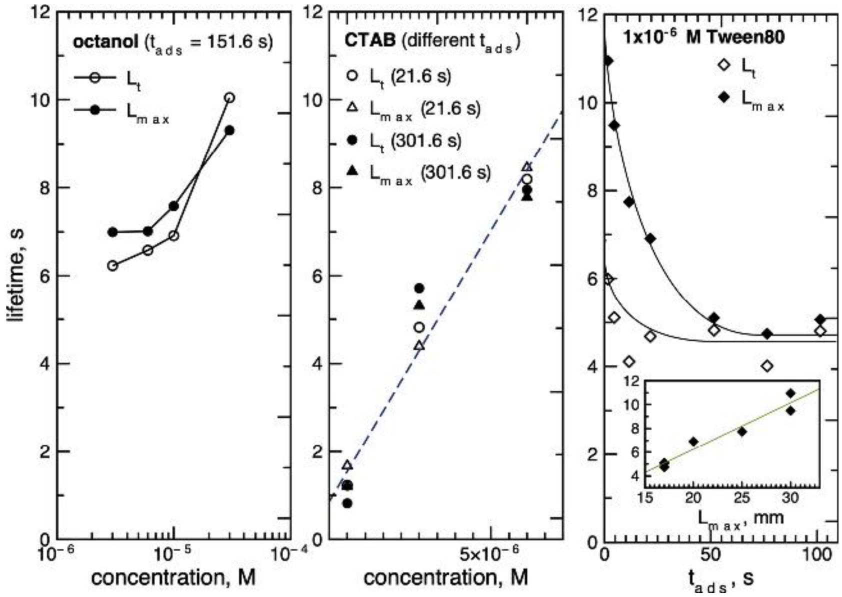

Fig. 10. Average bubble lifetimes determined for L_t and L_{max} for higher t_{ads} values (for experiments where the bubble trap was applied).

film stability during initial stage of the DAL formation revealed that the rotation of the applied bubble trap disturbed the drainage as a result of convectional flow of the liquid induced near the free solution surface. Additional liquid flow acted as external disturbances, which perturbed the quasi-static conditions of the liquid film drainage and caused its rupture at significantly higher thicknesses. Therefore, to study the influence of the DAL for higher values of the t_{ads}, new modified controlling algorithm or completely different bubble trap design has to be elaborated.

CRediT authorship contribution statement

M. Borkowski: Investigation, Data curation, Formal analysis, Writing - original draft, Visualization. **D. Kosior:** Data curation, Formal analysis, Writing - review & editing. **J. Zawala:** Conceptualization, Methodology, Software, Supervision, Funding acquisition, Writing - review & editing.

Declaration of Competing Interest

The authors declare that they have no known competing financial interests or personal relationships that could have appeared to influence the work reported in this paper.

Acknowledgement

Partial financial support from Polish National Science Centre (NCN - grant No. 2017/25/B/ST8/01247) is acknowledged with gratitude.

References

[1] D. Exerowa, P.M. Kruglyakov, Foam and Foam Films: Theory, Experiment, Application, Elsevier, 1997.
[2] A. Scheludko, Thin liquid films, Adv. Colloid Interface Sci. 1 (1967) 391–464.
[3] D. Exerowa, N.V. Churaev, T. Kolarov, N.E. Esipova, N. Panchev, Z.M. Zorin, Foam and wetting films: electrostatic and steric stabilization, Adv. Colloid Interface Sci. 104 (2003) 1–24.
[4] G. Gochev, Thin liquid films stabilized by polymers and polymer/surfactant mixtures, Curr. Opin. Colloid Interface Sci. 20 (2015) 115–123.
[5] B.W. Ninham, R.M. Pashley, P.L. Nostro, Surface forces: changing concepts and complexity with dissolved gas, bubbles, salt and heat, Curr. Opin. Colloid Interface Sci. 27 (2017) 25–32.
[6] M. Krasowska, M. Kor, P. Pawliszak, F.L. Bernardis, B.H. Bradshaw-Hajek, D.A. Beattie, Controlling bubble–Solid surface interactions with environmentally benign interfacial modifiers, J. Phys. Chem. C 123 (2019) 3645–3656.
[7] M. Krasowska, K. Malysa, D.A. Beattie, Recent advances in studies of bubble-solid interactions and wetting film stability, Curr. Opin. Colloid Interface Sci. 44 (2019) 48–58.
[8] E. Mileva, Impact of adsorption layers on thin liquid films, Curr. Opin. Colloid Interface Sci. 15 (2010) 315–323.
[9] V.V. Yaminski, S. Ohnishi, E.A. Vogler, R.G. Horn, Stability of aqueous films between bubbles. Part 1. The effect of speed on bubble coalescence in purified water and simple electrolyte solutions, Langmuir 26 (2010) 8061–8074.
[10] S.S. Dukhin, V.I. Kovalchuk, G.G. Gochev, M. Lotfi, M. Krzan, K. Malysa, R. Miller, Dynamics of Rear Stagnant Cap formation at the surface of spherical bubbles rising in surfactant solutions at large Reynolds numbers under conditions of small Marangoni number and slow sorption kinetics, Adv. Colloid Interface Sci. 222 (2015) 260–274.
[11] S.S. Dukhin, M. Lotfi, V.I. Kovalchuk, D. Bastani, R. Miller, Dynamics of rear stagnant cap formation at the surface of rising bubbles in surfactant solutions at large Reynolds and Marangoni numbers and for slow sorption kinetics, Colloids Surf. A 492 (2016) 127–137.
[12] M. Lotfi, D. Bastani, V. Ulaganathan, R. Miller, A. Javadi, Bubble in flow field: A new experimental protocol for investigating dynamic adsorption layers by using capillary pressure tensiometry, Colloids Surf. A 460 (2014) 369–376.
[13] D. Kosior, J. Zawala, Initial degree of detaching bubble adsorption coverage and the kinetics of dynamic adsorption layer formation, Phys. Chem. Chem. Phys. 20 (2018) 2403–2412.
[14] B. Jachimska, P. Warszynski, K. Malysa, Effect of motion on lifetime of bubbles at n-butanol solution surface, Colloids Surf. A 143 (1998) 429–440.
[15] B. Jachimska, P. Warszynski, K. Małysa, Effects of motion in n-hexanol solution on the lifetime of bubbles at the solution surface, Progr. Colloid Polym. Sci. 16 (2000) 120–128.
[16] D. Kosior, J. Zawala, R. Todorov, D. Exerowa, K. Malysa, Bubble bouncing and stability of liquid films formed under dynamic and static conditions from n-octanol solutions, Colloids Surf A 460 (2014) 391–400.
[17] F. Knelman, N. Dombrowski, D.M. Newitt, Mechanism of the bursting of bubbles, Nature (1954) 261.
[18] A.B. Pandit, J.F. Davidson, Hydrodynamics of the rupture of thin liquid films, J. Fluid Mech. 212 (1990) 11–24.
[19] J.M. Boulton-Stone, J.R. Blake, Gas bubbles bursting at a free surface, J. Fluid Mech. (1993) 437–466.
[20] P. Warszynski, B. Jachimska, K. Malysa, Experimental evidence of the existence of non-equilibrium coverages over the surface of the floating bubble, Colloids Surfaces A 108 (1996) 321–325.
[21] R. Manica, E. Klaseboer, D.Y.C. Chan, The impact and bounce of air bubbles at a flat fluid interface, Soft Matter 12 (2016) 3271–3282.
[22] R. Manica, E. Klaseboer, D.Y.C. Chan, The hydrodynamics of bubble rise nad impact with solid surfaces, Adv. Colloid Interface Sci. 235 (2016) 214–232.
[23] B. Liu, R. Manica, Q. Liu, E. Klaseboer, Z. Xu, G. Xie, Coalescence of bubbles with mobile interfaces in water, Phys. Rev. Let. 122 (2019).
[24] J. Zawala, K. Malysa, Influence of the impact velocity and size of the film formed on bubble coalescence time at water surface, Langmuir 27 (2011) 2250–2257.
[25] J. Zawala, S. Dorbolo, D. Terwagne, N. Vandewalle, K. Malysa, Bouncing bubble on a liquid/gas interface resting or vibrating, Soft Matter 7 (2011) 6719.
[26] E. Manev, R. Tsekov, B. Radoev, Effect of Thickness Non-Homogeneity on the Kinetic Behaviour of Microscopic Foam Film, J. Dispers. Sci. Technol. 18 (1997) 769–788.
[27] D. Langevin, Aqueous foams and foam films stabilised by surfactants. Gravity-free

studies, Comptes Rendus Mec. 345 (2017) 47–55.

[28] J. Zawala, K. Malysa, P.B. Kowalczuk, On importance of external conditions and properties of the interacting phases in formation and stability of symmetrical and unsymmetrical liquid films, Adv. Colloid Interface Sci. 276 (2020) 102085.

[29] J. Zawala, D. Kosior, K. Malysa, Formation and influence of the dynamic adsorption layer on kinetics of the rising bubble collisions with solution/gas and solution/solid interfaces, Adv. Colloid Interface Sci. 222 (2015) 765–778.

[30] V. Ulaganathan, M. Krzan, M. Lotfi, S.S. Dukhin, V.I. Kovalchuk, A. Javadi, D.Z. Gunes, C. Gehin-Delval, K. Malysa, R. Miller, Influence of β-lactoglobulin and its surfactant mixtures on velocity of the rising bubbles, Colloids Surf. A 460 (2014) 361–368.

[31] M. Krzan, J. Zawala, K. Malysa, Development of steady state adsorption distribution over interface of a bubble rising in solutions of n-alkanols (C5, C8) and n-alkyltrimethylammonium bromides (C8, C12, C16), Colloids Surfaces A 298 (2007) 42–51.

[32] J. Zawala, A. Niecikowska, Bubble-on-demand” generator with precise adsorption time control, Rev. Sci. Instrum. 88 (2017) 095106.

[33] A. Wiertel-Pochopien, J. Zawala, Influence of dynamic adsorption layer formation on bubble attachment to quartz and mica surfaces in solutions of pure and mixed surface-active substances, Physicochem. Probl. Mineral Process. 54 (4) (2018) 1083–1094.

[34] M. Krasowska, M. Kolasinska, P. Warszynski, K. Malysa, Influence of polyelectrolyte layers deposited on Mica surface on wetting film stability and bubble attachment, J. Phys. Chem. C 111 (2007) 5743–5749.

[35] B.P. Radoëv, D.S. Dimitrov, I.B. Ivanov, Hydrodynamics of thin liquid films effect of the surfactant on the rate of thinning, Colloid Polymer Sci. 252 (1974) 50–55.

[36] I.B. Ivanov, Effect of surface mobility on the dynamic behavior of thin liquid films, Pure Appl. Chem. 52 (1980) 1241–1262.

[37] I.B. Ivanov, D.S. Dimitrov, P. Somasundaran, R.K. Jain, Thinning of films with deformable surfaces: diffusion-controlled surfactant transfer, Chem. Eng. Sci. 40 (1985) 137–150.

[38] E.V. Aksenenko, Software tools to interpret the thermodynamics and kinetics of surfactant adsorption, 1st ed., Surfactants: Chemistry, Interfacial Properties, Applications vol. 13, Elsevier Science, 2001, pp. 619–648.

Advances in Colloid and Interface Science 317 (2023) 102916

Contents lists available at ScienceDirect

Advances in Colloid and Interface Science

journal homepage: www.elsevier.com/locate/cis

Historical Perspective

Coalescence of surface bubbles: The crucial role of motion-induced dynamic adsorption layer

Jan Zawala [a,b,*], Jonas Miguet [d], Preetika Rastogi [b,c], Omer Atasi [d], Mariusz Borkowski [a], Benoit Scheid [d], Gerald G. Fuller [b]

[a] Jerzy Haber Institute of Catalysis and Surface Chemistry Polish Academy of Sciences, ul. Niezapominajek 8, 30-239 Krakow, Poland
[b] Department of Chemical Engineering, Stanford University, Stanford, CA 94305, USA
[c] Department of Chemical Engineering, Indian Institute of Technology, Chennai 600036, Tamil Nadu, India
[d] TIPs, Fluid Physics Unit, Université Libre de Bruxelles, B-1050 Bruxelles, Belgium

ARTICLE INFO

Keywords:
Bubble
Coalescence
Dynamic adsorption layer
Foam film
Interferometry
Drainage
Direct numerical simulations

ABSTRACT

The formation of motion-induced dynamic adsorption layers of surfactants at the surface of rising bubbles is a widely accepted phenomenon. Although their existence and formation kinetics have been theoretically postulated and confirmed in many experimental reports, the investigations primarily remain qualitative in nature. In this paper we present results that, to the best of our knowledge, provide a first quantitative proof of the influence of the dynamic adsorption layer on drainage dynamics of a single foam film formed under dynamic conditions. This is achieved by measuring the drainage dynamics of single foam films, formed by air bubbles of millimetric size colliding against the interface between n-octanol solutions and air. This was repeated for a total of five different surfactant concentrations and two different liquid column heights. All three steps preceding foam film rupture, namely the rising, bouncing and drainage steps, were sequentially examined. In particular, the morphology of the single film formed during the drainage step was analyzed considering the rising and bouncing history of the bubble. It was found that, depending on the motion-induced state of adsorption layer at the bubble surface during the rising and the bouncing steps, single foam film drainage dynamics can be spectacularly different. Using Direct Numerical Simulations (DNS), it was revealed that surfactant redistribution can occur at the bubble surface as a result of the bouncing dynamics (approach-bounce cycles), strongly affecting the interfacial mobility, and leading to slower rates of foam film drainage. Since the bouncing amplitude directly depends on the rising velocity, which correlates in turn with the adsorption layer of surfactants at the bubble surface during the rising step, it is demonstrated that the lifetime of surface bubbles should intimately be related to the history of their formation.

1. Introduction

The motion of an air bubble in a Newtonian liquid can be divided into two limiting cases. The first case concerns so-called “clean” bubble rising due to gravity in clean liquids, free of surface-active molecules. The second case is encountered in solutions of surface-active species. In the former, the interface of the bubble and the continuous phase (air/liquid interface) is fully mobile leading to a lower viscous drag at the bubble surface as compared to that when surface-active species are present at the bubble interface. The rising velocity in the former case is higher in comparison to a solid sphere of identical size and density [1–5]. Similar to the latter case, it was theoretically shown by Frumkin and Levich [5,6] that the convective-diffusive kinetics, involving adsorption and desorption of surfactant molecules at the bubble surface, leads to a surface concentration gradient on a moving bubble, reducing its surface mobility. This situation is schematically illustrated in Fig. 1A. As a consequence of the bubble motion, the surface concentration of surfactants at the bubble rear pole is higher than the equilibrium value, while the top pole is largely depleted. In other words, the adsorption coverage at the bubble surface increases in the direction opposite to the bubble motion. In a limiting case, the leading part of the bubble can be almost free of surfactant molecules and hence fully mobile, whereas the rear part (so-called rear stagnant cap, RSC) is covered by a compressed adsorption layer and hence immobile [1,2,7–12]. This uneven

---

* Corresponding author at: Jerzy Haber Institute of Catalysis and Surface Chemistry Polish Academy of Sciences, ul. Niezapominajek 8, 30-239 Krakow, Poland.
E-mail address: jan.zawala@ikifp.edu.pl (J. Zawala).

https://doi.org/10.1016/j.cis.2023.102916
Received in revised form 27 April 2023;
Available online 18 May 2023
0001-8686/© 2023 The Authors. Published by Elsevier B.V. This is an open access article under the CC BY-NC-ND license (http://creativecommons.org/licenses/by-nc-nd/4.0/).

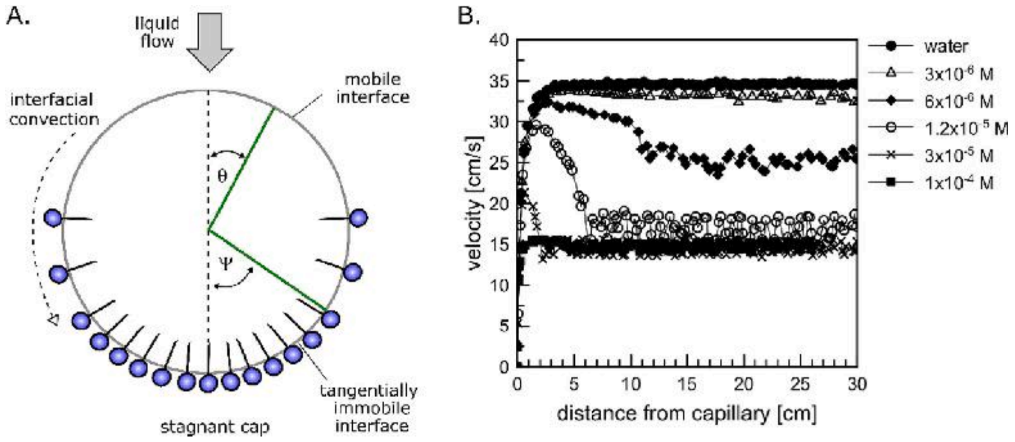

Fig. 1. (A) Dynamic adsorption layer according to the Rear Stagnant Cap (RSC) theory, where Ψ is the polar angle of the RSC, indicating the immobile part of the liquid/gas interface ([9]), (B) local velocity profiles (LVP) for an air bubble of radius 0.74 mm rising in n-octanol solutions of different concentrations (based on data taken from [3]).

distribution of surfactant molecules at the bubble surface leads to Marangoni stresses causing a retardation of the liquid/gas interface mobility, an increased drag coefficient and, consequently, a lower bubble rising velocity. The uneven adsorption layer formed under the above-described dynamic conditions is called the dynamic adsorption layer (DAL) [2,9].

The existence and kinetics of the development of the DAL, as well as the implication of its presence on the stability of liquid foam films once the bubble has collided with the solution/air interface, has been a subject of many theoretical and experimental studies [2,7–10,12–21]. It must however be underlined that all the experimental attempts undertaken so far were qualitative, and no direct evidence has been reported to date. The presence of theoretically postulated motion-induced DAL on the surface of a rising bubble has been confirmed in experiments, where the variations of the rising velocity of a bubble with time or distance traversed in a liquid column were determined [2,9,14,16,22–24]. It is known that the measurements of the bubble local velocity profiles (LVP) offer an insight into the development of the DAL structure and kinetics, which no other technique provides. An example of the LVP determined for n-octanol solutions of different concentrations and bubble of radius 0.74 mm is given in Fig. 1B [3]. It was experimentally observed that after the acceleration stage and before reaching the steady-state conditions (i.e., terminal velocity), the bubble velocity can pass through a maximum, the height and width of which are proportional to the solution concentration [3,4,9,18,25–29]. Next, when steady-state conditions are reached, the bubble rises with a terminal (constant) velocity, which is an indication of the existence of the fully developed DAL structure at its surface. Therefore, it is commonly accepted that the LVP, reflecting the parameters of a single bubble motion, is an indirect measure of the kinetics of the DAL formation [3,6,8,16] and dynamic changes in the drag coefficient. As seen in Fig. 1B for all studied n-octanol concentrations (in the range 3×10^{-6} - 1×10^{-4} M) and the particular bubble radius (0.74 mm), a distance of 15 cm was sufficient for steady DAL establishment [3,4]. The value of this distance, however, increases with the bubble radius [16,30].

The presence of DAL was also confirmed in experiments, where the stability of single foam bubbles [31–34] and wetting [7,14,35,36] films formed by a colliding bubble were assessed. In these experiments, the distance *L* between the bubble formation point (orifice) and the liquid/air or liquid/solid interfaces was adjusted to reflect the different stages of the DAL development at the rising bubble surface before its collision and liquid film formation. Two lengths of liquid columns were used for this purpose (short, where *L* was of the order of few centimeters, and long, with *L* ranging between 15 and 40 cm). It was found that the time of rupture of a single liquid film formed by the colliding bubble was significantly shorter for high values of *L*, despite the fact that a considerable increase in the equilibrium adsorption coverage at the bubble surface was expected since the bubble travelled a longer distance in the liquid column of a higher length *L*. The results suggested that despite the higher coverage, the drainage rate of the liquid film was higher in the longer column. This argument was used as a proof of a higher degree of mobility and the existence of a zone of depleted surfactant concentration at the bubble apex. This experimental argument, however, was based on the measurement of an indirect quantity, namely the lifetime of the bubble at the solution surface. It was supplemented by theoretical calculations using a model assuming wave-induced foam film drainage by Sharma and Ruckenstein [37], with the assumption of a non-uniform adsorption coverage at a liquid/gas interface as described by Ivanov et al. [38]. No experimental evidence of this phenomenon during the time evolution of the liquid film drainage was available to show variations of the bubble interface mobility. Recently, a new interesting experimental method, called "bubble in flow field" was reported [8], which mimics the situation of a rising bubble in surfactant solutions. A bubble was fixed at the capillary tip and the influence of the liquid flow, over the bubble surface, on the dynamic surface tension was determined using a capillary pressure tensiometer. Unfortunately, the experiments did not provide straightforward evidence for the DAL formation because, as the authors concluded, "…the redistribution of pre-adsorbed surfactants does not seem significant or does not lead to a measurable pressure change …". Therefore, the more direct quantitative proof of this phenomenon has not yet been obtained.

In all the experiments aimed at obtaining a direct proof of the DAL presence at a rising bubble surface by assessment of a single foam stability reported in the literature so far, the step of bubble bouncing, occurring after the collision with a solution surface, has been disregarded. It was assumed instead that due to large differences between timescales of bubble bouncing (up to 100–150 ms [39,40]) and foam film drainage formed by the colliding bubble (usually seconds and even minutes for surfactant solutions [41–43]), the bouncing should not significantly affect the DAL structure and, hence, the interfacial mobility. Although not obvious (due to negligible bubble mass), bubble bouncing is a well-established effect, discovered thanks to the use of high-speed videography [44]. The bubble bouncing kinetics at various interfaces has been widely investigated experimentally and theoretically [45–53], to elucidate the bubble coalescence dynamics and hence the mechanism of liquid film rupture. It is commonly accepted that bubble bouncing is a consequence of exchange between the kinetic energy associated with its motion (and accumulated in the liquid phase) and surface energy, which increases at the moment of collision, due to the bubble area enlargement [48,54,55]. Consecutive approach-bounce

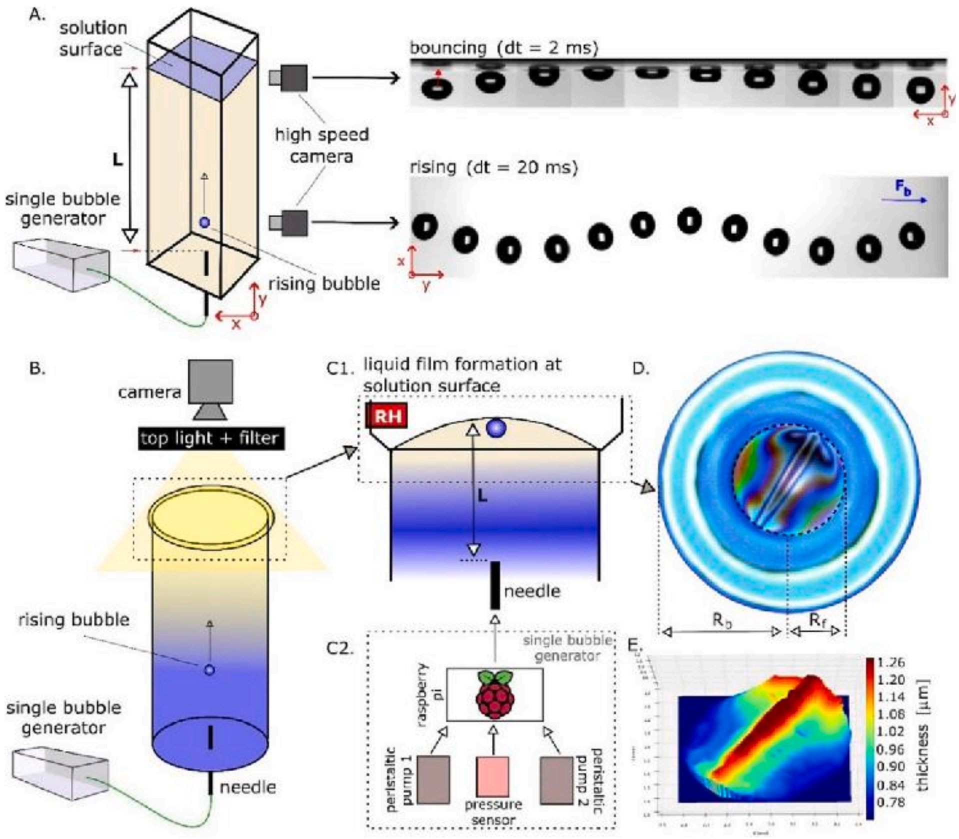

Fig. 2. Schematic illustration of the experimental set-up comprising glass liquid column either with square (A) or circle (B) cross-section, with the needle sealed at the bottom. A single bubble of radius R_b was generated using an automatic single bubble generator (C2). The rising step of the bubble was monitored as a function of distance from the capillary tip using high speed camera (A). Collision of a bubble with the solution surface located at two different distances ($L = 1$ and 40 cm) from the needle tip (A and B) was monitored either by (A) high speed camera to obtain data on the bubble bouncing dynamics and (B) DFI device (top CCD camera with filter) allowing for determination of interference patterns inside the foam film of radius R_f, and its thinning dynamics (D). Post-processed spatial distribution of thickness of the foam film (E). The relative humidity was measured by the RH sensor mounted above the solution surface (C1).

cycles of the bubble, related to this phenomenon, are associated with viscous losses causing a decrease in the bouncing amplitude and eventual capture of the bubble beneath the interface, where a liquid film is formed, and drainage initiates. For pure liquids, this picture was experimentally demonstrated both at liquid/gas and liquid/solid interfaces, where it was shown that supply of the kinetic energy to the system from an external source can cause formation of so-called immortal bubbles, bouncing indefinitely even at the surface of silicone oils of very low surface energy, of pure water or even of highly hydrophobic substrate [40,56–58]. In surfactant solutions, all the experimental and theoretical attempts were related to the investigation of bubble bouncing dynamics by assessment of the so-called restitution coefficient, which compares the rebound and approach velocities [50,59–63]. It was shown that the ability of the bubble to bounce from an interface is related to the degree of fluidity of the two interacting interfaces [64]. Moreover, as reported, due to lower bubble surface mobility, the bubble bouncing amplitude and duration decrease with increasing surfactant concentration and can be practically totally damped above a threshold concentration value, as a results of lower bubble approach speed and surface deformability, related to its immobilization as well as higher viscous dissipation of energy[23,61,65–69]. Increase in the concentration of surfactant in solution causes a decrease in restitution coefficients [70]. Due to lack of sufficient experimental tools for direct estimation of variations in surfactant distribution over the bouncing bubble surface, this important problem remains very poorly examined.

In this work, we present the experimental results on the influence of the distance traversed by a single bubble in a column filled with a surfactant solution (n-octanol - fatty alcohol chosen as a simple model of surface-active agent) on the time-evolution of the thickness of a single foam film formed at a free solution surface. Every step of the bubble's journey, from its creation and detachment to its coalescence at the surface, through the rising, bouncing and thinning steps are characterized experimentally and thoroughly examined. The aim of this paper is to study the influence of the non-homogeneous coverage of surfactants along the rising bubble surface (the DAL) on the drainage of the subsequently formed foam film at the solution surface. In our studies we adapted the experimental approach reported by Jachimska et al. [31,33] and Warszyński et al. [32], and supplement it with independent interferometry measurements, allowing direct determination of a single foam film drainage dynamics (after its formation by a bubble of relatively large size – radius 1.04 mm - and Reynolds numbers ranging between ca. 350–700), with the additional possibility of visualizing the liquid film morphology. Two different release depths for the bubbles have been prescribed, i.e. 1 cm (short column) and 20 or 40 cm (long column), in order to investigate the effect of a presumably different DAL on the bubble bouncing dynamics and liquid film drainage rates. The experimental investigations have been supplemented by Direct Numerical Simulations (DNS) allowing for reproduction of the bubble rising and bouncing steps, and providing valuable informations on the redistributions of surfactants during these steps. Overall, these results provide strong confirmation of the existence of the DAL on the rising bubble interface, which will be used to provide a plausible explanation of our results.

2. Experimental approach

2.1. Integrated set-up

Similar to many other experimental investigations, motion parameters of a single bubble rising and colliding with air/n-octanol solution interfaces were determined by means of video observations and image analysis [12,16,41,71]. Our experimental set-up is presented schematically in Fig. 2A. More details on the measurement methodology as well as algorithms used for determination of a bubble velocity were published elsewhere [22]. Briefly, a single bubble of equivalent radius R_b

was formed at a steel needle tip (inner diameter $d_c = 0.21$ mm) in a liquid column of square cross-section (40 × 40 mm). To maintain controlled release time delays between two successive bubbles (Δt_b), an automated bubble generator, the details of which can be found in [72], was employed. The growth time for a bubble was 100 ms, small enough to avoid full coverage of the interface by surfactants before release (see below) Motion of a single bubble released from the needle tip was monitored at the distance of 20 cm, using side high-speed camera (SpeedCam MacroVis, 100 frames per second). This distance was far enough for a bubble of sufficient size to reach its terminal velocity (steady-state conditions) in all studied cases (see Fig. 4C). Bubble velocities were calculated from the spatial evolution of its geometrical center position in time (considering only the vertical coordinate - $y_c(t)$) by a frame-by-frame analysis of the recorded images (using script written in Python 3.7). Bubble collision with the solution surface was recorded by this same high-speed camera with recording frequency increased to 1000 fps. The bubble dynamics beneath the air/solution interface were determined for two distances (L) covered by the bubble from the moment of its release to the moment of collision, namely: 1 cm (short column) and 20 cm (long column). The distance L was adjusted by tuning the volume of liquid in the column.

Details on materials used in the experiments are provided in Appendix A.

2.2. Dynamic fluid-film interferometry (DFI)

A schematic illustration of the set-up used to determine the drainage dynamics of a single foam film formed by a bubble colliding upon the liquid bath surface is presented in Fig. 2B. Similar to the experiments described above (bubble motion parameters determination), single bubbles of identical equivalent radii R_b (1.04 ± 0.04 mm) were used. The bubble was formed at the needle tip mounted at the bottom of the round glass columns of two different lengths, where the distance (L) covered by the bubble from the moment of its release to the moment of liquid film formation was equal to 1 cm (short column) and 40 cm (long column). According to the rear-stagnant cap theory, after terminal velocity establishment (under steady state conditions) the architecture of the dynamic adsorption layer does not change with the distance travelled by a bubble in solution of soluble surfactants (due to equilibrium between adsorption/desorption processes), therefore similar DAL states (and resultant surface concentrations) could be assumed both for $L = 20$ and $L = 40$ cm. The thinning dynamics of the foam (thin) film of lateral extension R_f was then measured using the Dynamic Fluid-Film Interferometer (DFI), which construction specific details were described elsewhere [73–75] and in the references therein. After its release from the needle tip and free gravity-driven rise in the liquid column, the bubble enventually partially protrudes through the surface, thus forming a thin liquid film (foam film). During the experiments reported in this paper, the original DFI set-up was modified to be suitable for the observation of the interference patterns observed at the surface of the film when appropriately illuminated with white light. In addition, the relative humidity (RH) above the liquid bath was monitored using a RH digital sensor. More details about the DFI procedure and liquid film thickness measurements are given in Appendix A (section A2 and A3).

2.3. Adsorption kinetics

To estimate concentration-dependent adsorption kinetics of n-octanol molecules at the liquid/gas interface, the freely available software developed by E. Aksenenko [76] was applied. The literature data for the parameters of the Frumkin isotherm, given by the following relations [77,78]:

$$bc = \frac{\Gamma\omega}{1-\Gamma\omega}e^{(-2a\Gamma\omega)} \tag{4}$$

Table 1
Literature parameters [22] of the Frumkin adsorption isotherm used in adsorption kinetics calculations.

b [dm^3/mmol]	1.34
ω [m^2/mol]	1.60×10^5
Γ_∞ [mol/cm^2]	6.25×10^{-10}
a	1.0
E_s [kJ/mol]	2.5

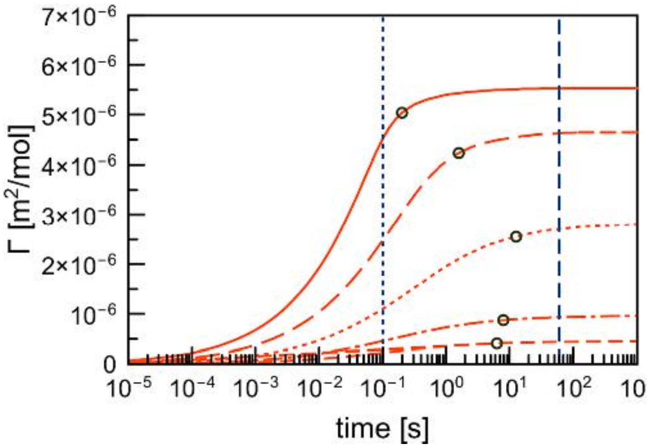

Fig. 3. Variations of calculated surface concentration as a function of time for all studied n-octanol bulk concentrations (short dash line - 5×10^{-5} mol/dm^3, dash-dot line - 1×10^{-4} mol/dm^3, dot line - 2.5×10^{-4} mol/dm^3, long dash line - 5×10^{-4} mol/dm^3, solid line - 1×10^{-3} mol/dm^3) – vertical doted and dashed lines indicate, respectively, the bubble growth time and the minimum equilibration time of the bath surface between each experiment. Points mark the time needed to reach 90% of $\boldsymbol{\Gamma_{eq}}$ value corresponding to the plateau value.

$$\Pi = -\frac{RT}{\omega}\left[ln(1-\Gamma\omega)+a(\Gamma\omega)^2\right] \tag{5}$$

were used in calculations. These parameters are tabulated in Table 1. In Eqs. (4)–(5), Π is the surface pressure, R is the gas constant, T is the temperature, Γ is the surface concentration, ω is the area per one adsorbed molecule in the close-packed monolayer (equal to $1/\Gamma_\infty$), b is the adsorption constant and a is a parameter related to the interaction (with some characteristic energy H_s) between adsorbed molecules, which is proportional to $-H_s/RT$. Using Frumkin isotherm constants and assuming diffusion-controlled adsorption kinetics, the development of the surface concentration at a liquid/gas interface as a function of time was calculated by numerical solution of the Ward-Tordai eq. [77]:

$$\Gamma(t) = 2\sqrt{\frac{D}{\pi}}\left(c_0\sqrt{t} - \int_0^{\sqrt{t}} c(0,t-t')d\sqrt{t'}\right) \tag{6}$$

where t is time, D is the surfactant diffusion coefficient in the solution, c_0 is the surfactant bulk concentration and $c(0,t)$ is the surfactant concentration in the surface sub-layer. The calculations were performed for flat liquid/gas interfaces (the radius of curvature tending towards infinity). The calculation results for all studied n-octanol concentrations, performed for the parameters obtained from Frumkin isotherm (see Table 1) are shown in Fig. 3. The bubble maximum growth time (100 ms) is marked with dotted vertical line. The vertical dashed line indicates minimum time maintained for bath surface equilibration (minimum time interval between bubble rupture and subsequent bubble arrival). Points indicate the time needed to reach 90% of Γ_{eq} ($\Gamma_{t=\infty}$), which we arbitrarily take as representative of an adsorption timescale.

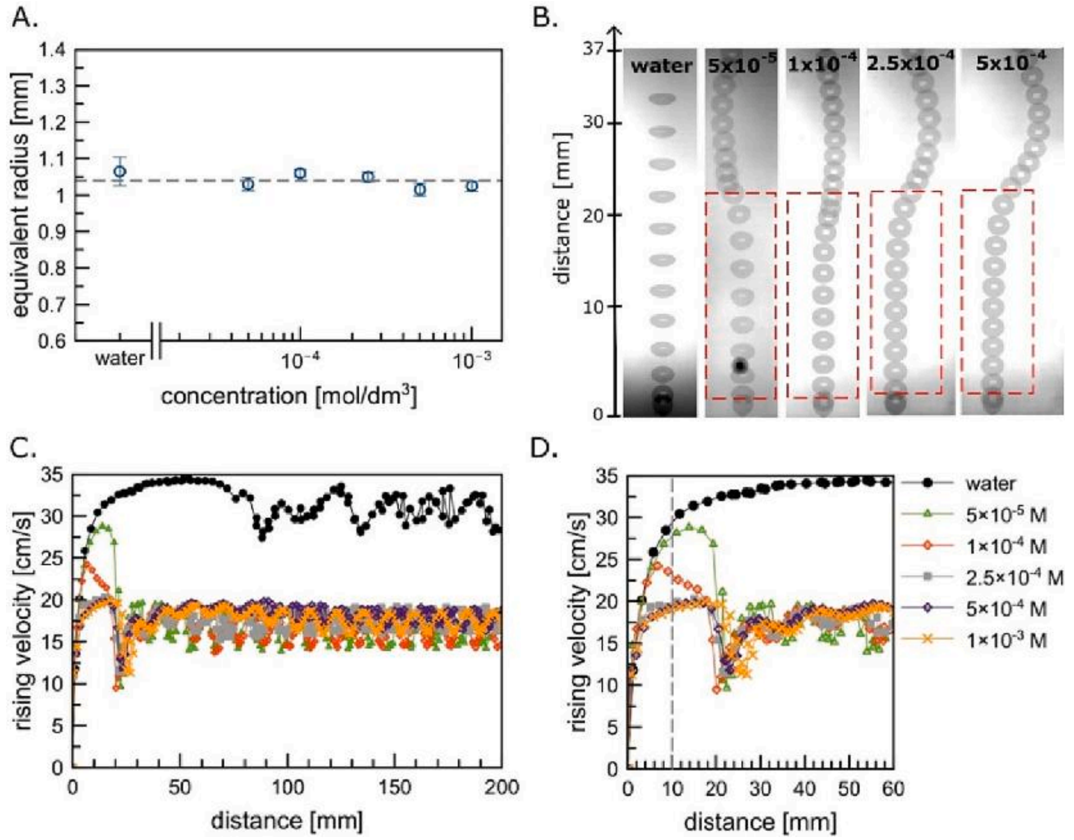

Fig. 4. Data on (A) equivalent radius (R_b) of a rising bubble as a function of n-octanol solution concentration. Bubble snapshots after release from the needle at the origin of the vertical axis) in (B) superimposed by intervals of 10 ms for each full movie frame (37 mm). (C,D) Vertical velocities (y-component) of the rising bubbles as a functions of the distance from the needle tip, showing the acceleration stage (outlined with red dashed line in B), maximum velocity and terminal velocity establishment. (For interpretation of the references to color in this figure legend, the reader is referred to the web version of this article.)

3. Sequential bubble history

3.1. Bubble rising

After release from the needle tip, the bubble accelerates in the liquid. As was previously reported in many papers [2–4,9,79,80], the bubble motion dynamics depend on the concentration of surface-active substances present in an aqueous phase. Fig. 4 presents the data on the motion parameters (local velocity profiles – LVP) of a single bubble observed in our studies. As seen in Fig. 4A, increase in n-octanol concentration did not affect much the R_b values (defined as the radius of the equivalent circle that has a surface area equivalent to the observed bubble), which remained almost constant in all experimental series, essentially because in most of the studies, the generation time (100 ms, see Fig. 3) was faster than the typical adsorption timescale. For the highest concentrations, slight decreases in R_b can be observed due to higher surface concentration, hence lower surface tension. For all cases presented in Fig. 4BCD, a clear bubble acceleration period is observed, magnitude of which determines the value of the bubble maximum velocity. As reported in the literature [3,4,22], the heights and widths of maxima in the LVPs depend on solution concentration. In our case the maxima widths were comparable, while their heights diminished with n-octanol concentration, being the biggest for 5×10^{-5} mol/dm^3, intermediate for 1×10^{-4} mol/dm^3 and the smallest (or even negligible) and almost constant for 2.5×10^{-4}, 5×10^{-4} and 1×10^{-3} mol/dm^3 (compare the areas outlined with red dashed lines in Fig. 4B). It is commonly accepted that the existence of a maximum in the LVP is an indication of formation of the DAL at the bubble surface, where the interface has not been yet immobilized by the surfactant non-uniform distribution and Marangoni effect. Gradual immobilization of the bubble surface starts just before the maximum, beyond which the bubble enters the deceleration stage, which indicates an increase in the hydrodynamic drag (C_D). Maximum C_D values are reached when the bubble starts to rise with the terminal (constant) velocity. It can be seen in Fig. 4CD that the moment of full immobilization of the bubble surface took place after ca. 30–40 mm for all studied n-octanol concentrations, what means that for distances >40 mm, the bubble velocity was stationary. Observed bubble path instabilities (referred sometimes as Leonardo's paradox [81]) have been the subject of many papers reporting experimental [82–86] as well as numerical studies [85,87–89]. As seen in Fig. 4B, the bubbles adopted a zig-zag path, rather than straight line, even in the case of water (after distance > ca. 50 mm). Detailed analysis of this phenomenon is out of the scope of this paper. It is, however, worth highlighting that, according to the analysis done in the literature on the basis of Galilei ($Ga = \rho\sqrt{gR_b}R_b/\mu$) and Bond ($Bo = \rho g{R_b}^2/\sigma$) numbers [88,90], describing the ratio of the gravitational force to the viscous and surface tension forces, respectively, our bubbles should rise in asymmetric and oscillatory regimes [90]. The oscillatory motion, therefore, is consistent with the observations already reported in the literature.

The LVPs given in Fig. 4C justify the column heights chosen to exhibit the effect of the DAL on the bubble once it reached the solution/air interface. Whatever the concentration, any height above 5 cm is enough to recover a constant ascension velocity and therefore, presumably, a steady adsorption layer. On the other hand, when the column height is 1 cm the velocity for the lowest concentrations is not yet steady and therefore the amount of adsorbed surfactants and their distribution are different from the steady velocity case and depend on concentration.

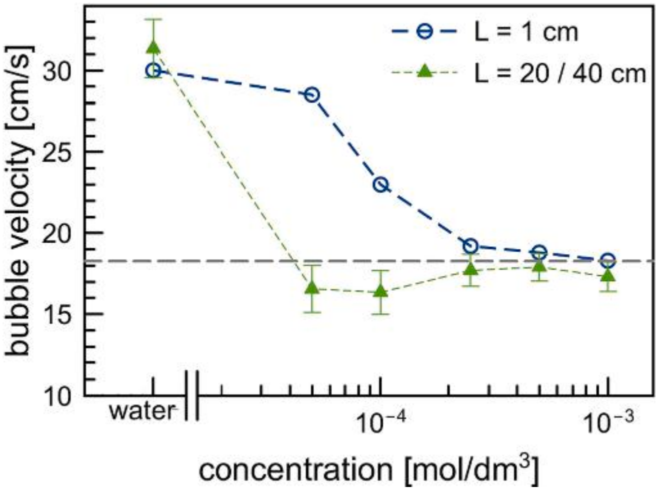

Fig. 5. Bubble velodity at the first collision with the air/liquid interface for the two column heights, as a function of n-octanol concentration.

3.2. *Bubble bouncing*

Because of the presence of maxima at the LVPs, the bubble velocity at the arrival on the surface differs significantly for the short column as compared to the velocity under steady-state conditions for the long column. Fig. 5 directly presents this comparison. As could be already deduced from the data presented in Fig. 4, the most significant difference in velocities at these distances can be observed for the smallest concentrations (5×10^{-5} and 1×10^{-4} mol/dm^3), where the difference between velocity at the $L = 1$ cm and terminal velocity was equal to ca. 12 and 6.5 cm/s, respectively. For higher concentrations, where the maxima at the LVPs were hardly definable (0.25–1×10^{-3} mol/dm^3), there was no such a difference.

It was found that these velocity differences have a profound influence on the colliding bubble bouncing dynamics at the air/solution interface. Fig. 6 presents the time evolutions of the bubble geometrical center position (vertical component y_c) and the bubble velocity during collision at the air/solution interface. The moment of bubble collision was adjusted to match the value of time equal to zero, so negative time values correspond to the bubble approach period. Fig. 6AC present the data for L = 1 cm, while Fig. 6BD for L = 20 cm. Clear differences in bouncing amplitudes and velocities of each subsequent bounce for corresponding concentrations can be observed. Due to significantly higher impact velocities for L = 1 cm, the bubble bouncing amplitudes and resultant velocity variations are the most pronounced for concentrations 5×10^{-5} and 1×10^{-4} mol/dm^3. For L = 20 cm, no significant differences in bouncing amplitudes and velocity changes can be observed for all ranges of the n-octanol concentrations, due to practically identical impact velocities in all cases (see green triangles in Fig. 5).

3.3. *Film drainage*

Time evolutions of the average liquid film thickness determined by means of image analysis for concentrations 5×10^{-5}, 1×10^{-4} and 2.5×10^{-4} mol/dm^3 are presented in Fig. 7. Each data point corresponds to the average of the reconstructed thickness maps (an example is given in Fig. 2D and presented in the Appendix A, section A3). For both column lengths, a repetition of the measurements was made with different bubbles and two different experimentalists to show the good reproducibility of the process ($c = 5 \times 10^{-5}$ M). The thinning dynamics for $L = 1$ cm are only weakly affected by the surfactant concentration, as all curves feature a significant overlap. On the other hand, the $L = 40$ cm case shows intrinsically different behaviors when the concentration is

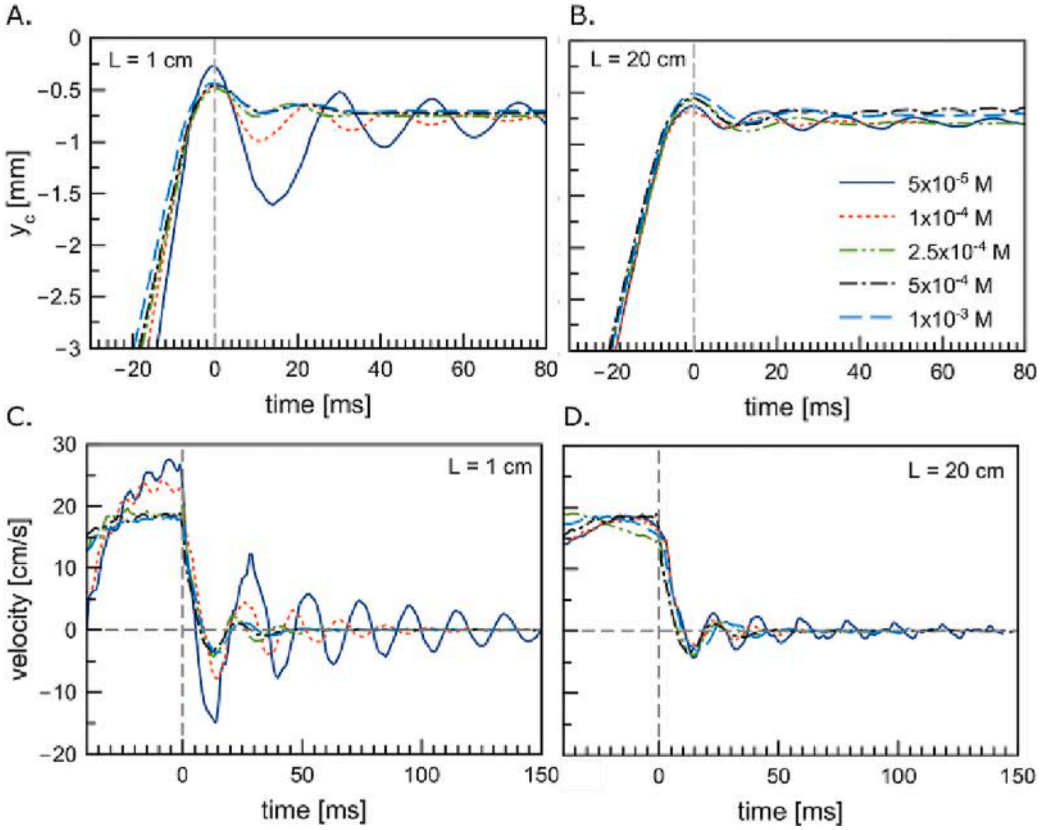

Fig. 6. Variations in the positions of the bubble geometrical center (A, B) and velocity (C, D) as a function of time, during a bubble collision and subsequent bouncing at the air/solution interface for different n-octanol concentrations, for $L = 1$ cm (movies) (A, C) and $L = 20$ cm (B, D) (movies).

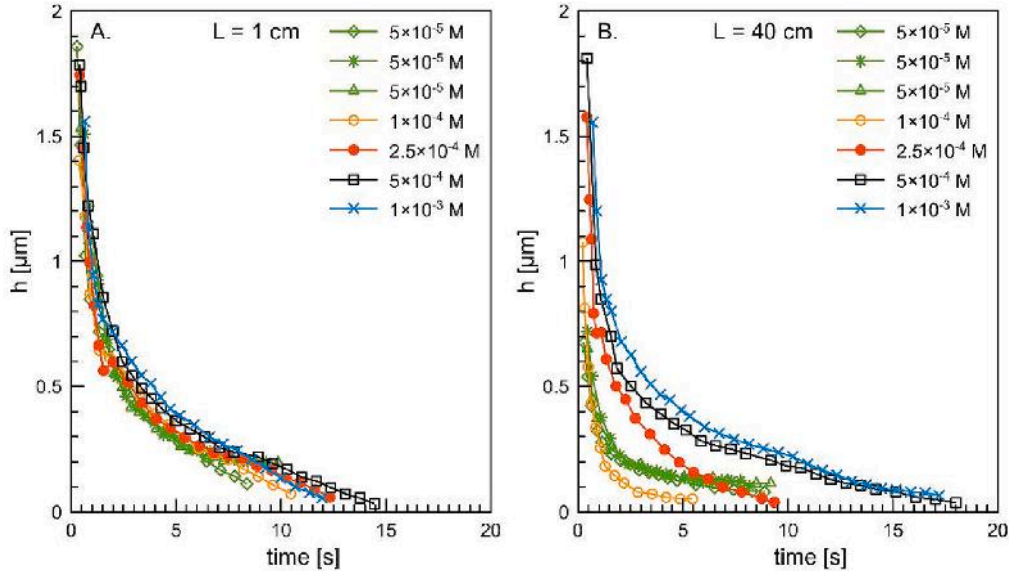

Fig. 7. Time evolution of the foam film thickness for short and long columns.

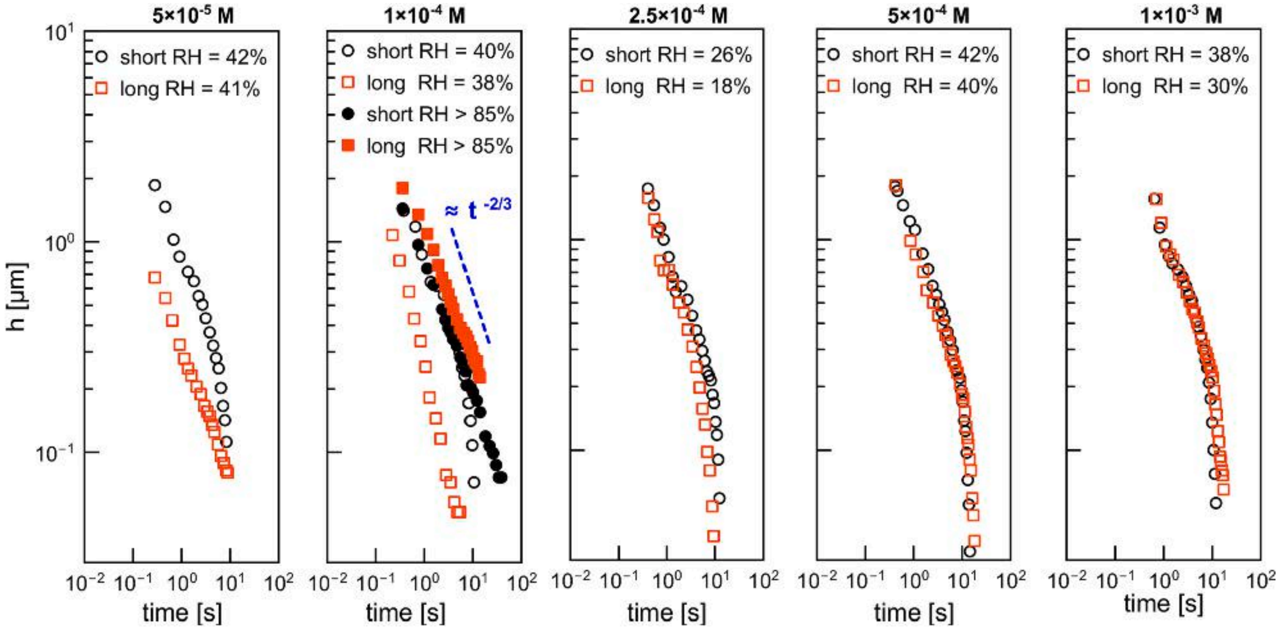

Fig. 8. Log/log representation of thickness measurements as a function of time, for all concentrations and column heights.

changed. In particular, the first measured thickness (the first frame where a clear pattern is observable with DFI) is lower for the two smallest concentrations as compared to the other ones.

Another representation of the thinning data is given in Fig. 8, in logarithmic scales, which compares the thinning behaviors for short and long columns for each concentration. For the three highest concentrations, the thinning dynamics are weakly affected by the column height. This is in line with the fact that the ascension velocity at one centimeter corresponds to the steady rising velocity (Fig. 4) of the system, suggesting that the surfactant concentration distribution is the same for both cases. Correspondingly, the approach velocity is the same for these concentrations (Figs. 4CD and 5) and so are the bouncing dynamics (Fig. 6). On the other hand, for the two smallest concentrations, where significant differences between the approach velocity are recorded at 1 cm and at 40 cm, the thinning dynamics are different in both cases. The first measured thickness is significantly smaller for the long column as compared to the short one, as if the system was ‘shifted’ to smaller thicknesses while featuring somewhat similar thinning dynamics revealing a power-law bahaviour, as will be discussed in the next section. The thinning dynamics were also recorded close to saturation conditions for the relative humidity (by closing the measurement cell) to assess the influence of evaporation.

4. Discussion

4.1. Role of the dynamic adsorption layer

Sequences of experimentally acquired photos of a single foam film at its initial stage of drainage for short and long columns for various n-octanol concentrations and a short qualitative analysis are presented in Appendix A (section A3). An important qualitative outcome of these series of images is that for all experiments we observe thin portions of the film appearing at the bottom of the bubbles and progressively colonizing the entire film. This is reminiscent of the so-called marginal regeneration observed in flat films [91,92] as well as on bubbles [93,94]. These thin film patches arise from the destabilization of the pinch that forms at the connection between the thin spherical cap and the thick meniscus [95]. Its extension is prescribed by the pressure jump between these two zones and determines the magnitude of the pressure gradient that drives the drainage.

Numerous authors have considered the problem of small draining surface bubbles in the presence of surfactants [93,96–98]. By small, we mean that the driving force both for the drainage and the shape of the bubble has a capillary origin. This implies that the bubble has a spherical cap shape beneath the original surface height with an unchanged radius of curvature. The protruding part of the surface bubble, where the thin foam film forms, however, must then have a radius twice as large, since there are two interfaces, to satisfy the equality of the pressure everywhere in the bubble according to: $\frac{4\gamma}{R_{film}} = \frac{2\gamma}{R_b}$. When the film becomes relatively thin, of the order of 1 μm, two contributions must be considered to describe the thinning of the film [99]: the capillary-induced drainage and the evaporation. Lhuissier &Villermaux [93] showed that under experimental conditions similar to our own, the drainage is limited by the existence of a pinch at the transition region between the top of the meniscus that connects the thin film to the bath. This region corresponds to the portion where the capillary pressure gradient between the thin film and the meniscus, that drives the flow, is set. This model provides the best scaling analysis to date to explain the power-law dependence of the thickness to time with an exponent $-2/3$. The data shown in Fig. 8 are all consistent with this dependence of the thickness at early times, as is illustrated with the corresponding slope for $c = 1 \times 10^{-4}$ M. We also observe at later times (this is particularly true at high concentration) a faster thinning regime, which is expected when evaporation starts to overcome the contribution of drainage to the overall thinning of the film. We actually observe this for all experiments far from humidity saturated conditions (the measured relative humidities values RH are given in the legend). The fact that late time thinning is dominated by evaporation is demonstrated for $c = 1 \times 10^{-4}$ M for the short column, when comparing humidity-saturated conditions (RH $>$ 85%) with non-saturation conditions. As seen for RH $=$ 40% the film thickness drops down due to faster evaporation in the late thinning regime, while the film thickness in saturated conditions ($>$ 85%) still follows the power law.

All these considerations suggest a scenario where, rather than impacting the drainage dynamic itself, the DAL presence affects the first instant of the drainage, say the initial thickness of the draining film, that is extremely difficult to access experimentally for the following reasons: (i) when it protrudes through the bath surface, the bubble conserves vibrational motions until the initial kinetic energy is completely dissipated: this renders the focusing of the interferometer complicated, (ii) if, as a crude approximation, we apply a Landau-Levich-Derjaguin model for the initial thickness of the film with an extraction velocity of 0.18 m/s (corresponding to most data, see Fig. 4), we find that the initial thickness is tens micrometers: well beyond the coherence length of visible light and out-of-range for interferometry. This initial thickness is in line with literature data obtained (a few hundreds of milliseconds after protrusion) by measuring the retractation velocity of the hole and applying a Taylor-Culick model to get the thickness [93,99], (iii) the film is still very thick at early times so unlikely to spontaneously burst; manual bursts are doable but not with a good precision and it was only done for $t > 1$ s [99], so the initial draining thickness measurement is not accessible with the Taylor-Culick model.

Describing the whole journey, step by step, first the bubbles are formed and released at the needle tip, which lasts 100 ms. This time scale is short in comparison to the adsorption time scale, so we can consider that small amounts of surfactants are adsorbed at this step. Then, the bubbles rise to the solution surface during a time that scales as $\frac{L}{V_t}$, where $V_t \approx 0.18$ m·s^{-1} is the terminal velocity. The rising time is roughly 60 ms for the short column and >2 s for the long one. During this step, surfactants adsorb onto the surface and are swept towards its bottom as the stagnant cap forms. Next, as the bubble impacts the surface, our measurements show that bouncing occurs only for the short column with the two lowest concentrations: 5×10^{-5} M and 1×10^{-4} M. This is because the velocity of impact, and thus the kinetic energy, is higher in these cases (Fig. 4). These bubbles then experience an inversion of the sense of the flow which should sweep the surfactants towards the bubble apex. We can therefore assume that some surfactants are present in these cases when the thin foam film is formed. On the other hand, when no bouncing occurs, that is, when the impact velocity and the associated kinetic energy are lower (terminal velocity of the rising bubble with fully or at least significantly developed stagnant cap), the upper surface of the bubble, where the foam film is formed, is initially free of surfactant. If the liquid is free of surfactant, no shear occurs on the interfaces and the drainage is expected to be extremely fast. Considering an initial inertia-limited flow, the timescale would be $\sqrt{\frac{\rho R^3}{\gamma}} \sim 10^{-2}$ s. This is contradicted by our experiments since the bubbles live roughly three orders of magnitude longer than this estimate. The DFI images show that there is a pinch at the bottom of the bubbles for all experiments. This pinch was studied theoretically by Aradian et al. [100] in a framework where a no-slip boundary condition was applied (the velocity at the interface is zero). On the other hand, Howell and Stone [101] showed that in the opposite case of a fully mobile film (the shear at the interface is zero), the pinch cannot form because the capillary-driven suction of the fluid is instantaneously transmitted throughout the film. We can argue that (i) if the upper surface of the bubble can be free of surfactant, the free surface, despite its deformation, must be at least partially mobile because marginal regeneration otherwise does not occur, (ii) as the mobile film falls within the meniscus, a local accumulation of surfactants at the bottom of the film leads to a local rigidification of the interface. For these reasons, the necessary quantity of surfactants to obtain a pinch is extremely small but it has a dramatic impact on the system. The model of Lhuissier&Villermaux predicts a lifetime of ~50 s but when accounting for the evaporation, as was done by Poulain et al., we recover timescales in line with the duration of our experiments (~10 s).

The scenario that we propose is therefore that for the three higher concentrations, the adsorption of surfactants is fast enough so that short and long columns present no significant difference. The faster adsorption timescale and rehomogenization of surfactant concentrations on the surface of the newly created thin film led to equivalently fast pinching and therefore equivalent drainage dynamics. On the contrary, for smaller concentrations, significant differences emerge between short and long columns. The long column case features an impact with no bouncing as discussed above. Since the concentrations are small, two arguments plead for a delayed rehomogenization as the new thin film is created: (i) the upper surface of the impacting bubble is full bare at the moment of impact, that is also the moment of the formation of the film (no bounce), (ii) the adsorption rate is lower for lower concentrations, which holds for both interfaces (there is indeed also a depletion of surfactants at the bath surface during the protrusion of the bubble) (iii) the stagnant cap angle on the bubble surface is also smaller for lower concentrations, leading to longer distances to be travelled by the surfactants to reach the thin film region. This delayed rehomogenization supports the scenario that the forming film initially drains without surfactant and therefore without pinch, as for bare bubbles. After few milliseconds, the rehomogenization of the interfaces allows for the formation of the pinch and both marginal regeneration and a dependence $h \propto t^{-2/3}$ are then recovered. Even if this rehomogenization delay only lasts few milliseconds, the drainage being exponential for bare bubbles, it can explain why the first measured thickness with the DFI is approximately twice smaller as compared to essentially all other experiments (see Fig. 8). For the corresponding short-column case, the impact

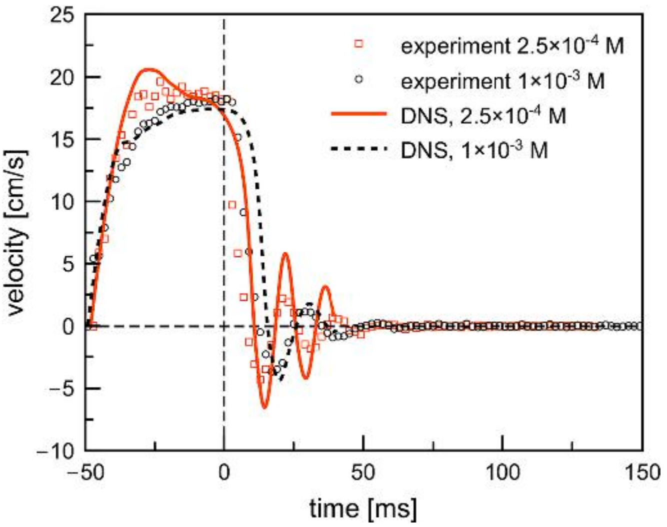

Fig. 9. Result of Direct Numerical Simulations (DNS) of the short-column case for n-octanol concentrations 2.5 × 10^{-4} M and 1 × 10^{-3} M (lines – numerical simulations, points – experimental data).

velocity is significantly higher. Because of the higher kinetic energy of these bubbles, pronounced bounces are observed, which leads to a rehomogenization of the surfactant before the thin film is created. The pinching therefore occurs equivalently faster in these situations as compared to experiments at higher concentration.

4.2. Flow redistribution of surfactants at a bubble surface

To visualize the redistribution of surfactant molecules at a bouncing bubble surface a few numerical simulations were conducted using the same numerical approach than the one presented in [102–104], and summarized in Appendix B. Due to computing limitations, the upper surface was treated as a rigid wall (as if the bath surface were non-deformable and rigidified by the presence of surfactants). The simulation results for the short-column case at 1 × 10^{-3} M and 2.5 × 10^{-4} M are given in Fig. 9 and compare satisfactorily to the experimental results for the velocity of the bubbles as they approach the interface. For 1 × 10^{-3} M, the bounces are very well captured by these simulations, both in terms of the amplitudes (and their damping) and frequency. For 2.5 × 10^{-4} M, the amplitude of the bounces is overestimated, probably because the energy dissipation due to the upper surface deformation is not accounted for (which is more pronounced experimentally in this case because the surface tension is higher for lower concentration). Yet, we consider these simulations as qualitatively representative of the system and we next analyze them in terms of convective transport and

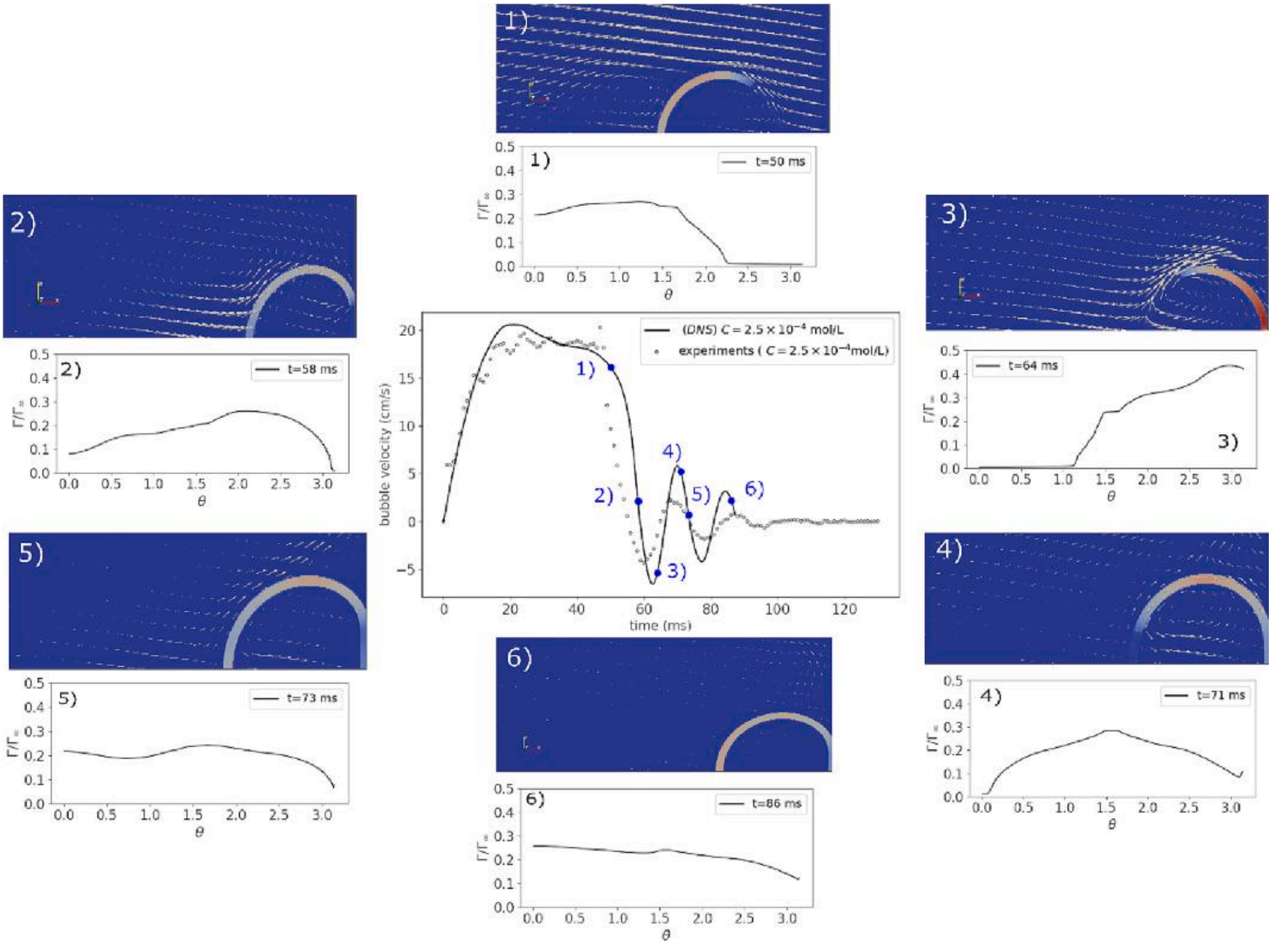

Fig. 10. Close-up on the surfactant distribution along the bubble surface for the n-octanol concentration 2.5 × 10^{-4} M from the simulations obtained on the basis of Direct Numerical Simulations (DNS). The arrows show the velocity field.

surface distribution of surfactants during this process.

Fig. 10 provides the surfactant distribution along the bubble surface for different times. The first one (1) is the moment just before the deceleration due to the presence of the interface. A very clear stagnant-cap-like structure is observed, with a bare interface near the apex and a covered interface everywhere else, i.e. in the cap region. The smaller surface concentration at the rear compared to, say, $\theta = 1.5$ *rad*, is due to the wake structure that creates a stagnation point where surfactants are swept from the back of the bubble (visible in Fig. 10, panel 1). The second time (2) is when the deceleration of the bubble is such that it is already deformed by the upper surface, but the apex is still free of surfactant. The velocity field shows that the upstream flow due to wake inertia is pushing upwards until time (3), where this flow has pushed almost all surfactants to the apex of the bubble. However, at time (3), the bubble is essentially undeformed because of its backwards motion due to the bounce: the final thin film has not emerged yet. On the contrary, (4), (5) and (6) show that, when the thin film is formed after the bubble has bounced, the rehomogeneization of the surfactants caused by the first bounce lead to an instantaneously populated interface, what is in good agreement with the scenario proposed earlier.

5. Conclusions

Systematic quantitative analysis of three steps related to formation and rupture of a single foam film at a solution surface, namely (i) free rise of an air bubble after release from the orifice, (ii) its collision with a liquid/gas interface and bouncing prior to kinetic energy dissipation, and (iii) drainage of a formed liquid film, allows revealing significant influence of the motion-induced adsorption layer at the bubble surface on the foam film drainage. It was undoubtedly proved based on direct interferometric experiments, that, despite longer residence time of the bubble prior to foam film formation in the longer liquid column (ca. 2 s), a film drainage could be faster comparing to the short column (where the bubble residence time prior to formation of the liquid film was equal to 60 ms, only). This indicates differences in the liquid/gas interface mobility causing different film drainage dynamics, related to more uniform adsorption coverage of the bubble colliding with bath surface located close to the needle tip. Comparison of the experimental observations with result of complementary numerical simulations, allowed for reproduction of all the stages of the bubble's journey and revealed that more uniform surface concentration at the top bubble surface in short column during the drainage stage is caused by the rehomogenization of the surfactant molecules before the thin film is formed. This effect is a consequence of bubble bouncing related to higher bubble impact velocity, causing inversion of the liquid flow, which sweeps the molecules towards bubble upper part during every bubble approach/bounce cycle. Using the single foam film as a sensitive tool for probing the liquid/gas interfaces properties, we unveil a new strong confirmation of existence of the DAL at the rising bubble interface, and both qualify and quantify its effect on the fate of surface bubbles.

Supplementary data to this article can be found online at https://doi.org/10.1016/j.cis.2023.102916.

Declaration of Competing Interest

Jan Zawala reports financial support was provided by National Science Centre Poland.

Data availability

Data will be made available on request.

Acknowledgements

J.Z. thanks the Polish National Agency for Academic Exchange for financial support in the frame of the Bekker Programme (PPN/BEK/2020/1/00025/DEC/1). Partial financial support from the NCN Sonata-Bis project No. 2020/38/E/ST8/00173 is gratefully acknowledged. P.R. is grateful for financial sponsorship from the United States-India Education Foundation (USIEF) under the Fulbright Nehru Doctoral Fellowship Program for academic exchange of doctoral candidates. B.S., J.M. and O.A. thank the F.R.S.-FNRS for financial support and the Institut de Mécanique des Fluides de Toulouse for the use of the JADIM code.

Appendix A. Coalescence of surface bubbles: the crucial role of motion-induced dynamic adsorption layer

A.1. Materials

N-octanol (simple fatty alcohol having 8 carbon atoms in a hydrophobic chain), purchased from Sigma Aldrich, was used in all experiments as a surface-active agent (purity ≥99%). Hellmanex III® and Mucasol®, commercially available glass cleaning liquids, were purchased from Sigma Aldrich. Milli-Q water (with a resistivity of 18.2 MΩ·cm) was used for the preparation of n-octanol solutions of various concentrations, ranging from 5×10^{-5} to 1×10^{-3} mol/dm^3 as well as for the final cleaning of all the glass components of the experimental set-up in all conducted experiments.

A.2. Dynamic Fluid-Film Interferometry experiments

The experiments were carried out at room temperature (21 °C ± 1°). To acquire the data on ambient relative humidity (RH), an RH sensor (coupled with the Raspberry Pi) was mounted just above the solution surface, acquiring the RH value every 2 s. The experiments were performed either for the liquid column open to the atmosphere, where the ambient relative humidity was ranging between 20 and 40%, or for the column covered by a glass slide. For covered columns, the experiments were started when the RH > 80%.

To faithfully acquire the interference patterns (by the top IDS camera equipped with the LED illumination and Edmund Optics 457/530/628 nm optical filter), the shape of the upper solution/air interface was kept curved in form of a spherical cap, so that the arriving bubble was self-centered at the apex. To extract the time evolution of the thickness of the foam films, an analysis of the reflection interference data, described in detail in ref. [74] (main text), was performed. A typical DFI image is given in Fig. 2D (main text of the paper). One can see the colored interference fringes that are then analyzed to provide a thickness map of the thin film (Fig. 2E in main text of the paper). This is obtained by observing the bubble vertically from the top. The much larger bubble extension, beneath the surface can also be observed, which is reminiscent of the small Bond number of the system (the radius is small as compared to the capillary length but large enough for a thin film to protrude above the bath surface).

The radius of the liquid film (R_f), defined in Fig. 2D (main text of the paper), formed at the solution surface was calculated as:

$$R_f = \left(\frac{F_b R_b}{\pi\sigma}\right)^{1/2} \tag{1}$$

while the bubble radius (R_b) was calculated according to:

$$R_b = \left(\frac{3}{4}\frac{d_c\sigma}{\Delta\rho g}\right)^{1/3} \tag{2}$$

resulting from balancing buoyancy ($F_b = \frac{4}{3}\pi R_b^3\Delta\rho g$) and capillary forces ($F_c \approx \pi d_c\sigma$), where d_c is the needle tip diameter. The theoretically calculated bubble radius for surface tension $\sigma = 72.4$ mN/m, phases density difference $\Delta\rho = 999$ kg/m^3 and gravity $g = 9.81$ m/s^2 was equal to 1.05 mm. It was found that with MilliQ water, the experimentally determined R_b was equal to 1.04 ± 0.04 mm, i.e. matched perfectly the theoretical value. Moreover, it was found that the average values of the R_f/R_b ratio measured experimentally (image analysis – see Fig. 2D in main text of the paper), were equal to 0.43 ± 0.02 and 0.44 ± 0.04 mm for short and long column respectively, i.e., in perfect agreement with the theoretical predictions calculated according to Eqs. (1)–(2) (using values of surface tension of studied n-octanol solutions). This was a good confirmation that, during the experiments, the whole liquid film area was captured and could be further quantitatively analyzed.

In all experiments, the generation time delay between two successive bubbles (Δt_b), was equal to at least 60 s, and was adjusted according to the bubble lifetime, in order to maintain equilibrium adsorption coverage at the solution surface (i.e. top liquid film interface), which could be disturbed during bubble rupture (coalescence). This time delay was chosen in accordance with the adsorption dynamics of n-octanol described in section 2.3 of the main text. Similarly, the generation time for the bubbles was reduced to 100 ms to be able to consider an initial ‘bare’ condition for the surfactant coverage (concentration of adsorbed surfactants is zero).

A.3. Analysis of time evolution of thickness of single liquid films formed by a bubble

Sequences of experimentally acquired photos (DFI method) of a single foam film at its initial stage of drainage for short and long columns for n-octanol concentration of 1×10^{-4} mol/dm^3 are presented in Fig. A1A and A1B, respectively. The images for comparable drainage times are shown. The color scale bar on the right of the image sequences illustrates the distribution of the film thickness in microns. The bubble/solution surface collision was adjusted for times equal to $t = 0$ s, which corresponds to the first instance where surface deformation is observed on the DFI images. The first image of each sequence corresponds to the moment of appearance of the interference patterns, which were clear enough for reliable image analysis. As a consequence, the sequence (and quantitative results on film thickness shown later in the paper) are shifted by a fraction of second. This short time shift (< 1 s) is related to the bubble collision, bouncing and motion before reaching the curved solution surface apex. For $L = 1$ cm (Fig. A1A) the interference patterns indicate that the drainage is much more homogenous and symmetrical as compared to that at $L = 40$ cm (Fig. A1B).

The effect of column length in film drainage dynamics for n-octanol concentration of 1×10^{-4} mol/dm^3 is illustrated also in Fig. A2, where chosen sequential images from the entire bubble lifetimes are shown for the short (Fig. A2A) and long (Fig. A2B) columns. In addition, spatial distributions of the film thickness obtained from image analysis are provided (bottom sequence for each column length showing the “maps” of thicknesses and illustrating the film topography at the mentioned time instant). As seen, in all cases the drainage of the film is very dynamic with large thickness inhomogeneities. However, as was already discussed above, the interference patterns for $L = 1$ cm are initially more symmetrical. After ca. 4 s they break into more random and complex shapes.

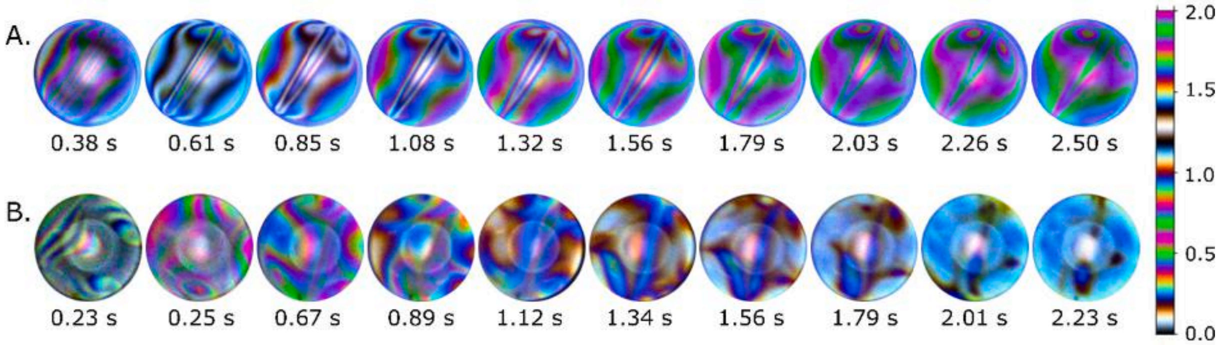

Fig. A1. Sequence of experimentally acquired DFI images of a foam film illustrating initial stage of its drainage in (A) short column and (B) long column at n-octanol solution of concentration 1×10^{-4} mol/dm^3 (see movie in the supplementary material). Values of time from the moment of the bubble collision and liquid film formation are given below each image.

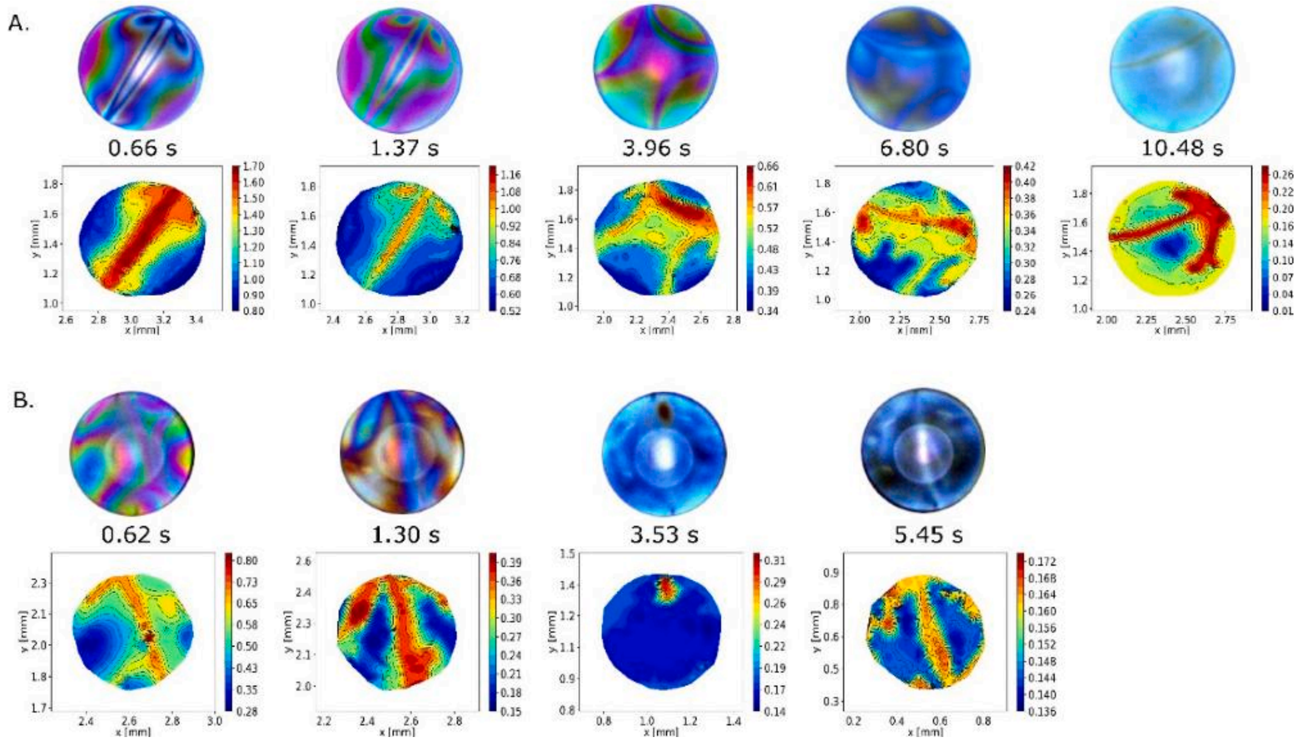

Fig. A2. Sequence of DFI images and corresponding color maps, illustrating spatial distribution of the thickness of a single foam film formed at 1×10^{-4} mol/dm^3 n-octanol solution in (A) short column and (B) long column. Values of time from the moment of the bubble collision and liquid film formation are given below each image.

Similar qualitative analysis for 5×10^{-4} mol/dm^3 n-octanol solution is presented in Fig. A3 for comparison (for $t < 3$ s). In this case, the interference patterns indicate slower drainage for both L values, which seem to be of similar rate. It is to be noted that for $L = 40$ cm, patterns at 5×10^{-4} mol/dm^3 n-octanol concentration are much more symmetrical, compared to the corresponding case in 1×10^{-4} mol/dm^3. Comparison of the last image of each sequence in Fig. A3A and A3B ($t \sim 2.5$ s) with the color scale bar suggests, however, that even at 5×10^{-4} mol/dm^3 n-octanol concentration, drainage rate is a bit higher for $L = 40$ cm. This effect is, however, more subtle compared to the lower concentration (1×10^{-4} mol/dm^3).

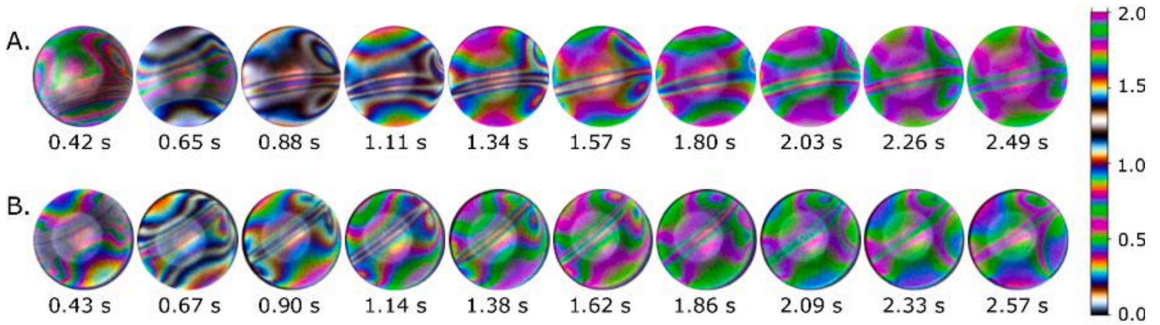

Fig. A3. Sequence of experimentally acquired DFI photos of a foam film illustrating initial stage of its drainage in (A) short column and (B) long column at n-octanol solution of concentration 5×10^{-4} mol/dm^3 (see movie in the supplementary material). Values of time from the moment of the bubble collision and liquid film formation are given below each image.

Appendix B. Coalescence of surface bubbles: the crucial role of motion-induced dynamic adsorption layer

This appendix gives information about the geometry and parameters that were used to obtain the simulation results presented in Figs. 12 and 13 of the main text. It also gives a summary of the numerical method.

B.1. Geometry

The geometry consists of an axi-symmetric bubble at a vertical distance of $L = 5d$ from a solid wall, where $d = 2\ \mathrm{mm}$ is the bubble diameter. At initial time, the liquid contains surfactants at concentration C_0, whereas the bubble surface is clean $\Gamma_0 = 0\ \mathrm{mol/m^3}$.

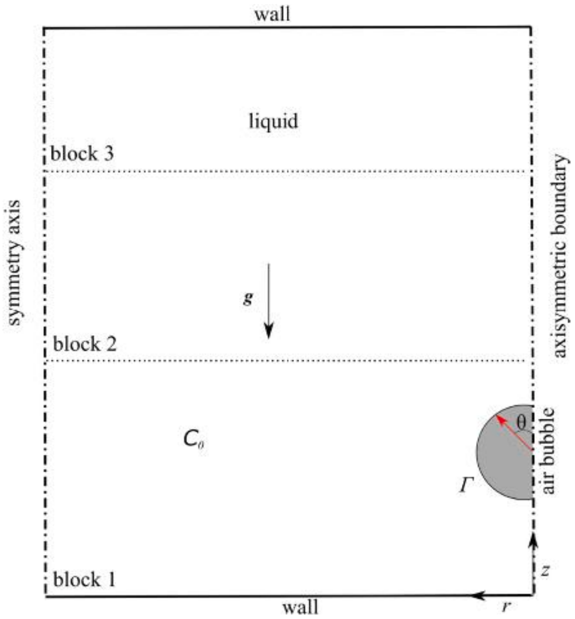

Fig. B1. Schematic of geometry of the computational domain used for the simulation. An initially spherical bubble with a diameter $d = 2$ mm is initialized at a distance of 10 mm from a solid surface. The bubble is immersed in a liquid (aqueous octanol solution) that has an octanol concentration of $\boldsymbol{C_0}$. Gravity is acting downwards. The computational domain is divided into 3 blocks along the *r* and *z* directions. For the sake of clarity, only the blocks along the *z* direction are depicted. The details of each blocks is given in Table 1.

B.2. Computational mesh

The mesh that was retained for the simulation consists of $n_z = 1170$ and $n_r = 400$ cells along the *z* and *r* direction respectively (see Fig. B1). The resolution of the film drainage process requires a fine mesh to resolve the capillary force and viscous stress in the film region. To have a fine mesh in the film region, an arithmetic evolution of the mesh size Δ*z* and Δ*r* was imposed. Practically, the domain was divided into 3 blocks in both the *r* and *z* directions (see Fig. B1). In each block an arithmetic sequence is used to generate the mesh, where the mesh is finer near the upper wall and near the bubble (see Table B1). For instance, for the first block in the *z* direction this gives

$$\Delta z_i = \Delta z_0 + q.i$$

and

$$l_1 = \sum_{i=0}^{i=N} \Delta z_i$$

where Δz_0 is the mesh size in the beginning of block 1 (, 2 or 3), Δz_i is the mesh size of the i'th element in the block and q is the common difference of the arithmetic sequence. Knowing the length of the block, l_1, the minimum value of Δ*z* in the block, Δz_0, and number of computational cells in the block, N_1, the unknown q_1 is deduced and the mesh is built as follows:

$$q_1 = 2\frac{l_1 - N_1\Delta z_0}{N_1(N_1+1)}$$

The parameters of the blocks along the *z* and *r* directions are summarized in Table B1.

Table B1
Details about the mesh used for the computations. The domain was cut into 3 blocks along the *z* and *r* directions respectively (see Fig. 1). Each block was assigned a given length, number of mesh element and a minimum mesh size. Given these parameters, the mesh was build following an arithmetic sequence.

Block number along *z* direction	Length (*l*)	Number of mesh element (*N*)	Minimum mesh size (Δz_0)	Maximum mesh size (Δz_{max})
1	5 mm	243	13.7 μm	27.4 μm
2	4 mm	403	7.1 μm	13.7 μm
3	3 mm	424	7.1 μm	7.1 μm

Block number along *r* direction	Length (*l*)	Number of mesh element (*N*)	Minimum mesh size (Δr_0)	Maximum mesh size (Δr_{max})
1	3.3 mm	194	17.0 μm	17.0 μm
2	3.3 mm	103	30.0 μm	30.0 μm
3	3.3 mm	102	30.0 μm	30.0 μm

B.3. Parameters

The physicochemical parameters used for the simulations are the ones of an aqueous octanol solution (see Table B2). The parameters of the Langmuir adsorption isotherm for this surfactant are summarized in Table B2.

Table B2
Physicochemical properties used for the simulations. The surfactants properties were taken from [B1] and calculated using algorithm described in the section 2.3 of the main text.

Surface tension [mN/m]	Density [kg/m^3]	Viscosity [Pa·s]	Maximum packing concentration [mol/m^2]	Equilibrium adsorption constant [m^3/mol·s]
70	1000	0.001	6.25×10^{-6}	2.4

B.4. The numerical method

Direct numerical simulations were performed by solving the one-fluid formulation of the Navier-Stokes equations coupled with the Level-Set method. We refer the reader to Atasi et al. [B2] and Abadie et al. [B3] for a detailed description of the method and its validation. In short, the Navier-Stokes equations are solved for two Newtonian and incompressible fluids using the finite volume method (second order accuracy in time and space). Continuity is ensured by a projection method, and the capillary contribution is taken into account by the classical continuum surface force method. The position of the interface is followed using the Level-Set method where the transport of the signed distance at the interface is controlled by the redistancing technique. The transport of surfactants in the liquid bulk, at the surface of the bubble and their exchange between the bulk liquid and the surface are solved using an Eulerian formulation of the transport equations [B4]. The Langmuir adsorption isotherm is used to describe the adsorption process and relate surface tension to surface concentration.

B.5. Computational requirements

Simulations were performed on 2 nodes using 72 cores for 3 days.

References

[B1] Chang, Chien-Hsiang, and Elias I. Franses. "Adsorption Dynamics of Surfactants at the Air/Water Interface: A Critical Review of Mathematical Models, Data, and Mechanisms." *Colloids and Surfaces A: Physicochemical and Engineering Aspects* 100 (July 1995): 1–45. doi:https://doi.org/10.1016/0927-7757(94)03061-4.

[B2] Atasi, O., B. Haut, A. Pedrono, B. Scheid, and D. Legendre. "Influence of Soluble Surfactants and Deformation on the Dynamics of Centered Bubbles in Cylindrical Microchannels." *Langmuir* 34, no. 34 (August 28, 2018): 10048–62.

[B3] Abadie, T., J. Aubin, and D. Legendre. "On the Combined Effects of Surface Tension Force Calculation and Interface Advection on Spurious Currents within Volume of Fluid and Level Set Frameworks." *Journal of Computational Physics* 297 (September 2015): 611–36.

[B4] Xu, Jian-Jun, and Hong-Kai Zhao. "An Eulerian Formulation for Solving Partial Differential Equations Along a Moving Interface," Journal of Scientific Computing (December 2003), Vol. 19.

References

[1] Reinhard Miller, Liggieri L. Bubble and drop interfaces. Brill; 2011.

[2] Dukhin SS, Miller R, Loglio G. Physico-chemical hydrodynamics of rising bubble. Stud. Interf. Sci. 1998;6:367–432. https://doi.org/10.1016/S1383-7303(98)80025-2.

[3] Krzan M, Zawala J, Malysa K. Development of steady state adsorption distribution over interface of a bubble rising in solutions of n-alkanols (C5, C8) and n-alkyltrimethylammonium bromides (C8, C12, C16). Colloids Surf. A Physicochem. Eng. Asp. 2007;298:42–51. https://doi.org/10.1016/j.colsurfa.2006.12.056.

[4] Krzan M, Malysa K. Profiles of local velocities of bubbles in n-butanol, n-hexanol and n-nonanol solutions. Colloids Surf. A Physicochem. Eng. Asp. 2002;207: 279–91. https://doi.org/10.1016/S0927-7757(02)00163-2.

[5] Levich VG. Physiochemical hydrodynamcis. Prentice-Hall; 1962.

[6] Frumkin AN, Levich VG. The effect of surface active substances on the motion at liquid interfaces. Zh Fiz Khim 1947;21:1183–204.

[7] Niecikowska A, Zawala J, Miller R, Malysa K. Dynamic adsorption layer formation and time of bubble attachment to a mica surface in solutions of cationic surfactants (C<inf>n</inf>TABr). Colloids Surf. A Physicochem. Eng. Asp. 2010:365: 14–20. https://doi.org/10.1016/j.colsurfa.2010.01.038.

[8] Lotfi M, Bastani D, Ulaganathan V, Miller R, Javadi A. Bubble in flow field: A new experimental protocol for investigating dynamic adsorption layers by using capillary pressure tensiometry. Colloids Surf. A Physicochem. Eng. Asp. 2014; 460:369–76. https://doi.org/10.1016/j.colsurfa.2013.11.011.

[9] Dukhin SS, Kovalchuk VI, Gochev GG, Lotfi M, Krzan M, Malysa K, et al. Dynamics of Rear Stagnant Cap formation at the surface of spherical bubbles rising in surfactant solutions at large Reynolds numbers under conditions of small Marangoni number and slow sorption kinetics. Adv. Colloid Interf. Sci. 2015;222: 260–74. https://doi.org/10.1016/J.CIS.2014.10.002.

[10] Ulaganathan V, Krzan M, Lotfi M, Dukhin SS, Kovalchuk VI, Javadi A, et al. Influence of β-lactoglobulin and its surfactant mixtures on velocity of the rising bubbles. Colloids Surf. A Physicochem. Eng. Asp. 2014;460:361–8. https://doi.org/10.1016/J.COLSURFA.2014.04.041.

[11] Zholkovskij EK, Koval'Chuk VI, Dukhin SS, Miller R. Dynamics of rear stagnant cap formation at low Reynolds numbers. 1. Slow sorption kinetics. J. Colloid Interface Sci. 2000;226:51–9. https://doi.org/10.1006/jcis.2000.6786.

[12] Ulaganathan V, Gochev G, Gehin-Delval C, Leser ME, Gunes DZ, Miller R. Effect of pH and electrolyte concentration on rising air bubbles in β-lactoglobulin solutions. Colloids Surf. A Physicochem. Eng. Asp. 2016;505:165–70. https://doi.org/10.1016/J.COLSURFA.2016.03.059.

[13] Manikantan H, Squires TM. Surfactant dynamics: Hidden variables controlling fluid flows. J. Fluid Mech. 2020:892. https://doi.org/10.1017/jfm.2020.170.

[14] Zawala J, Kosior D, Malysa K. Formation and influence of the dynamic adsorption layer on kinetics of the rising bubble collisions with solution/gas and solution/solid interfaces. Adv. Colloid Interf. Sci. 2015:222. https://doi.org/10.1016/j.cis.2014.07.013.

[15] Palaparthi R, Papageorgiou DT, Maldarelli C. Theory and experiments on the stagnant cap regime in the motion of spherical surfactant-laden bubbles. J. Fluid Mech. 2006;559:1–44. https://doi.org/10.1017/S0022112005007019.

[16] Pawliszak P, Ulaganathan V, Bradshaw-Hajek BH, Manica R, Beattie DA, Krasowska M. Mobile or immobile? Rise velocity of air bubbles in high-purity water. J. Phys. Chem. C 2019. https://doi.org/10.1021/acs.jpcc.9b03526.

[17] Zawala J, Todorov R, Olszewska A, Exerowa D, Malysa K. Influence of pH of the BSA solutions on velocity of the rising bubbles and stability of the thin liquid films and foams. Adsorption 2010;16. https://doi.org/10.1007/s10450-010-9232-3.

[18] Malysa K, Krasowska M, Krzan M. Influence of surface active substances on bubble motion and collision with various interfaces. Adv. Colloid Interf. Sci. 2005;114–115:205–25. https://doi.org/10.1016/J.CIS.2004.08.004.

[19] McLaughlin JB. Numerical simulation of bubble motion in water. J. Colloid Interface Sci. 1996;184:614–25. https://doi.org/10.1006/JCIS.1996.0659.

[20] Liao Y, McLaughlin JB. Bubble motion in aqueous surfactant solutions. J. Colloid Interface Sci. 2000;224:297–310. https://doi.org/10.1006/JCIS.2000.6741.

[21] Clift R, Grace JR, Weber ME. Bubbles, drops, and particles (dover civil and mechanical engineering). 1978. p. 380.

[22] Kosior D, Zawala J. Initial degree of detaching bubble adsorption coverage and the kinetics of dynamic adsorption layer formation. Phys. Chem. Chem. Phys. 2018;20:2403–12. https://doi.org/10.1039/c7cp06099h.

[23] Zawala J, Kosior D, Dabros T, Malysa K. Influence of bubble surface fluidity on collision kinetics and attachment to hydrophobic solids. Colloids Surf. A Physicochem. Eng. Asp. 2016;505:47–55. https://doi.org/10.1016/j.colsurfa.2015.12.023.

[24] Luo Y, Wang Z, Zhang B, Guo K, Zheng L, Xiang W, et al. Experimental study of the effect of the surfactant on the single bubble rising in stagnant surfactant solutions and a mathematical model for the bubble motion. Ind. Eng. Chem. Res. 2022;61:9514–27. https://doi.org/10.1021/acs.iecr.2c01620.

[25] Sam A, Gomez CO, Finch JA. Axial velocity profiles of single bubbles in water/frother solutions. Int. J. Miner. Process. 1996;47:177–96. https://doi.org/10.1016/0301-7516(95)00088-7.

[26] Tan YH, Finch JA. Frother structure-property relationship: Effect of hydroxyl position in alcohols on bubble rise velocity. Miner. Eng. 2016;92:1–8. https://doi.org/10.1016/J.MINENG.2016.02.003.

[27] Tan YH, Rafiei AA, Elmahdy A, Finch JA. Bubble size, gas holdup and bubble velocity profile of some alcohols and commercial frothers. Int. J. Miner. Process. 2013;119:1–5. https://doi.org/10.1016/J.MINPRO.2012.12.003.

[28] Krzan M, Malysa K. Influence of frother concentration on bubble dimensions and rising velocities 2002;36(1):65–76.

[29] Krzan M, Lunkenheimer K, Malysa K. On the influence of the surfactant's polar group on the local and terminal velocities of bubbles. Colloids Surf. A Physicochem. Eng. Asp. 2004;250:431–41. https://doi.org/10.1016/J.COLSURFA.2004.05.022.

[30] Zawala J, Swiech K, Malysa K. A simple physicochemical method for detection of organic contaminations in water. Colloids Surf. A Physicochem. Eng. Asp. 2007;302:293–300. https://doi.org/10.1016/j.colsurfa.2007.02.047.

[31] Jachimska B, Warszynski P, Malysa K. Influence of adsorption kinetics and bubble motion on stability of the foam films formed at n-octanol, n-hexanol and n-butanol solution surface. Colloids and Surfaces A. 2001;192(1–3):177–93.

[32] Warszyński P, Jachimska B, Matysa K. Experimental evidence of the existence of non-equilibrium coverages over the surface of the floating bubblevol. 108; 1996.

[33] Jachimska B, Warszyński P, Malysa K. Effects of motion in n-hexanol solution on the lifetime of bubbles at the solution surface. Progr. Colloid Polym. Sci. 2000;116:120–8.

[34] Borkowski M, Kosior D, Zawala J. Effect of initial adsorption coverage and dynamic adsorption layer formation at bubble surface in stability of single foam films. Colloids Surf. A Physicochem. Eng. Asp. 2020;589:124446. https://doi.org/10.1016/j.colsurfa.2020.124446.

[35] Wiertel-Pochopien A, Zawala J. Rupture of wetting films formed by bubbles at a quartz surface in cationic surfactant solutions. Chem. Eng. Technol. 2019;42:1371–80. https://doi.org/10.1002/ceat.201900003.

[36] Niecikowska A, Zawala J, Malysa K. Influence of n-alkiltrimethylammonium bromided (C8, C12, C16) and bubble motion on kinetics of bubble attachment to mica surface. Physicochem. Probl. Miner. Process 2011;46:237–48.

[37] Sharma A, Ruckenstein E. Effects of surfactants on wave-induced drainage of foam and emulsion films. Colloid Polym. Sci. 1988;266:60–9. https://doi.org/10.1007/BF01451533/METRICS.

[38] Ivanov IB, Dimitrov DS, Somasundaran P, Jain RK. Thinning of films with deformable surfaces: diffusion-controlled surfactant transfer. Chem. Eng. Sci. 1985;40:137–50.

[39] Krzan M, Lunkenheimer K, Malysa K. Pulsation and bouncing of a bubble prior to rupture and/or foam film formation. Langmuir 2003;19:6586–9. https://doi.org/10.1021/LA020919R/ASSET/IMAGES/LARGE/LA020919RF00004.JPEG.

[40] Zawala J. "Immortal" liquid film formed by colliding bubble at oscillating solid substrates. Phys. Fluids 2016:28: 057103. https://doi.org/10.1063/1.4948628.

[41] Gawel D, Zawala J. Stability of liquid films formed by a single bubble and droplet at liquid/gas and liquid/liquid interfaces in bovine serum albumin solutions. ACS Omega 2021;6:18289–99. https://doi.org/10.1021/acsomega.1c02188.

[42] Miguet J, Rouyer F, Rio E. The Life of a Surface Bubble. Molecules 2021;26(5):13172021.

[43] Miguet J, Pasquet M, Rouyer F, Fang Y, Rio E. Stability of Big Surface Bubbles: Impact of Evaporation and Bubbles Size. Soft Matter 2020;16:1082–90. https://doi.org/10.1039/C9SM01490J.

[44] Kirkpatrick RD, Lockett MJ. The influence of approach velocity on bubble coalescence. Chem. Eng. Sci. 1974;29(12):2363–73.

[45] Manica R, Klaseboer E, Chan DYC. The impact and bounce of air bubbles at a flat fluid interface. Soft Matter 2016;12:3271–82. https://doi.org/10.1039/c5sm03151f.

[46] Manica R, Klaseboer E, Chan DYC. Force balance model for bubble rise, impact, and bounce from solid surfaces. Langmuir 2015;31:6763–72. https://doi.org/10.1021/acs.langmuir.5b01451.

[47] Kosior D, Zawala J, Malysa K. Influence of n-octanol on the bubble impact velocity, bouncing and the three phase contact formation at hydrophobic solid surfaces. Colloids Surf. A Physicochem. Eng. Asp. 2014:441: 788–795. https://doi.org/10.1016/j.colsurfa.2012.10.025.

[48] Zawala J, Dabros T. Analysis of energy balance during collision of an air bubble with a solid wall. Phys. Fluids 2013:25: 123101. https://doi.org/10.1063/1.4847015.

[49] Fujasová-Zedníková M, Vobecká L, Vejrazka J. Effect of solid material and surfactant presence on interactions of bubbles with horizontal solid surface. Can. J. Chem. Eng. 2010;88:473–81. https://doi.org/10.1002/cjce.20326.

[50] Zednikova M, Crha J, Vobecká L, Basařová P, Vejrazka J, Tihon J. Collision of bubbles with solid surface in the presence of specific surfactants. Minerals 2021; vol 11:442. https://doi.org/10.3390/MIN11050442.

[51] Suñol F, González-Cinca R. Rise, bouncing and coalescence of bubbles impacting at a free surface. Colloids Surf. A Physicochem. Eng. Asp. 2010;365:36–42. https://doi.org/10.1016/J.COLSURFA.2010.01.032.

[52] Sato A, Shirota M, Sanada T, Watanabe M. Modeling of bouncing of a single clean bubble on a free surface. Phys. Fluids 2011;23:013307. https://doi.org/10.1063/1.3546019.

[53] Manica R, Hendrix MHW, Gupta R, Klaseboer E, Ohl CD, Chan DYC. Effects of hydrodynamic film boundary conditions on bubble–wall impact. Soft Matter 2013;9:9755–8. https://doi.org/10.1039/C3SM51769A.

[54] Tsao HK, Koch DL. Observations of high Reynolds number bubbles interacting with a rigid wall. Phys. Fluids 1997;9:44–56. https://doi.org/10.1063/1.869168.

[55] Canot É, Davoust L, el Hammoumi M, Lachkar D. Numerical simulation of the buoyancy-driven bouncing of a 2-D bubble at a horizontal wall. Theor. Comput. Fluid Dyn. 2003;17:51–72. https://doi.org/10.1007/S00162-003-0096-Y/METRICS.

[56] Zawala J, Dorbolo S, Vandewalle N, Malysa K. Bubble bouncing at a clean water surface. Phys. Chem. Chem. Phys. 2013;15:17324–32. https://doi.org/10.1039/c3cp52746h.

[57] Zawala J, Dorbolo S, Terwagne D, Vandewalle N, Malysa K. Bouncing bubble on a liquid/gas interface resting or vibrating. Soft Matter 2011;7:6719–26. https://doi.org/10.1039/c1sm05365e.

[58] Zawala J, Wiertel A, Niecikowska A, Malysa K. Influence of external vibrations on bubble coalescence time at water and oil surfaces—Experiments and modelling. Colloids Surf. A Physicochem. Eng. Asp. 2017:519:137–145. https://doi.org/10.1016/j.colsurfa.2016.05.054.

[59] Zenit R, Legendre D. The coefficient of restitution for air bubbles colliding against solid walls in viscous liquids. Phys. Fluids 2009;21:083306. https://doi.org/10.1063/1.3210764.

[60] Legendre D, Daniel C, Guiraud P. Experimental study of a drop bouncing on a wall in a liquid. Phys. Fluids 2005;17:097105. https://doi.org/10.1063/1.2010527.

[61] Krasowska M, Krzan M, Malysa K. Bubble collisions with hydrophobic and hydrophilic surfaces in alpha-terpineol solutions. Physicochem. Probl. Miner. Process. 2003;37:37–50.

[62] Legendre D, Zenit R, Daniel C, Guiraud P. A note on the modelling of the bouncing of spherical drops or solid spheres on a wall in viscous fluid. Chem. Eng. Sci. 2006;61:3543–9. https://doi.org/10.1016/J.CES.2005.12.028.

[63] Joseph GG, Zenit R, Hunt ML, Rosenwinkel AM. Particle–wall collisions in a viscous fluid. J. Fluid Mech. 2001;433:329–46. https://doi.org/10.1017/S0022112001003470.

[64] Vakarelski IU, Yang F, Thoroddsen ST. Free-rising bubbles bounce more strongly from mobile than from immobile water-air interfaces. Langmuir 2020;36:5908–18. https://doi.org/10.1021/ACS.LANGMUIR.0C00668/ASSET/IMAGES/LARGE/LA0C00668_0008.JPEG.

[65] Krasowska M, Malysa K. Time scale of the three-phase contact formation by the bubble colling with hydrophobic surface in n-pantenol and n-octanol solutions. Physicochem. Probl. Miner. Process. 2005;39:21–32.

[66] Kowalczuk PB, Zawala J, Kosior D, Drzymala J, Malysa K. Three-phase contact formation and flotation of highly hydrophobic polytetrafluoroethylene in the presence of increased dose of frothers. Ind. Eng. Chem. Res. 2016;55:839–43. https://doi.org/10.1021/acs.iecr.5b04293.

[67] Kosior D, Zawala J, Krasowska M, Malysa K. Influence of n-octanol and α-terpineol on thin film stability and bubble attachment to hydrophobic surface. Phys. Chem. Chem. Phys. 2013:15 :2586–2595. https://doi.org/10.1039/c2cp43545d.

[68] Kosior D, Zawala J, Todorov R, Exerowa D, Malysa K. Bubble bouncing and stability of liquid films formed under dynamic and static conditions from n-octanol solutions. Colloids Surf. A Physicochem. Eng. Asp. 2014:460: 391–400. https://doi.org/10.1016/j.colsurfa.2013.11.022.

[69] Wang S, Guo T, Dabiri S, Vlachos PP, Ardekani AM. Effect of surfactant on bubble collisions on a free surface. Phys. Rev. Fluids 2017;2:043601. https://doi.org/10.1103/PHYSREVFLUIDS.2.043601/FIGURES/8/MEDIUM.

[70] Sharma PK, Dixit HN. Energetics of a bouncing drop: Coefficient of restitution, bubble entrapment, and escape. Phy. Fluids 2020;32:112107.

[71] Borkowski M, Zawala J. Influence of temperature on rising bubble dynamics in water and n-pentanol solutions. Minerals 2021:11: 1067. https://doi.org/10.3390/min11101067.

[72] Zawala J, Niecikowska A. "Bubble-on-demand "generator with precise adsorption time control. Rev. Sci. Instrum. 2017:88: 095106. https://doi.org/10.1063/1.5001846/962889.

[73] Frostad JM, Tammaro D, Santollani L, Bochner de Araujo S, Fuller GG. Dynamic fluid-film interferometry as a predictor of bulk foam properties. Soft Matter 2016;12:9266–79. https://doi.org/10.1039/C6SM01361A.

[74] Chandran Suja V, Kannan A, Kubicka B, Hadidi A, Fuller GG. Bubble coalescence at wormlike micellar solution-air interfaces. Langmuir 2020;36:11836–44. https://doi.org/10.1021/acs.langmuir.0c01861.

[75] Chandran Suja V, Rodríguez-Hakim M, Tajuelo J, Fuller GG. Single bubble and drop techniques for characterizing foams and emulsions. Adv. Colloid Interf. Sci. 2020;286:102295. https://doi.org/10.1016/j.cis.2020.102295.

[76] Fainerman VB, Möbius D, Reinhard Miller. Surfactants: chemistry, interfacial properties, applications661; 2001.

[77] Fainerman VB, Miller R, Aksenenko EV, Makievski AV. Equilibrium adsorption properties of surfactant solutions single and mixed. Studies in Surface Science 2001;13:189–285.

[78] Ward AFH, Tordai L. Time-dependence of boundary tensions of solutions i. The role of diffusion in time-effects. J. Chem. Phys. 2004;14:453. https://doi.org/10.1063/1.1724167.

[79] Ulaganathan V, Krzan M, Lotfi M, Dukhin SS, Kovalchuk VI, Javadi A, et al. Influence of β-lactoglobulin and its surfactant mixtures on velocity of the rising bubbles. Colloids and Surfaces A. 2014;460:361–8.

[80] Kracht W, Finch JA. Effect of frother on initial bubble shape and velocity. Int. J. Miner. Process. 2010;94:115–20. https://doi.org/10.1016/j.minpro.2010.01.003.

[81] Prosperetti A. Bubbles. Phys. Fluids 2004;16:1852–65. https://doi.org/10.1063/1.1695308.

[82] Zenit R, Magnaudet J. Path instability of rising spheroidal air bubbles: A shape-controlled process. Phys. Fluids 2008;20:061702. https://doi.org/10.1063/1.2940368.

[83] Veldhuis C, Biesheuvel A, van Wijngaarden L. Shape oscillations on bubbles rising in clean and in tap water. Phys. Fluids 2008;20:040705. https://doi.org/10.1063/1.2911042.

[84] Tomiyama A, Celata GP, Hosokawa S, Yoshida S. Terminal velocity of single bubbles in surface tension force dominant regime. Int. J. Multiphase Flow 2002;28:1497–519. https://doi.org/10.1016/S0301-9322(02)00032-0.

[85] Ern P, Risso F, Fabre D, Magnaudet J. Wake-induced oscillatory paths of bodies freely rising or falling in fluids44; 2011. p. 97–121. https://doi.org/10.1146/ANNUREV-FLUID-120710-101250.

[86] Tagawa Y, Takagi S, Matsumoto Y. Surfactant effect on path instability of a rising bubble. J. Fluid Mech. 2014;738:124–42. https://doi.org/10.1017/JFM.2013.571.

[87] Herrada MA, Eggers JG. Path instability of an air bubble rising in water. Proc. Natl. Acad. Sci. 2023;120:e2216830120. https://doi.org/10.1073/PNAS.2216830120.

[88] Cano-Lozano JC, Bohorquez P, Martínez-Bazán C. Wake instability of a fixed axisymmetric bubble of realistic shape. Int. J. Multiphase Flow 2013;51:11–21. https://doi.org/10.1016/J.IJMULTIPHASEFLOW.2012.11.005.

[89] Antepara O, Balcázar N, Rigola J, Oliva A. Numerical study of rising bubbles with path instability using conservative level-set and adaptive mesh refinement. Comput. Fluids 2019;187:83–97. https://doi.org/10.1016/J.COMPFLUID.2019.04.013.

[90] Tripathi MK, Sahu KC, Govindarajan R. Dynamics of an initially spherical bubble rising in quiescent liquid. Nat. Commun. 2015:6. https://doi.org/10.1038/ncomms7268.

[91] Mysels Karol J, Frankel Stanley, Shinoda Kozo. Soap Films: Studies of Their Thinning and a Bibliography - Google Books. https://books.google.pl/books/about/Soap_Films.html?id=9OZMAQAAIAAJ&redir_esc=y; 1959 (accessed January 19, 2023).

[92] Seiwert J, Kervil R, Nou S, Cantat I. Velocity Field in a Vertical Foam Film. Phys. Rev. Lett. 2017;118:048001. https://doi.org/10.1103/PHYSREVLETT.118.048001/FIGURES/5/MEDIUM.

[93] Lhuissier H, Villermaux E. Bursting bubble aerosols. J. Fluid Mech. 2012;696:5–44. https://doi.org/10.1017/JFM.2011.418.

[94] Miguet J, Pasquet M, Rouyer F, Fang Y, Rio E. Marginal regeneration-induced drainage of surface bubbles. Phys. Rev. Fluids 2021;6:L101601. https://doi.org/10.1103/PHYSREVFLUIDS.6.L101601/FIGURES/5/MEDIUM.

[95] Shi X, Fuller GG, Shaqfeh ESG. Instability and symmetry breaking of surfactant films over an air bubble. J. Fluid Mech. 2022;953:A26. https://doi.org/10.1017/JFM.2022.888.

[96] Poulain S, Villermaux E, Bourouiba L. Ageing and burst of surface bubbles. J. Fluid Mech. 2018;851:636–71. https://doi.org/10.1017/JFM.2018.471.

[97] Miguet J, Pasquet M, Rouyer F, Fang Y, Rio E. Stability of big surface bubbles: impact of evaporation and bubble size. Soft Matter 2020;16:1082–90. https://doi.org/10.1039/C9SM01490J.

[98] Modini RL, Russell LM, Deane GB, Stokes MD. Effect of soluble surfactant on bubble persistence and bubble-produced aerosol particles. J. Geophys. Res.-Atmos. 2013;118:1388–400. https://doi.org/10.1002/JGRD.50186.

[99] Poulain S, Bourouiba L. Biosurfactants change the thinning of contaminated bubbles at bacteria-laden water interfaces. Phys. Rev. Lett. 2018;121:204502. https://doi.org/10.1103/PHYSREVLETT.121.204502/FIGURES/4/MEDIUM.

[100] Aradian A, Raphaël E, de Gennes PG. "Marginal pinching" in soap films. Europhys. Lett. 2001;55:834. https://doi.org/10.1209/EPL/I2001-00356-Y.

[101] Howell PD, Stone HA. On the absence of marginal pinching in thin free films. Eur. J. Appl. Math. 2005;16:569–82. https://doi.org/10.1017/S095679250500625X.

[102] Atasi O, Haut B, Pedrono A, Scheid B, Legendre D. Influence of soluble surfactants and deformation on the dynamics of centered bubbles in cylindrical microchannels. Langmuir 2018;34:10048–62. https://doi.org/10.1021/ACS.LANGMUIR.8B01805.

[103] Atasi O, Legendre D, Haut B, Zenit R, Scheid B. Lifetime of surface bubbles in surfactant solutions. Langmuir 2020;36:7749–64. https://doi.org/10.1021/ACS.LANGMUIR.9B03597.

[104] Rage G, Atasi O, Wilhelmus MM, Hernández-Sánchez JF, Haut B, Scheid B, et al. Bubbles determine the amount of alcohol in Mezcal. Sci. Rep. 2020;10:1–16. https://doi.org/10.1038/s41598-020-67286-x.

I&EC research
Industrial & Engineering Chemistry Research

Open Access
This article is licensed under CC-BY 4.0

Downloaded via 89.64.56.161 on August 30, 2023 at 10:06:38 (UTC).
See https://pubs.acs.org/sharingguidelines for options on how to legitimately share published articles.

Amino-Acids Surfactants and *n*-Octanol Mixtures—Sustainable, Efficient, and Dynamically Triggered Foaming Systems

Mariusz Borkowski, Piotr Batys, Oleg M. Demchuk, Przemyslaw B. Kowalczuk,* and Jan Zawala*

Cite This: *Ind. Eng. Chem. Res.* 2023, 62, 13498−13509 Read Online

ACCESS | Metrics & More | Article Recommendations

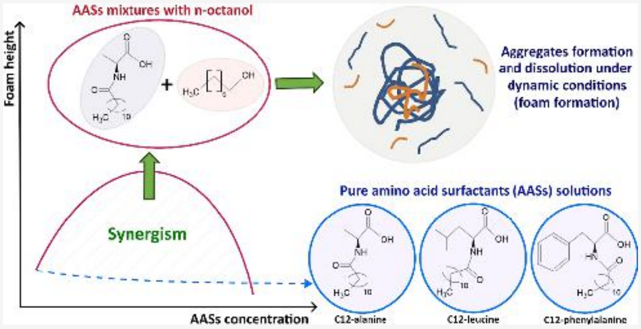
AASs mixtures with n-octanol
Foam height
Aggregates formation and dissolution under dynamic conditions (foam formation)
Synergism
Pure amino acid surfactants (AASs) solutions
AASs concentration
C12-alanine
C12-leucine
C12-phenylalanine

ABSTRACT: Surfactants with amino-acid heads (AASs), namely *N*-lauroyl-L-alanine (C_{12}-ALA), *N*-lauroyl-L-leucine (C_{12}-LEU), and *N*-lauroyl-L phenylalanine (C_{12}-PHE) were mixed with *n*-octanol (C_8OH) and thoroughly investigated via surface tension and foamability experiments. Significant differences between the selected AAS were observed. Moreover, the results obtained under equilibrium and dynamic conditions were remarkably different in terms of surface activity. The surface tension measurements (equilibrium conditions) indicated that the C_{12}-ALA/C_8OH mixture exhibits the highest synergistic effect. For the C_{12}-LEU/C_8OH system, a moderate synergism was observed, while for C_{12}-PHE/C_8OH, the effect was antagonistic. In contrast, in foamability experiments (dynamic conditions), all of the studied AAS/C_8OH mixtures exhibited a spectacular synergistic effect at a wide concentration range. The observed effect was referred to as convection-activated surface activity of AAS/C_8OH mixtures. The obtained experimental results were interpreted on the molecular level via all-atom detail molecular dynamics simulations (MD). The observed phenomenon was connected with the hydrogen bond-mediated aggregate formation in the bulk solution. Such aggregates act as reservoirs of surfactant molecules for supplementation of the adsorption coverage at the freshly formed liquid/gas interface. Additionally, the differences between the specific AAS were explained via the interplay of AAS−AAS and AAS-C_8OH hydrogen bond affinities. The presented results showed an interesting example of a foaming system in which the surface activity can be controlled in situ via convection. This finding also significantly expands the range of potentially interesting molecules that can be used as efficient foaming additives and impacts the current understanding of the role of hydrogen bonding in designing of tuneable surfactant mixtures.

1. INTRODUCTION

Surfactants, also known as surface-active substances (SAS), are a group of compounds with unique properties (e.g., the ability to lower the surface tension) that make them incredibly versatile and useful in a wide range of industrial, technological, and everyday human life applications. Some of the common applications of surfactants are emulsification, corrosion inhibition, wetting, foaming, cleaning, dispersing, and so on.[1−7] However, traditional surfactants are often derived from petroleum or other non-renewable sources and might have a negative impact on the environment and human life.[8] Therefore, there is a growing interest in the potential replacement of toxic petroleum-based surfactants by developing more sustainable surfactant formulations that can meet the needs of various industries while reducing the environmental impact (i.e., green surfactants).[6,8−12]

One of the promising approaches to achieving more sustainable surfactant formulations is the use of mixed surfactants.[13−19] Mixing of two or more different types of surfactants often demonstrates improved surface activity.[20−22] Such systems can exhibit synergistic effects that improve their performance, reduce consumption, and thus minimize waste generation.

However, despite the potential benefits of mixed surfactants, there are also several challenges associated with their use. For example, mixed surfactants can be difficult to synthesize, stabilize, and use effectively in various processes as they can form crystalline precipitates in aqueous solutions.[23−25] In addition, there are often trade-offs between the different properties of mixed surfactants and blends compositions, making it challenging to optimize their use for different applications.[26,27] Therefore, it is important to carefully consider the potential benefits and challenges of mixed surfactants when exploring their use in various applications.

Received: June 12, 2023
Revised: July 25, 2023
Accepted: July 27, 2023
Published: August 17, 2023

ACS Publications
© 2023 The Authors. Published by American Chemical Society

https://doi.org/10.1021/acs.iecr.3c01972

There is a large body of literature on the use of mixed surfactants; however, to the best of the authors' knowledge, no studies have been reported in the literature on the foaming properties of amino-acid surfactants (AASs) mixed with fatty alcohols. AASs are derived from natural amino acids and have a vast number of unique properties (e.g., mildness, biodegradability, low toxicity, good foaming, and stability over wide range of pH) that make them competitive with typical surface-active substances.[2,28−30] One of the key advantages of fatty alcohols is their biodegradability and low toxicity. They can be derived from renewable resources, such as vegetable oils and animal fats, which also makes them a more sustainable alternative to synthetic chemicals.

In this paper, we investigated the foaming properties of three AASs with different hydrophilic heads (amino acids), namely, *N*-lauroyl-L-alanine (C_{12}-ALA), *N*-lauroyl-L-leucine (C_{12}-LEU), and *N*-lauroyl-L phenylalanine (C_{12}-PHE), mixed with *n*-octanol (C_8OH) which is a simple fatty alcohol. First, we examined how the surfactants' type and dose change the surface tension and foamability of the mixed surfactants. Second, we performed MD simulations of the corresponding systems to analyze and understand the phenomenon on the molecular level. Third, we assessed how surfactant dose affected aggregate formation in the bulk of the mixed surfactant systems. Finally, we explained the quite unexpected discrepancy between equilibrium surface tension variations and foamability of mixed AASs/fatty alcohol solutions, defining the so-called convection-induced surface activity, directly related to the bulk aggregation phenomenon.

2. MATERIALS AND METHODS

2.1. Materials. All experiments were carried out in an aqueous solution of the AASs, whose synthesis pathways and detailed adsorption characteristics at the air/solution interface (including molecular dynamic simulations, DFT calculations, and derivation of the adsorption isotherm equation) were presented elsewhere.[31] To study the effect of non-ionic surfactant addition on the AASs solutions' foamability (i.e., foam height and stability), the experiments involved pure AASs solutions as well as blends of AASs with constant amounts of *n*-octanol (simple fatty alcohol with eight carbon atoms in the hydrophobic chain, C_8OH, see Figure 1D). Three AASs with different hydrophilic heads (amino acids), namely, *N*-lauroyl-L-alanine (C_{12}-ALA), *N*-lauroyl-L-leucine (C_{12}-LEU), and *N*-lauroyl-L phenylalanine (C_{12}-PHE), whose structures are shown in Figure 1, were chosen in this study. The AASs were synthesized by the condensation of a proper amino acid with dodecanoyl (lauroyl) chloride, obtained from the reaction of lauric acid with thionyl chloride. The detailed description of the AASs synthesis pathway, their purity analysis, and the crystal structures can be found elsewhere.[31,32] C_8OH (purity > 98%) was purchased from Merck. In two-component solutions, concentration of the chosen AAS, as the solution main component, was changed in a quite broad range, while the concentration of C_8OH (non-ionic additive) was kept constant and equal to either 1×10^{-4} or 5×10^{-4} mol/dm^3.

All solutions used in this study were prepared in ultrapure water (Direct-Q3 UV Water Purification System by Millipore, conductivity < 0.7 μS/cm, surface tension equal to 72.6 mN/m, and temperature equal to 22 ± 1 °C).

Before each experimental series, all glass parts of the laboratory equipment used for solutions preparation and physicochemical tests were washed with a diluted solution of Mucasol—Schülke (commercially available laboratory cleaning liquid) purchased from Sigma-Aldrich and then rinsed thoroughly with a large amount of Milli-Q water.

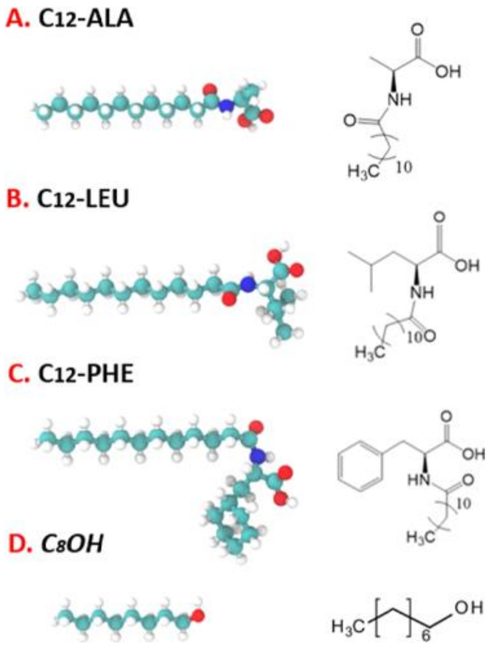

Figure 1. Chemical structure of (A) *N*-lauroyl-L-alanine (C_{12}-ALA), (B) *N*-lauroyl-L-leucine (C_{12}-LEU), (C) *N*-lauroyl-L phenylalanine (C_{12}-PHE), and (D) *n*-octanol (C_8OH).

2.2. Equilibrium Surface Tension Measurements. The equilibrium values of the surface tension for all tested systems (either pure or blended AASs/C_8OH solutions) were determined using a bubble shape method using a PAT-1 tensiometer (SINTERFACE Technologies, Berlin, Germany) with an automatic bubble volume correction algorithm. In these experiments, the surface tension values were determined by analyzing the shape of a submerged bubble attached to a U-shaped needle immersed in a quartz cuvette (25 mL) filled with the studied solution. The estimation of the surface tension was achieved by fitting the Young−Laplace equation to the bubble outline (acquired by a CCD camera) as a function of time. For all experiments, the surface tension was measured for 1 h, and the equilibrium surface tension values were calculated accordingly from the period, where the surface tension values started to be constant in time. All surface tension measurements were carried out at room temperature (22 ± 1 °C).

2.3. Foamability. Foamability and foam stability of pure AASs solutions of various concentrations, as well as their blends with constant C_8OH concentration, were assessed using a Dynamic Foam Analyzer (DFA100, KRÜSS GmbH) apparatus. The apparatus consisted of (i) a cylindrical column, (ii) two parallel electrodes with seven sensors to measure the foam liquid fraction at different heights, and (iii) two vertical rows of photodiodes as light sources (blue—λ = 469 mm) and light scanners for simultaneous automatic measurement of foam (H_f) and solution (H_s) heights as a function of time. The filter paper made of chemically pure cellulose with pore sizes equal to 12−15 μm, mounted at the bottom of the column, was used as an air disperser. In all foaming tests, after mounting the filter paper at the column bottom, the column was placed on the DFA100 stand and filled with 60 mL of the studied solution. The air was pumped through the disperser at

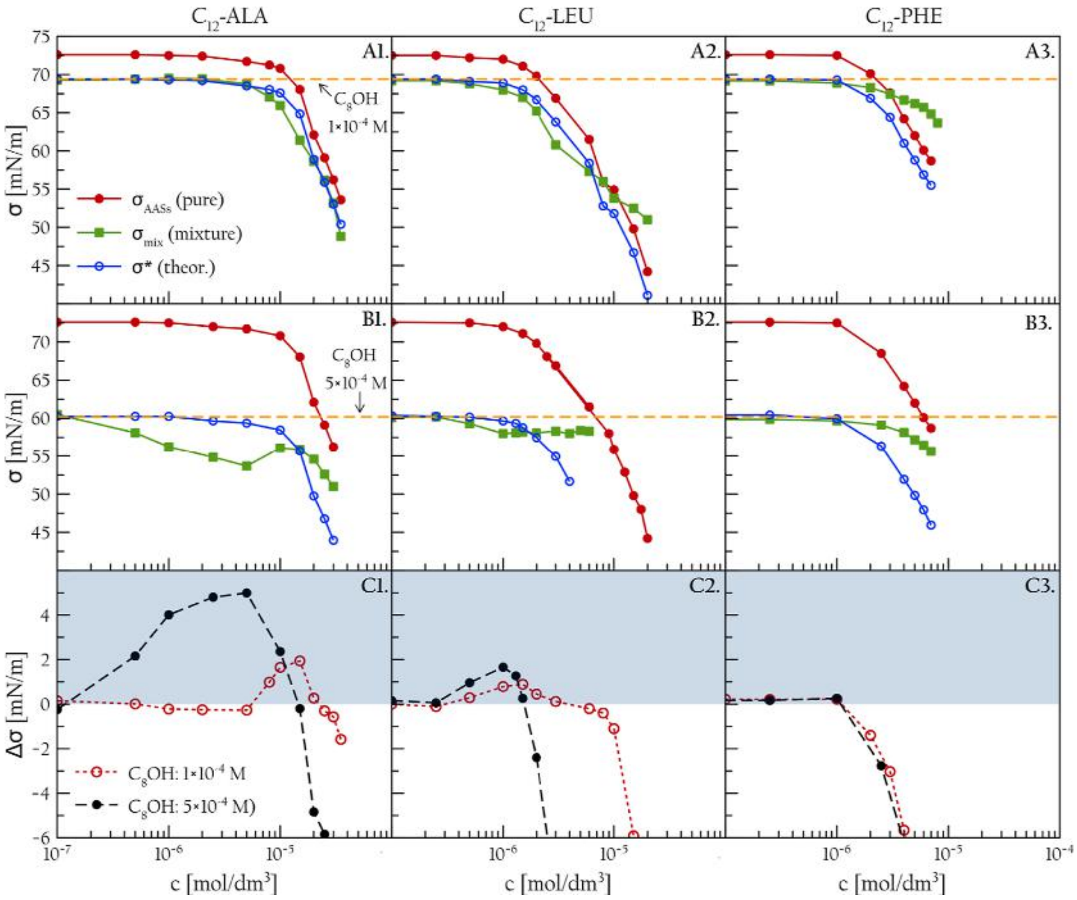

Figure 2. Data on surface tension of AASs solutions, either pure (full red circles) or mixed (green full squares) with two chosen C_8OH concentrations (1×10^{-4}—first row and 5×10^{-4} mol/dm^3—second row, with σ marked as horizontal dashed lines). The third row shows the data on $\Delta\sigma$, calculated according to eq 3.

a flow rate of 0.5 L/min for 60 s, and the H_f and H_s time evolutions, as well as the foam liquid content, were recorded by a PC, employing the ADVANCE software (KRÜSS GmbH). The experiments were carried out at room temperature (22 ± 1 °C).

2.4. Dynamic Light Scattering. Aggregation dynamics and aggregates' hydrodynamic radii were monitored by the dynamic light scattering (DLS) method in a Zetasizer ZS Malvern ZEN 3500 apparatus (with a laser of wavelength 532 nm). The measurements were conducted with the use of standard DLS quartz cuvettes. At least 10 independent runs for the aggregate size distribution determination in all prepared mixed AASs/C_8OH solutions were performed (count rate) in the time range of 36 min, with a time resolution equal to 4 min. Fresh solutions were used in these studies immediately after their preparation (by mixing the proper amounts of pure AASs and pure C_8OH solutions at proper concentrations). Blank tests, consisting of measurements of hydrodynamic radii of aggregates, which could be potentially formed in the one-component AASs and pure C_8OH solutions of concentrations corresponding to the concentrations used later in the mixtures, were also carried out. As discussed later, the blank tests did not reveal any aggregates' presence in the pure solutions.

2.5. Molecular Dynamics Simulations. The Gromacs 2019.2 package,[33,34] with the CHARMM[35] force field, was used for all-atom molecular dynamics (MD) simulations. The system setup and parameters were adapted from Yazhgur et al.[36] The structure and topology of AASs were generated using the CHARMM-GUI web server.[37−39] For C_8OH, the compatible CHARMM general force field was used.[40] For water, the modified TIP3P model of CHARMM was applied.[35,41] To make the simulation systems charge neutral, an adequate number of Br- ions was added. After 200 steps of energy minimization, the systems were simulated for 70 ns, while the first 20 ns were considered the initial equilibration period and disregarded from the analysis.

All MD simulations were run under constant temperature and volume (*NVT* ensemble) conditions. Temperature coupling was controlled via a V-rescale thermostat[42] at a temperature of 298 K and a coupling constant of 0.5 ps. Van der Waals interactions were described by the Lennard-Jones potential, which smoothly shifted to zero between 1.0 and 1.2 nm. The electrostatic interactions were modeled by the PME method,[43] corrected for the slab geometry,[44] with a 1.2 nm cut-off, 0.12 nm grid spacing, and fourth-order splines. Equations of motion were integrated using a leap-frog integration scheme and a 2 fs time step. Bonds involving hydrogen were constrained using the LINCS[45] and SETTLE[46] algorithms. All molecular visualizations employed the VMD software package.[47]

For the simulations, a periodic rectangular simulation box, 8 × 8 × 24 nm^3, consisting of an ~8 nm thick water slab, separated by a vacuum region, was used. Initial configurations were generated using PACKMOL.[48] Monolayers were constructed by randomly placing surfactant molecules into two monolayers at opposite orientations. Surfactant head-

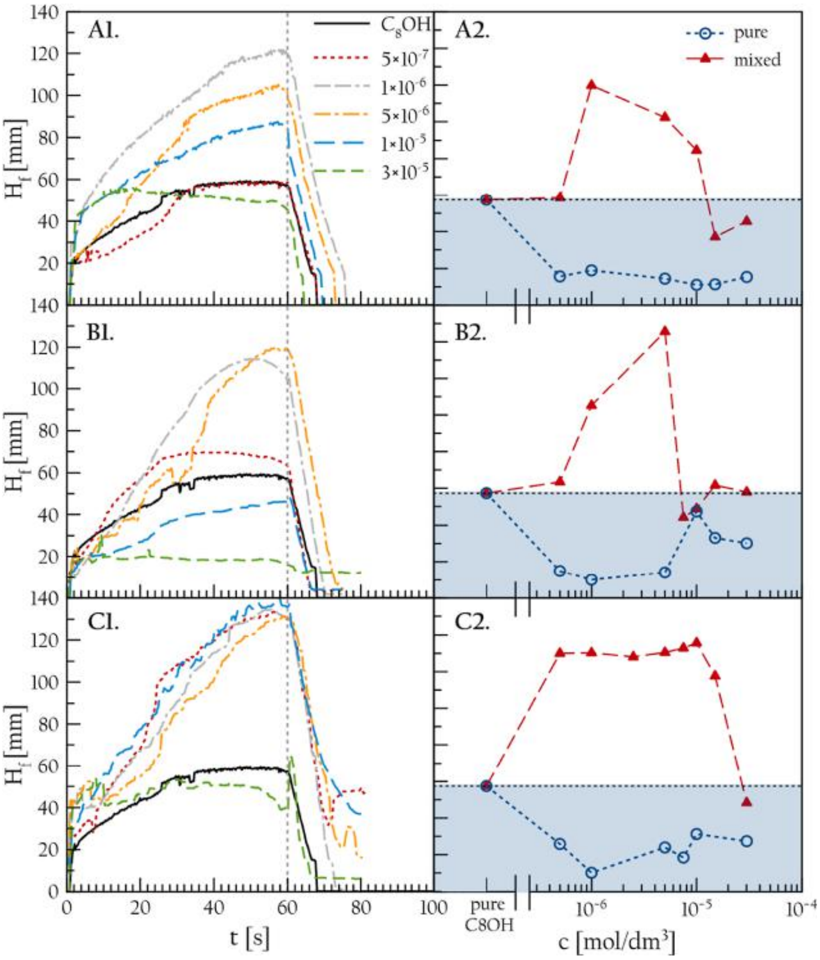

Figure 3. Height of the foam (H_f) as function of time (1) measured for C_8OH (5×10^{-4} mol/dm^3) mixed AASs/C_8OH solutions, and the maximum foam height both for pure and mixed systems after 60 s of gas supply (2) for (A) C_{12}-ALA, (B) C_{12}-LEU, and (C) C_{12}-PHE. In the case of (1), the data for AASs/C_8OH (5×10^{-4} mol/dm^3) mixed solutions are presented. For (2), both pure (hollow squares) and mixed systems (red triangles) are shown (data of figure are available in the open repository—https://doi.org/10.18150/CLCRGT).

groups were oriented toward the water slab, while the angle between the tail and the interface was chosen randomly. Amounts of surfactants on the surface were calculated based on their bulk concentration in pure one-component solutions, according to ref 31. In the case of surfactant mixtures, where their exact surface concentrations were not known experimentally, a simple addition was used as the initial approach.

3. RESULTS

3.1. Equilibrium Surface Tension Results. The data on equilibrium surface tension (σ) as a function of the AAS solution concentrations with and without C_8OH addition are presented in Figure 2. The experimental data for pure AASs solutions are given as full red circles. The corresponding experimental data for the two-component systems (σ_{mix}) are shown as full squares (first row of Figure 2, A1−A3, for AASs/C_8OH blends with a constant C_8OH concentration equal to 1×10^{-4} mol/dm^3; second row, B1−B3, for AASs/C_8OH blends with a constant C_8OH concentration equal to 5×10^{-4} mol/dm^3). For each data set, the σ values of pure C_8OH solutions of two chosen concentrations ($\sigma_{C_8OH}^{1\times10^{-4}} = 69.4 \pm 0.3$ and $\sigma_{C_8OH}^{5\times10^{-4}} = 60.2 \pm 0.1$ mN/m) are given in the corresponding figures as horizontal dashed lines. The third dependence presented in the first two rows of Figure 2 as blue hollow circles illustrates the theoretical surface tension values (σ^*), which would result from the simple summation of the effect of the decrease of surface tension of pure AASs solutions (σ_{AASs}) caused only by the C_8OH addition (with respect to water). The values of σ^* were calculated as

$$\sigma_{H_2O} - \sigma^* = [\sigma_{H_2O} - \sigma_{AASs}(c)] + [\sigma_{H_2O} - \sigma_{C_8OH}^{1\times10^{-4}}] \quad (1)$$

$$\sigma_{H_2O} - \sigma^* = [\sigma_{H_2O} - \sigma_{AASs}(c)] + [\sigma_{H_2O} - \sigma_{C_8OH}^{5\times10^{-4}}] \quad (2)$$

where σ_{H_2O} was taken as 72.6 mN/m.

As seen in Figure 2, addition of C_8OH significantly reduced the AAS solution surface tension, and obviously, this effect is higher for higher concentrations of the non-ionic additive in all studied cases. This surface tension drop, especially for small AAS concentrations, is obvious and was expected as a consequence of a C_8OH molecule excess in the solution.

It can be noticed, however, that the course of the theoretical surface tension values' (σ^*) variations for higher AASs concentrations shows significant discrepancies in comparison to values obtained experimentally for mixed solutions (presented in Figure 2 as green squares). This phenomenon, much smaller and almost negligible in the case of $c_{C_8OH} = 1 \times 10^{-4}$ mol/dm^3, can be very well distinguished for higher C_8OH concentrations (5×10^{-4} mol/dm^3). Although this effect is clearly visible, its magnitude and direction strictly depend on the type of amino acid in the AASs headgroup. As was previously proposed in ref 16, to visualize this effect, the value of $\Delta\sigma$ can be compared for both pure and mixed systems. According to this concept, for all studied AASs, the values of $\Delta\sigma$ were calculated as

$$\Delta\sigma = \sigma^* - \sigma_{\text{mix}} \tag{3}$$

The values of $\Delta\sigma$ are presented in the last row of Figure 2 (C1−C3) for both C_8OH concentrations studied. The physical meaning of the $\Delta\sigma$, after the discussion presented in ref 16, can be interpreted as follows:

- if $\Delta\sigma = 0$, the non-ionic additive (C_8OH) has no effect in the observed variations of the AASs solution surface tension,
- if $\Delta\sigma > 0$, the effect of the solution surface tension decrease is higher than could be expected, indicating the existence of the so-called synergistic effect,
- if $\Delta\sigma < 0$, the solution surface tension decrease is weaker than could be expected, indicating the existence of the so-called antagonistic effect.

The $\Delta\sigma$ analysis performed for cationic/non-ionic binary mixtures of classical surfactants can be used as a very convenient tool for fast and simple estimation of synergistic effect concentration ranges and values of the so-called critical synergistic concentration (CSC), i.e., the maximum concentration for which the synergistic effect is no longer visible (when $\Delta\sigma$ starts to be negative or equal zero). It was shown that the CSC values calculated from $\Delta\sigma$ analysis (CSC_σ) agreed perfectly with the CSC calculated from trends observed in variations of the solutions foamability (CSC_{DFA}) and can be used as a predictor of this important quantity.

As seen in Figure 2C, for the studied system of mixed surfactants, $\Delta\sigma = 0$ can be noticed only for small AASs concentrations. For C_{12}-ALA and C_{12}-LEU in some specific concentration ranges, $\Delta\sigma$ starts to be greater than zero, indicating the existence of a synergistic effect. As a result, the mixed components interact in some specific manner at the air/solution interface, and, as a consequence, the overall surface concentration is higher compared to that of a pure AASs mixture, and the surface tension decrease is strengthened. This effect is much more pronounced for C_{12}-ALA (Figure 2C1) and a higher concentration of C_8OH. For mixed C_{12}-ALA and C_8OH ($c_{C_8OH} = 1 \times 10^{-4}$ mol/dm^3), the synergistic effect is smaller, and its starting point is significantly shifted toward a higher concentration. For C_{12}-LEU, the synergistic effect is similar for both studied c_{C_8OH} with only a slight concentration shift. It can be noticed that for both C_{12}-ALA and C_{12}-LEU, when some specific AASs concentration is exceeded, the synergistic effect disappears. As it was discussed elsewhere, this concentration value corresponds to the so-called CSC.[49] In the case of the C_{12}-PHE surfactant, the overall picture is quite different. After the initial span within which $\Delta\sigma = 0$, the $\Delta\sigma$ value drops around $c_{\text{C12-PHE}} = 1 \times 10^{-6}$ mol/dm^3 and starts to be negative for both C_8OH concentrations, which indicates that the observed effect of C_8OH addition is antagonistic, instead of synergistic. Here, this effect does not depend on the concentration of C_8OH. It is worth highlighting here that both effects assessed based on the analysis of equilibrium surface tension values are rather small. For $c_{C_8OH} = 5 \times 10^{-4}$ mol/dm^3, in the case of C_{12}-ALA and C_{12}-LEU the maximum $\Delta\sigma$ value was equal to ca. 5 and 2.5 mN/m, respectively, while for C_{12}-PHE, it was ca. −8 mN/m.

3.2. Foamability and Foam Stability Analysis.

Since the magnitude of either synergistic or antagonistic effects postulated based on the $\Delta\sigma$ analysis presented above was generally higher for the higher C_8OH concentration used in this study (see Figure 2), the foamability experiments were performed only for mixed solutions with $c_{C_8OH} = 5 \times 10^{-4}$ mol/dm^3. Figure 3 shows the time evolution of the foam height (H_f) in AASs/C_8OH mixed surfactant solutions (Figure 3A1−C1), as well as the maximum foam height ($H_f^{\max}$) taken after 60 s (Figure 3A1−C2), as a function of the concentration of amino acid surfactants. The maximum foam height was read off from the moment when the air supply to the column was stopped (it is marked with a vertical dashed line in Figure 3A1−C1). In Figure 3A2,B2,C2, the full red triangles represent the data taken for mixed systems, while the hollow blue circles represent pure AASs solution. For pure AASs, the foamability was rather poor, and the $H_f^{\max}$ data for these systems (right column of Figure 3, blue circles) correspond to the maximum possible foam height registered during experiments. Furthermore, the mean liquid fraction (ϕ) measured (data not presented) was much higher than the threshold value assumed for the so-called wet (unstable) foams ($\phi > 10\%$).[50,51]

As seen for C_{12}-ALA and C_{12}-LEU solutions, a spectacular increase in foamability in the presence of C_8OH was revealed in some specific AASs concentration ranges. Compared to pure 5×10^{-4} mol/dm^3 C_8OH, the $H_f^{\max}$ in mixed surfactant systems could be even higher than twice. Keeping in mind that the foamability of pure C_{12}-ALA and C_{12}-LEU solutions was almost negligible ($H_f^{\max}$ ca. 20−30 mm), the observed effect is quite spectacular and correlates qualitatively with changes in the solution surface tension (see Figure 2). Surprisingly, for C_{12}-PHE solutions, where, according to the $\Delta\sigma$ analysis, the antagonistic effect for foamability was expected, the $H_f^{\max}$ was even higher, and the evident synergistic effect could be observed for the widest concentration range (between ca. 5×10^{-7} and 2×10^{-5} mol/dm^3). In other words, in this case, the best foamability performance was revealed. It is worth adding that, despite the significant synergistic effect related to the C_8OH presence in AASs solutions and foamability enhancement (in specific concentration ranges determined in Figure 3), the foam stability was quite low. The so-called time of deviation (t_{dev}), allowing foam stability assessment, calculated according to the procedure described in refs 49 and 50 was smaller than 1 s for all AASs surfactants studied (which is a characteristic feature of wet foams).

In contrast to the discussion presented in ref 16, in the case of mixed AASs/C_8OH systems, there is no general quantitative agreement between CSC_σ and CSC_{DFA}, the values of which, read from Figures 2 and 3, are gathered in Table 1. For C_{12}-ALA, the agreement seems to exist, but for C_{12}-LEU, the CSC_σ is smaller than CSC_{DFA} almost by an order of magnitude. For C_{12}-PHE, due to the fact that the $\Delta\sigma$ analysis suggested the existence of an antagonistic effect, the CSC_σ value could not be determined, but the CSC_{DFA} was easily distinguished.

In order to understand the mechanism of such unexpected behavior of the AASs/C_8OH mixtures on the molecular level, molecular dynamic (MD) simulations were performed to provide additional insight into the interfacial properties and adsorption layer architecture.

3.3. MD Simulations.

The experiments revealed that the C_8OH addition significantly enhances the foamability of AASs

Table 1. Values of the Critical Synergistic Concentrations Determined from Adsorption Isotherms (CSC_σ) and Foamability Tests (CSC_{DFA})

AASs	c_{C_8OH} [M]	CSC_σ [M]	CSC_{DFA} [M]
C12-ALA	1×10^{-4}	2.2×10^{-5}	
	5×10^{-4}	1.4×10^{-5}	1.3×10^{-5}
C12-LEU	1×10^{-4}	3.8×10^{-6}	
	5×10^{-4}	1.6×10^{-6}	9.3×10^{-6}
C12-PHE	1×10^{-4}	N/A	
	5×10^{-4}	N/A	2.1×10^{-5}

solutions in certain AASs concentration ranges, despite quite different adsorption performances of surfactants molecules at the solution/gas interface, assessed from the surface tension analysis. To analyze and understand this phenomenon on the molecular level, MD simulations of the corresponding systems were performed. The mixed surfactant systems, i.e., C_{12}-ALA, C_{12}-LEU, and C_{12}-PHE, with various C_8OH concentrations, were simulated at the liquid/gas interface. The changes in the surface tension as a function of the number of surfactants at the interface are presented in Figure 4. It should be mentioned that the surface tension of pure water determined for the TIP3P model is slightly different than the experimental value. Therefore, to enable comparison with experiments, the surface tensions for all systems were normalized by the value obtained

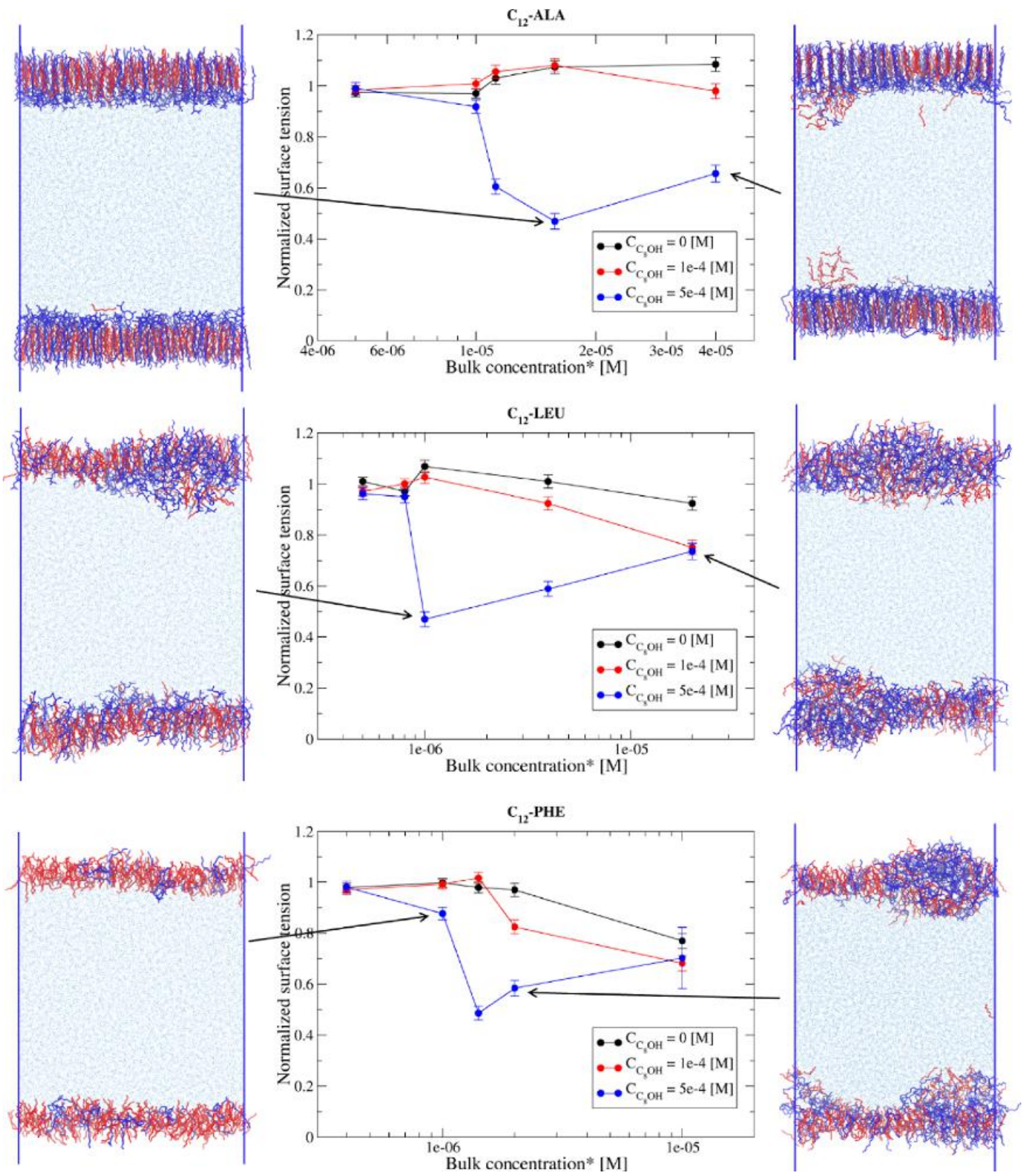

Figure 4. Normalized surface tensions for surfactants as a function of their concentration and C_8OH addition, determined from MD simulations. The snapshots correspond to the final configurations of the systems marked with arrows. In all snapshots, the C_8OH and AASs molecules are marked in red and blue, respectively.

for TIP3P water. The snapshots presented in Figure 4 represent the final structures of the selected systems. For all studied surfactants, at the highest C_8OH concentration, the normalized surface tension exhibits a minimum. A similar effect was also observed experimentally, especially in foamability experiments. However, when comparing the MD data with the equilibrium surface tension measurements, the agreement is only visible for C_{12}-ALA. It should be noted here that the amounts of specific surfactants at the interface used in the simulations were calculated based on the molecule surface concentration measured experimentally for pure one-component solutions separately, at various bulk concentrations. In the case of surfactant mixtures, the exact amounts were not known, and simple addition was used. This can lead to some discrepancies between the simulations and experimental observations.

Nevertheless, MD simulation can provide a reasonable molecular origin of the observed synergistic effect. For pure AASs, as well as at low C_8OH concentrations, no minimum in the surface tension was observed, which agrees with the experimental data (see Figure 2). At higher C_8OH concentrations, the interface seems to be overpacked with the surfactants. In contrast to the CTAB/C_8OH mixed surfactant systems, where the increase in the number of surfactants leads to a more ordered monolayer, in the case of AASs, the surfactants tend to aggregate in micelles (see snapshots in Figure 4). For some systems, e.g., C_{12}-ALA, the micelles diffuse toward the bulk solution. The minimum in surface tension is therefore observed for the highly packed monolayers, obtained at high concentrations of C_8OH and moderate concentrations of the AASs. Further increase in the AASs concentration can induce micelle formation, and the monolayer itself becomes less organized.

To better understand the behavior of the AAS surfactants, the number of hydrogen bonds between the AAS−AAS and AAS-C_8OH in the systems with a higher C_8OH concentration was calculated. For the sake of comparison, the number of hydrogen bonds was normalized by the number of AAS molecules in the systems and plotted as a function of their surface concentration (Γ_{AAS}) (see Figure 5). As can be seen, the hydrogen bonds are present in all systems, in contrast to the previously studied CTAB/C_8OH systems. Therefore, the first conclusion, which could be drawn, is that introducing additional interactions in the system, i.e., hydrogen bonding, might disturb the surfactant ordering in the monolayer in comparison to systems without hydrogen bonds (e.g., CTAB/C_8OH). The number of hydrogen bonds formed between surfactants can also explain the differences observed between AASs with various amino acid headgroups. The AAS-C_8OH hydrogen bond formation affinity decrease is C_{12}-ALA > C_{12}-LEU > C_{12}-PHE. This reflects the interaction strength between AAS and C_8OH and therefore the stability of such mixtures at the interface. C_{12}-ALA, together with C_8OH, due to their strong hydrogen bonding interactions, can be expected to form a relatively stable interfacial monolayer. This is reflected by the equilibrium surface tension experiments via strong synergistic effect observed for C_{12}-ALA. Such effect is less pronounced in the case of C_{12}-LEU and almost disappears for C_{12}-PHE.

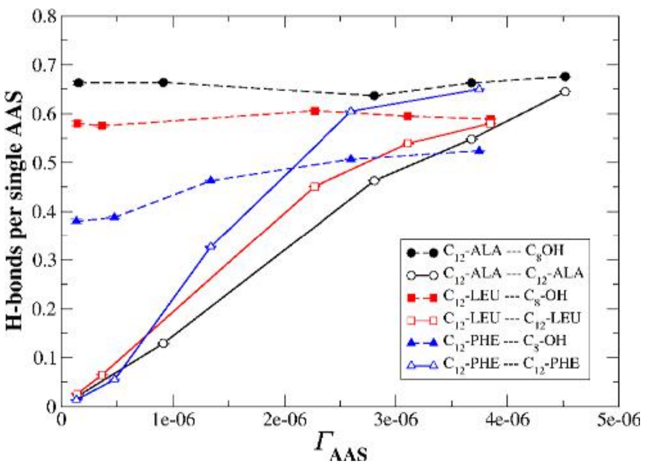

Figure 5. Number of hydrogen bonds per single AAS molecule as a function of its surface concentration (Γ_{AAS} [mol/m^2]). The C_8OH concentration equals 5×10^{-4} mol/dm^3.

Moreover, significant differences can be observed in AAS−AAS hydrogen bonding (Figure 5). The hydrogen bond formation affinity between the AAS molecules decreases as follows: C_{12}-PHE > C_{12}-LEU > C_{12}-ALA. This finding is in line with the dimerization enthalpies, previously determined for these surfactants.[31] Also, only for C_{12}-PHE, the number of AAS−AAS hydrogen bonds is larger than that of AAS-C_8OH hydrogen bonds for moderate and high surface concentrations (Γ_{AAS}). This suggests that C_{12}-PHE prefers to be surrounded by other C_{12}-PHE molecules rather than C_8OH. Therefore, its ability for micelle formation should be the strongest.

Considering the differences in hydrogen bonding as well as the observed initial micelle formation (Figure 4), one can conclude that if the micelles are present in the system, their formation will be driven by hydrogen bond interaction. Considering that C_8OH molecules do not form hydrogen bonds with themselves, one can expect that the micelles will be rich in AAS surfactants. At the same time, the interfacial layer would be AAS-depleted, where the degree of depletion would be related to the amino acid headgroup type, i.e., less depleted for C_{12}-ALA and the most depleted for C_{12}-PHE. This explains well the experimental observations from the equilibrium surface tension measurements, where the synergistic effect is visible for C_{12}-ALA but not for C_{12}-PHE.

However, it is also interesting to understand what triggers the synergistic effect during the foamability experiments. Contrary to the measured equilibrium surface tensions, the surface tensions calculated from MD simulations (Figure 4) clearly indicate that if both AAS and C_8OH molecules are present in the interfacial layer, their surface tension should decrease. Such discrepancy between the surface tensions measured experimentally and via MD can be related to the fact that the amounts of surfactants in MD simulations are fixed, so the above-mentioned depletion effect of ASS in the interfacial layer, suggested to occur in equilibrium experiments, cannot be accurately accounted for in MD. Therefore, one can expect that the foamability process itself, via constant mixing and new interface formation, enriches the interfacial layer in AAS surfactants.

Overall, based on the MD simulations results, one can conclude that under these experimental conditions, the shift in the CSC and the presence of micelles in the solution can be expected for all AASs at moderate and high bulk concentrations.

3.4. Examination of Aggregation Effect.

The MD simulations suggested that addition of C_8OH can lead to aggregate formation in the bulk of the tested mixed surfactant

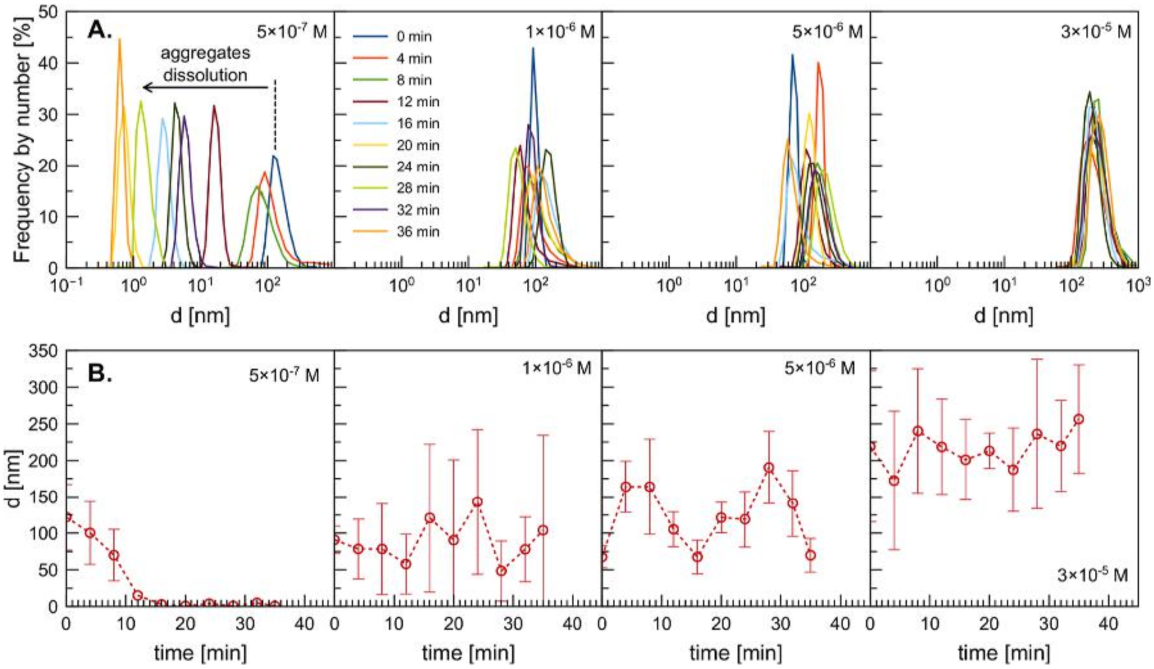

Figure 6. Distributions of the hydrodynamic diameters of the aggregates in time for C_{12}-ALA solutions of various concentrations in the presence of 5×10^{-4} mol/dm^3 C_8OH.

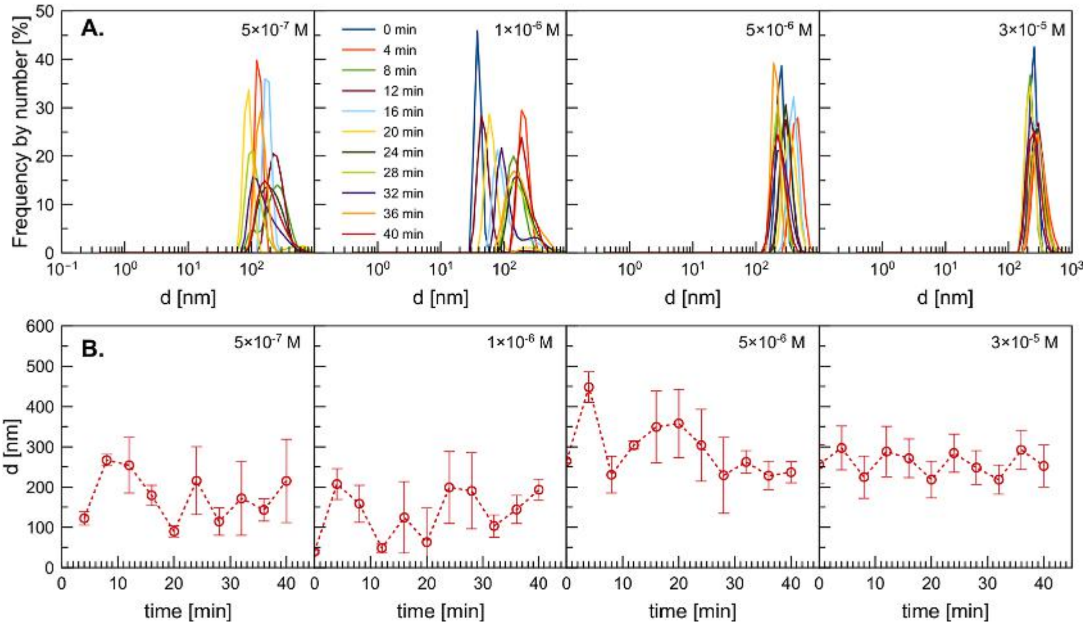

Figure 7. Distributions of the hydrodynamic diameters of the aggregates in time for C_{12}-PHE solutions of various concentrations in the presence of 5×10^{-4} mol/dm^3 C_8OH.

systems, and this effect should increase with increasing AASs concentration. To verify this assumption, dynamic light scattering (DLS) measurements were performed for selected AASs/C_8OH mixtures. Before the main experiments, blank tests were carried out using the pure solutions of C_8OH (5×10^{-4} mol/dm^3) and C_{12}-ALA (3×10^{-5} M, the highest AASs concentration measured in this study). No aggregation was observed in both cases. Next, similar experiments for mixed AASs/C_8OH solutions were performed—after mixture preparation, the DLS cuvette was immediately filled and put into the apparatus, and the hydrodynamic diameter was read at equal time intervals (every 4 min) for 36 min (this was the time corresponding to the equilibrium surface tension establishment). The results of the DLS experiments for solutions of C_{12}-ALA and C_{12}-PHE mixed with 5×10^{-4} mol/dm^3 C_8OH are presented in Figures 6 and 7, respectively.

For the C_{12}-ALA/C_8OH mixed surfactants (Figure 6), clear aggregates' presence in the bulk was revealed. As seen, for the lowest C_{12}-ALA concentration in the mixture, these aggregates were unstable—their number and diameter were gradually diminishing with time till practically complete dissolution. For the c_{AASs} equal to 1×10^{-6} and 5×10^{-6} mol/dm^3, i.e., those lying inside the range where synergistic effects were observed, only slight variations in the aggregates size could be noticed.

For the highest concentration, aggregates were stable with time. Moreover, in the solutions with higher AASs concentration, the aggregates' mean hydrodynamic diameter increased with the concentration from 90 ± 30 nm for 1×10^{-6} mol/dm^3 and 120 ± 40 nm for 5×10^{-6} mol/dm^3 to 215 ± 25 nm for 3×10^{-5} mol/dm^3.

A similar situation can be observed for the C_{12}-PHE/C_8OH blends (Figure 7). Here, however, the aggregates were much more stable at the lowest concentration (5×10^{-7} mol/dm^3), and for $c_{\text{C12-PHE}} = 1 \times 10^{-6}$ and 5×10^{-6} mol/dm^3, only slight variations in their size could be noticed. Again, stability of the aggregates with a mean diameter of 260 ± 30 nm is the largest for $c_{\text{C12-PHE}} = 3 \times 10^{-5}$ mol/dm^3.

4. DISCUSSION

The experiments and simulations confirmed that

- the addition of C_8OH to the AASs solution, in the case of all studied AASs, induces the synergistic effect, which is quite small in the case of equilibrium surface tension variations but spectacular in the case of solution foaming performance,
- C_8OH renders the bulk aggregates formation, which does not exist in pure AASs solutions, and whose time stability depends on AASs concentration (i.e., ratio between AASs and C_8OH amount in the blend), and
- the synergistic effect for all studied AASs can be related to the formation of micelles (aggregates), which causes small surface tension variations under equilibrium conditions. Since the foam formation is highly dynamic, the aggregates are transported by convection (via constant mixing) to the freshly formed air/liquid interface.

The aggregation phenomenon explains the small and negative values of $\Delta\sigma$ calculated based on the proposed synergistic effect analysis. Excess of the AASs molecules in the bulk, in the presence of C_8OH, leads to mixed bulk micellar structures formation—the molecules cannot enter the adsorption layer because, as was shown by MD simulations, the densely packed monolayer is already formed there. The negative value of $\Delta\sigma$ revealed for the C_{12}-PHE surfactant directly shows the highest tendency of aggregation and mixed micelles formations in the case of this compound (which was confirmed by the results of MD simulations). As was shown in ref 31, the pure ASSs do not have the critical micelle concentrations (CMC) due to their solubility limit. Nevertheless, they can form intermolecular hydrogen bonds. Addition of C_8OH allows for mixed micelle formation, which results in a significant decrease in CMC.

The reason for the significant discrepancy between the synergistic effect determined based on equilibrium surface tension and solution foamability, in comparison to the results shown in our earlier studies, should be directly associated with the aggregation effect. Aggregates can act as reservoirs of AASs and *n*-octanol molecules, which, after release to the bulk and re-adsorption, cause a significantly higher (than expected) decrease in the solution surface tension due to specific interactions at the solution/air interface. In the case of solution foaming performance, the aggregates dissolution is triggered by the constant formation of new interfaces (constant and fast increase of the interfacial area)—due to the increase of the surface concentration, the surfactant bulk concentration is depleted, which disturbs the system equilibrium and shifts the aggregation constant toward release of the free surfactant molecules. In the case of low c_{AASs}, where unstable aggregates were revealed, this phenomenon exists, but most probably, the aggregates dissolution is quite fast and occurs just at the beginning of foam formation. For higher AASs concentrations, where stable aggregate formation was observed (see Figures 6 and 7), gradual depletion of the surfactant bulk concentration can be constantly re-supplied by molecules coming out from the dissolving micelle-like structures. On the other hand, due to the highly dynamic nature of the foam formation process, the aggregates can be transported to the foam layer and then adsorbed at the freshly formed air/solution interface directly from the liquid film, separating the air bubbles. The aggregates, therefore, can be considered as internal reservoirs of the mixed foaming agents, whose interactions at the interface (causing the formation of dense monolayers—see Figure 4) significantly increase the mixed solutions foamability. This effect, however, depends on the conditions rendering the aggregates stable. When the concentration of AASs/C_8OH molecules is large enough compared to the growing interfacial area (increasing interfacial area does not render significant bulk concentration depletion), the aggregates are very stable, and the foaming process does not change their stability. Furthermore, this effect can explain significantly higher CSC_{DFA} values compared to the CSC_{σ}—the latter (if determined based on equilibrium surface tension values) is sensitive only to the free surfactant molecules, which, in the case of proper AASs/C_8OH blends, are trapped inside the micelles.

To verify this mechanism, an additional experiment was performed. A mixed C_{12}-ALA/C_8OH solution of concentrations $1 \times 10^{-6}/5 \times 10^{-4}$ mol/dm^3, respectively, was put into the column of the DFA apparatus, and the foamability test was performed. Next, the liquid sample was taken (i) during the foam formation process (just before the $H_f^{\max}$ was reached) and (ii) after the complete foam column collapse. Next, the hydrodynamic aggregates diameter was measured in both samples (10 independent runs for each sample). It was revealed that the aggregates were bigger by ca. 30 nm in the sample taken after the foaming procedure and the foam column disappearance (see Figure 8). This experiment confirms that indeed, the aggregates can act as reservoirs of free molecules for supplementation of the adsorption coverage at the freshly formed liquid/gas interface.

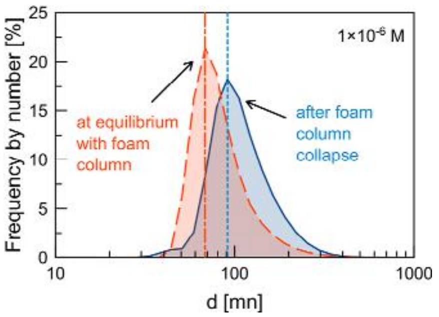

Figure 8. Aggregates diameter (d) distributions in the sample of solution taken from underneath the foam column (red) and after foam column (blue) collapse in C12-ALA solution of concentration 1×10^{-6}, mixed with 5×10^{-4} mol/dm^3 C_8OH ($\Delta d \approx 30$ nm).

5. CONCLUSIONS

The foaming properties of C_{12}-ALA, C_{12}-LEU, and C_{12}-PHE surfactants mixed with C_8OH were thoroughly investigated via surface tension and foamability experiments and complemented by all-atom detail MD simulations. The surface tension measurements revealed significant differences between the used AAS at equilibrium conditions, i.e., the highest synergistic effect was observed for the C_{12}-ALA/C_8OH system, while for C_{12}-PHE/C_8OH, the effect was antagonistic. In contrast, under dynamic conditions (foamability experiments), all studied AAS/C_8OH mixtures exhibited a spectacular synergistic effect at a wide concentration range, in comparison to the one-component systems. We connected the observed phenomenon with the hydrogen bond-mediated aggregate formation in the bulk solution. Moreover, we explained the differences between the specific AAS via the interplay of AAS−AAS and AAS-C_8OH hydrogen bond affinities.

The presented results point toward more general conclusions, which might be potentially applied to a much broader range of surfactant mixtures: (i) the molecule's hydrogen bonding affinity can be used to control the foaming properties, (ii) bulk aggregates can act as surfactant reservoirs, activated by the strong convection (mixing or flotation, and this effect can be generally described as convection-activated surface activity), (iii) surfactants with low solubility (lack of CMC) or relatively weak surface activity at the equilibrium conditions can still be considered as potentially efficient foaming additives, and (iv) molecules with considerable affinity to form hydrogen bonds, such as AAS presented here, can possibly strengthen the interactions with hydrophilic surfaces (e.g., oxide minerals) via hydrogen bonding.

The revealed discrepancy between CSC_σ and CSC_{DFA} is an additional confirmation of the crucial importance of the convection-activated surface activity in the magnitude of the synergistic effect for the studied mixed AASs and *n*-octanol solutions. Moreover, it shows that the CSC value is not universal, and in specific systems, it cannot be simply predicted from the equilibrium surface tension data. Convection-activated surface activity causes the CSC_{DFA} value to depend strongly on the foam formation dynamics (gas flow rate, foaming time, foam column height), i.e., on the parameters directly determining the rate of depletion in the AASs bulk concentration and the kinetics of the aggregates decomposition.

■ AUTHOR INFORMATION

Corresponding Authors

Przemyslaw B. Kowalczuk − *Department of Geoscience and Petroleum, Norwegian University of Science and Technology, 7031 Trondheim, Norway;* orcid.org/0000-0002-1432-030X; Email: przemyslaw.kowalczuk@ntnu.no

Jan Zawala − *Jerzy Haber Institute of Catalysis and Surface Chemistry, Polish Academy of Sciences, 30-239 Krakow, Poland;* orcid.org/0000-0003-4542-2226; Email: jan.zawala@ikifp.edu.pl

Authors

Mariusz Borkowski − *Jerzy Haber Institute of Catalysis and Surface Chemistry, Polish Academy of Sciences, 30-239 Krakow, Poland;* orcid.org/0000-0002-2276-2247

Piotr Batys − *Jerzy Haber Institute of Catalysis and Surface Chemistry, Polish Academy of Sciences, 30-239 Krakow, Poland;* orcid.org/0000-0002-2264-3053

Oleg M. Demchuk − *Faculty of Medicine, The John Paul II Catholic University of Lublin, 20-708 Lublin, Poland*

Complete contact information is available at: https://pubs.acs.org/10.1021/acs.iecr.3c01972

Notes

The authors declare no competing financial interest.

■ ACKNOWLEDGMENTS

Partial financial support from the Polish National Science Centre grant no. (2020/38/E/ST8/00173 and 2022/45/N/ST8/02307) is acknowledged with gratitude. P.B. and J.Z. acknowledge the partial financial support to the project by the statutory research fund of ICSC PAS. We gratefully acknowledge Poland's high-performance computing infrastructure PLGrid (HPC Centers: ACK Cyfronet AGH) for providing computer facilities and support within computational grant no. PLG/2023/016229.

■ REFERENCES

(1) Atta, D. Y.; Negash, B. M.; Yekeen, N.; Habte, A. D. A State-of-the-Art Review on the Application of Natural Surfactants in Enhanced Oil Recovery. *J. Mol. Liq.* **2021**, *321*, 114888.

(2) Tripathy, D. B.; Mishra, A.; Clark, J.; Farmer, T. S. Synthesis, chemistry, physicochemical properties and industrial applications of amino acid surfactants: A review. *C. R. Chim.* **2018**, *21*, 112−130.

(3) Liu, P.; Wu, J.; Pei, X.; Cui, Z.; Jiang, J.; Song, B.; Binks, B. P. Recyclable Surfactant Containing a Dynamic Covalent Bond and Relevant Smart Emulsions. *Green Chem.* **2022**, *24*, 7612−7621.

(4) Xu, M.; Li, Q.; Xie, M.; Jia, Y. G.; Yang, Y.; Chen, Y. Engineering Air-in-Water Emulsion as Adaptable Multifunctional Sealant. *Chem. Eng. J.* **2022**, *429*, 132200.

(5) Litauszki, K.; Gere, D.; Czigany, T.; Kmetty, Á. Environmentally Friendly Packaging Foams: Investigation of the Compostability of Poly(Lactic Acid)-Based Syntactic Foams. *Sustainable Mater. Technol.* **2023**, *35*, No. e00527.

(6) Stie, M. B.; Kalouta, K.; da Cunha, C. F. B.; Feroze, H. M.; Vetri, V.; Foderà, V. Sustainable Strategies for Waterborne Electrospinning of Biocompatible Nanofibers Based on Soy Protein Isolate. *Sustainable Mater. Technol.* **2022**, *34*, No. e00519.

(7) Lin, H.; Chen, K.; Zheng, S.; Zeng, R.; Lin, Y.; Jian, R.; Bai, W.; Xu, Y. Facile Fabrication of Natural Superhydrophobic Eleostearic Acid-SiO2@cotton Fabric for Efficient Separation of Oil/Water Mixtures and Emulsions. *Sustainable Mater. Technol.* **2022**, *32*, No. e00418.

(8) Johnson, P.; Trybala, A.; Starov, V.; Pinfield, V. J. Effect of Synthetic Surfactants on the Environment and the Potential for Substitution by Biosurfactants. *Adv. Colloid Interface Sci.* **2021**, *288*, 102340.

(9) Gallou, F.; Isley, N. A.; Ganic, A.; Onken, U.; Parmentier, M. Surfactant Technology Applied toward an Active Pharmaceutical Ingredient: More than a Simple Green Chemistry Advance. *Green Chem.* **2016**, *18*, 14−19.

(10) Tang, J.; He, J.; Xin, X.; Hu, H.; Liu, T. Biosurfactants Enhanced Heavy Metals Removal from Sludge in the Electrokinetic Treatment. *Chem. Eng. J.* **2018**, *334*, 2579−2592.

(11) Verma, S. P.; Sarkar, B. Rhamnolipid Based Micellar-Enhanced Ultrafiltration for Simultaneous Removal of Cd(II) and Phenolic Compound from Wastewater. *Chem. Eng. J.* **2017**, *319*, 131−142.

(12) Viisimaa, M.; Karpenko, O.; Novikov, V.; Trapido, M.; Goi, A. Influence of Biosurfactant on Combined Chemical−Biological Treatment of PCB-Contaminated Soil. *Chem. Eng. J.* **2013**, *220*, 352−359.

(13) *Mixed Surfactant Systems*; Masahiko, A., Ed.; Taylor & Francis eBooks, 1992. https://www.taylorfrancis.com/books/edit/10.1201/

9781420031010/mixed-surfactant-systems-masahiko-abe (accessed Feb 27, 2023).

(14) Liang, X.; Zhang, M.; Guo, C.; Abel, S.; Yi, X.; Lu, G.; Yang, C.; Dang, Z. Competitive Solubilization of Low-Molecular-Weight Polycyclic Aromatic Hydrocarbons Mixtures in Single and Binary Surfactant Micelles. *Chem. Eng. J.* **2014**, *244*, 522−530.

(15) Chiwetelu, C. I.; Hornof, V.; Neale, G. H.; George, A. E. Use of Mixed Surfactants to Improve the Transient Interfacial Tension Behaviour of Heavy Oil/Alkaline Systems. *Can. J. Chem. Eng.* **1994**, *72*, 534−540.

(16) Wiertel-Pochopien, A.; Batys, P.; Zawala, J.; Kowalczuk, P. B. Synergistic Effect of Binary Surfactant Mixtures in Two-Phase and Three-Phase Systems. *J. Phys. Chem. B* **2021**, *125*, 3855−3866.

(17) Khan, A.; Marques, E. F. Synergism and Polymorphism in Mixed Surfactant Systems. *Curr. Opin. Colloid Interface Sci.* **1999**, *4*, 402−410.

(18) Polowczyk, I.; Kruszelnicki, M.; Kowalczuk, P. B. Oil Agglomeration of Metal-Bearing Shale in the Presence of Mixed Cationic-Anionic Surfactants. *Physicochem. Probl. Miner. Process.* **2018**, *54*, 1052−1059.

(19) Rangsunvigit, P.; Imsawatgul, P.; Na-ranong, N.; O'Haver, J. H.; Chavadej, S. Mixed Surfactants for Silica Surface Modification by Admicellar Polymerization Using a Continuous Stirred Tank Reactor. *Chem. Eng. J.* **2008**, *136*, 288−294.

(20) Lin, S. Y. A.; Lin, Y. Y.; Chen, E. M.; Hsu, C. T.; Kwan, C. C. A Study of the Equilibrium Surface Tension and the Critical Micelle Concentration of Mixed Surfactant Solutions. *Langmuir* **1999**, *15*, 4370−4376.

(21) Wang, Y.; Jiang, Y.; Geng, T.; Ju, H.; Duan, S. Synthesis, Surface/Interfacial Properties, and Biological Activity of Amide-Based Gemini Cationic Surfactants with Hydroxyl in the Spacer Group. *Colloids Surf., A* **2019**, *563*, 1−10.

(22) Bera, A.; Ojha, K.; Mandal, A. Synergistic Effect of Mixed Surfactant Systems on Foam Behavior and Surface Tension. *J. Surfactants Deterg.* **2013**, *16*, 621−630.

(23) Stellner, K. L.; Scamehorn, J. F. Surfactant Precipitation in Aqueous Solutions Containing Mixtures of Anionic and Nonionic Surfactants. *J. Am. Oil Chem. Soc.* **1986**, *63*, 566−574.

(24) Kume, G.; Gallotti, M.; Nunes, G. Review on Anionic/Cationic Surfactant Mixtures. *J. Surfactants Deterg.* **2008**, *11*, 1−11.

(25) Stellner, K. L.; Amante, J. C.; Scamehorn, J. F.; Harwell, J. H. Precipitation Phenomena in Mixtures of Anionic and Cationic Surfactants in Aqueous Solutions. *J. Colloid Interface Sci.* **1988**, *123*, 186−200.

(26) Ramezani, M.; Lashkarbolooki, M.; Abedini, R. Experimental Investigation of Different Characteristics of Crude Oil on the Interfacial Activity of Anionic, Cationic and Nonionic Surfactants Mixtures. *J. Pet. Sci. Eng.* **2022**, *214*, 110485.

(27) Poorsargol, M.; Alimohammadian, M.; Sohrabi, B.; Dehestani, M. Dispersion of Graphene Using Surfactant Mixtures: Experimental and Molecular Dynamics Simulation Studies. *Appl. Surf. Sci.* **2019**, *464*, 440−450.

(28) Bordes, R.; Holmberg, K. Amino Acid-Based Surfactants – Do They Deserve More Attention? *Adv. Colloid Interface Sci.* **2015**, *222*, 79−91.

(29) Guo, J.; Sun, L.; Zhang, F.; Sun, B.; Xu, B.; Zhou, Y. Review: Progress in Synthesis, Properties and Application of Amino Acid Surfactants. *Chem. Phys. Lett.* **2022**, *794*, 139499.

(30) Qiao, W.; Qiao, Y. The Relationship Between the Structure and Properties of Amino Acid Surfactants Based on Glycine and Serine. *J. Surfactants Deterg.* **2013**, *16*, 821−828.

(31) Borkowski, M.; Orvalho, S.; Warszyński, P.; Demchuk, O. M.; Jarek, E.; Zawala, J. Experimental and Theoretical Study of Adsorption of Synthesized Amino Acid Core Derived Surfactants at an Air/Water Interface. *Phys. Chem. Chem. Phys.* **2022**, *24*, 3854−3864.

(32) Miroslaw, B.; Demchuk, O. M.; Luboradzki, R.; Tyszczuk-Rotko, K. Low-Molecular-Weight Organogelators Based on N-Dodecanoyl-L-Amino Acids—Energy Frameworks and Supramolecular Synthons. *Materials* **2023**, *16*, 702.

(33) Berendsen, H. J. C.; van der Spoel, D.; van Drunen, R. GROMACS: A message-passing parallel molecular dynamics implementation. *Comput. Phys. Commun.* **1995**, *91*, 43−56.

(34) Lindahl, E.; Hess, B.; van der Spoel, D. GROMACS 3.0: A Package for Molecular Simulation and Trajectory Analysis. *J. Mol. Model.* **2001**, *7*, 306−317.

(35) MacKerell, A. D.; Bashford, D.; Bellott, M.; Dunbrack, R. L.; Evanseck, J. D.; Field, M. J.; Fischer, S.; Gao, J.; Guo, H.; Ha, S.; Joseph-McCarthy, D.; Kuchnir, L.; Kuczera, K.; Lau, F. T. K.; Mattos, C.; Michnick, S.; Ngo, T.; Nguyen, D. T.; Prodhom, B.; Reiher, W. E.; Roux, B.; Schlenkrich, M.; Smith, J. C.; Stote, R.; Straub, J.; Watanabe, M.; Wiórkiewicz-Kuczera, J.; Yin, D.; Karplus, M. All-Atom Empirical Potential for Molecular Modeling and Dynamics Studies of Proteins. *J. Phys. Chem. B* **1998**, *102*, 3586−3616.

(36) Yazhgur, P.; Vierros, S.; Hannoy, D.; Sammalkorpi, M.; Salonen, A. Surfactant Interactions and Organization at the Gas-Water Interface (CTAB with Added Salt). *Langmuir* **2018**, *34*, 1855−1864.

(37) Jo, S.; Kim, T.; Iyer, V. G.; Im, W. CHARMM-GUI: A Web-Based Graphical User Interface for CHARMM. *J. Comput. Chem.* **2008**, *29*, 1859−1865.

(38) Brooks, B. R.; Brooks, C. L.; Mackerell, A. D.; Nilsson, L.; Petrella, R. J.; Roux, B.; Won, Y.; Archontis, G.; Bartels, C.; Boresch, S.; Caflisch, A.; Caves, L.; Cui, Q.; Dinner, A. R.; Feig, M.; Fischer, S.; Gao, J.; Hodoscek, M.; Im, W.; Kuczera, K.; Lazaridis, T.; Ma, J.; Ovchinnikov, V.; Paci, E.; Pastor, R. W.; Post, C. B.; Pu, J. Z.; Schaefer, M.; Tidor, B.; Venable, R. M.; Woodcock, H. L.; Wu, X.; Yang, W.; York, D. M.; Karplus, M. CHARMM: The Biomolecular Simulation Program. *J. Comput. Chem.* **2009**, *30*, 1545−1614.

(39) Lee, J.; Cheng, X.; Swails, J. M.; Yeom, M. S.; Eastman, P. K.; Lemkul, J. A.; Wei, S.; Buckner, J.; Jeong, J. C.; Qi, Y.; Jo, S.; Pande, V. S.; Case, D. A.; Brooks, C. L.; MacKerell, A. D.; Klauda, J. B.; Im, W. CHARMM-GUI Input Generator for NAMD, GROMACS, AMBER, OpenMM, and CHARMM/OpenMM Simulations Using the CHARMM36 Additive Force Field. *J. Chem. Theory Comput.* **2016**, *12*, 405−413.

(40) Vanommeslaeghe, K.; Hatcher, E.; Acharya, C.; Kundu, S.; Zhong, S.; Shim, J.; Darian, E.; Guvench, O.; Lopes, P.; Vorobyov, I.; Mackerell, A. D. CHARMM General Force Field: A Force Field for Drug-like Molecules Compatible with the CHARMM All-Atom Additive Biological Force Fields. *J. Comput. Chem.* **2009**, *31*, 671−690.

(41) Jorgensen, W. L.; Chandrasekhar, J.; Madura, J. D.; Impey, R. W.; Klein, M. L. Comparison of Simple Potential Functions for Simulating Liquid Water. *J. Chem. Phys.* **1983**, *79*, 926−935.

(42) Bussi, G.; Donadio, D.; Parrinello, M. Canonical Sampling through Velocity Rescaling. *J. Chem. Phys.* **2007**, *126*, 014101.

(43) Essmann, U.; Perera, L.; Berkowitz, M. L.; Darden, T.; Lee, H.; Pedersen, L. G. A Smooth Particle Mesh Ewald Method. *J. Chem. Phys.* **1995**, *103*, 8577−8593.

(44) Yeh, I. C.; Berkowitz, M. L. Ewald Summation for Systems with Slab Geometry. *J. Chem. Phys.* **1999**, *111*, 3155−3162.

(45) Hess, B.; Bekker, H.; Berendsen, H. J. C.; Fraaije, J. G. E. M. LINCS: A Linear Constraint Solver for Molecular Simulations. *J. Comput. Chem.* **1997**, *18*, 1463−1472.

(46) Miyamoto, S.; Kollman, P. A. Settle: An Analytical Version of the SHAKE and RATTLE Algorithm for Rigid Water Models. *J. Comput. Chem.* **1992**, *13*, 952−962.

(47) Humphrey, W.; Dalke, A.; Schulten, K. VMD: Visual Molecular Dynamics. *J. Mol. Graph.* **1996**, *14*, 33−38.

(48) Martinez, L.; Andrade, R.; Birgin, E. G.; Martínez, J. M. PACKMOL: A Package for Building Initial Configurations for Molecular Dynamics Simulations. *J. Comput. Chem.* **2009**, *30*, 2157−2164.

(49) Zawala, J.; Wiertel-Pochopien, A.; Larsen, E.; Kowalczuk, P. B. Synergism between Cationic Alkyltrimethylammonium Bromides (C_nTAB) and Nonionic *n*-Octanol in the Foamability of Their Mixed Solutions. *Ind. Eng. Chem. Res.* **2020**, *59*, 1159−1167.

(50) Lunkenheimer, K.; Malysa, K.; Winsel, K.; Geggel, K.; Siegel, S. Novel Method and Parameters for Testing and Characterization of Foam Stability. *Langmuir* **2010**, *26*, 3883−3888.

(51) Kim, I. J.; Park, J. G.; Han, Y. H.; Kim, S. Y.; Shackelford, J. F.; Kim, I. J.; Park, J. G.; Han, Y. H.; Kim, S. Y.; Shackelford, J. F. Wet Foam Stability from Colloidal Suspension to Porous Ceramics: A Review. *J. Korean Ceram. Soc.* **2019**, *56*, 211−232.

https://doi.org/10.1021/acs.iecr.3c01972
Ind. Eng. Chem. Res. 2023, 62, 13498−13509

Załącznik nr10

Kraków, 11.09.2023 r.
Miejscowość, data

Mariusz Borkowski
Imię (imiona) i nazwisko kandydata

OŚWIADCZENIE KANDYDATA

(wypełniają tylko osoby, których rozprawa doktorska stanowi zbiór artykułów)

Niniejszym oświadczam, że mój udział w artykule naukowym autorstwa: Mariusz Borkowski, Jan Zawała p.t. *Influence of Temperature on Rising Bubble Dynamics in Water and n-pentanol Solutions*, wchodzącym w skład zbioru opublikowanych i powiązanych tematycznie artykułów naukowych, stanowiących rozprawę doktorską mojego autorstwa p.t. *Influence of liquid physicochemical properties on single bubble motion and stability of foam films and foams* polegał na:

- wykonaniu przeglądu literaturowego
- uczestnictwie w opracowaniu koncepcji oraz idei badawczej,
- uczestnictwie w opracowaniu metodologii opisanych badań,
- opracowaniu i wykonaniu aparatury badawczej,
- uczestnictwie w walidacji opracowanej metody badawczej,
- przeprowadzeniu wszystkich pomiarów oraz eksperymentów,
- uczestnictwie w formalnej analizie wyników badawczych,
- przygotowaniu grafik oraz wizualizacji danych,
- przygotowaniu wstępnej wersji manuskryptu publikacji naukowej,
- uczestnictwie w przygotowaniu ostatecznej wersji manuskryptu
- uczestnictwie w pracach związanych z recenzją oraz edytowaniem manuskryptu.

11.09.23

....
Data, czytelny podpis współautora

---

[1] niepotrzebne skreślić

Załącznik nr10

Kraków, 11.09.2023 r.
Miejscowość, data

Jan Zawała
Imię (imiona) i nazwisko współautora

OŚWIADCZENIE WSPÓŁAUTORA

(wypełniają tylko współautorzy publikacji wchodzącej w skład zbioru artykułów stanowiących rozprawę doktorską)

Niniejszym oświadczam, że mój udział w artykule naukowym autorstwa: Mariusz Borkowski, Jan Zawała p.t. *Influence of Temperature on Rising Bubble Dynamics in Water and n-pentanol Solutions*, wchodzącym w skład zbioru opublikowanych i powiązanych tematycznie artykułów naukowych stanowiących rozprawę doktorską autorstwa Mariusza Borkowskiego p.t. *Influence of liquid physicochemical properties on single bubble motion and stability of foam films and foams* polegał na:

- uczestnictwie w opracowaniu koncepcji oraz idei badawczej,
- uczestnictwie w opracowaniu metodologii opisanych badań,
- napisaniu oprogramowania służącego analizie uzyskanych obrazów,
- uczestnictwie w walidacji opracowanej metody badawczej,
- uczestnictwie w formalnej analizie wyników badawczych,
- pozyskaniu zasobów do prowadzenia badań,
- selekcji danych,
- uczestnictwie w przygotowaniu manuskryptu publikacji naukowej,
- uczestnictwie w pracach związanych z recenzją oraz edytowaniem manuskryptu,
- nadzorze nad prowadzonymi badaniami,
- administrowaniu,
- zagwarantowaniu finansowania.

11.09.2023, Jan Zawała
Data, czytelny podpis współautora

¹niepotrzebne skreślić

Załącznik nr10

Kraków, 11.09.2023 r.
Miejscowość, data

Mariusz Borkowski
Imię (imiona) i nazwisko kandydata

OŚWIADCZENIE KANDYDATA

(wypełniają tylko osoby, których rozprawa doktorska stanowi zbiór artykułów)

Niniejszym oświadczam, że mój udział w artykule naukowym autorstwa: Mariusz Borkowski, Sandra Orvalho, Piotr Warszyński, Oleg M. Demchuk, Ewelina Jarek, Jan Zawała p.t. *Experimental and theoretical study of adsorption of synthesized amino acid core derived surfactants at an air/water interface*, wchodzącym w skład zbioru opublikowanych i powiązanych tematycznie artykułów naukowych, stanowiących rozprawę doktorską mojego autorstwa p.t. *Influence of liquid physicochemical properties on single bubble motion and stability of foam films and foams* polegał na:

- uczestnictwie w opracowaniu koncepcji oraz idei badawczej,
- uczestnictwie w opracowaniu metodologii pozyskania opisanych badań,
- przeprowadzeniu wszystkich pomiarów eksperymentalnych (napięcia powierzchniowe, miareczkowania pH i konduktometryczne),
- uczestnictwie w opracowaniu metodologii pozyskania opisanych badań,
- uczestnictwie w formalnej analizie i interpretacji wyników badawczych,
- przygotowaniu grafik oraz wizualizacja danych,
- przygotowaniu wstępnej wersji manuskryptu publikacji naukowej,
- uczestnictwie w przygotowaniu ostatecznej wersji manuskryptu,
- nadzorze nad prowadzonymi badaniami,
- uczestnictwie w przygotowaniu manuskryptu publikacji naukowej,
- uczestnictwie w pracach związanych z recenzją oraz edytowaniem manuskryptu,

11.09.23

Data, czytelny podpis współautora

---

[1] niepotrzebne skreślić

Załącznik nr10

Prague (Czech republic), 11.09.2023 r.

Sandra Orvalho
Name (names) and surname of co-author

CO-AUTHOR DECLARATION

(to be filled by co-authors of publications from PhD thesis article list)

I hereby declare that my participation in the article co-authored by: Mariusz Borkowski, Sandra Orvalho, Piotr Warszyński, Oleg M. Demchuk, Ewelina Jarek, Jan Zawała p.t. *Experimental and theoretical study of adsorption of synthesized amino acid core derived surfactants at an air/water interface*, a part of published and thematically linked scientific articles constituting PhD thesis of Mariusz Borkowski entitled: *Influence of liquid physicochemical properties on single bubble motion and stability of foam films and foams* includes:

- participation in developing the concept and research idea,
- participation in development of the experimental methodology,
- participation in formal analysis and interpretation of research results,
- participation in preparation of a manuscript,
- participation in work related to reviewing and editing the manuscript,
- supervision of a part of conducted research,
- administration.

15.09.2023, SOrvalho
Date, signature of the co-author

Załącznik nr10

Kraków, 11.09.2023 r.
Miejscowość, data

Piotr Warszyński
Imię (imiona) i nazwisko współautora

OŚWIADCZENIE WSPÓŁAUTORA

(wypełniają tylko współautorzy publikacji wchodzącej w skład zbioru artykułów stanowiących rozprawę doktorską)

Niniejszym oświadczam, że mój udział w artykule naukowym autorstwa: Mariusz Borkowski, Sandra Orvalho, Piotr Warszyński, Oleg M. Demchuk, Ewelina Jarek, Jan Zawała p.t. *Experimental and theoretical study of adsorption of synthesized amino acid core derived surfactants at an air/water interface*, wchodzącym w skład zbioru opublikowanych i powiązanych tematycznie artykułów naukowych stanowiących rozprawę doktorską autorstwa Mariusza Borkowskiego p.t. *Influence of liquid physicochemical properties on single bubble motion and stability of foam films and foa*ms polegał na:

- wykonaniu symulacji metodą dynamiki molekularnej,
- wykonaniu symulacji metodą DFT,
- wykonaniu dopasowań modelu teoretycznego do danych eksperymentalnych
- walidacji opracowanej metody badawczej,
- uczestnictwie w formalnej analizie i interpretacji wyników badawczych,
- uczestnictwie w przygotowaniu grafik oraz wizualizacji danych,
- uczestnictwie w przygotowaniu manuskryptu publikacji naukowej,
- uczestnictwie w pracach związanych z recenzją oraz edytowaniem manuskryptu.

5.10.23 ....
Data, czytelny podpis współautora

---

[1] niepotrzebne skreślić

Załącznik nr10

Lublin, 11.09.2023 r.
Miejscowość, data

Oleg M. Demchuk
Imię (imiona) i nazwisko współautora

OŚWIADCZENIE WSPÓŁAUTORA

(wypełniają tylko współautorzy publikacji wchodzącej w skład zbioru artykułów stanowiących rozprawę doktorską)

Niniejszym oświadczam, że mój udział w artykule naukowym autorstwa: Mariusz Borkowski, Sandra Orvalho, Piotr Warszyński, Oleg M. Demchuk, Ewelina Jarek, Jan Zawała p.t. *Experimental and theoretical study of adsorption of synthesized amino acid core derived surfactants at an air/water interface*, wchodzącym w skład zbioru opublikowanych i powiązanych tematycznie artykułów naukowych stanowiących rozprawę doktorską autorstwa Mariusza Borkowskiego p.t. *Influence of liquid physicochemical properties on single bubble motion and stability of foam films and foams* polegał na:

- uczestnictwie w opracowaniu metodologii pomiarów,
- syntezie związków chemicznych i ich wydzieleniu i oczyszczeniu,
- analizie NMR i wyznaczeniu temperatur topnienia,
- uczestnictwie w przygotowaniu ostatecznej wersji manuskryptu,
- uczestnictwie w przygotowaniu grafik oraz wizualizacji danych,
- uczestnictwie w pracach związanych z recenzją oraz edytowaniem manuskryptu.

11.09.2023
....
Data, czytelny podpis współautora

---

[1]niepotrzebne skreślić

Załącznik nr10

Kraków, 11.09.2023 r.
Miejscowość, data

Ewelina Jarek
Imię (imiona) i nazwisko współautora

OŚWIADCZENIE WSPÓŁAUTORA

(wypełniają tylko współautorzy publikacji wchodzącej w skład zbioru artykułów stanowiących rozprawę doktorską)

Niniejszym oświadczam, że mój udział w artykule naukowym autorstwa: Mariusz Borkowski, Sandra Orvalho, Piotr Warszyński, Oleg M. Demchuk, Ewelina Jarek, Jan Zawała p.t. *Experimental and theoretical study of adsorption of synthesized amino acid core derived surfactants at an air/water interface*, wchodzącym w skład zbioru opublikowanych i powiązanych tematycznie artykułów naukowych stanowiących rozprawę doktorską autorstwa Mariusza Borkowskiego p.t. *Influence of liquid physicochemical properties on single bubble motion and stability of foam films and foams* polegał na:

- uczestnictwie w wykonywaniu obliczeń teoretycznych,
- uczestnictwie w formalnej analizie wyników badawczych,
- uczestnictwie w przygotowanie manuskryptu publikacji naukowej,
- uczestnictwie w pracach związanych z recenzją oraz edytowaniem manuskryptu

11.09.2023 Jarek Ewelina
Data, czytelny podpis współautora

---

[1] niepotrzebne skreślić

Kraków, 11.09.2023 r.
Miejscowość, data

Jan Zawała
Imię (imiona) i nazwisko współautora

OŚWIADCZENIE WSPÓŁAUTORA

(wypełniają tylko współautorzy publikacji wchodzącej w skład zbioru artykułów stanowiących rozprawę doktorską)

Niniejszym oświadczam, że mój udział w artykule naukowym autorstwa: Mariusz Borkowski, Sandra Orvalho, Piotr Warszyński, Oleg M. Demchuk, Ewelina Jarek, Jan Zawała p.t. *Experimental and theoretical study of adsorption of synthesized amino acid core derived surfactants at an air/water interface*, wchodzącym w skład zbioru opublikowanych i powiązanych tematycznie artykułów naukowych stanowiących rozprawę doktorską autorstwa Mariusza Borkowskiego p.t. *Influence of liquid physicochemical properties on single bubble motion and stability of foam films and foams* polegał na:

- uczestnictwie w opracowaniu koncepcji oraz idei badawczej,
- uczestnictwie w opracowaniu metodologii pozyskania opisanych badań,
- uczestnictwie w formalnej analizie i interpretacji wyników badawczych,
- pozyskaniu zasobów do prowadzenia badań,
- selekcji danych,
- uczestnictwie w przygotowaniu manuskryptu publikacji naukowej,
- uczestnictwie w pracach związanych z recenzją oraz edytowaniem manuskryptu,
- nadzorze nad prowadzonymi badaniami,
- administrowaniu,
- zagwarantowaniu środków finansowych (projekt NCN).

11.09.2023
Data, czytelny podpis współautora

[1]niepotrzebne skreślić

Załącznik nr10

Kraków, 11.09.2023 r.
Miejscowość, data

Mariusz Borkowski
Imię (imiona) i nazwisko kandydata

OŚWIADCZENIE KANDYDATA

(wypełniają tylko osoby, których rozprawa doktorska stanowi zbiór artykułów)

Niniejszym oświadczam, że mój udział w artykule naukowym autorstwa: Mariusz Borkowski, Dominik Kosior, Jan Zawała, p.t. *Effect of initial adsorption coverage and dynamic adsorption layer formation at bubble surface in stability of single foam films*, wchodzącym w skład zbioru opublikowanych i powiązanych tematycznie artykułów naukowych, stanowiących rozprawę doktorską mojego autorstwa p.t. *Influence of liquid physicochemical properties on single bubble motion and stability of foam films and foams* polegał na:

- przeprowadzeniu wszystkich pomiarów oraz eksperymentów,
- uczestnictwie w selekcji danych,
- uczestnictwie w formalnej analizie i interpretacji wyników badań i obliczeń,
- przygotowaniu manuskryptu publikacji naukowej,
- przygotowaniu grafik oraz wizualizacja danych,

11.09.23
....
Data, czytelny podpis współautora

---

[1] niepotrzebne skreślić

Kraków, 11.09.2023 r.
Miejscowość, data

Dominik Kosior
Imię (imiona) i nazwisko współautora

OŚWIADCZENIE WSPÓŁAUTORA

(wypełniają tylko współautorzy publikacji wchodzącej w skład zbioru artykułów stanowiących rozprawę doktorską)

Niniejszym oświadczam, że mój udział w artykule naukowym autorstwa: Mariusz Borkowski, Dominik Kosior, Jan Zawała, p.t. *Effect of initial adsorption coverage and dynamic adsorption layer formation at bubble surface in stability of single foam films*, wchodzącym w skład zbioru opublikowanych i powiązanych tematycznie artykułów naukowych stanowiących rozprawę doktorską autorstwa Mariusza Borkowskiego p.t. *Influence of liquid physicochemical properties on single bubble motion and stability of foam films and foams* polegał na:

- uczestnictwie w selekcji danych do publikacji,
- wykonaniu obliczeń teoretycznych na podstawie analitycznych modeli wyciekania filmów pianowych,
- uczestnictwie w formalnej analizie i interpretacji wyników,
- udziale w procesie recenzji oraz edycji manuskryptu.

Dominik Kosior
....
Data, czytelny podpis współautora
11/09/2023

---

[1] niepotrzebne skreślić

Załącznik nr10

Kraków, 11.09.2023 r.
Miejscowość, data

Jan Zawała
Imię (imiona) i nazwisko współautora

OŚWIADCZENIE WSPÓŁAUTORA

(wypełniają tylko współautorzy publikacji wchodzącej w skład zbioru artykułów stanowiących rozprawę doktorską)

Niniejszym oświadczam, że mój udział w artykule naukowym autorstwa: Mariusz Borkowski, Dominik Kosior, Jan Zawała, p.t. *Effect of initial adsorption coverage and dynamic adsorption layer formation at bubble surface in stability of single foam films*, wchodzącym w skład zbioru opublikowanych i powiązanych tematycznie artykułów naukowych stanowiących rozprawę doktorską autorstwa Mariusza Borkowskiego p.t. *Influence of liquid physicochemical properties on single bubble motion and stability of foam films and foams* polegał na:

- udziale w opracowaniu koncepcji oraz idei badawczej,
- uczestnictwie w opracowaniu metodologii opisanych badań,
- uczestnictwie w przygotowaniu niezbędnego oprogramowania,
- uczestnictwie w nadzorze nad prowadzonymi badaniami,
- zagwarantowaniu środków finansowych (grant NCN),
- udziale w procesie tworzenia tekstu manuskryptu,
- udziale w procesie recenzji oraz edycji manuskryptu.

11.09.2023
Data, czytelny podpis współautora

[1]niepotrzebne skreślić

Załącznik nr10

Kraków, 11.09.2023 r.
Miejscowość, data

Jan Zawała
Imię (imiona) i nazwisko współautora

OŚWIADCZENIE WSPÓŁAUTORA

(wypełniają tylko współautorzy publikacji wchodzącej w skład zbioru artykułów stanowiących rozprawę doktorską)

Niniejszym oświadczam, że mój udział w artykule naukowym autorstwa: Jan Zawała, Jonas Miguet, Preetika Rastogi, Omer Atasi, Mariusz Borkowski, Benoit Scheid, Gerald G. Fuller p.t. *Coalescence of surface bubbles: The crucial role of motion-induced dynamic adsorption layer*, wchodzącym w skład zbioru opublikowanych i powiązanych tematycznie artykułów naukowych stanowiących rozprawę doktorską autorstwa Mariusza Borkowskiego p.t. *Influence of liquid physicochemical properties on single bubble motion and stability of foam films and foams* polegał na:

- udziale w opracowaniu koncepcji oraz idei badawczej,
- udziale w opracowaniu metodologii badań,
- udziale w napisaniu oprogramowania służącego analizie uzyskanych filmów,
- udziale w przeprowadzeniu głównych pomiarów eksperymentalnych,
- udziale w walidacji opracowanej metody badawczej,
- udziale w formalnej analizie i interpretacji wyników badawczych,
- pozyskaniu zasobów do prowadzenia badań,
- udziale w selekcji danych,
- udziale w przygotowanie manuskryptu publikacji naukowej,
- udziale w pracach związanych z recenzją oraz edytowaniem manuskryptu,
- nadzorze nad prowadzonymi badaniami,
- administrowaniu.

11.09.2023
Data, czytelny podpis współautora

[1] niepotrzebne skreślić

Brussels (Belgium), 11.09.2023 r.

Jonas Miguet
Name (names) and surname of co-author

CO-AUTHOR DECLARATION

(to be filled by co-authors of publications from PhD thesis article list)

I hereby declare that my participation in the article co-authored by: Jan Zawala, Jonas Miguet, Preetika Rastogi, Omer Atasi, Mariusz Borkowski, Benoit Scheid, Gerald G. Fuller entitled: *Coalescence of surface bubbles: The crucial role of motion-induced dynamic adsorption layer* a part of published and thematically linked scientific articles constituting PhD thesis of Mariusz Borkowski entitled: *Influence of liquid physicochemical properties on single bubble motion and stability of foam films and foams* includes:

- participation in development of the methodology of the described research,
- participation in theoretical simulations,
- participation in formal analysis and interpretation of research results,
- participation in preparation of a manuscript,
- participation in work related to reviewing and editing of the manuscript.

September 15th 2023
Date, signature of the co-author

[1] niepotrzebne skreślić

Załącznik nr10

Kraków, 11.09.2023 r.

Preetika Rastogi
Name (names) and surname of co-author

CO-AUTHOR DECLARATION

(to be filled by co-authors of publications from PhD thesis article list)

I hereby declare that my participation in the article co-authored by: Jan Zawala, Jonas Miguet, Preetika Rastogi, Omer Atasi, Mariusz Borkowski, Benoit Scheid, Gerald G. Fuller entitled: *Coalescence of surface bubbles: The crucial role of motion-induced dynamic adsorption layer* a part of published and thematically linked scientific articles constituting PhD thesis of Mariusz Borkowski entitled*: Influence of liquid physicochemical properties on single bubble motion and stability of foam films and foams* includes:

- participation in formal analysis and interpretation of research results,
- participation in experiments related to quantitative determination of foam film drainage dynamics
- participation in review and editing of the manuscript.

Preetika Rastogi

15th September, 2023
....
Date, signature of the co-author

[1] niepotrzebne skreślić

Załącznik nr10

Kraków, 11.09.2023 r.

Omar Atasi
Name (names) and surname of co-author

CO-AUTHOR DECLARATION

(to be filled by co-authors of publications from PhD thesis article list)

I hereby declare that my participation in the article co-authored by: Jan Zawala, Jonas Miguet, Preetika Rastogi, Omer Atasi, Mariusz Borkowski, Benoit Scheid, Gerald G. Fuller entitled: *Coalescence of surface bubbles: The crucial role of motion-induced dynamic adsorption layer* a part of published and thematically linked scientific articles constituting PhD thesis of Mariusz Borkowski entitled: *Influence of liquid physicochemical properties on single bubble motion and stability of foam films and foams* includes:

- performance of theoretical simulations,
- formal analysis and interpretation of research results,
- preparation of a manuscript for a scientific publication
- review and editing.

18/09/23
Date, signature of the co-author

[1] niepotrzebne skreślić

Załącznik nr10

Kraków, 11.09.2023 r.
Miejscowość, data

Mariusz Borkowski
Imię (imiona) i nazwisko kandydata

OŚWIADCZENIE KANDYDATA

(wypełniają tylko osoby, których rozprawa doktorska stanowi zbiór artykułów)

Niniejszym oświadczam, że mój udział w artykule naukowym autorstwa: Jan Zawala, Jonas Miguet, Preetika Rastogi, Omer Atasi, Mariusz Borkowski, Benoit Scheid, Gerald G. Fuller p.t. *Coalescence of surface bubbles: The crucial role of motion-induced dynamic adsorption layer*, wchodzącym w skład zbioru opublikowanych i powiązanych tematycznie artykułów naukowych, stanowiących rozprawę doktorską mojego autorstwa p.t. *Influence of liquid physicochemical properties on single bubble motion and stability of foam films and foams* polegał na:

- uczestnictwie w opracowaniu hipotezy badawczej i planu badań
- przygotowaniu i przeprowadzeniu badań wstępnych,
- udziale w pracach związanych z przygotowaniem manuskryptu,
- udziale w analizie i interpretacji wyników badawczych
- udziale w pracach związanych z recenzją oraz edytowaniem ostatecznej wersji manuskryptu,

11.09.23
……………………………………………
Data, czytelny podpis współautora

Załącznik nr10

Kraków, 11.09.2023 r.

Benoit Scheid
Name (names) and surname of co-author

CO-AUTHOR DECLARATION

(to be filled by co-authors of publications from PhD thesis article list)

I hereby declare that my participation in the article co-authored by: Jan Zawala, Jonas Miguet, Preetika Rastogi, Omer Atasi, Mariusz Borkowski, Benoit Scheid, Gerald G. Fuller entitled: *Coalescence of surface bubbles: The crucial role of motion-induced dynamic adsorption layer* a part of published and thematically linked scientific articles constituting PhD thesis of Mariusz Borkowski entitled: *Influence of liquid physicochemical properties on single bubble motion and stability of foam films and foams* includes:

- conceptualization,
- methodology,
- formal analysis of research results,
- preparation of a manuscript for a scientific publication
- review and editing

18/9/2023
Benoit Scheid, Professor

---

[1]niepotrzebne skreślić

Załącznik nr10

Kraków, 11.09.2023 r.

Gerald G. Fuller
Name (names) and surname of co-author

CO-AUTHOR DECLARATION

(to be filled by co-authors of publications from PhD thesis article list)

I hereby declare that my participation in the article co-authored by: Jan Zawala, Jonas Miguet, Preetika Rastogi, Omer Atasi, Mariusz Borkowski, Benoit Scheid, Gerald G. Fuller entitled: *Coalescence of surface bubbles: The crucial role of motion-induced dynamic adsorption layer* a part of published and thematically linked scientific articles constituting PhD thesis of Mariusz Borkowski entitled: *Influence of liquid physicochemical properties on single bubble motion and stability of foam films and foams* includes:

- conceptualization,
- methodology,
- formal analysis and discussion of research results,
- preparation of a manuscript for a scientific publication
- review and editing

September 16, 2023;
Date, signature of the co-author

---

[1] niepotrzebne skreślić

Załącznik nr10

Kraków, 11.09.2023 r.
Miejscowość, data

Mariusz Borkowski
Imię (imiona) i nazwisko kandydata

OŚWIADCZENIE KANDYDATA

(wypełniają tylko osoby, których rozprawa doktorska stanowi zbiór artykułów)

Niniejszym oświadczam, że mój udział w artykule naukowym autorstwa: Mariusz Borkowski, Piotr Batys, Oleg M. Demchuk, Przemysław B. Kowalczuk, Jan Zawala p.t. *Amino-Acids Surfactants and n-Octanol Mixtures-Sustainable, Efficient, and Dynamically Triggered Foaming Systems*, wchodzącym w skład zbioru opublikowanych i powiązanych tematycznie artykułów naukowych, stanowiących rozprawę doktorską mojego autorstwa p.t. *Influence of liquid physicochemical properties on single bubble motion and stability of foam films and foams* polegał na:

- udziale w opracowaniu koncepcji oraz idei badawczej,
- udziale w opracowaniu metodologii opisanych badań,
- przeprowadzeniu wszystkich pomiarów oraz eksperymentów,
- udziale w formalnej analizie i interpretacji wyników badawczych,
- przygotowaniu grafik oraz wizualizacja danych,
- udziale w przygotowaniu manuskryptu publikacji naukowej,
- udziale w pracach związanych z recenzja oraz edytowaniem manuskryptu,

11.09.23
....
Data, czytelny podpis współautora

[1]niepotrzebne skreślić

Kraków, 18.09.2023 r.

Piotr Batys
Imię (imiona) i nazwisko współautora

OŚWIADCZENIE WSPÓŁAUTORA

(wypełniają tylko współautorzy publikacji wchodzącej w skład zbioru artykułów stanowiących rozprawę doktorską)

Niniejszym oświadczam, że mój udział w artykule naukowym autorstwa: Mariusz Borkowski, Piotr Batys, Oleg M. Demchuk, Przemyslaw B. Kowalczuk, Jan Zawala p.t. *Amino-Acids Surfactants and n-Octanol Mixtures-Sustainable, Efficient, and Dynamically Triggered Foaming Systems*, wchodzącym w skład zbioru opublikowanych i powiązanych tematycznie artykułów naukowych stanowiących rozprawę doktorską autorstwa Mariusza Borkowskiego p.t. *Influence of liquid physicochemical properties on single bubble motion and stability of foam films and foams* polegał na:

- udziale w opracowaniu metodologii opisanych badań,
- przeprowadzeniu symulacji metodą dynamiki molekularnej,
- udziale w formalnej analizie wyników badawczych i ich interpretacji,
- udziale w przygotowaniu manuskryptu publikacji naukowej,
- udziale w pracach związanych z recenzją oraz edytowaniem manuskryptu.

18.09.2023 Piotr Batys
....
Data, czytelny podpis współautora

[1]niepotrzebne skreślić

Załącznik nr 10

Lublin, 11.09.2023 r.
Miejscowość, data

Oleg M. Demchuk
Imię (imiona) i nazwisko współautora

OŚWIADCZENIE WSPÓŁAUTORA

(wypełniają tylko współautorzy publikacji wchodzącej w skład zbioru artykułów stanowiących rozprawę doktorską)

Niniejszym oświadczam, że mój udział w artykule naukowym autorstwa: Mariusz Borkowski, Piotr Batys, Oleg M. Demchuk, Przemyslaw B. Kowalczuk, Jan Zawala p.t. *Amino-Acids Surfactants and n-Octanol Mixtures-Sustainable, Efficient, and Dynamically Triggered Foaming Systems*, wchodzącym w skład zbioru opublikowanych i powiązanych tematycznie artykułów naukowych stanowiących rozprawę doktorską autorstwa Mariusza Borkowskiego p.t. *Influence of liquid physicochemical properties on single bubble motion and stability of foam films and foams* polegał na:

- syntezie, oczyszczeniu i wydzieleniu badanych związków,
- udziale w przygotowaniu manuskryptu publikacji naukowej,
- udziale w pracach związanych z recenzja oraz edytowaniem manuskryptu.

11.09.2023
....
Data, czytelny podpis współautora

[1] niepotrzebne skreślić

Załącznik nr10

Trondheim (Norwegia), 11.09.2023 r.
Miejscowość, data

Przemysław B. Kowalczuk
Imię (imiona) i nazwisko współautora

OŚWIADCZENIE WSPÓŁAUTORA

(wypełniają tylko współautorzy publikacji wchodzącej w skład zbioru artykułów stanowiących rozprawę doktorską)

Niniejszym oświadczam, że mój udział w artykule naukowym autorstwa: Mariusz Borkowski, Piotr Batys, Oleg M. Demchuk, Przemyslaw B. Kowalczuk, Jan Zawala p.t. *Amino-Acids Surfactants and n-Octanol Mixtures-Sustainable, Efficient, and Dynamically Triggered Foaming Systems*, wchodzącym w skład zbioru opublikowanych i powiązanych tematycznie artykułów naukowych stanowiących rozprawę doktorską autorstwa Mariusza Borkowskiego p.t. *Influence of liquid physicochemical properties on single bubble motion and stability of foam films and foams* polegał na:

- uczestnictwie w opracowaniu metodologii opisanych badań,
- udziale w formalnej analizie i interpretacji wyników badawczych,
- udziale w przygotowaniu manuskryptu publikacji naukowej,
- udziale w pracach związanych z recenzją oraz edytowaniem manuskryptu,
- nadzorze nad prowadzonymi badaniami.

11.09.2023

....
Data, czytelny podpis współautora

[1] niepotrzebne skreślić

Załącznik nr10

Kraków, 11.09.2023 r.
Miejscowość, data

Jan Zawała
Imię (imiona) i nazwisko współautora

OŚWIADCZENIE WSPÓŁAUTORA

(wypełniają tylko współautorzy publikacji wchodzącej w skład zbioru artykułów stanowiących rozprawę doktorską)

Niniejszym oświadczam, że mój udział w artykule naukowym autorstwa: Mariusz Borkowski, Piotr Batys, Oleg M. Demchuk, Przemyslaw B. Kowalczuk, Jan Zawala p.t. *Amino-Acids Surfactants and n-Octanol Mixtures-Sustainable, Efficient, and Dynamically Triggered Foaming Systems*, wchodzącym w skład zbioru opublikowanych i powiązanych tematycznie artykułów naukowych stanowiących rozprawę doktorską autorstwa Mariusza Borkowskiego p.t. *Influence of liquid physicochemical properties on single bubble motion and stability of foam films and foams* polegał na:

- udziale w opracowaniu koncepcji oraz idei badawczej,
- udziale w opracowaniu metodologii opisanych badań,
- udziale w formalnej analizie i interpretacji wyników badawczych,
- pozyskaniu zasobów finansowych do prowadzenia badań
- udziale w selekcji danych,
- udziale w przygotowaniu manuskryptu publikacji naukowej,
- udziale w pracach związanych z recenzją oraz edytowaniem manuskryptu,
- nadzorze nad prowadzonymi badaniami,
- administrowaniu.

11.09.2023
....
Data, czytelny podpis współautora

---

[1]niepotrzebne skreślić